Thermal analysis of combined Organic Rankine-Vapour compression system for heating and cooling applications

By

Mohammed Ridha Jawad Al-Tameemi

Submitted in fulfilment of the requirements for the degree of
Doctor of Philosophy (PhD)

System, Power & Energy Research Division
School of Science and Engineering
College of Engineering
University of Glasgow
Glasgow, UK

September 2019

Abstract

Climate change due to global warming is a matter of major global concern. Greenhouse gases emissions are a key culprit in this process. It is therefore important to reduce energy consumption in order to protect the environment. The decarbonisation of the heating sector would have a significant positive impact on the environment.

A wide range of heating technologies have been investigated and developed, such as gas boilers, electric restrictive heaters, heat pumps (HP), and others. In order to reduce fossil fuel consumption and greenhouse gas emissions, researchers have focused on improving the performance of the existing technologies as well as on developing new fuel-efficient systems such as cogeneration and trigeneration cycles. These integrated technologies allow the production of multi-mode energies including heating, cooling, and/or mechanical power from the same primary energy source. The energy source can be a fossil fuel, or renewable energy such as solar, geothermal, biomass or wasted heat. Waste heat utilization (from a data centre, internal combustion engine, chamber exhaust stream, etc.) also has the potential of enhancing the system performance by reducing fuel consumption.

In this thesis, an innovative gas fuelled heating system based on a combined heat engine and its reverse heat pump cycle is proposed and investigated. This system consists of a gas burner, an organic Rankine cycle power generator, and an air source heat pump vapour compression cycle. For the theoretical analysis, in-house MATLAB code is developed, and the steady state results are compared with the results acquired from ASPEN PLUS as a benchmark. Both software programs use REFPROP as the database for working fluid thermophysical properties. In order to identify a suitable working fluid for each cycle, a comparative study on various working fluids was initially carried out. The selection of refrigerant was based on performance and environmental safety profile. The proposed cycle is designed for domestic hot water supply and utilizes gas burner flue gases and ambient air to enhance the system overall fuel to heat efficiency while maintaining the heat pump cycle in a frost free state at low ambient temperature. The combined cycle shows promising performance, with a fuel to heat efficiency of 136%. However, the results also show that ambient air temperature fluctuations can have a significant impact on the combined system's performance. To tackle this, various control strategies are proposed and investigated. Also, a dynamic model has been built using ASPEN PLUS software to simulate and validate the control strategy.

Abstract

Waste heat can offer a steadier heat source than ambient air. Chapter six proposes a combined system where the waste heat from the data centre is recovered to provide a cooling effect for the data centre, with the recovered heat used for central heating. The results show that the system can maintain the data center (DC) room temperature at between 18-25 ^{o}C and heat the returnee water from 50-80 ^{o}C. The obtained fuel to heat efficiency is 137%. In addition, various control strategies have been proposed to tackle the variations in the DC workload. A dynamic model is used to display the control strategies parameters with respect to time.

Another intended application for the proposed system is the production of refrigeration load by waste heat recovery from a diesel engine exhaust stream, as presented in chapter seven. The results show that 47% of the wasted heat can be converted by the combined cycle into useful refrigeration, with an outlet air temperature of -18 ^{o}C. A control strategy (in steady and dynamic modes) is proposed to simulate the combined cycle under variable diesel engine speed and load.

Acknowledgements

First and foremost, I wish to offer this endeavour to Allah (Almighty God), the most merciful, for the wisdom, strength, peace of mind and good health he bestowed upon me which allowed me to finish this thesis.

I would like to express my sincere gratitude to my supervisor, Dr. Zhibin Yu, for his continuous support and guidance during my PhD study, and for his patience, motivation, enthusiasm and immense knowledge.

My sincere thanks also to the Iraqi government, especially the Ministry of Higher Education and Scientific Research, and to the University of Diyala and its School of Engineering for giving me this scholarship opportunity and supporting me and my family by all necessary means.

I am forever in debt to my family, especially my loving mother (Najiyah Hussein) who blessed me with her continuous prayers and encouraged me throughout my study. To the spirit of my beloved father who has passed away. Also, to my kind and supportive wife, who was always by my side when I needed her most and helped me so much in completing this thesis, and also to my kids (Farah and Yasameen) who were my inspiration during this journey. Last but not least, to my sisters and my relatives for believing in me.

My thanks and appreciation go to my colleagues, friends and department staff who have helped me in various ways, with special thanks to Dr. Youcai Liang, Dr. Guopeng Yu, and Dr. Peter Collings.

Finally, I would like to thank all the lovely staff at the University of Glasgow including those at the Language Centre, the administration team, library and IT staff, and all the other university people who made my studies at the University of Glasgow such a great experience.

Author's Declaration

I declare that, unless explicitly stated to be the contribution of others, that this thesis is entirely my own work and has not been submitted for any other degree, at the University of Glasgow or elsewhere.

Mohammed Al-Tameemi

September 2019

Preface

Publications

1. Collings, P., **Al-Tameemi, M.**, Yu, Z., *A Combined Organic Rankine Cycle-Heat Pump System for Domestic Hot Water Applications.* 12th International Conference on Heat Transfer, Fluid Mechanics and Thermodynamics, Malaga, Spain, 11 - 13 Jul 2016.

2. Liang, Y., **Al-Tameemi M.**, Yu Z., *Investigation of a gas-fuelled water heater based on combined power and heat pump cycles*. Applied Energy, 2018. 212: pp. 1476-1488.

3. **Al-Tameemi M.**, Liang, Y., Yu, Z., *Numerical analysis of a heat pump based on combined thermodynamic cycles using ASPEN plus software*. HEAT POWERED CYCLES, 2018, Conference Proceedings, pp. 412.

4. **Al-Tameemi M.**, Liang, Y., Yu, Z., *Combined ORC-HP thermodynamic cycles for DC cooling and waste heat recovery for central heating*. Energy Procedia, 2019. 158: pp. 2046-2051

Table of Contents

List of Tables

List of Figures

List of Symbols

Symbols	Description
A_{rcs}	Refrigerant cross section area
Bo	Boiling Number
C	Kinetic energy
Co	Convection Number
C_p	Specific heat
D	Pipe diameter
f	Friction Factor
Frl	Froude Number
g	Gravity
h	Specific Enthalpy
$\bar{h}$	Molar Enthalpy of substance
$\bar{h}^o$	Molar Enthalpy of substance at reference state
$\bar{h}_f^o$	Molar Enthalpy of combustion
I	Exergy destruction
k	Thermal Conductivity
$\dot{m}$	Mass flow rate
N	Number of Moles
Nu	Nusselt Number
P	Pressure
Pcr	Critical pressure
Pr	Prandtl Number
Re	Reynolds Number
s	Specific Entropy
Q	Heat
t	Wall thickness
T	Temperature
U	Total heat coefficient
V_r	Refrigerant volume

W	Work
x	Quality
Zg	Potential energy
α	Heat Transfer Coefficient
β	Plate Chevron Angle
μ	Dynamic Viscosity
v	Kinematic Viscosity
ρ	Density
μ	Efficiency
Subscripts	
evap	Evaporator
ref	Refrigerant
cond	Condenser
mix	Mixture
P	Products
R	Reactants
w	Water
cw	Cold water
cs	Cold stream
HS	Hot stream
inj	Injection
suc	Suction
exh	Exhaust

Abbreviations

AC	Air conditioner
ALT	Atmospheric lifetime
AR	Absorption Refrigeration
CCHP	Combined cooling, heating and power
CHP	Combined heat and power
COP	Coefficient of performance
COP_S	Coefficient of performance of a system
CRS	Cascade refrigeration system
DC	Data center
DE	Diesel engine
GSHP	Ground source heat pump
GPHP	Gas powered heat pump
GWP	Global warming potential
HP	Heat pump
HPGHP	Hybrid powered gas engine heat pump
HXs	Heat exchangers
ICE	Internal combustion engine
LMTD	Logarithm means temperature difference
LPG	Liquefied petroleum gas
ORC	Organic Rankin cycle
PCM	Phase change material
PEMFC	Proton exchange membrane fuel cell
PPTD	Pinch point temperature difference
ODP	Ozone depletion potential
SE	Stirling Engine

Chapter 1: Introduction

1.1 Overview

Over the last decade, dependence on fossil fuel as an energy source has increased remarkably. It is estimated that overall global oil consumption in 2010 was around 86.4 million barrel/day. However, the daily demand for crude oil has been predicted to reach over 100 million barrel/day by 2019 [1]. This growth in demand leads to various environmental and economic challenges, as fossil fuel usage has numerous major impacts such as acid precipitation, ozone layer damage, resource depletion, and global warming [2]. Fossil fuel combustion contributes to around 65% of total global greenhouse gas emissions. Coal, oil, and natural gas produce 45%, 35% and 20% of these emissions respectively [3]. The depletion of fossil fuel reserves and ever-increasing prices are further future challenges. To overcome these challenges, two main approaches can be taken: to develop and enhance the use of alternative energy sources, especially renewable energy sources such as solar, geothermal, wind, biomass and waste heat, and to enhance the energy efficiency of existing technologies [4].

1.2 Available heating technologies

1.2.1 Electric heaters

Electric heaters are among the most readily available heating technologies that produce heat from electricity by thermal resistance. Although their use is gradually declining due to more advanced heating technology, they are still a viable option in areas where electricity production is both low cost, and comes with low greenhouse gas emissions. For instance, in Québec/Canada, 98% of electricity produced by hydro-electric dams, so electric heaters are an attractive low-cost residential heating choice [5].

It is well known that electric heaters can convert nearly 100% of the supplied electricity into heat. Balke, E. et al. [6] conducted an experimental and theoretical study on various residential water heating technologies including solar thermal, heat pump (HP), electric resistive heaters, and combinations of them. Although the results showed that electric heaters achieved the lowest coefficient of performance (COP) of 0.95, they achieved quite steady performance over the

course of a year, with mild decline in performance during summer months due to the reduction in heat load with the higher input water temperature and without a proportional change in total energy consumption. In contrast, a solar thermal preheat tank supplying HP water heater achieved a COP of 2.87 compared to 1.9 for HP alone.

1.2.2 Gas Boilers

A gas boiler is a popular choice for district heating, particularly in countries where natural gas represents a significant energy source. For instance, in Europe, 80% of energy is provided by natural gas [7], while in Beijing/China, 11.6 billion cubic meters of natural gas were utilised in 2015 for district heating in winter [8]. Conventional gas boilers have an energy efficiency of around 90%, with a significant amount of heat rejected in the form of flue gases [9]. The emission flue gas temperature ranges between 150-200 ^{o}C, which holds about 10-12% of the fuel's lower caloric value [9, 10]. Recovering heat from the boiler exhaust stream (in a condensing boiler) therefore has the potential to improve the boiler's efficiency and decrease CO_2 emissions by reducing natural gas consumption. Since natural gas is a high hydrogen compound, its combustion will generate water vapour with a latent heat occupying approximately 70-80% of the overall exhaust heat [8, 10]. However, to recover heat from this latent heat loss, the flue gases need to be cooled down to a temperature below the dew point, which is around 55 ^{o}C.

Three main heat recovery methods have been proposed in the literature: economizer, air preheater, and heat pump. Economizers use the boiler's returnee water as a cold source with which to exchange heat with the exhaust stream. However, the boiler feed water temperature usually ranges between 45-60 ^{o}C, which is close to the flue gas condensation point, thus limiting the amount of heat recovery [8, 10]. Since most latent heat is still in the flue gas, the boiler efficiency improvement achieved is small, at about 2%, making overall efficiency approximately 93% [9, 10]. An air preheater is another method for flue gas heat recovery. It uses a boiler's oxidising air to cool the flue gas. In addition to heat exchange, the flue gas undergoes phase change, while the air has no phase change. This leads to incompatible thermal capacity between the two streams, which will limit the heat recovery capacity [8, 10]. The most promising method for flue gas heat recovery is the use of HPs. The heat pump is used to generate cold water at between 20-30 ^{o}C, which is used as a cold source to exchange heat with the flue

gas. Thus, the flue gas temperature can be decreased to around 25-35 ºC, well below the gas dew point. This leads to vapour condensation, with a significant amount of latent heat released for recovery. The use of HP as a heat recovery method has increased boiler efficiency by around 10-12% [11, 12].

1.2.3 Heat pump systems

Heat pump technology is a sufficiently simple and mature reverse heat engine that uses mechanical power to generate heat transfer between heat source and sink. The principle of a heat pump operation has been understood for decades, and the first-ever published scientific application of a reversed heating engine as a heat pump for building heating and cooling was presented by Lord Kelvin in 1852. In the early 20th century, the Scottish engineer and university professor James Albert Ewing included in his book *The Steam Engine and Other Heating Engines* descriptions of refrigeration and the use of a reverse heating engine in building heating [13, 14].

Today, heat pump systems are widely used in different applications, such as space heating and cooling, refrigeration, and hot water supply on both industrial and residential scales. The principal function of a HP cycle is either heat rejection into the environment to cool a space, or heat extraction from a source to be used for heating. Various forms of thermodynamic cycles can be used to achieve these functions, the predominant one being the vapour compression cycle. In this cycle, the refrigerant gas is initially evaporated, and is then compressed and condensed in order to transfer heat from source to sink, as shown in Figure 1.1.

Heat pumps represent an efficient and attractive heating and cooling technology as they can transfer heat from source to sink using less work than is required to convert primary energy to heat. i.e., the quantity of heat delivered is higher than the power required. Thus, heat pumps are highly energy efficient, as is represented by their COP [14, 15]. In the UK, most air sourced and ground sourced HP systems already in use have a COP range of between 1.2-3.6 [16].

Various types of heat source are used in the HP cycle, such as air, ground source, water, and solar, as will be discussed in more detail later in this chapter.

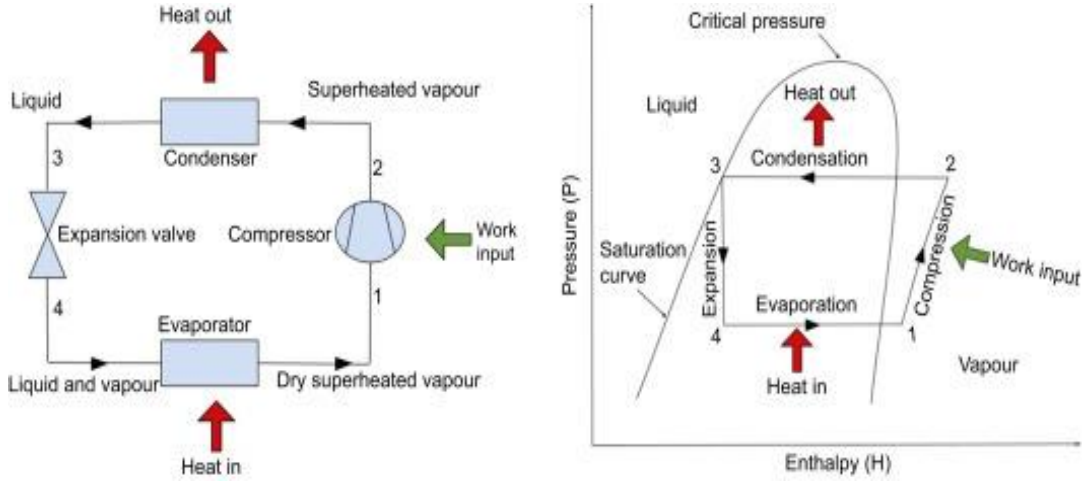

Figure 1.1: A conceptual model of a heat pump (left) and an idealized cycle represented on an enthalpy-pressure (right) [13].

1.2.4 Combined heat and power systems (CHP)

Combined heat and power (CHP) are integrated systems which simultaneously produce electricity and heating from a single energy source. The energy source can be from fossil fuels (e.g. natural gas or coal), nuclear fuel, or renewable sources (e.g. geothermal, solar, or biomass). Combined cooling, heating and power (CCHP) is slightly different from CHP in that it also produces an additional cooling effect. A CHP system can convert 60-80% of the primary energy source into useful thermal energy [17, 18]. Generally, there are two types of CHP: topping cycle and bottoming cycle. In a topping cycle, the fuel is used to mainly generate electricity, with the additional heat generated used for additional applications such as industrial processes if high grade heat is generated, or space heating and hot water supply using low grade heat. In the bottoming cycle, heat production is the primary application and any extra-energy not used for heating is converted into electricity. CHP usually consist of a prime mover such as an Organic Rankine cycle (ORC) or a Stirling engine (SE), etc. and a heat recovery system (usually a heat exchanger) [19]. The different types of prime mover used in CHP systems are discussed in chapter two.

1.3 Types of heat sources

Various types of environmental heat source have been used in HP, ORC and CHP cycles, such as air, water, ground, waste heat and solar.

Ideally, a heat source should have the following properties:

- High and stable temperature during the various seasons
- Widely available
- Not corrosive or pollutant
- Favourable thermophysical properties
- Low investment and operation costs

1.3.1 Air source

Air is an attractive heat source as it is free and readily available, and when used as a heat source, the heat exchanger can be compact, with low thermal resistance. Thus, the system can be more economical in terms of capital cost. However, some challenges arise when air is used; for instance, air is more volatile than other heat sources, leading to fluctuations in system performance with ambient temperature variations. Furthermore, in a HP cycle, the moisture in ambient air can lead to frost formation on the evaporator, particularly when temperatures fall below 2-5 ^{o}C. This will require a reversal of the heat pump cycle or the use of other energy consuming means to defrost the exchanger, leading to degraded performance [13, 14]. In a cold climate, the capacity of the HP can decline dramatically with colder outdoor temperatures, particularly for ambient temperatures in the sub-zero region where the heating load is required the most. In this situation, an alternative heating source is frequently required, such as exhaust air.

1.3.2 Waste heat sources

Waste heat is a viable heat source which can offer various temperature ranges. It is also a free energy source that would otherwise be wasted in the environment. Its recovery is capable not only of enhancing system performance, but also aiding the reduction of greenhouse gas emissions.

Various forms of waste heat have been used in the literature, such as exhaust air from a ventilation system, flue gases from combustion process, data centre (DC) waste heat, and others. Hebenstreit, B. et al. [12] showed that using HP cycle for waste heat recovery from a biomass boiler has both environmental and economic benefits. The study showed that operation costs decreased by approximately 2-13 %. Likewise, waste heat recovered from a coal fired power plant flue gases via a condensing heat exchanger has the advantage of increasing the longevity of the equipment and reducing the dust (residual particles) in the flue gases, which can have a positive environmental impact [20]. Wei, M. et al. [10] conducted an experimental study on a vapour compression heat pump for waste heat recovery from a boiler's exhaust stream. The use of vapour HP improved boiler efficiency by over 10%, with the flue gas temperature reduced to below 30 ^{o}C.

Oró, E., et al [21] proposed the use of DC wasted heat to heat water in a nearby swimming pool. In this design, the heat is transferred through water to water heat exchangers and the returnee water temperature is used to cool the DC. The results showed that recycling wasted heat can reduce natural gas consumption by approximately 54%, with an associated redaction in operational expenses of 16%. In another study, a vapour compression heat pump system was proposed for DC waste heat recovery [22]. The HP cycle is used to upgrade the temperature of the wasted heat up to 70 ^{o}C, which could be convenient for domestic hot water and district heating networks. The COP achieved ranged between 3-6 for different wasted heat stages recovered by various heat pump configurations.

Ebrahimi, K. et al. [23] conducted a thermodynamic and economic analysis of an ORC module for DC waste heat recovery for electricity production. The results show that R134a and R245fa as IT server coolant and ORC refrigerant respectively had the best thermal efficiency for the selected DC operating conditions.

Waste heat from diesel engine flue gasses is also a viable heat source which can offer a high temperature range. Diesel engine waste heat recovery via an ORC cycle is presented in chapter two.

1.3.3 Ground or Geothermal source

Ground or geothermal source, including groundwater, is another attractive heat source due to the relatively stable temperatures involved, with lower variations throughout the year than ambient air. It also has a higher thermal capacity, with temperatures closer to the intended indoor temperature, resulting in higher thermal efficiency due to smaller differences between the source and sink temperatures [13, 14, 24]. However, a system for extracting heat from the ground is often expensive to design and install, and requires the involvement of different types of expertise. In addition, leaking from the coils and pipes of the system poses a problem [14].

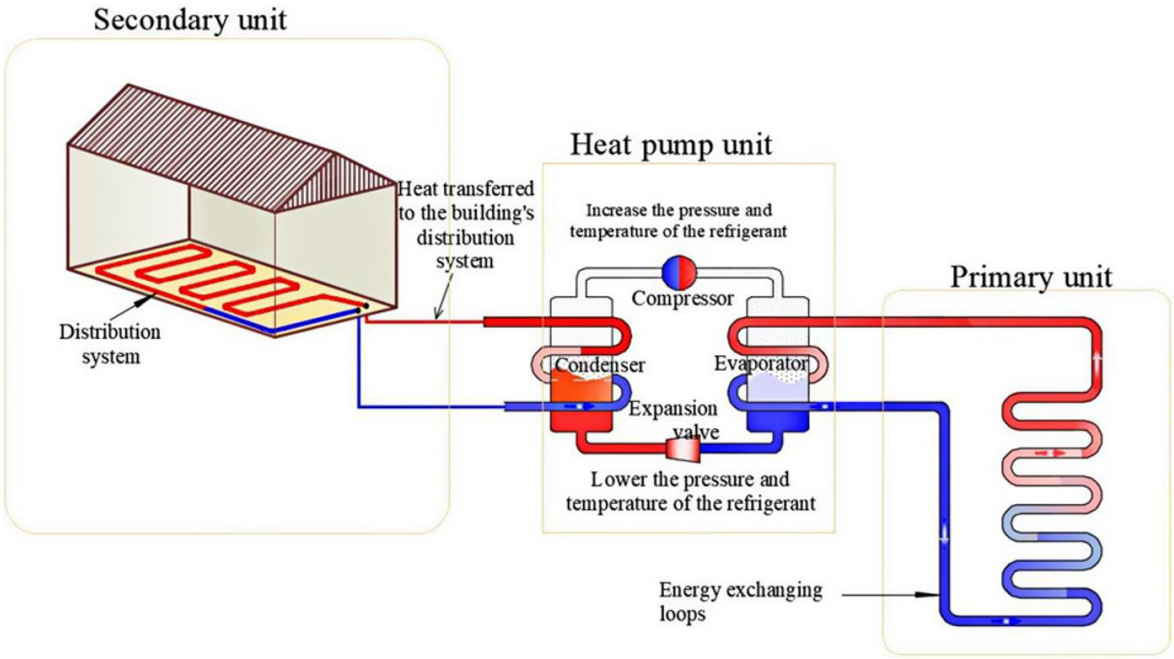

Figure 1.2: Ground source heat pump schematic diagram [24].

In ground source heat pump system (GSHP), heat can be extracted from the ground using pipes that are laid down either horizontally or vertically, depending on the area available, intended

system use, and cost. GSHP system can utilise a geothermal source temperature of up to 73 ^{o}C for district heating [25]. Generally, GSHP is composed of a primary unit (heat exchanger), a secondary unit (network of underfloor pipes for heat distribution), and a heat pump unit, as shown in Figure 1.2 [24]. GSHP can also be classified into open loop and closed loop systems based on the connection between the ground heat exchanger and the HP unit. In an open loop system, groundwater is pumped through the HP to extract heat, while in a closed loop system, a heat carrier fluid is used as intermediate medium between the ground and the working fluid, for example water, water with biocide, antifreeze, or a saline solution [24, 26].

Zhen, J. et al. [27] carried out field measurements on a groundwater sourced heat pump system designed for an airport on the Tibetan plateau, and compared the results with an existing HP in the same region. The results showed that GSHP can achieve a higher and more stable COP of around 5 compared to a COP of between 1.98-2.89 for an air sourced heat pump. Three years of data from a large scale GSHP for a building at De Montfort University/UK showed satisfactory system performance with a seasonal performance factor of between 2.49-2.97. In addition, the fluctuations in the ground loop average fluid temperature were relatively minimal compared to air temperature variations over the course of the year [28].

For a geothermally driven ORC cycle, the cycle configuration can be either a binary or a single cycle design. In a binary geothermal power plant, heat from the geothermal fluid is exchanged with the ORC working fluid via the evaporator. While in a single cycle, the ORC working fluid draw the heat directly from the geothermal heat source. Liu X. et al [29] investigate the performance of an ORC cycle with R245fa under difference geothermal heat source inlet temperature (80-180 ^{o}C). The results showed that the ORC cycle can produce a net power output between 0.473-17.05 kW and an overall efficiency of around 8%. The performance of an ORC cycle with R245fa and two stage evaporation designed for geothermal power production is presented by Li, T. et al [30].The results showed that two stage ORC can produce more power output than single stage evaporation process, particularly for the intermediate geothermal water temperature of 105 ^{o}C.

1.3.4 Water source

Water is another good heat source with relatively steady temperature compared to air. Various source of water can be used, such as surface water, groundwater (which can be considered a geothermal source), seawater, and wastewater. Surface water sources such as rivers and lakes are good heat sources in principle, but have the limitation of low temperatures in winter months (between 2-4 ^{o}C), with a risk of freezing and consequent frosting on the evaporator. In contrast, seawater can have a temperature of around 5-8 ^{o}C, with a very low risk of freezing. However, its use is usually limited to medium-large scale heat pump installations. Fouling is another drawback of seawater use, which requires the use of corrosion-resistant heat pump parts [14, 31].

Wastewater is another attractive source due to its relatively high and constant temperature performance over the course of a year. Examples of wastewater are public sewage water, industrial effluents, cooling water from power plants or industrial processes, etc. [32, 33]. Similar to seawater, wastewater can also cause fouling deposits on the heat exchangers resulting in reductions in performance, and it may even block the heat exchanger [32].

Liu, Z. et al. [34] conducted an evaluation of a river water sourced HP system used in an energy station in Shanghai/China. The results supported a linear relationship between river water and air temperature throughout the year. In winter heating mode, the COP of the HP unit alone and the overall COP of the system (including the river water pump power consumption) were 7.4 and 5.2, respectively. In cooling mode, the COP values were 6.5 and 2.6, respectively. Similarly, Zou and Xie [35] also reported that lake water temperature has a linear relationship with air temperature. In their experimental study, a lake water sourced HP used in a university building achieved average COP values of 4.27 and 3.81 for cooling and heating modes, respectively.

1.3.5 Solar source

Solar heat source systems can have similar behaviour to air source systems in terms of variability of performance and low efficiency in certain circumstances. However, in contrast to air, which is free source, solar heat is usually costly to obtain. In addition, an additional back-up or storage system is often required with solar source due to its dependency on daily

irradiation levels. It is therefore mostly used as a supporting system to an existing heating technology [36, 37].

Energy and exergy analysis has been carried out on a novel solar driven combined heat and power system [38]. The combined ORC- absorption HP system is totally dependent on solar as the primary energy source. The results showed that the cooling power increased by 48.5% by adopting the double effect absorption chiller. Simultaneously, in spite of a fall in net power production by 27%, the combined system heat and power efficiency increased by 96% as a result of the 20.5% rise in heating power. Also, the solar collectors had the highest exergy destruction rate among all system components.

A thermal energy storage (TES) system integrated with an ORC power cycle driven by a non-concentrated solar array collector has also been designed and examined [39]. A mathematical evaluation was carried out to compare and contrast the climates of Cyprus and the UK over specific months (January, April and July). The results showed that by using evacuated flat-plate collectors, the solar-CHP system achieved 4.4-6.4% solar to electricity conversion efficiency in the UK, and 6.3-7.3% in the Cyprus.

A hybrid combined heating and power system was proposed by Wang and Yang [40]. The system consists of a biomass gasification subsystem to power an internal combustion engine for electricity generation. Exhaust gas from the ICE is used to drive an absorption chiller, which is used to produce chilled water while the wasted heat from the biomass gasification process and ICE assisted by the solar evacuated collector are used to supply hot water. The results showed that the proposed combined system achieved a primary energy ratio and exergy efficiency of 57.9% and 16.1%, respectively. In addition, the reduction in carbon dioxide emissions was 95.7%.

1.4 Challenges in existing heating technologies

The main challenges encountered in existing heating technologies can be summarized as follow:

1. Electric heaters can achieve a maximum COP of 1 with limited options of development due to the simplicity in design and work concept.

2. In a gas burner, a significant amount of heat is rejected in the flue gases, which will limit the system thermal efficiency to around 90% for most condensed gas boilers.

3. The main challenge faced by an air source HP system can be summarized as follow:

    - The fluctuation in system performance with ambient air variations on daily and seasonal bases. As ambient temperature declines, the temperature lift across the HP cycle will rise, leading to a reduction in the COP.

    - A low ambient temperature can result in frost formation on the HP evaporator, leading to further reductions in performance.

    - Furthermore, in a HP cycle used for hot water supply, the required water temperature is often high (usually above 65 ^{o}C to ensure the death of any legionella bacteria). Such a high temperature will reduce the COP of the system, as high discharge pressure is required.

    - An electrically driven HP system experiences energy losses during electricity transmission through the power grid. This will reduce the system's overall fuel to heat efficiency.

4. In a standalone ORC power plant, not all the heat produced can be converted into useful mechanical work because part of the heat should be rejected into the environment as wasted heat in order to satisfy the second law of thermodynamic.

5. In CHP system producing multi energy modes such as power, heating and cooling demands, can face challenges in balancing between these energy modes particularly during the various seasons of the year.

1.5 Motivation for the present work

The motivation behind the current study is to design and investigate a combined system that can overcome the challenges faced by standalone HP, ORC and gas burner as follow:

- To overcome ambient temperature fluctuation in HP system, a mixture of ambient air and gas burner flue gases is used to feed the heat pump evaporator. This can also ensure that frost formation on the evaporator is prevented.

- To avoid the high temperature lift in the HP system, water heating is designed to occur in two stages, through HP and ORC condensers respectively. This will reduce the discharge pressure required for the HP cycle and maintain a high COP.

- In the combined system, all the mechanical power produced from the ORC power plant will be transferred by direct coupling with the HP cycle to be transformed into heat energy. This will eliminate both the electric generator of the ORC system and the electric motor of the HP, thereby avoiding electrical transmission losses.

- By recovering all the heat rejected in the gas burner exhaust stream, the gas burner efficiency is expected to improve. In addition, the rejected heat from the ORC cycle is totally recovered. This will improve the overall fuel to heat efficiency of the combined system.

1.6 Aims of this research

The aims of this research is to theoretically investigate a gas driven combined ORC-HP system as follow:

- Comparing different working fluids for HP and ORC cycles respectively in terms of efficiency, safety and environmental aspects.

- Investigating and comparing the combined system performance using different configurations, including combined system with and without post heater, a combined system with HP condenser as the first heating stage and a system with ORC condenser as the first heating stage.

- Investigating the combined system for the following applications: domestic hot water supply, data centre cooling with simultaneous central heating, and providing refrigeration load from diesel engine waste heat.

- Implementing various control strategies to achieve the maximum obtainable combined system thermal efficiency when working conditions varies. These working conditions includes variations in ambient air temperature, Data centre workload, and diesel engine power production.

To achieve these, the combined cycle has been thermodynamically analysed in terms of the first and second laws of thermodynamics. An in-house MATALB code is developed for this purpose and the results are compared and validate with that obtained from ASPEN PLUS software [41]. In both simulation models, REFPROP database [42] is used to obtain the thermophysical properties of the working fluids to ensure accurate comparison of the obtained results.

1.7 Outline of the thesis

A brief introduction of the available heating technologies with their used heat sources and prime movers has been provided in this chapter. An extensive literature review of the various combined heat and power cycles that have been used in different applications is presented in

chapter two. This literature review is used as guidance with which to understand the thermodynamic principles and concepts behind each of these technologies, their design methodology and optimisation approaches, and as verification for the current research. Chapter three demonstrates the theoretical laws and mathematical equations adopted in this work.

Chapter four presents a comparative assessment of various working fluids for both ORC and HP cycles in terms of system performance in heating and cooling modes, and their respective environmental impacts. Chapter five describes the design and efficiency performance of the proposed combined system used for domestic hot water supply. It also discusses the proposed control strategy to tackle the effects of ambient temperature variation on the system performance. The results of these strategies have been verified by a dynamic model using ASPEN PLUS software.

Chapter six focuses on the use of the combined system for waste heat recovery from a small-scale data centre to provide cooling. The recovered heat is used to produce hot water for a central heating application. To tackle the variations in data centre cooling load, various control strategies were proposed and investigated.

Chapter seven discusses the use of the combined ORC-HP cycle as a bottoming cycle for a diesel engine. The heat recovered from the diesel engine flue gases is used to power the ORC cycle which then mechanically drive the HP cycle to provide refrigeration load. The simulation is conducted under the diesel engine rated condition. In addition, the effects of various diesel engine power and rotation speed on the combined system performance are studied.

Finally, chapter eight presents a summary of the work presented in this thesis with a plan for future work.

Chapter 2: Literature review

2.1 Introduction

In cold countries such as the UK, heating applications consume approximately 50% of the energy produced, which is heavily reliant on burning fossil fuels such as natural gas and coal. Such consumption accounts for nearly one third of carbon emission. In addition, the ever-increasing demand for, and cost of, fossil fuel, along with tighter environmental regulations regarding CO_2 gas emissions, have motivated researchers to focus on innovative fuel-efficient technologies. Cogeneration, trigeneration and multigeneration technologies have gained great attention in recent years due to their potential to provide more efficient usage of available energy sources. Cogeneration technology generally involves combined heat and power, combined cooling and power, and combined cooling and heating. Trigeneration involves the combination of cooling, heating and power. These integrated technologies allow the simultaneous production of heating, cooling and/or electrical or mechanical energy (power) from the same energy source. The energy source can be a non-renewable one such as oil, coal, or natural gas, or a renewable one such as solar, geothermal, biomass, wasted heat, or other types of renewable energy sources.

The essential part of any combined heat and power system is the prime mover, which means an engine that provides the CHP system with its mechanical power. This can be achieved by converting the chemical energy contained in fossil fuels into mechanical work such as reciprocating internal combustion engines, steam or gas turbines. In additions to the heat generated from combustion, ORC and Stirling engine can be powered by renewable energy sources. Fuel cells can also be used as a prime mover for the CHP due to its ability to supply power as a form of direct current in an electrochemical process similar to batteries [19]. In the following section, a brief description of the main prime movers will be presented.

2.2 Types of prime movers for CHP systems

2.2.1 Steam turbine

The steam turbine (also called the Rankine cycle) is one of the oldest and most established heat engines. Water, as the working fluid for this cycle, is boiled and superheated using a high energy heat source such as fossil fuels or nuclear reaction. This high energy fluid is then expanded through the turbine in a single or multiple stages to generate mechanical power. The turbine shaft is connected to the electrical generator to transform the mechanical work into electrical power, while the high-temperature and low-pressure water vapour is condensed through the condenser by a heat sink. This latent thermal energy is used for heating applications. A high pressure liquid pump is used to pump the condensed water to the boiler to continue the cycle over [19].

2.2.2 Gas turbine

A gas turbine cycle works on the thermodynamic principle of the Brayton cycle. It mainly consists of a compressor, a turbine, a combustion chamber, and an electric generator as shown in Figure 2.1. The ambient air is compressed by the compressor then mixed with the fuel inside the combustion chamber. A combustion process takes place to generate high pressure and temperature gases. The combustion products are expanded through the turbine to generate mechanical power which is used to generate electricity via a motor generator. The high temperature exhaust gas stream at the turbine outlet (450-600 ^{o}C) has the potential to be recovered for heating applications or power production [43, 44].

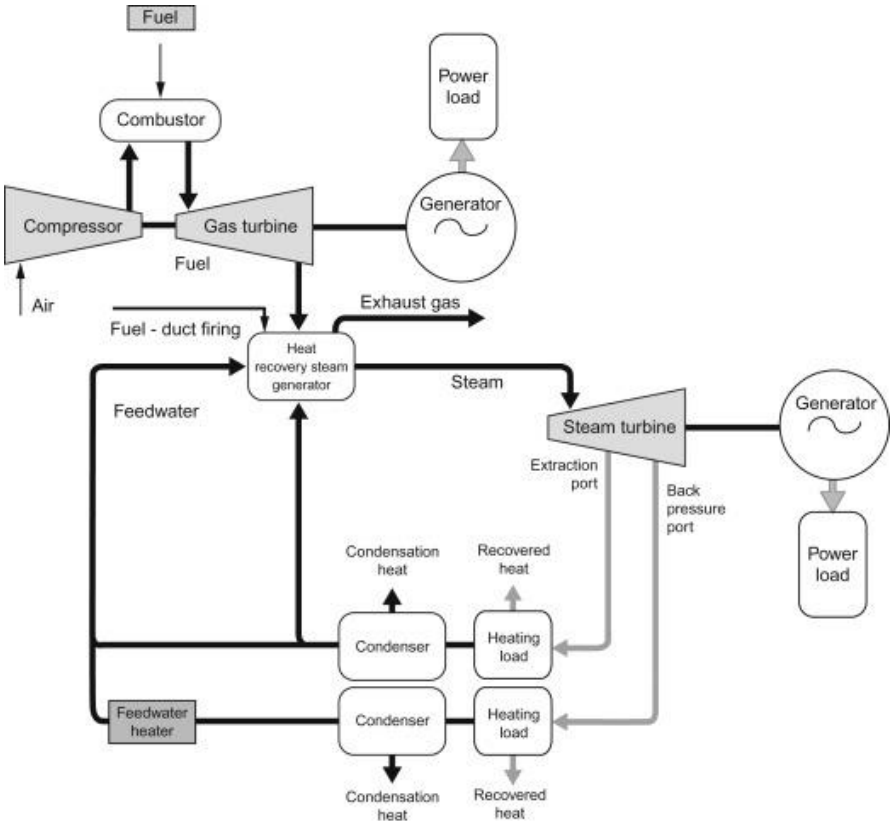

Figure 2.1: Schematic of a gas turbine combined CHP cycle [43]

2.2.3 Reciprocating internal combustion engines

In a typical internal combustion engine (ICE), the pistons of the engine complete four main process (strokes) to convert the combustion reaction into mechanical power. Two common types of ICE are in service nowadays, the spark ignition engine which is fuelled by natural gas or gasoline, and the diesel engine where diesel fuel is ignited by the compression stroke. According to the second law of thermodynamics, not all the heat generated from the combustion process can be transferred into mechanical work. It is estimated that around 55% of the energy available in the fossil fuel is wasted in the ICE, of which 30-40% is contained in exhaust gases and 15% in jacket water [45]. It has been found that the temperature of the coolant fluid of the engine jacket can range between 80-90 ^{o}C, and the temperature of the combustion product exhaust stream can reach 400-600 ^{o}C. This wasted energy has the potential to be recovered by the CHP system to produce power and heating simultaneously, and even a cooling effect, as shown in Figure 2.2.

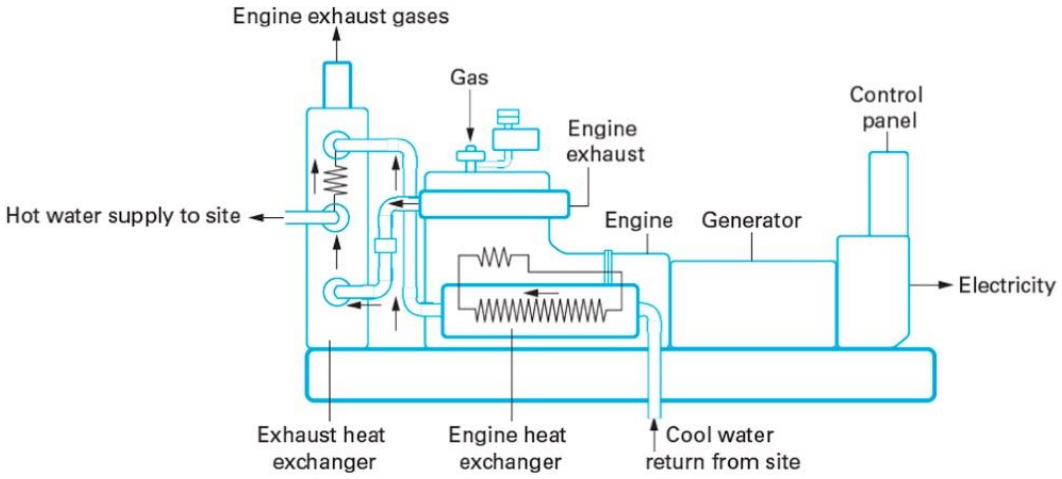

Figure 2.2: A packaged internal combustion engine CHP system [44]

2.2.4 Stirling engines

A Stirling engine is classified as a heat engine which operates on the Carnot cycle principle in which the working fluid, such as air or helium, undergoes four thermodynamic processes: compression, heating, expansion, and finally cooling, as shown in Figure 2.3. Stirling engines are approximately 30% efficient in converting heat into mechanical power. It is estimated that the fuel to electricity efficiency of a Stirling engine used as a micro CHP can reach 38% when its rejected heat is recovered [46]. However, some drawbacks related to electric power generation are encountered, such as low electric efficiency, difficulties in controlling the power system caused by the different types of heat exchangers used, and the requirement for high pressure working fluid.

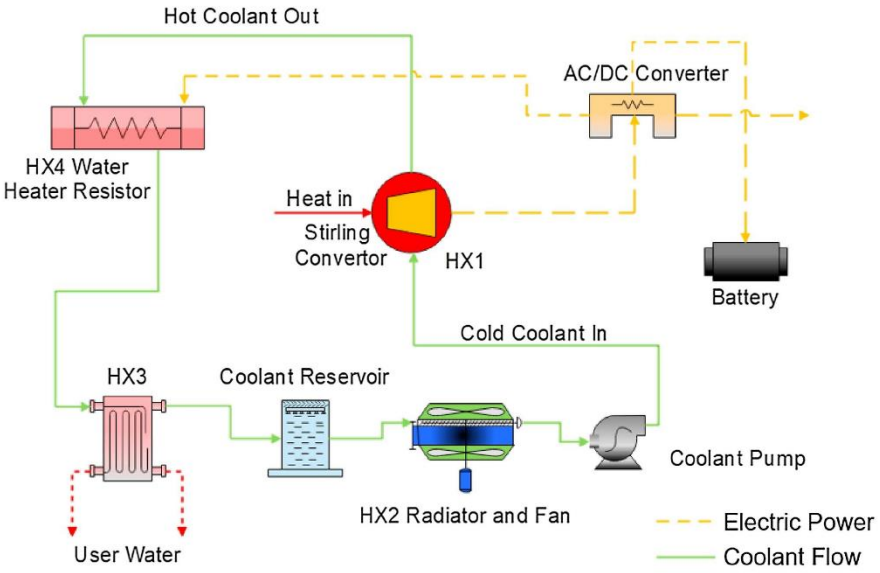

Figure 2.3: Configuration of the CCHP system with an SE prime mover [46]

2.2.5 Organic Rankine cycle

An organic Rankine cycle is a heat engine similar to a steam turbine which uses organic fluid rather than water as a refrigerant, and offers the potential of converting low grade thermal energy (less than 230 ^{o}C) into useful mechanical work, because organic fluids have lower boiling points and higher molecular masses. In addition, in an ORC cycle, lower evaporation pressure and a superheated degree of working fluid at the evaporator exit are required compared to the Rankine cycle. Furthermore, the selected working fluid should ideally be dry fluid to avoid condensation of the working fluid through the expansion process [47, 48]. The main parts of an ORC are an evaporator, a turbine, a condenser, and a pump. The evaporator, also called a boiler, is a heat exchanger used to evaporate the working fluid by exchanging thermal energy with the heat source. The result of the evaporation process is a high pressure and temperature refrigerant vapour which will expand through the turbine to produce mechanical power. After that, the refrigerant is condensed by the condenser heat exchanger through rejecting the heat of vaporization to the coolant. The condensed liquid refrigerant is pumped to the evaporator by a liquid pump to restart the cycle. Other parts can be added to the ORC to improve the cycle efficiency, such as a recuperator, which is a heat exchanger used to transfer heat between the

refrigerant at the expander exit, and an evaporator inlet. In addition, a storage tank and controlling valves could be added, as shown in Figure 2.4.

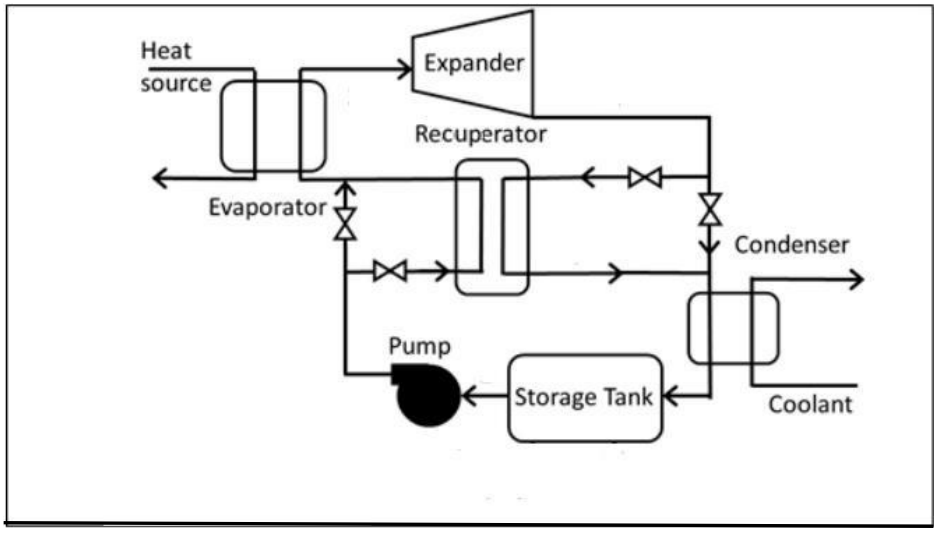

Figure: 2.4: Block diagram of the Organic Rankine cycle [48]

2.3 literature review on combined technologies

Different integrated systems have been proposed and investigated in the literature. Those which are of particular interest to this thesis are presented below:

2.3.1 Combined heat pump systems

Various heat pump cycles have been integrated in the literature using different prime movers such as gas turbine, internal combustion engine and ORC cycle. These combined systems that are designed for heating and cooling applications are presented below:

2.3.1.1 Gas turbine powered HP system

The use of a gas turbine as a prime mover in a CHP system has been proposed by a number of researchers. The integration involves a gas turbine powered by natural gas being used to drive various heat recovery technologies, such as absorption HP system, GSHP, absorption chiller, or conventional heat exchanger.

Zhao, X., et al. [49] presented a flue gas recovery system for a CHP gas turbine power plant driven by natural gas for a district heating application. The proposed system involves an absorption HP system to reduce the return water temperature for further heat recovery and hence enhance the overall system thermal efficiency. Furthermore, the new system layout was compared with a traditional gas boiler district heating system. The results showed that the new design configuration can secure a heating utility by area of 660 thousand m^2 greater than the gas boiler. The new technology can reduce the flue gas temperature to 11 ^oC, meaning that the flue gas thermal capacity is greater than the old design by 69 MW. In addition, the energy consumption is reduced by 6% and the HP achieved a COP of 25 which can be considered a significant improvement over the electrical HP. Moreover, the new design configuration can reduce CO_2 and NOx emissions by 16.2 thousand and 6 tons per year, respectively.

Kang, S., et al. [50] proposed a combined heat and power system involving integrating a gas turbine with a ground source heat pump cycle to provide domestic hot water. The new proposed system was compared with the traditional combined CHP-GSHP system. The reference system consists of a gas turbine powered by natural gas to produce electrical power; the wasted heat is

recovered by a heat exchanger to generate the first domestic hot water steam at a temperature of 55 ^{o}C, while some of the electricity generated from the gas-turbine is used to power the GSHP compressor and liquid pump. The GSHP is used to produce a second hot water stream at the same temperature as the first stream. In contrast to the original combined CHP-GSHP system, the new proposed integrated system generates only one domestic hot water flow, but in two separated heating stages. The first heating stage is carried out in the GSHP condenser to warm the cold tap water to around 35 ^{o}C. After that, the water reaches its desired and final temperature (55 ^{o}C) at the outlet of the heat exchanger by recovering heat from the gas turbine exhaust flue gas, which has a temperature of 508 ^{o}C. The results for the new integrated approach showed that reducing the HP condenser pressure to generate warm water of 35 ^{o}C leads to a lower pressure ratio and therefore better COP. This improves the overall combined system efficiency. The performance comparison between the two approaches can be summarized as follows: for the new proposed system, the total system energy efficiency is higher by 3.9%, and the GSHP COP increased from 5.06 to 6.95. In addition, the net output power is greater than the original cycle by 669 kW.

Cai, B., et al. [51] proposed a new novel CHP coupled with a ground source heat pump system for further heat recovery from the natural gas exhaust stream. The new system configuration was analysed thermodynamically, tested experientially and compared with a traditional cogeneration system. In the traditional CHP-GSHP system, the high-grade heat contained in the exhaust stream rejected from a gas turbine power plant is used to heat cold water. The remaining heat in the stream is rejected into the environment at a temperature of around 140 ^{o}C. Some of the power generated from the gas turbine is used to drive the compressor of a GSHP system. This HP system is used to generate another hot water stream using a vapour compression HP cycle. In the proposed system, the exhaust stream that would otherwise be rejected into the environment is directed to a geothermal well for further heat extraction, reducing the exhaust stream temperature to around 50 ^{o}C. This heat can be transferred and stored via a polyethylene material heat exchanger. The advantages of this new system arrangement are that it improves the COP by reducing HP cycle condensation pressure, and solves the imbalance problem of heat being added and removed from and to the soil in the GSHP system. In addition, by adapting the polyethylene heat exchanger, the exhaust stream temperature will drop below the dew point. Thus, the condensed exhaust stream will accumulate acid and therefore minimise sulphur emissions into the environment. The analytical results

showed that the first and second thermodynamic laws of the new proposed cycle can be improved by 10.7% and 10.4% respectively compared with conventional systems.

Lei, H., et al. [52] conducted a comparative study of different supplementary heat strategies on CHP comprised of a micro gas turbine coupled with an absorption chiller driven by flue gas energy. The function of such a small-scale system is to provide cooling, heating and power energy. This study addressed one of the main practical challenges of any CHP system, which is when the CHP system has to work in partial load conditions due to an imbalance between the user demand for power and thermal energy and the maximum system output. Four different heat supplementary strategies are proposed and analysed when the exhaust flue gases of the gas turbine are insufficient to drive the absorption chiller. In strategy one, the flue gas temperature is increased at a constant flue gas mass flow rate while in strategy two, only the exhaust mass flow is increased. Increased gas turbine power is the approach adopted in strategy three, and the fourth method involves adjusting flue gas mass flow and temperature taking into consideration the absorption chiller cooling capacity and the COP. The results showed that the first control strategy achieved better system performance than the other methods.

2.3.1.2 Gas powered HP system (GPHP)

Recently, scientific researchers have focused on designing and improving heating and cooling technologies with the advantage of waste heat recovery. Among these devices is the gas-powered heat pump cycle (GPHP), which consists of conventional vapour compression cycle driven by a gas fuelled internal combustion engine. The wasted heat from the gas engine (exhaust gas and engine cylinder jacket) is recovered by the HP cycle to enhance system heating efficiency.

An experimental and theoretical research was conducted by Yang, Z., et al. [53] to study the performance of the GPHP as a water heater applicant. The HP cycle in that study utilizes the ambient air temperature as a heat source for its evaporator. The water is separately heated and stored in two tanks by the heat rejected from the heat pump condenser and by utilizing the waste heat from the gas engine cylinder and exhaust. The recovered waste heat from the gas engine is proposed to solve the evaporator frosting issue when the system works at low temperatures and in a high humidity climate. The results illustrated that heating capacity rises with increasing

shaft engine rotation speed and water flow, but drops with rising water temperature. Moreover, three different defrost processes were proposed and analysed. Method one uses wasted heat only; method two reverses the HP cycle and the third approach involves a combination of both. The experimental test showed that although method one takes more time, it increases the water temperature in the storage tank through the operating time; the other two methods showed the opposite trend.

Hu, B., et al. [54] carried out an experimental and theoretical study centring around a GPHP system for heating purposes. In this study's system, the heat source for the HP evaporator is a mixture of ambient air and flue gases. The heat contained in the engine jacked coolant is used to superheat the working fluid at HP compressor inlet. The results showed that the combined system operational performance is highly dependent on ambient air temperature and gas engine speed. It also concluded that the gas engine speed should be set as low as possible to achieve the required heating capacity for optimum engine thermal efficiency.

In order to explore the stability and reliability of a combined gas engine air to water HP system for domestic hot water application, Liu, F., et al. [55] built and tested an experimental prototype. In this system, the engine waste heat (jacket and exhaust) is recovered to heat the water. Another hot water stream is generated from the HP cycle by utilizing a low-grade heat source (ambient air temperature). The results showed that the system can produce a range of hot water at between 40-60 ^{o}C. Moreover, in winter, it is recommended to meet the demand for high temperature water from the recovered wasted heat engine rather than the HP condenser to ensure that the gas engine speed and the HP temperature lift can operate constantly and at as low a level as possible to achieve the highest efficiency of performance.

Another experimental study by Liu, F., et al. [56] was carried out on a combined system designed to provide hot and cold water simultaneously. The hot water is produced by utilizing the wasted heat from the gas engine case and exhaust, and the HP cycle is used as a water cooler by absorbing heat from the cold tank water and rejecting it to the environment. The results showed that the evaporator water inlet temperature and the engine speed are the main parameters affecting both the system primary energy ratio (PER) and heat pump COP. The ambient air temperature has a direct effect on cooling capacity and hence on total capacity. The

proposed system can provide hot water at between approximately 40-62 ^{o}C, and cold water between 6.7-19.3 ^{o}C.

It is evident that the gas engine speed has a significant impact on engine performance. In the gas engine HP system, the engine speed should be adjusted to satisfy the variation in heating and cooling loads. Therefore, various studies have proposed hybrid powered gas engine HP systems (HPGHP) which feature a dual energy source to tackle this problem. This new type of system is based on combining the gas engine with an electric motor powered by a battery pack. The electric motor works as a generator to charge the battery, and when it is fully charged it can act as a prime mover for the compressor. By efficiently switching between both power sources modes, i.e., distributing the required compressor torque between the engine, motor or both, fuel consumption can be kept to a minimum. The proposed HPGHP system shows superior thermal, economic and environmental performance compared with traditional GPHP [57, 58].

2.3.2 Combined gas burner-ORC system

A gas burner is a primitive technology that mainly relies on burning natural gas, crude oil, and coal. The heat generated from the burner can be used to thermally drive a power cycle such as an ORC cycle. In addition, the wasted heat contained in the exhaust stream as a combustion by-product has high thermal energy. This wasted heat has attracted the attention of many researchers who have suggested recovery methods using various technologies such as CHP systems.

A small scale micro CHP consisting of an ORC power plant powered by natural gas-fired was designed and tested experientially [59]. The intended design for this system is a miscellaneous heating application, while the electricity generated is considered as a beneficial by-product. The cold tap water is heated to 65-85 ^{o}C in the gas burner, then this heat is transferred to the working fluid in the evaporator. The return water can be used for space heating, hot water supply, and domestic washing. In addition, the sink water in the condenser is also used in mixed heating applications. Isopentane is selected as the working fluid due to its proper thermophysical properties and environmentally friendly behaviour. An in-house vane expander was designed and manufactured specifically for the study. Thermodynamic analysis was carried out on the

combined CHP system in terms of the first and second laws of thermodynamics. The results showed that the maximum achievable expander output power is 77.4 W when the heat source temperature is 84 ^{o}C. In addition, the net cycle electrical efficiency is 1.66%. The combined system heating efficiency varied slightly at different heat source temperatures, but it is highly dependent on the water heating device.

An experimental research was conducted by Zhou, N., et al. [47] to design and construct an ORC cycle for low temperature flue gas waste heat recovery from an industrial process. In this system, typical ORC cycle components including a fin-tubes evaporator, a double tube sides condenser, a scroll expander and a liquid pump are used. In addition, R123 is used as the working fluid for its merits such as non-flammability, non-toxicity, low cost and environmental friendliness. The heat source for the test rig is an exhaust gas stream of low temperatures varying between (90-250 ^{o}C), from burning liquefied petroleum gas (LPG) mixed with ambient air in a stove. The heat sink is cold water circulated from a storage tank to condensate the refrigerant in the condenser. The study investigated the relations between the main cycle design parameters, including evaporator pressure, heat source temperature, R123 superheat degree, expander output power, cycle efficiency, heat recovery efficiency, and exergy efficiency. The main findings showed that increasing evaporator pressure results in a rise in turbine output power, cycle thermal efficiency and exergy efficiency. Increasing the heat source temperature leads to higher expander output power, greater energy recovery, and a rise in exergy efficiency. Increasing the refrigerant superheat degree reduces the cycle performance. Overall, the cycle produced net mechanical power of 0.645 kW with a total thermal efficiency of 8.5%.

Peris, B., et al. [60] conducted an experimental study on a regenerative ORC power cycle for the combined purpose of electrical power and thermal heat production. The combined cycle is thermally fed by a thermal oil close loop heated by a gas boiler to simulate the heat capturing process from low grads heat source temperatures in the range of 90-150 ^{o}C. In addition, the rejected heat from the cycle condenser is used to produce hot water at between 30-90 ^{o}C. Moreover, R245fa refrigerant is used as the working fluid and the volumetric expander is measured in the test bench. The results showed that increasing the thermal oil inlet temperature and cycle pressure ratio will result in higher thermal energy being captured by the ORC evaporator. This in turn increases the net power output from the expander. However, at each heat source temperature, the hot water outlet temperature declines as the cycle pressure ratio

increases, due to the decline in the ORC condenser pressure which is responsible for the final water temperature. Therefore, in this test, the cycle achieved a maximum thermal energy input of 390 kW, a thermal energy output of 350 kW, and a hot water temperature of 90 ^{o}C. In addition, the highest obtainable net electrical power and gross electric power were reported as 30.91 kW and 36.58 kW, respectively. More results showed that the cycle thermal efficiency increases with the pressure ratio, reaching a value of 7.92% at the maximum gross electric power and 9.4% at the highest net electric power. At a cycle pressure ratio of between 2-3, the expander isentropic efficiency achieved its highest value of 70%.

2.3.3 Diesel engine driven ORC cycle

Various studies in the open literature have investigated the use of the ORC thermodynamic cycle for waste heat recovery (WHR) from diesel engines. It has been established that a typical diesel engine (DE) rejects around half of the total energy it consumes through the exhaust and coolant streams in order to produce useful mechanical work [45, 61, 62]. These thermal fluids (exhaust and coolant streams) have the potential to be reused as a heat source for an ORC cycle for power production.

Yu, G., et al. [45] presented a simulation model to evaluate the performance of a real ORC cycle bottoming diesel engine for waste heat recovery from the engine jacket cylinder and exhaust. A schematic diagram of this system is shown in Figure 2.5. Extensive thermodynamic analysis was carried out on the waste heat recovered, ORC output power, system efficiency, exergy destruction, and efficiency. DE working conditions such as engine load and speed, and exhaust mass flow rate and temperature, were collected experimentally from a heavy-duty turbocharged six-cylinder DE used in a generator plan.

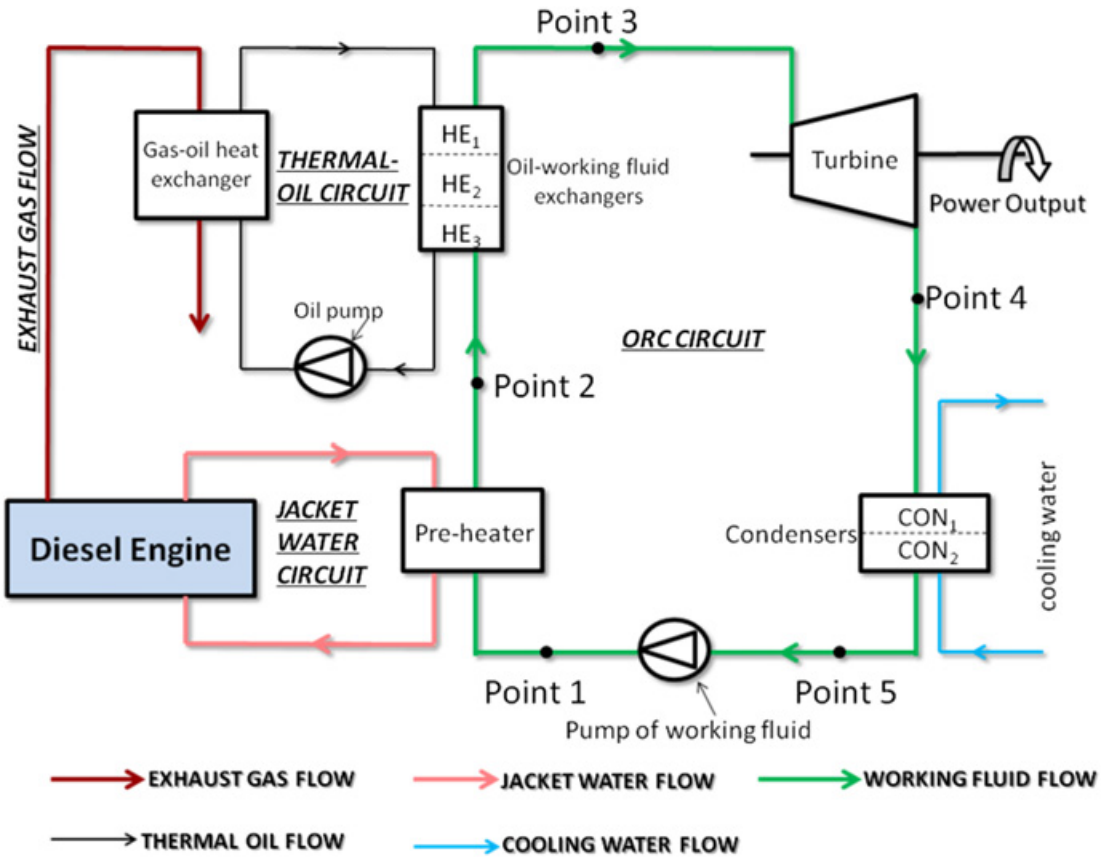

Figure 2.5: Schematic diagram of the bottoming ORC of a diesel engine [45]

The results showed that when the engine load varies from high to low, high thermal energy is recovered from the exhaust stream (75%) compared with a lower value acquired from the engine cylinder (9.5%). The ORC cycle achieved 14.5 kW net output power, recovery efficiency of 9.2%, and exergy efficiency of 21.7% under a rated engine condition. In addition, combining the ORC-DE has the potential to improve the DE thermal efficiency to 6.1%, and the ORC thermal efficiency up to 5.8% at an evaporation pressure of 30-31 bar.

Bombarda, P., et al. [62] conducted a comparison study between ORC/Kalina cycles via a bottoming diesel engine exhaust for waste heat recovery purposes. The engine used was designed to work as an electrical generator with a capacity of 8900 kWe. A mixture of Ammonia and water, and Hexamethyldisilane are used as working fluids for the Kalina and ORC cycles, respectively. The comparison results showed that the recovered net output power from Kalina and ORC cycles was 1615 and 1603 kW, respectively. However, the Kalina cycle required a high pressure value of approximately 100 bar to reach maximum performance, compared with

the ORC cycle which required only 10 bar. The Kalina cycle achieved slightly higher cycle performance, however this was only achievable at low logarithmic mean temperature differences in the heat recovery exchanger, which requires a large exchanger surface area. In addition, using a high pressure Kalina cycle could add more challenges to the basic cycle configuration in which the cycle should work either using high turbine rotational speeds or a multistage configuration. Also, to avoid possible corrosion in the Kalina cycle components, expensive materials are required.

Steady and transient simulations were carried out by Zhao, M., et al. [61] to evaluate the performance of a diesel engine combined with an ORC power cycle for WHR. The results for a diesel engine operating in different working conditions were experimentally tested. The engine performance was evaluated and compared both with and without the ORC cycle. The results showed that the main important performance parameters for the DE combined with ORC cycle improved; the net power output increased by 4.13 kW, the fuel consumption fell by 3.61 g/ (kW h), and the thermal efficiency improved by 0.66%. The transient results also support the benefits of using the ORC cycle, which obtained total combined cycle output power of 168.24 kW.

The ORC evaporator can have a significant impact on system performance. Therefore, a number of studies have focused on this part. An experimental and theoretical study on combined ORC-DE was conducted by Koppauer, H., et al. [63]. In this study, two heat exchangers (HXs) instead of one for an ORC evaporator were set in the test rig. One is placed after the exhaust aftertreatment, and the other is installed in the exhaust recirculation. Water mass flow is proposed to maintain the ORC condenser pressure below atmospheric pressure to maximize the turbine output power and hence the system recovering efficiency. In this study, steady and dynamic mathematical models were drawn from the literature with further development. The results of both models were validated with those obtained from the experimental rig. The results revealed that the evaporator steady state model achieved good accuracy with only a small fraction of error. In addition, the dynamic simulation results were in agreement with those acquired from the transit behaviour of the test rig. Furthermore, a control and optimization method has been developed which utilizes the steady state model and takes into account the practical design parameters, such as the decomposition temperature of Ethanol as the ORC

working fluid. This method can be directly used to identify the operating points in the combined ORC-DE cycle in order to maximize the energy recovered and the expansion power output.

A dynamic model of a 2-phase heat exchanger for use in a DE-ORC system has also been developed [64]. The system is designed to recover waste heat mainly from the main exhaust and gas recirculation streams. Mass and energy balance equations were used to describe the two-phase heat exchanger model. The finite difference method and moving boundary approach were adopted in this model and it was compared with other dynamic models available in the literature. The modified model is based on simulating the phase change of the Ethanol as the ORC working fluid and the moving boundary approach of the multi-phase across the heat exchanger during the heat transfer process. The results were verified with experimental data from a combined DE-ORC system. The results showed that the developed model has the potential of predicting the working fluid and exhaust gas temperature with an average error of less than 4%. This can provide the confidence needed to use the modified model in the dynamic evaluation and control strategy of a complete waste heat recovery system.

A thermodynamic model of a dual loop ORC system for waste heat recovery from a compressed natural gas engine was proposed [65]. The study conducted a comparison of the thermodynamic and economic performance of this system using various working fluids. In addition, the effects of various ORC parameters on system performance were investigated, including superheat degree, evaporation pressure, the condensation temperature of high- and low temperature loops of the ORC cycle, and the exhaust temperature. The results showed that higher evaporator pressure and condensation temperature in both loops have positive impacts on the thermodynamic performance of the system, while variations in superheat degree and exhaust temperature have no significant impact on the thermo-economic performance. In addition, R245fa in both loops achieved better ORC performance than the other working fluids examined in this study. The study also supported that this system can achieve a maximum net power output of 23.62 kW at the rated condition with a low electricity production cost. The dual loop ORC system also achieved thermal efficiency in the range of 8.97-10.19% in the selected operating conditions.

Some researchers have studied which ORC configuration layouts could be suitable for DE waste heat recovery. Four different small-scale ORC power cycle layouts using R245fa as

working fluids were investigated on one study [66]. The difference between these is only in the management of the recovery mechanism from the engine coolant and exhaust streams. The aim is to recover wasted heat from internal combustion engine coolant and exhaust streams. The study was carried out on a small Yanmar diesel engine, model number TF120M. It consists of a one-cylinder engine with 8.8 kW rated power at 2400 RPM. The study investigated design and performance parameters such as refrigerant superheat degree, expander rotational speed, and brake specific fuel consumption for the four proposed configurations under the rated condition of the DE. The four configurations can be described as follows: a simple structure ORC (ORC-simp) where both coolant and exhaust stream are used as a heat source to evaporate the R245fa. In the ORCR-1 configuration, a recuperator is adapted between a liquid pump and a coolant heater. In this case, the recuperator acts as a preheater to recapture the heat available in the R245fa flow leaving the expander. In ORCR-2, recuperator is installed between the coolant heater and the exhaust heater as an additional heat exchanger. The last configuration is ORC-pre, in which the refrigerant is preheated by the coolant heat exchanger before the evaporation process. A thermal oil circuit is used in the exhaust heater to protect the ORC refrigerant from the high temperature exhaust gases.

The results showed that increasing the degree of refrigerant superheat at the ORC evaporator exit will result in keeping the ORC-simp thermal efficiency nearly constant (6.4%), while slightly improving the other three cycles' efficiency. In addition, the results indicated that when R245fa is superheated below 110 ^{o}C, this could lower ORCR-2's efficiency compared with ORC-simp. This happens because the efficiency in the ORC-2 layout depends on the temperature of the refrigerant at the expander exit which in this case is lower than the engine coolant temperature. Also, the study found that the superheating degree has limited effect on the ORC power output, recording average values of 0.59 kW for ORC-simp and 0.5 kW for ORC-pre. The comparison results between the four configurations prove that the ORC-pre cycle has a better thermal performance but generates less power. As a result, the simple ORC configuration for waste heat recovery from coolant and the exhaust of the internal combustion engine has the potential to produce the highest power but has slight thermal efficiency. However, this can be reversed if the ratio between the engine coolant and exhaust is in the range of 0.5-0.7, because the ORC-pre is unable to recover all the heat available in the coolant stream. Therefore, it is recommended that the ORC-simp should be modified into ORC-pre in this ratio range. In addition to the higher power output, the scroll turbine rotation speed of the ORC-simp

(3200 RPM) is higher than that of the ORC-pre (1000 RPM) in the superheat degree range of 80-160 ^{o}C. Moreover, the ORC-simp cycle rejects less heat to the environment via the condenser compared with the other proposed configurations, which means it has a valuable advantage in waste heat recovery technology from ICE. The analysis of the engine fuel consumption under the engine rated condition showed that the ORC-simp has a lower fuel consumption ratio by 6.1% compared with ORCR-1 and ORC-pre which increases the fuel savings by 7.4% and 5.2%, respectively. In addition, the overall cycle efficiency of the ORC-simp, ORCR-1 and ORC-pre could be enhanced by 6.5%, 8.0% and 5.4%, respectively.

The selection of working fluid for an ORC to be used as a waste heat recovery system with DE is also important. Many studies have supported that using alkane-based working fluids in the ORC cycle can achieve better performance in medium-high temperature waste heat recovery from a diesel engine. However, their use is also associated with difficulties in selecting and designing proper expanders due to their over-large expansion ratio. To overcome this problem, Liu, P., et al. [67] proposed a two-stage expansion with interheating for ORC working with alkanes to achieve multi-stage heat recovery from exhaust gas, EGR gas (Exhaust Gas Recirculation) and engine coolant in a truck DE. A comparison study for the system performance using different alkane working fluids was conducted and the proposed system was compared with a preheating-regenerative ORC system for DE waste heat recovery. The results showed that cyclic alkanes performed better than linear alkanes in terms of net power output, thermal efficiency, and exergy losses; however, they recover less heat from engine coolant. In addition, the proposed system can generate 6.7% more output power than the preheating-regenerative ORC system as it can recover 100% of waste heat from exhaust gas and 71.8% from ERG gas.

It has been found that pure hydrocarbon refrigerants have good efficiency compared with other working fluids; however, flammability and explosivity are the main drawbacks to their use. To reduce these drawbacks, Song and Gu [68] suggested mixing them with a retardant in an ORC system for engine WHR. Refrigerants such as R141b and R11 are proposed as retardants to form zeotropic mixtures with hydrocarbon fluids. In addition to suppressing flammability, the zeotropic mixture offers better temperature matches between the refrigerant and the heat source and sink, which can reduce the rate of exergy destruction in the heat exchangers. The simulation results showed that the zeotropic mixture (50% cyclohexane and 50% R141b) can improve the

ORC output expansion power by 13.3% compared with pure cyclohexane. In addition, exergy destruction is reduced in both the evaporator and condenser, by 30% and 14%, respectively.

The mechanical output power of the combined ORC-DE cycle can be used in different applications. Salek, F., et al. [69] carried out a thermodynamic simulation to investigate the potential of recovering the wasted thermal energy available in the DE exhaust stream for use as a cooling load. In this system, the mechanical energy generated in the ORC power unit drives an Ammonia absorption refrigeration cycle. The three thermodynamic cycles are integrated as a combined cooling, heating and power technology. The results show that adopting the Ammonia absorption refrigeration cycle increases the bottoming ORC cycle efficiency, leading to a further rise in the output power of the entire system. In addition, DE efficiency improves by 4.65%. From the literature, DE coupled with ORC can only recover 7-8% of the thermal energy contained in the exhaust stream; however, this study's proposed system can recover 2% more than the compared cycle. Increasing the engine load leads to further energy being rejected from the exhaust stream, which can lead to a higher cooling load. By adding a preheat heat exchanger at the thermal interface point between the ORC-HP cycle, a 5 kW increment in the ORC feeding power is reported, which will boost the ORC output turbine expansion power. The interface point is where the R24fa liquid stream exiting the pump is in thermal contact with the Ammonia fluid leaving the heat exchanger. The exhaust stream temperature is set to 100 ^{o}C to avoid possible condensation of formation of sulfuric and nitric acid. The study also found that maintaining the exhaust gases temperature at below the 220 ^{o}C at the HP heat exchanger exit can avoid degradation in the HP COP. Using two HXs between the exhaust gas flue and both the ORC working fluid and HP refrigerant causes 0.5% mechanical power loss; however, the recovered energy from integrating these cycles has the potential to cover that loss.

Some researchers have suggested that coupling ORC-DE can have some drawbacks, including a rise in back pressure and ORC refrigerant decomposition. Turbocharged diesel engine type IVECO F1C 3.0 L combined with ORC power plan has been tested experimentally in this context [70]. This study discussed the following design assessment points: the effects of back pressure as a consequence of bottoming an ORC power unit on the engine exhaust stream, and the effects of increasing the mobile DE system weight due to adding the ORC unit. The proposed mechanical control mechanism, an Inlet Guide Vane (IGV), is used in this study to

ease the back-pressure problem. The recovery evaluation is carried out on an existing ORC cycle based on an off-design mode, and the expander is evaluated under variable engine speed.

The results show that engine back pressure can significantly affect the thermal interface process between the ORC evaporator and the engine exhaust. In addition, the shell and finned tube heat exchangers are favoured over a plate type for this application. Despite a small impact on the brake specific fuel consumption (less than 1%), the back pressure can be reduced to 175 mbar for an exhaust stream flow rate equal to 500 kg/h, by adopting the IGV control system on the turbocharger. By using a plate HX for an ORC evaporator designed for a pressure drop of 350mbar and an exhaust mass flow rate of 500 kg/h, engine boost pressure increases, causing a rise in the turbocharged speed at different DE speeds. Although engine fuel consumption unexpectedly increases by 2-5 % with the increase in the gas mass flow, the shell and finned tube heat exchangers can keep the fuel consumption rate below 1% at all engine speeds.

From the off-design results, and during the steady refrigerant flow rate in the ORC evaporator, thermos-fluid consequences such as an incomplete evaporation process and a fluid stability problem can occur. These drawbacks could have consequences in relation to the performance parameters of the expander, in terms of its volumetric efficiency and recoverable mechanical power. These drawbacks in the off-design mode can be minimized by adapting the multivariable mechanism control system in which the ORC working fluid density and mass flow rate, turbine speed, and exhaust mass flow can all be varied. Extra weight of 50 kg from the ORC power unit is added to the original track vehicle weight (3350 kg). In addition, a larger radiator surface area is needed for the DE to reject heat from the ORC condenser to the environment. An increment of 1% of fuel consumption is required to compensate to the increase in the track weight. In this study, utilizing the ORC power as a recovery unit shows a gross benefit of 4-5% and presents the potential of the cycle improvement in terms of proper design and control mechanisms.

In order to prevent the decomposition of the ORC working fluid, Shu, G., et al. [71] suggested adapting the thermal oil circuit as intermediate oil storage (OS) between the DE exhaust stream and the ORC cycle. They experimentally tested a standalone DE (without an OS system) with a capacity of 240 kW to investigate the variable exhaust stream properties. After that, the performance of a combined DE with OS/ORC cycle was also measured when exposed to a

variable high temperature exhaust stream. The results showed that in standalone mode, the temperature of the ORC working fluid can reach 202-480 ºC. This could put the refrigerant at a high risk of decomposition. In this case, the maximum ideal thermal energy obtained from the engine exhaust is 142.2 kW at an engine speed and load of 2000 RPM and 100% respectively. In the combined DE-OS/ORC system, even when the temperature of the exhaust stream is in the range of 200-480 ºC, the OS system maintains R123 temperature of between 81-222.5 ºC which is safely away from the decomposition range. Thus, the maximum heat recovered by the OS system is reduced to 72.63 kW, leading to net output power of 9.67 kW. In addition to reducing the decomposition problem, adapting the oil storage approach can bring significant inertia to the response of the combined system when the DE operates with a fluctuating performance. The combined ORC/OS show a roughly steady net power output even when the engine is shut down. Furthermore, in this mode, evaporator and condenser pressure is found to be almost constant throughout variable DE working conditions, which supports system safety and performance.

Since the combined ORC-DE system works under highly transient operation conditions due to variable DE output power demand which consequently produces transient exhaust streams in terms of both quantity and quality, a number of studies have focused on the dynamic modelling of the combined ORC-DE cycle.

Xu, B., et al. [72] developed a dynamic model to predict the transient behaviour of the combined ORC-DE system for heat recovery purposes. This model implemented individually the four basic ORC components in addition to control valves, junctions, and a reservoir. The heat transfer process in the heat exchangers is modelled based on energy, mass and momentum equations, and correlations of heat transfer coefficient and pressure drop across the heat exchangers are derived. Then, the model is employed for the entire combined system. The combined dynamic model is validated in terms of step-changes in the engine working conditions (speed-torque). The results showed that the vapour refrigerant temperature and pressure at ORC evaporator outlet can be successfully predicted with mean errors of around 2% -3%, respectively.

Huster, W., et al. [73] performed a dynamic evaluation of an ORC cycle driven by thermal energy rejected from the DE. The ORC targeted components are the evaporator and the

condenser. The adapted two-phase heat transfer method takes the moving boundary approach. The validation of this model is carried out with different experimental data. The results showed a mean temperature error for all measured temperatures of less than 4%. In addition, the mean relative error for the refrigerant temperature exiting the evaporator is less than 1%, and only increases to 5.5% at high-pressure levels.

Table 2.1 shows a summary of the available literature on the combined DE-ORC cycle for heat recovery. It is clear that the single stage ORC layout is the most commonly adopted configuration and that various working fluids have been used, with R245fa being frequently used.

Table 2.1 Comparison of combined DE-ORC cycles at rated condition or maximum DE load as reported in the literature.

Author/Year	Cycle description	ORC working fluid	Exhaust stream mass flow, kg/s	Exhaust stream temperature, ^{o}C	ORC output power, kW	ORC cycle Efficiency, %	Evaporation pressure, bar	Type of the study
Bombarda, P., et al. 2010 [62]	Single stage ORC	Hexamethyldisiloxane	35	346	1603	21.5	10	Simulation
Yu, G., et al. 2013 [45]	Single stage ORC	R245fa	0.2752	519	14.5	9.2	30-31	Simulation
Song and Gu 2015 [68]	Single stage ORC	Cyclohexane/R141b (0.5/0.5)	1.983	300	88.7	17	none	Simulation
Shu, G., et al. 2016 [71]	Single stage ORC	R123	0.388	202-480	9.67	14.15	16	Experimental
Zhao, M., et al. 2017 [61]	Single stage ORC	R245fa	0.199	353	4.13	none	9	Simulation
Yang, F., et al. 2017 [65]	Dual loop ORC	R245fa	0.05-0.28	447.6	23.62	8.97–10.19	25	Simulation
Lu, Y., et al. 2017 [66]	Single stage ORC	R245fa	0.0005486 fuel mass	587	0.59	6.2	none	Experimental and simulation
Liu, P., et al. 2018 [67]	Two-stage expansion	Cyclopentane	0.237	517.3	20.89	14-19.3	40.6	Simulation

2.3.4 Combined Organic Rankine Cycle-Vapour Compression Cycle

A combined Organic Rankine Cycle-Vapour Compression Cycle (ORC-VCC) is a promising integrated technology. The aim of this combined system is to convert heat energy into mechanical shaft power via the ORC subsystem, which in turn drives the VCC-compressor. Since the organic working fluids in the ORC cycle have a lower boiling point than water, low heat sources such as solar, geothermal or waste heat can be used to run the ORC. On the other hand, the VCC is the reverse cycle of the ORC, which can consume low power to transfer heat from a low heat source to a high heat sink. Therefore, a combination of the two has the potential to reduce both dependence on fossil fuel and greenhouse gas emissions.

Various ORC-VCC combined systems have been proposed in the literature. Aphornratana and Sriveerakul [74] presented a combined ORC-VCC refrigeration cycle, in which the two cycles are integrated using a free piston expander-compressor unit as a coupling device. The two systems share the same working fluid (either R134a or R22) and condenser, as shown

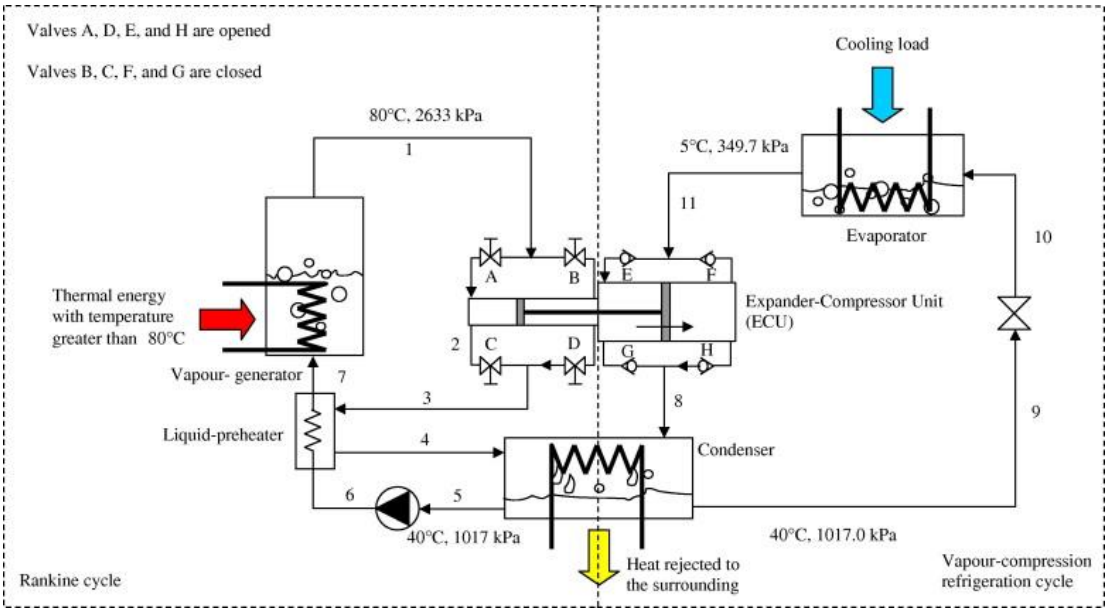

Figure 2.6: Schematic diagram of combined ORC-VCC refrigeration system [74].

in Figure 2.6. The main operating conditions include an ORC vapour generator (evaporator) temperature of between 60-90 ^{o}C, a condenser temperature of between 30-50 ^{o}C, and HP

evaporator temperature of between -10 to 10 ^{o}C. The results showed that this combined system can achieve a COP value of between 0.1 to 0.6. In addition, the system with R22 as the working fluid shows better COP performance than R134a for all operating temperature ranges.

Wang, H., et al. [75] proposed a combined ORC-VCC as a thermally activated cooling technology. The cycle can be powered by solar-thermal, geothermal or waste heat to produce a cooling effect and/or mechanical power if needed. These authors proposed that the cycle can be used solely for cooling during summer months, whereas in winter, all the heat can be converted to electricity. During spring and autumn, both cooling and electricity will be produced based on the demand. The effects of various cycle configurations on the overall system performance in terms of the gross coefficient of performance were studied. The results showed that the system can achieve an overall COP of 0.54 (basic cycle design), 0.63 (with sub-cooling) and 0.66 (with sub-cooling and recuperation). Thus, the advanced cycles with sub-cooling or cooling-recuperation achieve a 22% improvement on the overall COP compared to the basic cycle design.

The effects of various working fluids and their thermophysical properties on the cycle performance have also been studied. Kim and Perez-Blanco [76] conducted a thermodynamic analysis of a combined ORC-VCC system for the cogeneration of power and refrigeration using a low-grade sensible heat source. Various working fluids were investigated, including R143a, R22, R134a, R152a, Propane, Ammonia, Isobutane and Butane. The system performance was analysed in terms of net power production, refrigeration capacity, and thermal and exergy efficiencies. The results showed that for the pure refrigeration case, higher thermal efficiency and refrigeration per unit mass are achieved when working fluids are at high critical temperatures, with the exception of Ammonia. Both Butane and Isobutane show good refrigeration capacity at low turbine inlet pressure, but they are flammable. In contrast, R134a and R152a enhance refrigeration load at a higher turbine inlet pressure. In terms of cogeneration, increasing the turbine inlet temperature results in a significant increase in the net power production with a concomitant slight reduction in refrigeration duty. Thus, the exergy efficiency has a peak value with respect to the turbine inlet temperature and pressure. Although a higher exergy efficiency is favourable regarding power production, the study's authors concluded that a higher refrigeration capacity can be more advantageous from the energy point of view, both of which are irrespective of economic considerations.

Another thermodynamic analysis of a combined ORC-VCC system using different low Global Warming Potential (GWP) working fluids was conducted [77]. In this study, the selected working fluids are HFO-1336mzz or HCFO-1233zd (for ORC cycle) and HFO-1234yf or HFO-1234ze (for VCC cycle). Both the ORC-evaporation temperature and the ORC-VCC recuperator efficiency have a positive effect on ORC efficiency, while the VCC evaporation temperature and the condensation temperature have a negative effect on the ORC cycle efficiency. Overall, HFO-1336mzz achieves higher thermal and electrical efficiency under the selected operating conditions. Similarly, using HFO-1234ze in the VCC results in greater ORC thermal and ORC-VCC recuperator efficiencies due to the associated higher compressor discharge pressure. Overall, the ORC cycle achieves a thermal efficiency of between 10.6% and 15%, while the VCC COP ranges between 2.7 and 8. The gross combined cycle thermal and electrical COPs range between (0.3-1.1 thermal) and (15-110 electrical) respectively. If the system is used purely for electric generation with no cooling load, the annual energy saving is estimated to be 118,637 kWh. The expected payback time for this system is 3.3 years.

Asim, M., et al. [78] proposed an integrated ORC-VCC in which the VCC is an air conditioner (AC). Both cycles share a heat exchanger which acts as a condenser in the VCC and an evaporator in the ORC cycle. The waste heat rejected by the air-conditioning system is converted into electricity by the ORC cycle. Twelve different working fluids (6 for the ORC cycle and 6 for the VCC) are compared under a constant VCC condensation temperature of 50 ^{o}C. R600a-R123 pairs (as a working fluid for the AC and ORC cycles, respectively) achieve the best combined cycle performance. The ORC cycle can generate 1.41 kW of electricity from the recovering heat rejected by the VCC condenser. The thermal and exergy efficiencies of the ORC cycle are 3.05% and 39.3%, respectively. The overall system efficiency can be improved from 3.1 for a standalone AC to 3.54 for the combined system.

Saleh [79] conducted an extensive investigation into a combined ORC-VCC systems in terms of energy and exergy analysis, system performance under various working fluids, and working parameters. The results indicated that the higher the critical temperature of the working fluid, the better the COP and exergy efficiency achieved. R602 had the best performance with an overall COP of 0.596 and exergy efficiency of 31.03%. Both COP and exergy efficiency increase with a rising ORC boiler temperature and drop with increases in condenser temperature. Increasing the HP evaporator temperature has a negative impact on exergy

efficiency and a positive influence on the overall COP. Similarly, increasing the turbine and compressor efficiencies from 60% to 90% enhances both COP and exergy efficiency by approximately 50%.

Yu, H., et al. [80] investigated the integration of an ORC with an HP cycle to enhance net power output through waste heat recovery. The results showed that system performance is dependent on the ORC evaporation temperature, the working fluid latent to sensible heat ratio, and waste heat inlet temperature. The integration is assumed to be profitable when the following conditions are satisfied: the ORC working fluid critical temperature is lower than the waste heat inlet temperature, the latent to sensible heat ratio is small, and the COP of the HP is satisfactory. The resultant improvement in net power output and waste heat recovery were 9.37% and 12.04%, respectively.

Different designs and applications of the combined ORC-VCC system have been proposed in the literature. Patel, B., et al. [81, 82] presented an integrated ORC with a cascade VCC and vapour absorption refrigeration system, as shown in Figure 2.7. The ORC cycle is used to power the vapour compression refrigeration system and to provide the thermal requirements of the vapour absorption refrigeration system by utilising the high temperature working fluid at the ORC-expander outlet. The thermal efficiency achieved by the ORC subsystem and the combined system are 7% and 79%, respectively. The calculated COP of the vapour compression, vapour absorption and cascade system are 4.41, 0.75, and 0.54, respectively. The thermos-economic evaluation reveals that the system can achieve energy efficiency of 22.3% for the cooling mode and 79% for cogeneration mode (i.e., cooling and heating). The calculated simple payback period thus ranges between 5.26 years (for the base case) and 4.5 years (for the optimised case).

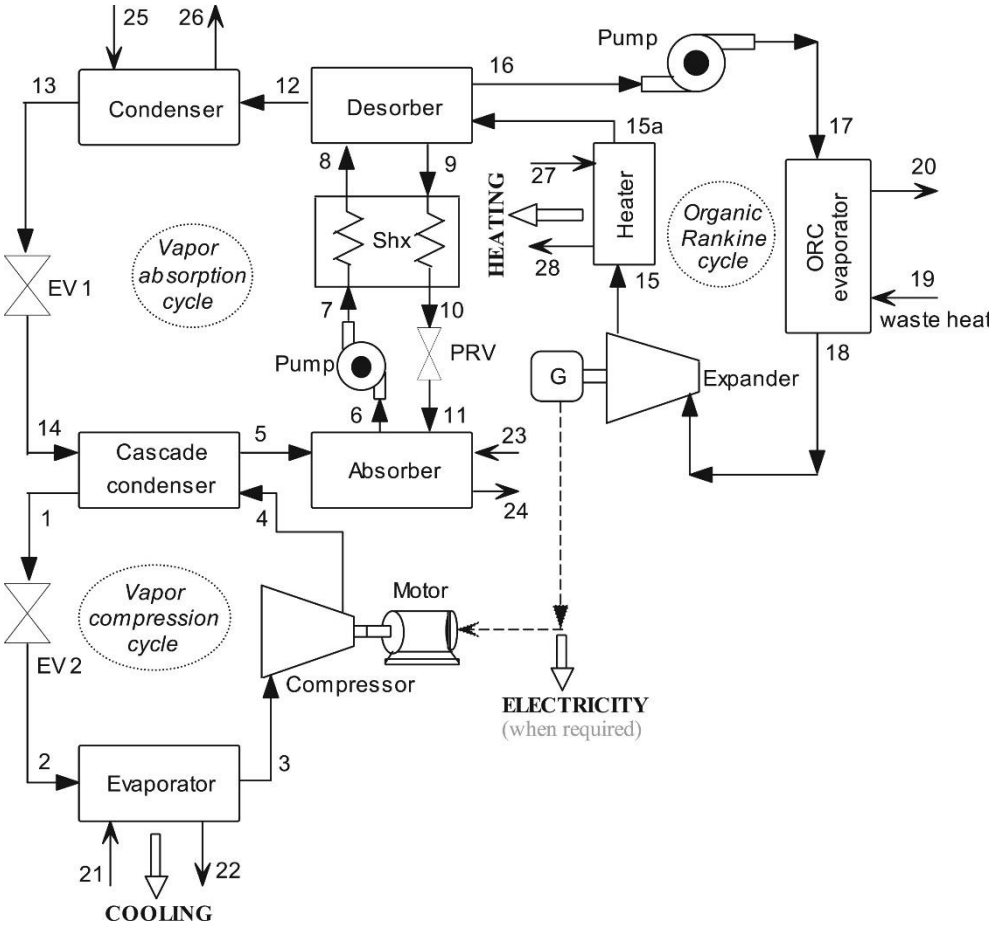

Figure 2.7 ORC integrated cascade vapour compression-absorption refrigeration system [81]

In a follow-up study, Patel, B., et al. [83] use a solar biomass as the heat source for the integrated ORC-cascade vapour compression-absorption system to make the system independent of both fossil fuels and the electric grid. The proposed hybrid system achieved an overall efficiency of 47.1% for a 30.7 kW cooling load. In addition, CO_2 emissions are reduced by 549 t/y compared to coal-based electricity and 233 t/y for natural gas-based electricity.

Another cascade refrigeration system (CRS) linked to ORC cycle was proposed by Lizarte, R., et al. [84]. This cascade system consists of a high temperature circuit (HTC) and a low temperature circuit (LTC) connected thermally via a heat exchanger which acts as an evaporator for the HTC and a condenser for the LTC. The proposed system is designed for low-evaporation temperature applications (-55 to -30 ^{o}C). The selected working fluids are Toluene (for ORC cycle) and Ammonia/CO_2 (for CRS). The simulation results showed that the overall COP and

exergy efficiency are mainly affected by the evaporation temperature of the ORC cycle, the LTC temperature, and the condensation temperatures. The system can achieve a maximum COP of 0.79 (at an ORC evaporation temperature of 315 ^{o}C) and a peak exergy efficiency of 31.6% (at an ORC evaporation temperature of 255 ^{o}C).

Bounefour and Ouadha [85] studied a combined system with a cascade evaporation in the ORC cycle, with the aim of improving power production. The new design was compared to a standard ORC-VCC combined system. A rang of working fluids were also compared in terms of both design performances. Waste heat from a marine diesel engine is used to drive the ORC cycle in both designs. The results showed that the addition of the cascade evaporation did improve the ORC cycle performance; however, the overall combined system performance was comparable to a standard ORC-VCC. In addition, Butane and Isobutane achieved better refrigerating effects than R134a.

A similar cycle configuration was used to aid Claude liquefaction by cooling hydrogen gas before entering liquefaction [86]. In this study, geothermal water is used as the heat source for the ORC cycle. The combined system can cool hydrogen gas to -40 ^{o}C before entering the liquefaction process with no extra work consumption. This proposed geothermally assisted hydrogen liquefaction cycle can produce a reduction in hydrogen liquefaction production cost of approximately 34% compared to the values cited in the literature.

An ORC-VCC cycle has also been combined with a hybrid proton exchange membrane fuel cell (PEMFC) and solar energy in a residential micro-CCHP system [87]. The function of this ORC cycle is to produce domestic hot water and mechanical power, while the VCC cycle produces cooling/heating capacity. The proposed system can produce up to 14.5 kW of heating/cooling capacity and around 8 kW of electricity based on the operating conditions.

Collings, P., et al. [88] investigated a gas driven ORC-vapour compression HP for domestic hot water supply. This system has a direct coupling between the ORC-turbine and the HP-compressor. The heat generated from natural gas combustion in the boiler is transferred to the ORC cycle to produce the required mechanical power for the HP cycle. Cold tap water is assumed to be heated from 10 to 60 ^{o}C, in three stages: HP-condenser, ORC-condenser and post heater heat exchanger. The waste heat contained in the flue gases is recovered by the post heater

heat exchanger to lift the water temperature to the designated target. R134a and Hexane are the working fluids selected for the HP and ORC cycles, respectively. The results showed that the COP and thermal efficiency of the HP and ORC cycles are approximately 5 and 20%, respectively. In addition, the combined system can achieve an overall fuel to heat efficiency of between 136%-164% for an ambient temperature range of (-5 to 15 ^{o}C).

A similar gas driven ORC-HP integrated system has been investigated under various operating conditions for hot water supply [89]. The main parameters that affect the combined system performance were studied. Two system designs, one with a post-heater heat exchange and one without it, were proposed and compared. In addition, a comparison of the system performance under three ORC working fluids (R123, R 245fa and Hexane) was conducted. The results showed that ambient air temperature and ORC-condensation temperature have significant impacts on system performance. As ambient temperature increases from -5 to 5 ^{o}C, the heating capacities of the HP-condenser and post heater heat exchanger increase. In addition, the HP COP increases with the rise in ambient temperature, reaching a maximum value of 5.56 at an air temperature of 5 ^{o}C. In contrast, a higher ORC-condensation temperature leads to lower ORC thermal efficiency. At an ORC-condenser temperature of 61 ^{o}C, the system achieves its optimum performance, with an ORC thermal efficiency of 15.34% and a fuel to heat efficiency of 147.1%. Hexane, as an ORC working fluid, achieves better ORC thermal efficiency and overall fuel to heat efficiency than R123 and R245fa. The comparative results for systems with or without the post-heater heat exchanger showed that the role of the post-heater to the water heating is limited as it can only add 0.28 kW of heat to the water. Furthermore, a combined system without post-heater showed comparable results with a minimal effect on system performance and fuel to heat efficiency (134% to 147% with post heater -132% to 145% without post-heater).

2.4 Literature review on modelling of VCC and ORC cycles

In general, HP and ORC systems modelling can vary in complexity based on the intended application and system design. The aim of the modelling can include; energy analysis, design configuration, performance with various working fluid, performance over time and control system design. The most commonly used modelling approaches are summarized as follow:

1. *Balanced energy method*: This modelling approach could be either theoretical or empirical and it is mainly used for seasonal energy use and economics. In this method, the system performance is assumed constant and can be obtained from either the manufacturer or experimental or field measurement. In addition, there is no limitation on heat source availability. The heating demand for the HP cycle is assumed to be fully satisfied. However, the limitations of this modelling method is the lack of accuracy and utility [90].

2. *Steady state method*: It is a theoretical evaluation used for system design and sizing. This approach usually begins by adopting the mass conservation principle, in which refrigerant mass flow across the cycle components is equal. Next, the energy conservation principle is applied which involved applying the first law of thermodynamic to each cycle part and on the overall cycle with the assumption of neglecting the kinetic and potential energies. Then a non-conservation of entropy principle is used to identify the entropy rate balance for the system components. Exergy analysis usually follows with the aim of estimating the exergy destruction rate and exergy efficiency of individual cycle components and the overall system [91].

Number of simulation studies in the open literature have adopted the steady state model to investigate the performance of the HP and ORC cycles in terms of energy and exergy analysis. Mikielewicz, D. and Wajs, J. [92] have conducted a study on a single stage and cascade HP system employing a high heat source and condensation temperatures. Wang, G-B. and Zhang X-R. [93] carried out thermoeconomic evaluation of a transcritical CO_2 HP system for district heating and cooling. Another thermoeconomic study is conducted using steady state model to investigate a HP cycle coupled with desalination system [94]. An energy and exergy analysis is also conducted on a HP cycle integrated with vapor injection system and an economizer [95].

For an ORC cycle, many studies have investigated the performance of an ORC cycle as a waste heat recovery system from an internal combustion engine. These studies were mainly conducted using the steady state model in terms of mass, energy and entropy conservation laws [45, 68, 96].

For a combined ORC-VCC system, most of the studies mentioned in the literature review (section 2.3.4) have adopted the steady state model to evaluate the system performance.

3. *Fitted (regression) model*: It is an empirical approach for seasonal energy use and economics evaluation. This method is based on using equations or curve fitting if detailed performance data for the device is known from experimental or manufacturer source. It have the advantage of being easy to generate and use with high accuracy. Yet, the accuracy of the results is limited to the range of data available for the fitted model [97].

Underwood, C., et al. [97] have adopted the fitted model to investigate the performance of three scroll compressor for domestic air source HP water heater. Woodland, B., et al. [98] have conducted an experimental study on a small-scale organic Rankine cycle with R134a as working fluid. The performance curve of a compressor rotating in reverse as an expander was used in their mathematical model. Similarly, expander performance curve for an ORC cycle with R245fa refrigerant is used in another research by Declaye, S., et al. [99]. Experimental test was conducted on an automotive electric scroll compressor using empirical equation [100].

4. *Dynamic state method:* It is theoretical method to study the variation in cycle performance with respect to time, particularly when independent variables and boundary conditions are not constant. For most thermal cycles, steady state evaluation is considered satisfactory if the system dependent parameters are thermally stabilised within the relevant time-step for that system. For instance, in a heat pump cycle, if the response to the input variable occurs within seconds up to a few minutes, then the steady state simulation (also called the quasi steady state) satisfies the performance evaluation process. However, when more detailed information about the system performance is required or when control strategies are investigated, then a dynamic model is likely to be needed [90].

Underwood [90] has illustrated a steady state and a full dynamic model for a heat pump cycle used in a ground source heat pump system. The evaporator and condenser dynamic model was

conducted under the assumptions of no momentum conservation or pressure losses, with axial variation in flow direction. Another dynamic simulation of an air sourced HP system is conducted with the aim of keeping the evaporator frost-free. The mathematical model was compared with experimental results which showed good agreement [101].

Table 2.2 Summary of previous simulation studies on combined ORC-VCC system

Author/Year	Heat source	Working fluid		Application	Mechanism of ORC-VCC coupling	Remarks of the study
		ORC	VCC			
Aphornratana and Sriveerakul 2010 [74]	Thermal energy at temperatures > 80 ºC	R22, R134a	R22, R134a	Cooling load	Expander-compressor unit consists of two free piston (first works as ORC expander and the second as VCC compressor.	ORC-VCC share condenser. COPs (0.1 - 0.6). Evaporator capacity for R22 (1-1.4 kW), and for R134a (0.7 kW).
Wang, H., et al. 2011 [75]	The cycle can use renewable energy (solar, geothermal or waste heat)	R245fa	R245fa	Cooling and/or electricity	The mechanism of coupling is not described. ORC expander power is assumed to be fully consumed by the VCC compressor.	ORC-VCC share condenser. COPs (0.54-0.66). Cooling load (5.3 kW). COPs can be improved by 22% when using subcooling and cooling recuperation.

Kim and Perez-Blanco 2015 [76]	Low grade sensible heat: 150 ^{o}C.	R143a, R22, R134a, R152a, propane, ammonia, isobutane and Butane	R143a, R22, R134a, R152a, propane, ammonia, isobutane and Butane	Refrigeration only when all the power generated is consumed within the cycle, or refrigeration and electricity	The mechanism of coupling is not described. The net power production is equal to the subtraction of compressor and pump power from expander power.	ORC-VCC share condenser. Pure refrigeration capacity: Butane or Isobutane (140 kW), R134a or R152a (170 kW). Cogeneration mode (Isobutane): thermal efficiency (50-75%), net power (25-30 kW), refrigeration capacity (140-160 kW).
Molés, F., et al. 2015 [77]	Low temperature heat source	1336mzz	1234ze	Cooling load or electricity when cooling is not required.	The mechanism of coupling is not described. ORC expander power is assumed to be fully consumed by the VCC compressor.	ORC efficiency 12.4%, VCC COP 6.16. Cooling load 100 kW, electricity 16.23 kW.
Asim, M., et al. 2017 [78]	Waste heat from AC air conditioner	R123	R600a	Electricity	VCC is not driven by the ORC.	COPs improved from (3.1-3.54). ORC electric output power 1.41 kW and thermal efficiency 3.05%. AC cooling capacity 35 kW.

Chang, H., et al. 2017 [87]	Hybrid proton exchange membrane fuel cell (PEMFC) and solar energy	Dimethylpentane	R290	Domestic hot water, heating and cooling capacity and electricity	The mechanism of coupling is not described. ORC expander power is assumed to be fully consumed by the VCC compressor.	Electric power 8 kW, cooling/heating capacity 14.5 kW. Total system efficiency 75.4-85%.
Patel, B., et al. 2017 [81, 82]	Waste heat	n-pentane	R410A	Study a: Cooling, heating and electricity. Study b: Cooling only, or cooling and heating	For both studies, ORC-VCC coupled via electric generator and motor.	COP of VCC (4.41) and VAR (0.75). ORC efficiency (6.99%). COPs (0.54). Trigeneration efficiency (79%). Heating load (77.99 kW), cooling load (30.7 kW), net power output in study a (0.58 kW).
Patel, B., et al. 2017 [83]	Solar-biomass	n-pentane	R410A	Cooling and heating	ORC-VCC coupled via electric generator and motor.	Heating load 77.9 kW, cooling load 30.7 kW, overall system efficiency 47.1%.

Lizarte, R., et al. 2017 [84]	Renewable energy from 100-350 ^{o}C.	toluene	NH_3, CO_2	Refrigeration	The mechanism of coupling is not described. ORC expander runs the two HP compressors of the cascade refrigeration system.	COP of the cascade system:(1.15-1.5), ORC efficiency (9.4-12.4%), HP evaporator capacity (9.45 kW), overall system COP (0.79).
Bounefour and Ouadha 2017 [85]	Marine DE exhaust stream	propane, butane isobutane, propylene and R134a	propane, butane, isobutane, propylene and R134a	Refrigeration only	The mechanism of coupling is not described. ORC expander power is assumed to be fully consumed by the VCC compressor.	ORC-VCC share condenser. COP of HP (5.4), ORC thermal efficiency 11.3%. butane achieved better refrigeration and COP than the others.
Kaska, O., et al. 2018 [86]	Geothermal source at 200 ^{o}C.	ORC1 (R141b), ORC2 (Isobutane)	R23	Cooling effect to cool hydrogen to -40 ^{o}C	The mechanism of coupling is not described. ORC-VCC expander power is assumed to be fully consumed by the two compressors.	Combined ORC-VCC coupled with another ORC. Hydrogen liquification cost can be reduced by 39.7% compared to literature values.

Saleh 2018 [79]	Low-temperature heat source (geothermal or waste heat) with a temperature of around 110°C.	R602	R602	Electricity or refrigeration	The mechanism of coupling is not described. ORC expander power is assumed to be fully consumed by the VCC compressors.	ORC-VCC share condenser. Refrigeration load 280-320 kW. Highest COPs 0.99.
Yu, H., et al. 2018 [80]	Waste heat source, 150 ºC	R236fa	n-hexane	Electricity	VCC is not driven by the ORC. HP system is used to upgrade the wasted heat to increase ORC power production.	HP COP (2.65), power consumed (169 kW), ORC thermal efficiency (10.07%), waste heat recovered (820 kW), net power output (805 kW).

Table 2.3 Summary of experimental studies on standalone HP cycle

Author/Year	Type of HP cycle	Pressure (P) in bar, Temperature (T) in ^{o}C or pressure ratio (PR)	COP	Refrigerant	Application
Nenkaew, P. and C. Tangthien. 2015 [102]	Water source HP in a cascade system	Pcond=12.5 Pevap=4	5-6	R22/R134a	Chilled water for cooling and hot water for heating
He, Z. et al 2017 [103]	Combined ORC and HP as heat utilization system using low-grade heat source	Pcond=12.4-19.2 Tcond 75-95 Pevap=4.4-6.8 Tevap 48-52	1.1-3.6	R142b	Heating load
Kong, X. et al 2018 [104]	Solar assisted HP water heater with direct-expansion	Tcond=54.4 Tevap=7.2	3	R134a	Domestic hot water supply
Shen, J, et al 2018 [105]	Air source HP with dual mode	PR=3.8 for single cycle PR=5.5 for cascade cycle	Single 1.7-2.6 Cascade 1.58-1.85	R22/R134a	Heating for drying process
Kong, X. et al 2018 [106]	Solar-assisted heat pump with direct expansion	Pcond=12-22 Pevap=3.9-6	3.6-5.7	R134a	Domestic hot water supply
Xu, Y. et al 2019 [107]	Air-source heat pump with dual mode	PR =5-9 for single stage, PR=3-5.5 for cascade	1.69-2	R404A, R134a	Hot water supply
Liu, T. et al 2019 [108]	Domestic air conditioning/ heat pump system	Pcond= 19.4 Pevap=5	COP_c 2.2-2.8 COP_h 2.9-3.1	R22	Cooling and heating load

Fannou, J-L. et al 2019 [109]	Ground source heat pump system with direct expansion	Tcond=41.5 Tevap=3 PR=2.9	2.6	R22	Cooling load
Yang, L-X. et al 2019 [110]	CO_2 transcritical air source HP	Pcond=80-87 Pevap=33-40	3.9-5.2	CO_2	Hot water supply
Guo, X, et al 2019 [111]	HP system with domestic drain water as a heat source	Tcond =35 Tevap=-10	2.5	R22	Hot water supply
Mota-Babiloni, A. et al 2019 [112]	VCC with and without internal heat exchanger	Tcond =32.5 and 40 Tevap= -5 to 15	R134a 1.6-3.9 R513A 1.7-4	R134a, R513A	Refrigeration load
Li, Z. et al. 2019 [113]	VCC with Oil-free compressor	Tcond=40-50 Tevap= -3 to 17 PR=2-4	R1234yf = 1.8-4.4 R134a = 2.3-4.8	R1234yf, R134a	Refrigeration load
Liang, Y. et al 2019 [114]	VCC with Oil-free compressor	Tcond=23.4 Tevap= 2.4	3.28	R134a	Domestic hot water supply

Table 2.4 Summary of experimental studies on standalone ORC cycle

Author/Year	Type of ORC cycle	Pressure (P) in bar, Temperature (T) in ^{o}C or pressure ratio (PR)	Refrigerant	Power output, kW	Thermal efficiency, %
Yun, E, et al 2015 [115]	ORC with multiple expanders used in parallel	Tsource=120 Tsink =24	R245fa	3.5	7.5
Lei, B. et al, 2016 [116]	ORC with single screw expander	Pevap=6-11 PR= 8.5	R123	8.35	7.98
Pu, W. et al 2016 [117]	Organic Rankine cycle for low grade thermal energy recovery	Pcond =1.7 Pevap= 6	R245fa	1.979	4
Pang, K-C. et al 2017 [118]	ORC for low grade thermal energy recovery	Tcond=25 Tevap=119	mixture of R245fa:R123 2:1	1.66	4.7-4.8
Li, L. et al 2017 [119]	Small scale ORC for low grade heat recovery	Pcond=2-3.8 Pevap= 15-16 PR=7.3	R245fa	4.6-5.4	0.15-0.45
Yang, S.-C., et al 2017 [120]	3 kW ORC for low grade waste heat	Tcond= 21.8-43.6 Tsource=100	R245fa	2.64	5.92
Nematollahi, O. et al, 2018 [121]	Small scale ORC with compact metal-foam evaporator	Tsource =80-120 Tevap= 70	R245fa	0.3-1.8	3.5-6.6

Kim, J-S. et al 2019 [122]	ORC using radial inflow turbine	Pcond= 2.1 Tcond=35 Pevap=3.9 Tevap= 55	R245fa	36	--
Chen, J. et al 2019 [123]	ORC for power production	Pcond=2.9 Tcond=30 Pevap=11 Tevap= 90	R245fa	2.42-3.55	5.2-7.3
Zhang, H-H. et al, 2019 [124]	Regenerative organic Rankine cycle	Tcond= 23-30 Tevap=80-110	R123	0.6112	1.61-2.97
Yamaguchi, T. et al, 2019 [125]	Small scale ORC for recovering geothermal energy	Tcond=35.5 Tevap=83	R245fa	0.0512	7.7
Collings, P. et al 2019 [126]	Small-Scale ORC Using a Positive Displacement Expander with a Regenerator	Pcond=1.4 Pevap=5.82	R245fa	Net power 0.262	6.8

2.5 Summary and discussion of literatures related to ORC and VCC cycles

Various integrated designs of the combined ORC-VCC cycle have been proposed in the literature. Table 2.2 summarizes the main findings related to this system. In terms of applications, this combined cycle was mainly designed for cooling, refrigeration and/or electricity generation [74-78, 80, 82, 84-86]. These is limited studies on the use of this combined system for heating applications particularly on for domestic hot water and central heating applications.

From design prospective, the mechanism of coupling between ORC and VCC cycles is not described. Most researches have assumed that the power produced by the ORC expander is fully consumed by the VCC compressor. This have the proposed advantage of eliminating the conversion loses associated with use of electric generator and motor [77, 79]. Other studies have proposed that the ORC power is used to electrically drive the HP cycle via a generator and motor [81-83].

Working fluids have a significant impact on the performance of a combined ORC-VCC system. Various working fluids have been selected and analysed in the literature. Kim and Perez-Blanco [76] and Bounefour and Ouadha [85] conducted a comparison study involving different working fluids used in a combined ORC-VCC cycle in which both cycles share the same working fluids. The results supported that different refrigerants achieved high performance in different applications. For example, R134a or R152a are found to be favourable for refrigeration uses, while Isobutane shows better performance for cogeneration applications [85].

Various methods have been used in the literature to assess combined cycle performance, including individual cycle efficiency as well as combined system efficiency. Some researchers have defined combined system efficiency as the ratio of HP evaporator thermal energy to net ORC evaporator thermal energy and pump work [74-77]. This ratio has mainly been used for systems designed to produce cooling, refrigeration, or electricity production. The combined cycle efficiency is highly dependent on the type of refrigerant and the working conditions. In average, the combined system efficiency (COPs) ranged between 0.5-0.6 for most cooling and refrigeration application. While for heating application, limit researches have shown the combined system can achieved an overall efficiency of 0.7-0.8.

Table 2.3 summarizes the main outcome of a standalone VCC studied experimentally in the literature. For heating and cooling applications, the VCC performance varied mainly with the selected working fluid and evaporation and condensation pressure and temperature. Various pure and mixed refrigerant are used including; R22, R134a, R142b, R404a, CO2, R1234yf and R513a. The average coefficient of performance for most experimentally test VCC cycle is approximately 3 for heating application and around 2.5 for cooling and refrigeration.

Table 2.4 listed some experimental researches conducted on standalone ORC cycle. Similar to the VCC, ORC performance mainly influence by the refrigerant used and pressure ratio between the evaporator and condenser. The main selected working fluids are R245fa and R123. On average, the ORC can produce an output power between 2.5-3.5 kW and have thermal efficiency in the range of 4-7%.

2.6 Justifications for the current research

The literature review in this chapter has illustrated that cogeneration and trigeneration integrated systems are innovative technologies in which the primary energy source can be converted into multi energy mode with the potential of recovering wasted heat to enhance the overall system thermal performance. Therefore, these technologies have been used in a wide spectrum of applications. Furthermore, they have the potential of reducing fossil fuel consumption and greenhouse gas emissions.

An ORC heat engine and its reverse vapour compression cycle are mature and efficient cycles that can be used on their own, combined with other cycles, or combined with each other. Combining ORC with VCC system has the advantage of eliminating some of the limitations encountered in a standalone HP and ORC cycles mentioned in chapter one. In addition, the ORC cycle is different from other prime movers in that it rejects heat in the form of latent heat through working fluid condensation rather than sensible heat. This means that more heat can be recovered making the ORC a more efficient heat recovery system. The same concept is true for the heat pump cycle. Based on these factors, an integrated ORC-VCC system have been designed and investigated in this research.

Working fluids selection is shown to have a significant influence on thermodynamic cycle performance. Some studies have suggested using different working fluids in each cycle rather than sharing the same one. The advantage of this approach is that it can enhance system efficiency and avoid the complexity involved in using controls and adjustment devices such as expansion valves and mixing chambers. To investigate and select the most appropriate working fluids for the ORC and VCC cycles proposed in our research, a list of working fluids have been studied and compared in chapter four.

From an applications point of view, the combined ORC-VCC has mainly been investigated in relation to cooling/refrigeration, electricity, or a combination of the two. Limited research is available on the application of the combined cycle in heating applications. Thus, the combined system designed in this research is investigated mainly for heating applications including domestic hot water supply and central heating as well as cooling applications. Furthermore, the use of combined ORC-VCC cycle as a waste heat recovery system from diesel engine wasted

heat is an interesting topic that has not been extensively investigated in the literature. This investigation will allow to evaluate the effectiveness of the combined ORC-VCC system in converting the wasted heat into useful refrigeration load.

The definition of combined system efficiency is necessarily influenced by the cycle design and objective. In our study, in addition to the HP coefficient of performance and ORC thermal efficiency, the concept of fuel to heat efficiency is used in the evaluation of the combined cycle performance. The fuel to heat efficiency is defined as the total heating capacity of the system added to water to the heat released from burning the fuel. This parameter is useful when the primary energy source is the combustion of fossil fuels.

To the best of the author's knowledge, based on the extensive literature review, the integrated system investigated in this thesis has never been proposed before. In our research we therefore propose a novel configuration of a gas fuelled ORC-VCC system with direct coupling between the ORC turbine and HP compressor. The ORC output power and heat is fully utilized for heat application. Furthermore, heat in ambient air is utilized in the HP cycle as a free energy source. The system is designed to recover wasted heat from burner flue gases, diesel engine exhaust, or data centre IT equipment to enhance system performance. Different working fluids are used in each cycle based on their performance. The intended applications of this system include domestic hot water, data centre cooling with simultaneous central heating, and providing a refrigeration load.

Chapter 3: Theory of the combined ORC-VCC cycles

3.1 Introduction

In this part of the thesis, the thermodynamic concept of the organic Rankine cycle and its reverse heat pump cycle are described thermodynamically. The mathematical algorithm for the power transferred between the two cycles and the thermal energy received and rejected in both cycles are described theoretically. A performance evaluation of the combined cycle is described based on first and second laws of thermodynamics. The thermal modelling of the gas burner and the optimization procedure using the pinch point temperature approach for the heat exchangers are also set out. The MATLAB code used in modelling the combined cycle is explained in detail using the working fluid thermophysical properties software. This chapter also describes the dynamic model and the PID controller used in the control strategy.

3.2 Vapour compression heat pump cycle (VCC-HP)

A vapour compression heat pump cycle is a reverse heat engine cycle which consumes mechanical power to pump heat from a low grade heat source into a high temperature heat sink. In addition to the working fluid, four main thermodynamic processes are essential to accomplish this: the compression process state (1-2), the condensation process state (2-3), the expansion process state (3-4), and the evaporation process state (4-1), as shown in the T-s (temperature entropy) diagram in Figure (3.1) [127].

Each thermodynamic process can be mathematically analysed using the steady state flow energy equation and by neglecting the changes in kinetic energy ${C^2}/{2} = 0$ and potential energy $Zg = 0$ as shown in Equation 3.1.

$$\dot{m}\left(h_1 + \frac{C_1^2}{2} + Z_1 g\right) + \dot{Q} + \dot{W} = \dot{m}\left(h_2 + \frac{C_2^2}{2} + Z_2 g\right) \tag{3.1}$$

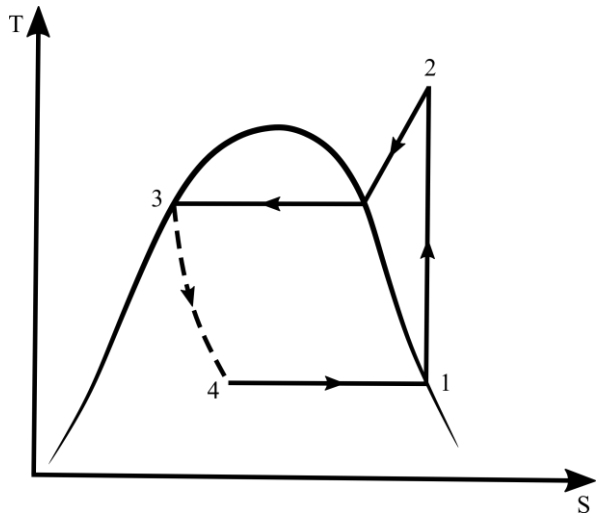

Figure 3.1: T-s diagram for a typical refrigeration or (heat pump) cycle [127].

3.2.1 HP evaporation process

By neglecting the work done in Equation 3.1 and assuming isothermal heat transfer process, the latent heat is equal to the product of the enthalpy difference across the evaporator unit times the refrigerant mass flow, as given in Equation 3.2:

$$Q_{HP-evap} = \dot{m}_{HP-ref.} \times (h_1 - h_4) \tag{3.2}$$

Where:

h_1	The specific enthalpy of the HP refrigerant at the evaporator exit
h_4	The specific enthalpy of the HP refrigerant at the evaporator inlet
$\dot{m}_{HP-ref.}$	The HP working fluid mass flow rate

3.2.2 HP compression process

By assuming an adiabatic thermodynamic process across the compressor (Q=0), the work consumed by the compressor is the enthalpy difference at the compressor unit inlet (h_1) and the outlet (h_2) multiplied by the working fluid mass flow; see Equation 3.3:

$$W_{HP} = \dot{m}_{HP-ref.} \times (h_2 - h_1) \tag{3.3}$$

This mechanical work is used to increase the working fluid pressure and hence the temperature between the evaporator and the condenser. Therefore, the difference between the evaporation and condensation temperatures is called the temperature lift across the HP cycle.

3.2.3 HP condensation process

In making the same assumptions regarding the heat and work used in the evaporator, the condensation process is carried out by rejecting the latent heat to the sink source. The total amount of the thermal energy is equal to the difference in the specific enthalpy at the condenser inlet (h_2) and outlet (h_3) multiplied by the working fluid mass flow rate($\dot{m}_{HP-ref.}$), as demonstrated in Equation 3.4:

$$Q_{HP-cond.} = \dot{m}_{HP-ref.} \times (h_2 - h_3) \tag{3.4}$$

3.2.4 HP expansion process

The function of the expansion valve is to reduce the pressure of the refrigerant from the high discharged pressure (condenser pressure) to the low suction pressure (evaporator pressure). This process in the analytical evaluation is assumed to be an isenthalpic expansion process. In other words, the enthalpy of the refrigerant before and after the expansion valve is equal.

$$h_3 = h_4 \tag{3.5}$$

3.2.5 Heat pump first law of thermodynamic

The Carnot law for a heat pump cycle states that the maximum theoretical efficiency is equal to the ratio between the temperature of the hot reservoir over the temperature difference between the hot and cold reservoirs. Therefore, the actual heating coefficient of performance for a HP cycle is equal to the ratio between the total heat rejected by the condenser over the work consumed by the compressor, which is given in Equation 3.6:

$$COP_{heating} = \frac{Q_{HP-cond.}}{W_{HP}} \tag{3.6}$$

Meanwhile for the refrigerator, it is the ratio between the thermal energy absorbed by the evaporator over the compressor power as shown in Equation 3.7:

$$COP_{cooling} = \frac{Q_{HP-evap}}{W_{HP}} \tag{3.7}$$

The coefficient of performance (COP) is used as an evaluation performance parameter for a heat pump cycle. The COP reported in the literature for a vapour compression heat pump cycle ranges between (2.5-5) however, it is dependent on the temperature lift across the HP cycle (heat source and sink temperatures) and the working fluid used. Correa and Cuevas [128] conducted a simulation study on an air-water heat pump, and their results showed that the annual COP varied between 2.54 and 2.6. Ju, F., et al. [129] carried out an experimental study on a heat pump water heater adopting an eco-friendly working fluid which was a mixture (12%/88% by mass) of R744/R290 instead of R22. The results showed that the HP system with the mixture working fluid achieved a COP of 4.731, 11% higher than that of R22. Willem, H., et al. [130] reported in their review study that most of the current heat pump water heat systems achieve a COP of between 1.8-2.5; however, some innovative new technologies have been implemented on a HP cycle that could enhance the COP to a range of 2.8-5.5. An example of these technologies is the multi-functional (combined heating and cooling) application. Liang, Y., et al. [89] investigated a combined ORC-HP gas fuelled water heater. The working fluid for the HP cycle was R134a and the optimum COP obtained in their steady state simulation results was around 5.

3.3 Organic Rankine cycle (ORC)

An organic Rankine cycle refers to a heat engine using organic fluid instead of water to produce mechanical work by absorbing thermal energy from a high temperature heat source and rejecting part of it to the low-grade heat sink. The four-main thermodynamic processes of the ORC are demonstrated in the T-s diagram shown in Figure 3.2.

The working fluid flows in a close loop around the cycle, and each process is denoted by a number at the beginning and the end.

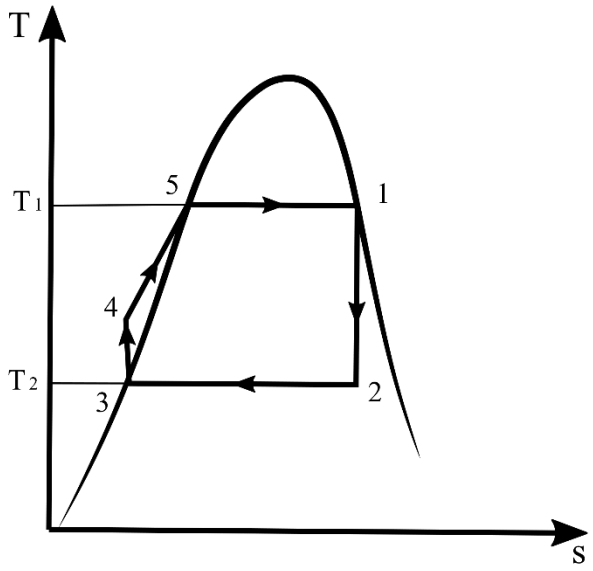

Figure 3.2: T-s diagram for water as a working fluid in a conventional Rankine cycle [127].

Each process can be analysed using the steady state flow energy Equation 3.1 and by adopting the same assumptions of neglecting the kinetic and potential energies.

3.3.1 ORC evaporator

The latent thermal energy absorbed by the ORC working fluid in the evaporator (state 4-5-1 in Figure 3.2) [127], is the product of the enthalpy difference across the evaporator multiplied by the ORC refrigerant mass flow, as shown in Equation 3.8:

$$Q_{ORC-evap} = \dot{m}_{ORC-ref.} \times (h_1 - h_4) \tag{3.8}$$

Where:

h_1	The specific enthalpy of the refrigerant at the evaporator exit
h_4	The specific enthalpy of the refrigerant at the evaporator inlet
$\dot{m}_{ORC-ref.}$	The working fluid mass flow rate

3.3.2 ORC expander

The mechanical power produced by the ORC expander is equal to the enthalpy difference at the turbine inlet and outlet multiplied by the ORC refrigerant mass flow:

$$W_{turbine} = \dot{m}_{ORC-ref.} \times (h_2 - h_1) \tag{3.9}$$

In modelling the combined ORC and HP cycles in this thesis, it is assumed that all the power produced by the ORC expander is fully transferred and consumed by the HP compressor.

3.3.3 ORC condenser

In the condenser, the condensation process is carried out by rejecting the latent heat to the sink stream. The total amount of thermal energy is equal to the difference in the enthalpy at the condenser inlet (h_2) and outlet (h_3) multiplied by the working fluid mass flow rate ($\dot{m}_{ORC-ref.}$) (state 2-3 in Figure 3.2):

$$Q_{ORC-cond.} = \dot{m}_{ORC-ref.} \times (h_3 - h_2) \tag{3.10}$$

3.3.4 ORC liquid pump

After the working fluid is fully condensed, the pump is used to pump the refrigerant liquid at high pressure to the evaporator to complete the cycle. The power consumed by the ORC liquid pump is the enthalpy difference across the pump multiplied by the working fluid mass flow, as given in Equation 3.11:

$$W_{ORC-pump} = \dot{m}_{ORC-ref.} \times (h_3 - h_4) \tag{3.11}$$

3.3.5 ORC first law of thermodynamic

The maximum theoretical efficiency of a Carnot cycle heat engine is equal to the ratio between the difference in temperature between the hot and cold reservoirs over the temperature of the hot reservoir. Therefore, the simplest form of the ORC thermal efficiency is the useful network produced by the cycle divided by the thermal energy absorbed by the ORC evaporator:

$$\eta_{ORC} = \frac{W_{turbine} - W_{ORC-pump}}{Q_{ORC-evap}} \tag{3.12}$$

This equation is widely used in the steady state evaluation of the ORC. The range of values for the η_{ORC} reported in the open literature vary between 6-13 % depending on the heat source temperature, the cycle configuration, the working fluid used, and the cycle application. A regenerator ORC cycle was experimentally examined by Li, J., et al. [131]. In their study, ranges of heat source of about (70, 80, 90, 100 ^{o}C) were used. R123 was the working fluid used in the cycle. The results showed that the cycle achieved 7.4% thermal efficiency at a heat source of 80 ^{o}C. An experimental investigation was conducted on a 3 kW ORC cycle using R245fa as a working fluid [120]. Thermal oil at temperature of 100 ^{o}C was used as a heat source. The maximum thermal efficiency achieved by the cycle during the test was 5.87%. Chen, J., et al. [123] conducted an experimental study on ORC using R245fa as a working fluid. The results showed that the cycle can produce output power of between 2.42-3.55 kW, and the electrical power consumed by the liquid pump ranged between 0.44-0.49 kW. Moreover, the overall thermal efficiency achieved by the cycle varied between 5.2-7.3%. Another experimental study conducted on a small ORC rig using R245fa refrigerant revealed that the cycle can achieve a total thermal efficiency of 7.7% with a total output power of 51.2 W [125].

3.4 Thermal balance model across the ORC-VCC heat exchangers

One of the general assumptions adopted in modelling the heat exchanger is that no heat is lost between the hot and cold streams during the heat exchange process. In other words, this case study assumes that all the sensible heat available in the heat source stream passing through the evaporators will be transferred to the working fluid flow. Also, in the condenser, all the latent heat contained in the working fluids will transfer to the sink stream.

As was demonstrated in chapter one, the heat sources for the HP cycle can be classified according to availability, such as ambient air stream, geothermal energy, waste heat from industrial process, flue exhaust gases from internal combustion engine, data centre rejected heat, solar power, and even river, lake or ocean thermal energy.

In this thesis's modelling, the heat source for the HP evaporator is ambient air, with or without exhaust flue gas from the gas burner. Therefore, Equation 3.2 is modified as follows:

$$\dot{m}_{HP-ref.} \times (h_1 - h_4) = \dot{m}_{mix} \times C_{P-mix} \times (T_{mix-in} - T_{mix-out}) \quad (3.13)$$

Where:

T_{mix-in}	Temperature of the mixed stream at evaporator inlet
$T_{mix-out}$	Temperature of the mixed stream at evaporator exit
C_{P-mix}	Specific heat of the mixed stream
$\dot{m}_{mix}$	Mass flow of the mixed stream

The heat source of the ORC cycle can be classified according to type and availability, such as waste heat from industrial processes, solar power, geothermal energy, ocean thermal energy, and biomass energy [47, 48]. Furthermore, the heat source can also be named according to its stream temperatures into low temperature (<230 ^{o}C), medium temperature (230-650 ^{o}C), and high temperature (>650 ^{o}C) [47].

For an ORC cycle adopting the heat source from burning natural gas, Equation 3.8 can be written in the following form:

$$\dot{m}_{ORC-ref.} \times (h_1 - h_4) = (\dot{m}_{CH4} + \dot{m}_{air}) \times (\sum h_P - \sum h_R) \quad (3.14)$$

Where:

$\sum h_P$	Summation of the combustion products enthalpies.
$\sum h_R$	Summation of the combustion reactants enthalpies.
$\dot{m}_{CH4}$	Mass flow of the natural gas.
$\dot{m}_{air}$	Mass flow of air entering the burner.

In the condenser, the sink stream could be any fluid that is used to carry the rejected condensation thermal energy, such as air or water. For the HP condenser (the first heating stage), all the thermal energy rejected by the HP working fluid is assumed to be completely transferred to the cold tap water. Therefore, Equation 3.4 is rewritten again:

$$\dot{m}_{HP-ref.} \times (h_2 - h_3) = \dot{m}_w \times C_{pw} \times (T_{Cw-in-HP} - T_{Cw-out-HP}) \quad (3.15)$$

Where:

$T_{Cw-in-HP}$	Temperature of the cold tap water entering the HP condenser
$T_{Cw-out-HP}$	Temperature of the tap water leaving the HP condenser
C_{pw}	Specific heat of the water
$\dot{m}_w$	Mass flow rate of the tap water

After that, the water enters the second heating stage (ORC condenser) with the same mass flow and temperature at the HP condenser outlet. Equation 3.10 might be updated as follows:

$$\dot{m}_{ORC-ref.} \times (h_3 - h_2) = \dot{m}_w \times C_{pw} \times (T_{Cw-out-HP} - T_{Cw-out-ORC}) \quad (3.16)$$

3.5 Pinch point temperature difference approach (PPTD)

In the optimization procedure of modelling a heat exchanger, the pinch point temperature difference approach (PPTD) can be adopted. This method is based on the fact that in a heat exchanger, in order to secure an optimal heat transfer process between the hot and the cold streams, the temperature of the hot fluid should be higher than the cold stream across all the heat exchanger's cross sectional area, as shown in Figure 3.3.

The figure shows the T-Q (temperature-heat capacity) curve of a typical heat transfer process in a counterflow heat exchanger. It shows that the hot stream is located above the cold stream. It is clear that there is a variable temperature difference between the two streams across the heat exchanger. When the temperature difference reaches its lowest value (the smallest gap), this point is known as the Pinch Point.

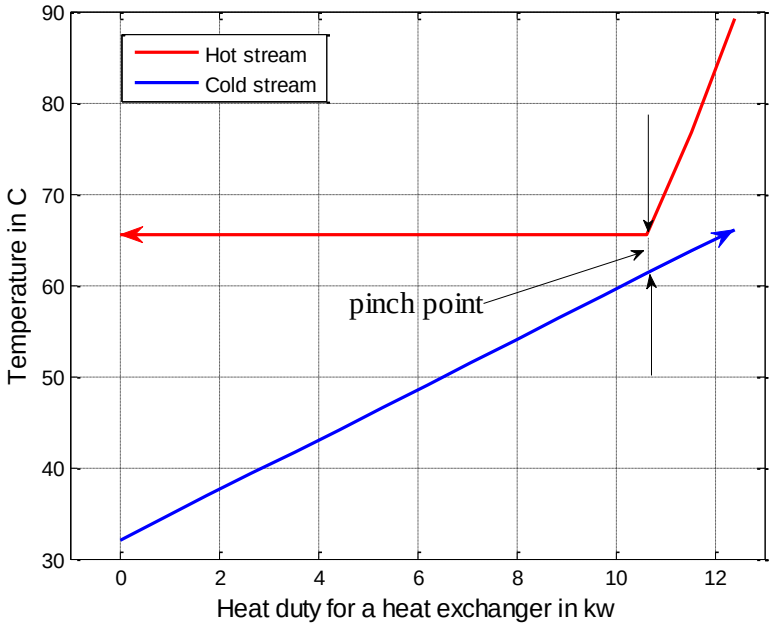

Figure 3.3: Pinch point in a counterflow heat exchanger

To increase the ORC and HP cycles' Carnot efficiency, lowering the pinch point temperature difference in all the heat exchangers is recommended. This could be explained as follows: for the ORC cycle, reducing the pinch point difference in the ORC evaporator will increase the average temperature of thermal energy added to the cycle, and will reduce the temperature of

the energy rejected by the ORC condenser. Both effects will enhance cycle efficiency [132]. For the HP cycle, the opposite trend is expected because the VCC is the reverse cycle of the ORC cycle. So, lower condensation and evaporation temperatures in the HP cycle can be achieved by reducing the pinch point temperature difference in the HP condenser and evaporator to increase HP cycle efficiency. However, reducing the pinch point temperature difference will also increase the HX heat transfer area. Therefore, the optimum pinch point is selected depending on the cycle's working parameters, such as the evaporator inlet temperature, the cycle's practical application, and others.

To give a few examples, Cao, Y., et al. [133] selected >5 K as a pinch point in the evaporator of an ORC cycle bottomed with a gas turbine to recover wasted heat. Andreasen, J., et al. [134] adopted a 10 ^{o}C pinch point for an ORC boiler powered by heat source at a temperature of between 120 and 90 ^{o}C, while for the condenser the pinch point was 5 ^{o}C. Dong, B., et al. [135] used 20 ^{o}C for the ORC evaporator and 10 ^{o}C for the ORC condenser. Some of the reported pinch points for the HP cycle can be summarized as follows: Ju, F., et al. [136] conducted an experiential and simulation study on a heat pump water heater. They used a pinch point temperature difference of 3 and 7 K in the counterflow condenser and evaporator respectively, citing several references from the literature [137, 138]. Gu, Z., et al. [139] studied a combined ORC and HP system theoretically and experimentally. The adopted pinch point for both cycles' heat exchangers was 5 ^{o}C. Schimpf and Span [140] carried out a simulation study on a combined ORC-GSHP system assisted by solar energy. The pinch point was selected depending on the application of the combined system. For the space heating mode, and for the HP cycle, $\Delta T_{pinch-evap}$ and $\Delta T_{pinch-cond}$ were 5 K while for domestic hot water, the pinch points were 4.5 K for the evaporator and 4 K for the condenser. For the ORC cycle, the pinch points were 4 and 3 K for the evaporator and the condenser, respectively.

The optimization process of a heat exchanger model, including working fluids mass flow rate and temperature, have to satisfy the pinch point condition, i.e., the minimum pinch point should be secured.

3.6 Isentropic efficiency of the ORC expander and the HP compressor

In both the ORC and HP cycles, the expander and compressor are the main part of the combined system. The compressor/expander performance is defined as the isentropic efficiency against the pressure ratio [97]. The isentropic efficiency measures the irreversibility occurring through the compression and expansion process [141]. In addition to the isentropic efficiency and the pressure ratio, the shaft rotation speed and the working fluid can also affect the expander's efficiency. The performance curve of these devices is usually provided by the manufacturer or measured experimentally throughout tests. The typical trend of the performance curve is that the efficiency is increased with a linear rise in the pressure ratio reaching the maximum value before declining gradually. Thus, there is a peak expander efficiency at a specific pressure ratio, as shown in Figure (3.4).

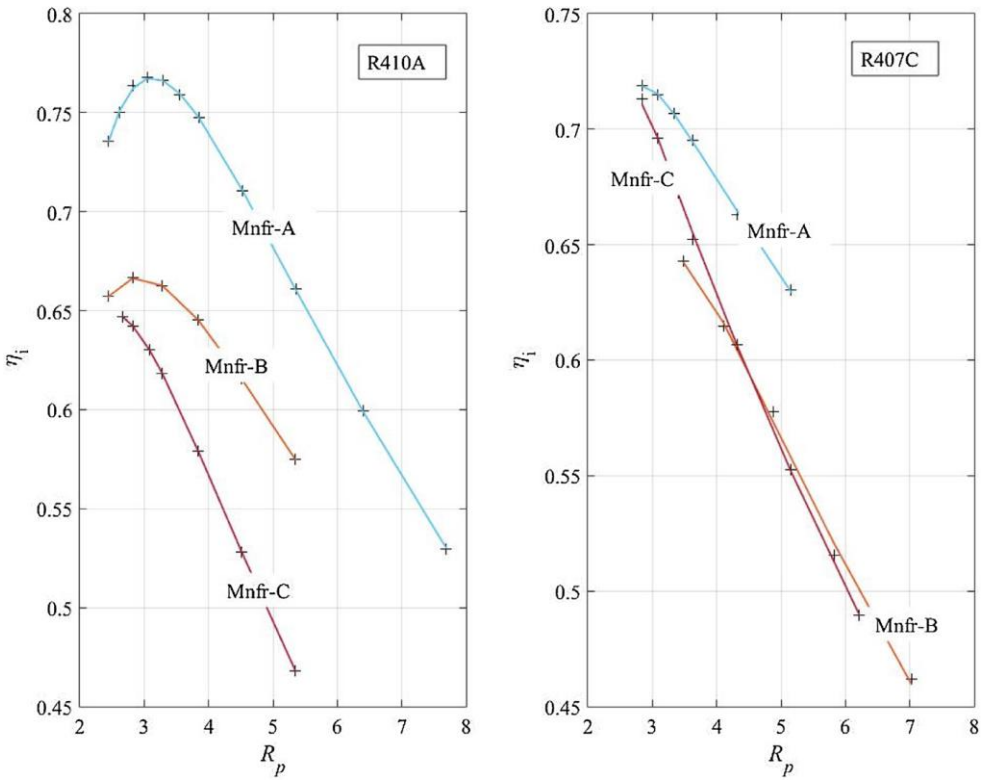

Figure 3.4: An example of typical expander performance [97].

3.7 Modelling the gas burner

3.7.1 Chemical combustion equation

In the gas burner, Methane reacts chemically with the Oxygen in the air to release thermal energy. Since Nitrogen is already contained in the air, this gas should appear in the equation of combustion. It is common in combustion calculation to consider air as consisting of 21% O_2 and 79% N_2. Thus, the combustion reaction equation is written as follows:

$$CH_4 + 2(O_2 + 3.76N_2) \Longrightarrow CO_2 + 2H_2O + 7.52N_2$$

The left-hand side of the above equation shows the chemical components entering the combustion chamber (gas burner), while the right side represents the products of the combustion which will appear in the exhaust gases. In addition, both sides of the equation involve the same number of atoms of each element [127]. Also, it is clear that the left-hand side has the exact amount of oxygen to combust all molecular of Methane; therefore, no Oxygen and/or Methane is left in the product-side. This air to fuel ratio $\left({}^{Air}/_{Fuel}\right)$ is called the theoretical or (Stoichiometric) ratio. If the fuel and air are mixed with a ratio less than the Stoichiometric ratio then the mixture is called a *rich* mixture (it has no excess air). In contrast, it is called *weak* or *lean* if it has excess air [142]. In real applications it is recommended to have excess air for the combustion process.

The percentage of excess air can be calculated using the following equation:

$$excess\ \ air_{\%} = \frac{\left({}^{Air}/_{Fuel}\right)_{actual} - \left({}^{Air}/_{Fuel}\right)_{\text{Stoichiometric}}}{\left({}^{Air}/_{Fuel}\right)_{actual}} \tag{3.17}$$

3.7.2 First law of combustion

The enthalpy of reaction can be estimated when the values of *enthalpy of formation* on the molar base at the reference temperature for all elements of reactants and products are known.

A simple definition of the enthalpy of formation is the rise in enthalpy when a substance is formed from its basic natural elements and in the standard reference state. When a change in enthalpy occurs due to the complete combustion of a substance at a constant pressure and temperature, it is known as the *enthalpy of combustion*. In most cases, the reference state temperature and pressure are 25 ºC and 1bar, respectively [142].

By neglecting the changes in kinetic and potential energy, the first law of thermodynamic of the combustion reaction process in a gas burner can be written as:

$$Q = \sum_{prod} N_i\left(\bar{h}_f^o + \bar{h} - \bar{h}^o\right)_i - \sum_{react} N_i\left(\bar{h}_f^o + \bar{h} - \bar{h}^o\right)_i \quad (3.18)$$

Where:

N_i	Number of moles of substance i
$\bar{h}_f^o$	Molar enthalpy of combustion
$\bar{h}$	Molar enthalpy of the substance
$\bar{h}^o$	Molar enthalpy of the substance at reference state

3.8 Evaluation of the combined system performance

The simple definition of any thermodynamic system's efficiency is the ratio between the energy gained over the energy expended. By interpolating this definition to the combined ORC-HP system, the combined system efficiency can be defined as the ratio of energy added to the water to the total energy released from burning the fuel in the gas burner, known as the fuel to heat efficiency:

$$Fuel\ to\ heat\ efficiency = \left(\frac{Q_{Total-added-\ water}}{Q_{Total-released}}\right) \times 100 \quad (3.19)$$

Where the total heat added to the water $Q_{Total-added-\ water}$ also called the total system heating capacity, is the summation of the thermal capacities of the HP condenser, the ORC condenser and the post heater heat exchanger.

$$Q_{Total-added-\,water} = Q_{HP-cond.} + Q_{ORC-cond.} + Q_{post\ heater} \tag{3.20}$$

While the total heat released from burning CH_4 is given by:

$$Q_{Total-released} = \dot{m}_{CH4} \times Methane\ heating\ value \tag{3.21}$$

At this stage, the final water temperature can be calculated as follows:

$$T_{w\_final} = \frac{(Q_{Total-added-\,water} + C_{p-water} \times T_{w_{in}} \times \dot{m}_{water})}{(C_{p-water} \times \dot{m}_{water})} \tag{3.22}$$

3.9 Heat exchanger areas

The process of heat transfer in heat exchanger areas such as the evaporator and condenser is a complicated mechanism which mainly depends on the working fluid properties and flow characteristics as well as the heat exchanger's geometry. It is general practise in many researches that the heat transfer process is usually modelled by adopting previously developed sim-empirical correlations. However, the validity of these correlations is limited to certain applications and ranges of boundary conditions.

The most commonly used correlation is as follows:

$$\alpha = N_u \frac{k}{D} \tag{3.23}$$

Where:

α	Overall heat transfer coefficient of the flow
N_u	Nusselt number
D	Pipe diameter or distance separation of the plates in the heat exchanger
k	Flow thermal conductivity

N_u is called the Nusselt number, which is the ratio of convective to conductive heat transfer between the flow and the wall inside the heat exchanger. The above equation can be rewritten as follows:

$$\alpha = \left(c_1 R_e^{c_2} P_r^{c_3} \left(\frac{\mu_f}{\mu_w}\right)^{c_4}\right) \times \frac{k}{D} \tag{3.24}$$

Where:

R_e	Reynolds number
P_r	Prandtl number
μ_f	Dynamic viscosity of the bulk flow
μ_w	Dynamic viscosity of the wall

The Reynolds number is the ratio of inertial to viscous forces in the fluid flow, which is written as:

$$R_e = \frac{\rho u D}{k} \tag{3.25}$$

Where ρ and u are the density and velocity of the fluid flow respectively.

The Prandtl number is the ratio of viscous to thermal diffusion, which is defined as:

$$P_r = \frac{C_p \mu}{k} \tag{3.26}$$

Where C_p is the fluid specific heat.

The overall heat transfer coefficient (U) can be calculated when the Nusselt numbers for cold and hot steams inside the heat exchanger are identified, using the following equation:

$$\frac{1}{U} = \frac{1}{\alpha_{cold}} + \frac{t}{k} + \frac{1}{\alpha_{hot}} \tag{3.27}$$

Where (t) is the wall thickness in the heat exchanger, and α_{cold} is the overall heat transfer coefficient of the cold flow, while α_{hot} is the overall heat transfer coefficient of the hot flow.

The heat transfer area is calculated by the following equation:

$$Area = \frac{Q}{U\Delta T_m} \tag{3.28}$$

Where Q is the total thermal capacity of the heat exchanger, and ΔT_m is the Logarithmic means temperature difference (LMTD), which is given by:

$$\Delta T_m = \frac{(\Delta T_1 - \Delta T_2)}{\ln(\frac{\Delta T_1}{\Delta T_2})} \tag{3.29}$$

ΔT_1 and ΔT_2 are the temperature differences between the hot and cold streams on the heat exchanger exit and inlet, respectively.

Quoilin, S., et al. [143] adopted the following correlation for the single phase heat transfer coefficient in a corrugated plate heat exchanger with a 30^o Chevron angle:

$$N_u = cR_e^m P_r^n \tag{3.30}$$

Where, m=0.5 for laminar flow (Re<400) and m=0.7 for turbulent flow (Re>400) and n=1/3 in both cases. The coefficient C is identified experimentally as follows:

Condenser	Evaporator
Turbulent vapor C=0.84	Turbulent vapor C=0.063
Turbulent water C=0.72	Turbulent air C=0.101
Laminar liquid C=0.4	Laminar liquid C=1.29

While for a boiling heat transfer coefficient, the correlation by Hsieh and Lin [144] is adopted:

$$\alpha_{boiling-2ph} = C\alpha_l B_o^{0.5} \tag{3.31}$$

The subscript $2ph$ refers to two phase flows, α_l is the all liquid non-boiling heat transfer coefficient, and B_o is the boiling number for the refrigerant.

In the condenser, the heat transfer coefficient is calculated using Kuo, W., et al.'s [145] correlation, as follows:

$$\alpha_{condesnation-2ph} = C\alpha_l\left(0.25C_o^{-0.45}Fr_l^{0.25} + 75B_o^{0.75}\right) \tag{3.32}$$

Fr_l is the Froude number for the liquid phase refrigerant, and C_o is the convective number.

Deutz, K., et al. [141] used the following correlations for their single phase heat transfer coefficient, assuming a smooth condenser tube:

When Re < 2300,

Nu = 3.6568, reported in Baehr and Stephan [146].

When 2300 < Re < 10, 000, Gnielinski's correlation is used [147]:

Where:

$$f = \frac{1}{(0.79ln(R_e)-1.64)^2} \tag{3.33}$$

When Re > 10000, the Dittus-Boelter correlation is used [148]

$$N_u = 0.023R_e^{0.8}P_r^{0.4} \tag{3.34}$$

For a two phase condensation process, the Shah's correlation [149] is adopted:

$$N_u = 0.023R_e^{0.8}P_r^{0.4}\left((1-x)^{0.8} + \frac{3.8(1-x)^{0.04}x^{0.75}}{P_r^{0.38}}\right) \tag{3.35}$$

Where (x) is the vapour quality.

Liang, Y., et al [89] used the following correlation for single phase heat transfer in a condenser plate heat exchanger for both refrigerant and water:

$$\frac{1}{\sqrt{f}} = \frac{cos\beta}{\sqrt{0.18tan\beta + 0.36sin\beta + \frac{f_o}{cos\beta}}} + \frac{(1-cos\beta)}{\sqrt{3.8f_1}} \tag{3.36}$$

Where β is the Chevron angle, the optimum value is 60^o [150], and the coefficient f is given by:

When R_e<2000, f_o=$\frac{64}{R_e}$, $f_1 = \frac{579}{R_e} + 3.85$

When $R_e \geq 2000$, $f_o = (1.8logR_e - 1.5)^{-2}$, $f_1 = \frac{39}{Re^{0.289}}$

To calculate the heat transfer coefficient for a two-phase evaporation process, Cooper's pool [151] boiling correlation is used:

$$\alpha_e = 1.5 \times 55 \times \left(\frac{P_e}{P_{cr}}\right)^{(0.12-0.2lnP_R)} \times \left(-ln\left(\frac{P_e}{P_{cr}}\right)\right)^{-0.55} \times q^{0.67} \times M^{-0.5} \tag{3.37}$$

Where P_{cr} is the critical pressure of the working fluid, R_p is the mean asperity height which is taken as 0.3 μm in this study, q represents the heat flux, and M is the molar mass of the working fluid.

For the condensation process, the following correlation is adopted:

$$\alpha_{cond} = \alpha_l\left(0.25C_o^{-0.45}F_{rl}^{0.25} + 75 \times B_o^{0.75}\right) \tag{3.38}$$

Where the subscript (l) denotes the liquid phase and (α_l) is given by:

$$\alpha_l = 0.2092 \times \left(\frac{k_l}{D}\right) \times R_{el}^{0.78}P_{rl}^{0.33}\left(\frac{\mu}{\mu_w}\right)^{0.14} \tag{3.39}$$

C_o (convection number) is given by:

$$C_o = \left(\frac{\rho_v}{\rho_l}\right)\left(\frac{1}{x-1}\right)^{0.8} \tag{3.40}$$

And F_{rl} and B_o (boiling number) are given by:

$$F_{rl} = \frac{G^2}{(\rho_l^2 g d_e)} \tag{3.41}$$

$$B_o = \frac{q}{G \times i_{fg}} \tag{3.42}$$

Where G (kg/m^{2}s) is the refrigerant mass flux, g is the gravity acceleration (m/s^2), and i_{fg} is the enthalpy of vaporization (kJ/kg).

$$R_{el} = \frac{G \times D}{\mu_l} \tag{3.43}$$

$$P_{rl} = \frac{C_{pl} \times \mu_l}{k_l} \tag{3.44}$$

3.10 Second law efficiency and exergy destruction

Second law efficiency is defined as the ratio between the actual cycle efficiency compared with the maximum theoretical reversible cycle efficiency. Equation 3.45 shows the second law efficiency of a heat pump cycle:

$$\eta_{second\_law} = \frac{COP}{COP_{Carnot}} \tag{3.45}$$

Exergy, also called *availability*, is defined as the maximum theoretical (reversible work) that can be obtained from a system in a given state, working under constant reservoir pressure and temperature. However, in any real thermodynamic process, the exergy can be destroyed, unlike the energy, to satisfy the second law of thermodynamic. The *irreversibility* or (exergy destruction) is defined as the difference between the theoretical reversible work and the actual work.

In an actual thermodynamic system, once the irreversibilities of a component have been estimated, the development and improvement process is guided towards that part in order to reduce the exergy destruction. This has the consequence of improving the device efficiency and hence the overall system performance.

In this thesis, both terms, *irreversibility* and *second law efficiency,* have been used to compare the performance of proposed system components against the ideal one. The evaluation is carried out as follows:

Irreversibility (I) across a compressor, turbine, pump, and expansion valve is given by:

$$I = \dot{m}_{ref} \times T_o \times (s_{out} - s_{in}) \tag{3.46}$$

Where:

T_o	Temperature in the reference state
s	Entropy
$\dot{m}_{ref}$	Working fluid mass flow

In a heat exchanger there are two streams; one is the hot flow carrying the heat, and the other is the cold stream which should receive the rejected heat.

The exergy destruction in the hot stream is expressed as follows:

$$I_{Hs} = \dot{m}_{Hs} \times (h_{HS-in} - h_{HS-out} - T_o \times (s_{HS-in} - s_{HS-out})) \tag{3.47}$$

While the exergy destruction in the cold stream is:

$$I_{CS} = \dot{m}_{CS} \times \left(h_{\,CS-out} - h_{\,CS\_in} - T_o \times (s_{\,CS\_out} - s_{\,CS\_in})\right) \tag{3.48}$$

The total exergy destruction across a heat exchanger is the exergy destruction difference in both streams.

3.11 Modelling the combined ORC and HP cycles

The majority of studies in the open literature adopted the energy and exergy equations mentioned above in the modelling of the ORC and HP cycles. In this thesis, a MATLAB code is developed for this purpose. The rule of this code is to conduct optimization process by varying one or two independent variables to achieve the pre-selected working conditions and design assumptions targeted in this study. The outcome of this optimization approach is to identify the design parameters for the steady state mode. This approach is called *design mode* which involves identifying the refrigerant state at the inlet and outlet of each cycle components. MATLAB code is also used to show the correlation between the different variables and their effect on the system performance.

There are also a number of reliable software packages that were used to model various power and thermal cycles. Keinath and Garimella [152] used Engineering Equation Solver software in their study. Recently, ASPEN PLUS software in its newer version has been introduced to provide steady and dynamic simulations. In our study, ASPEN PLUS software package is used to validate the steady state results obtained from MATLB code. After obtaining the steady state results from both models, ASPEN PLUS software has been used in the *off design mode*. This mode involve setting the heat exchangers areas at constant values based on the steady state results in order to conducted control strategies. The results of these control strategies have then been verified using the dynamic mode.

3.11.1 Thermophysical properties software

To estimate the thermophysical properties of the working fluids, different software programs, databases and subroutines have also been used by researchers and are claimed to have good precision to some extent. The majority of them have used NIST REFPROP software [42] for its accuracy and ability to link up with other programming language software such as the MATLAB [97, 153-156]. Others have used different equations; for example, Saleh, B., et al. [132] and Lai, N., et al. [156] used the BACKONE equation of state in modelling a low temperature ORC cycle. Zhang, S., et al. [157] used a generalized Cubic Equation of State in the theoretical modelling of a water to water heat pump system.

In this thesis simulation work, REFPROP software has been linked with the MATLAB code to estimate the transport properties of the working fluid. In addition, it has been adopted as a property method in the ASPEN PLUS software.

3.11.2 Assumptions adopted in the modelling process

The main assumptions adopted in the modelling procedure can be summarized as follows:

1. In chapter five, the combined system is designed to heat water at constant total thermal capacity. The typical total thermal capacity for a common household is 20 kW.

2. Tap water temperature ranges between 7-10 ^{o}C, therefore a constant value of 10 ^{o}C is adopted.

3. No pressure drop is assumed across the cycle components and connected pipes.

4. In the gas burner, air has a mix ratio of 79% nitrogen and 21% oxygen by volume. The combustion efficiency is assumed to be 100% and the total heat released from burning the Methane is transferred to the ORC working fluid and the exhaust stream, with no heat lost to the surrounding environment.

5. The temperature of the exhaust stream leaving the post heater (T_{15}) is assumed to be a value higher than the dew point to prevent corrosion.

6. Methane heating value in this model is taken as constant at the reference state, which is equal to 55.5 kJ/kg.

7. The power produced by the ORC cycle directly drives the HP compressor, and mechanical losses are negligible.

8. The pinch point temperature difference is set to 3 ^{o}C in both the HP and ORC condensers.

3.12 MATLAB code

In this section, the MATLAB code used to analysis the combined cycle is described in detail including the programming procedures and REFPROP correlations.

3.12.1 Steady state model

The steady state model is used to describe the optimum performance of a thermodynamic cycle that has reached a thermal balance between a heat source and a heat sink. At this point, the main design parameters such as pressure, temperature, enthalpy, and entropy can be identified at each state point across the cycle. Furthermore, the obtained thermophysical properties can be used to estimate the heat and power transfer between the cycle components. In addition, the HXs area can be calculated.

3.12.1.1 HP cycle model

As was mentioned above in section (3.11.2), there are no pressure drops during the condensation and evaporation process, so, the pressure at states 1 and 4 is equal to the HP evaporator pressure. In addition, $P_2 = P_3$ = HP discharged pressure, as shown in Figure 3.5 and 3.6 a. The HP evaporator saturated pressure is estimated here using REFPROP by assuming the refrigerant is fully evaporated at the evaporator exit, and by assuming an evaporation temperature that secure the minimum pinch point temperature difference with the designed air temperature at the evaporator exit [97]. This assumption is satisfied in the fact that in the HX heat transfer process, the hot stream should be higher than the cold stream.

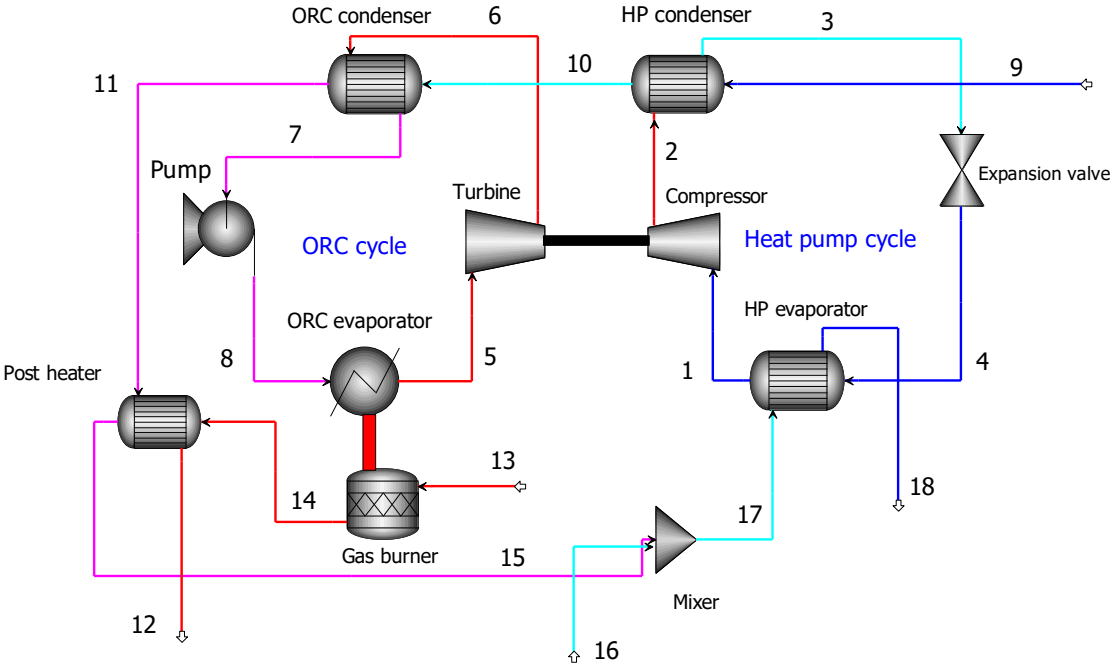

Figure 3.5: Schematic diagram of the proposed natural gas fuelled water heater system.

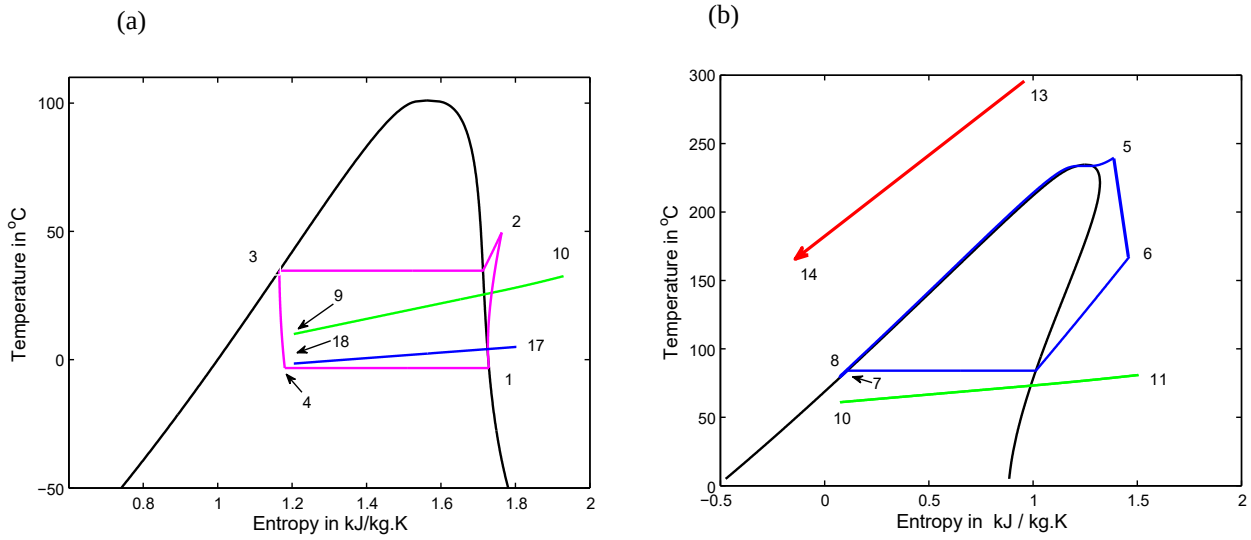

Figure 3.6 (a): T-s diagram for HP cycle; (b) T-s diagram for ORC cycle.

$$T_{HP-evap} = T_{air-out} - \Delta T_{pinch\ point}$$

$$P_{HP-evap} = refpropm('P','T', T_{HP-evap}, 'Q', 1, HP_{refigerant})$$

Then, the other refrigerant properties of the HP refrigerant at state (1) can be calculated using the following REFPROP code:

$$h_1 = refpropm('H',' P', P_{HP-evap}, 'Q', 1, HP_{refigerant})$$

$$s_1 = refpropm('s',' P', P_{HP-evap}, 'H', h_1, HP_{refigerant})$$

Similarly, the HP condensation pressure is calculated by assuming that the refrigerant is fully condensed at the HP condenser outlet, and assuming an initial temperature value for the water leaving the HP condenser. By adapting the $\Delta T_{pinch\ point}$ approach and maintaining the hot stream (refrigerant flow) at a higher temperature than the cold stream (tap water), the HP saturated condensation temperature can be given as follows:

$$T_{HP-cond} = T_{water-out} + \Delta T_{pinch\ point}$$

$$P_{HP-cond} = refpropm('P','T', T_{HP-cond}, 'Q', 0, HP_{refigerant})$$

At state 2 (the isentropic state), the entropy is equal to that of state 1; therefore, enthalpy is given by:

$$h_{2,iso} = refpropm('H','^{P'}, P_{HP-cond}, 's', s_1, HP_{refigerant})$$

Then, the actual enthalpy at state 2 can be calculated from the isentropic efficiency equation $\eta_{iso,comp}$ of the compressor.

$$h_2 = \frac{\left(h_{2,iso} - h_1 + h_1 \times \eta_{iso,comp}\right)}{\eta_{iso,comp}}$$

After that, the entropy and the temperature at state 2 can be calculated as follows:

$$s_2 = refpropm('s','P',P_{HP-cond},'H',h_2,HP_{refigerant})$$

$$T_2 = refpropm('T','H',h_2,'s',s_2,HP_{refigerant})$$

Hence, the enthalpy at state 3 is calculated by assuming that the refrigerant quality is equal to zero.

$$h_3 = refpropm('H','P',P_{HP-cond},'Q',0,HP_{refigerant})$$

Next, the entropy and the condensation saturated temperature can be estimated:

$$s_3 = refpropm('s','P',P_{HP-cond},'H',h_3,HP_{refigerant})$$

$$T_3 = refpropm('T','P',P_{HP-cond},'H',h_3,HP_{refigerant})$$

An isenthalpic expansion process is assumed in the expansion valve.

After that, the quality and the entropy at state 4 are calculated using the following equations:

$$s_4 = refpropm('s','P',P_{HP-evap},'H',h_3,HP_{refigerant})$$

$$q_4 = refpropm('Q','H',h_3,'s',s_4,HP_{refigerant})$$

By adopting the thermal balance approach across the HP condenser, the refrigerant mass flow can be calculated using Equation 3.13 and by assuming the inlet and outlet water temperature and mass flow. After that, the HP cycle main design parameters can be calculated. These include evaporator thermal capacity, compressor work, condenser thermal capacity, and COP by executing Equations 3.2-3.4 and 3.6.

3.12.1.2 ORC cycle model

The same approach used in modelling the HP cycle is also used in relation to the ORC cycle. ORC evaporator pressure is set to a value close to the critical pressure to maximize ORC

thermal efficiency. The appropriate values for different working fluids are available in a wide range of textbooks and also from REFPROP.

The ORC evaporation temperature (state 5) is chosen according to the type of the working fluid used. For wet and isentropic fluids no superheat degree is required, so the refrigerant is assumed to be fully vaporized at the evaporation saturated temperature. In contrast, for dry working fluids a degree of superheat is recommended to ensure that no wet fluid can damage the turbine plates. However, in all cases, the superheat degree should be carefully checked, particularly on the T-s diagram for further confirmation.

$$T_5 = T_{critical} + Degree\ of\ superheat$$

Next, other thermophysical properties of the working fluid can be calculated as follows:

$$h_5 = refpropm('H','T',T_5,'P',P_{ORC-evap},ORC_{refigerant})$$

$$s_5 = refpropm('s','P',P_{ORC-evap},'H',h_5,ORC_{refigerant})$$

The condensation temperature (T_7) is set to a value close to the final water heating temperature value. Therefore, the condensation pressure is calculated by assuming that the vapour fraction is equal to zero at the condenser exit.

$$P_{ORC-cond} = refpropm('P','T',T_7,'Q',0,ORC_{refigerant})$$

The enthalpy of the isentropic state at the turbine exit is given by:

$$h_{6,iso} = refpropm('H','P',P_{ORC-cond},'s',s_5,ORC_{refigerant})$$

Next, the enthalpy and other properties at the turbine exit (state 6) are estimated based on the turbine isentropic efficiency equation:

$$h_6 = h_5 - h_5 \times \eta_{expander_{iso}} + h_{6,iso} \times \eta_{expander_{iso}}$$

$$s_6 = refpropm('s','P',P_{ORC-cond},'H',h_6,ORC_{refigerant})$$

At state 7:

$$h_7 = refpropm('H','P',P_{ORC-cond},'Q',0,ORC_{refigerant})$$

$$s_7 = refpropm('s','P',P_{ORC-cond},'H',h_7,ORC_{refigerant})$$

The isentropic state at the pump outlet state 8, is:

$$h_{8,iso} = refpropm('H','P',P_{ORC-evap},'s',s_7,ORC_{refigerant})$$

By assuming a constant value for the liquid pump isentropic efficiency, the enthalpy at state 8 is given by:

And the entropy at state 8 is given by:

$$s_8 = refpropm('s','P',P_{ORC-evap},'H',h_8,ORC_{refigerant})$$

Due to the assumption of direct coupling between the ORC turbine and the HP compressor, the ORC mass flow is calculated using Equation 3.9 by assuming (W_{comp}= $W_{turbine}$).

At this point, ORC performance parameters such as evaporator and condenser thermal duties, the first and second laws of thermodynamics, and the final water temperature can be evaluated via Equations 3.8-3.11, 3.12, 3.16 and 3.45.

3.12.1.3 Gas burner model

In the gas burner code, the standard enthalpy of combustion ($\bar{h}_f^o$) for pure substances such as O_2 and N_2 are equal to zero, while CH_4, CO_2 and H_2O are set as constant values based on the literature [142].

It is assumed that the term $\left(\bar{h} - \bar{h}^o\right)$ is equal to zero for the reactants based on the assumption that these products are entering the gas burner with the same temperature as the reference state.

When calculating the enthalpy ($\bar{h}$) of CO_2 and H_2O, these gases are assumed to be ideal gases, and thus their enthalpy values are a function of temperature only. The enthalpy values for these products for a wide range of temperatures (0-1000 ^oC) has therefore been adapted from a reliable source [142] and loaded into the MATLAB program as an external function code. This code allows the recall of the enthalpy value when the exhaust temperature is entered. It also provides the ability to adjust the enthalpy by an interpolation process when the exact exhaust temperature is not available in the source data.

3.12.1.4 Modelling the post heater

The post heater is a simple heat exchange. Its thermal capacity is calculated by assuming a constant temperature value at state 15 (T_{15}). After that, the final water temperature is calculated from the thermal balance across the post heater as follows:

$$\dot{m}_{exh} \times (h_{14} - h_{15}) = \dot{m}_w \times (h_{12} - h_{11}) \tag{3.49}$$

3.12.2 Varying one or two parameters in the combined system

The MATLAB code has been developed to model the combined cycle when one or two independent parameters are optimized. A one and/or two nested loop technique has been used to iterate the whole combined cycle parameters. For a single nested loop, the loop boundary is: $for\ i = 1{:}n$, while for a double iteration loop the boundaries are: $for\ i = 1{:}n$ for the first loop and $for\ j = 1{:}n$ for the second loop. Where (n) is the final boundary value.

Therefore, the results could either be expressed as a one-dimensional vector as follows:

$$h_1 = \left(h_1(i), \dots \dots \dots h_1(i{:}n)\right)$$

Or as a two-dimensional matrix:

$$h_7 = \begin{bmatrix} h_7(i,j) & \cdots & h_7(i{:}\,n,j) \\ \vdots & \ddots & \vdots \\ h_7(i,j{:}\,n) & \cdots & h_7(i{:}\,n,j{:}\,n) \end{bmatrix}$$

3.12.3 Pinch point temperature difference (PPTD) model

A number of studies available in the open literature used a simplified pinch point approach by securing a minimum pinch point of 3-5 ^{o}C at the HX exit. However, this procedure cannot precisely predict the pinch point between the hot and cold streams across all the heat exchanger sectional areas, as shown in Figure (3.3). Therefore, an in-depth investigation has been carried out in the modelling of all heat exchangers in this thesis. A developed MATLAB sub-code is used to calculate the temperature difference between the two streams along the entire length of the heat exchangers.

The pinch point can be identified when the temperature, enthalpy, and entropy for both streams across the heat exchanger have been calculated. The process of pinch point calculation for the HP condenser is shown below. The same principle can be applied to the other heat exchangers.

The enthalpy of the refrigerant stream across the condenser is divided into the number of segments between h_{in} and h_{out}. In MATALB, the (*linspace)* function can be used for this purpose:

$$H_{segment} = linspace(h_2, h_3, n) \tag{3.50}$$

Where (n) is the number of segments.

The refrigerant entropy can be calculated using the same method as above, while the temperature is calculated using the REFPROP call function (*refpropm*) which requires two identified thermophysical properties, enthalpy and condenser pressure. This temperature code

should be iterated, using a nested loop, from (1 to n) to cover the temperature range across the condenser. The result is a vector of the refrigerant temperature through the HP condenser.

For the water stream, the water temperature is calculated from the sensitive heat equation by dividing the condenser heating capacity into segments from 0 to n, as was explained in Equation 3.50. The water entropy is calculated using the *refpropm* function. The result is water temperature as a vector. The minimum PPT can be estimated by subtracting the refrigerant and water temperature vectors, and the minimum value is the PPT.

3.13 Dynamic modelling by ASPEN PLUS

The dynamic model in this work is limited to the role of control strategies adopted for the combined system. Therefore, the mathematical model will be applied to specific parts such as the HP evaporator and/or condenser.

The continuity and energy balance equations for evaporator and condenser are given as:

$$\frac{\partial}{\partial t}(\rho_r A_{rcs}) + \frac{\partial m_r}{\partial z} = 0 \tag{3.51}$$

$$\frac{\partial}{\partial t}(\rho_r A_{rcs}) + \frac{\partial}{\partial z}(m_r h_r) + U_r L_{rp}(T_r - T_m) = 0 \tag{3.52}$$

Where the following subscripts apply: r means refrigerant, Arcs denotes the cross section area, U_r is the thermal transmittance of the working fluid, L is the effective length, and m is the wall material.

The discretised form of the above continuity and energy equations for the *n*th zone as explained in Figure (3.7) can written as:

$$\frac{\left(\rho_{r,n}A_{rcs}\right)-\left(\rho_{r,n}A_{rcs}\right)^{-}}{\Delta t}+\frac{m_{r,j}-m_{r,j-1}}{\Delta z}=0$$

Or (3.53)

$$\frac{V_{r,n}}{\Delta t}\left(\rho_{r,n}-\bar{\rho}_{r,n}\right)+m_{r,j}-m_{r,j-1}=0$$

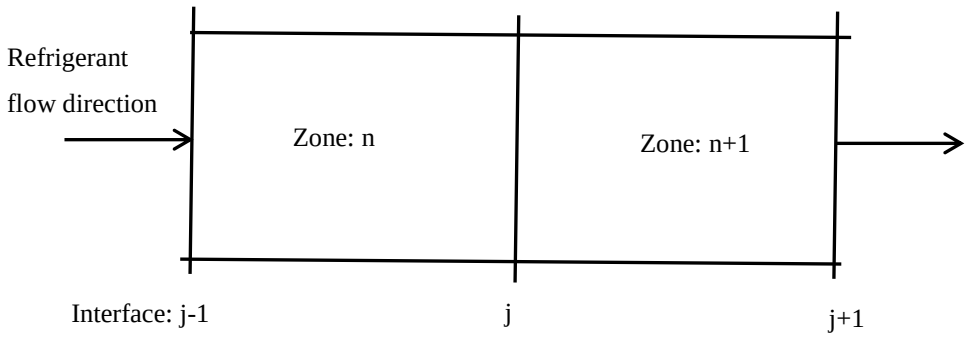

Figure 3.7: Discretisation scheme for the evaporator and condenser

The superscript (-) represents the value at the previous time step.

$$\frac{\left(\rho_{r,n}h_{r,n}A_{rcs}\right)-\left(\rho_{r,n}h_{r,n}A_{rcs}\right)^{-}}{\Delta t}+\frac{m_{r,j}h_{r,j}-m_{r,j-1}h_{r,j-1}}{\Delta z}+U_{r,n}A_{m,n}\left(T_{r,n}-T_{m,n}\right)=0$$

Or:

$$\frac{V_{r,n}}{\Delta t}\left[\left(\rho_{r,n}h_{r,n}\right)-\left(\rho_{r,n}h_{r,n}\right)^{-}\right]+m_{r,j}h_{r,j}-m_{r,j-1}h_{r,j-1}+U_{r,n}A_{m,n}\left(T_{r,n}-T_{m,n}\right)=0$$

Both of the above equations together represent Equation 3.54.

By multiplying Equation 3.53 by $h_{r,n}$ to eliminate $\rho_{r,n}$, then subtracting the results from Equation 3.54, we arrive at Equation 3.55, below:

$$\frac{V_{r,n}\bar{\rho}_{r,n}}{\Delta t}\left(h_{r,n}-\bar{h}_{r,n}\right)+m_{r,j}\left(h_{r,j}-h_{r,n}\right)+m_{r,j-1}\left(h_{r,n}-h_{r,j-1}\right)+U_{r,n}A_{m,n}\left(T_{r,n}-T_{m,n}\right)=0$$

By eliminating the interface variables $h_{r,j}$ and $h_{r,j-1}$, Equation 3.55 will become:

$$\begin{aligned}\frac{V_{r,n}\bar{\rho}_{r,n}}{\Delta t}\left(h_{r,n}-\bar{h}_{r,n}\right)&+h_{r,n}\max\left(m_{r,j},0\right)-h_{r,n+1}\max\left(-m_{r,j},0\right)-m_{r,j}h_{r,n})\\&+m_{r,j-1}h_{r,n}-h_{r,n}\max(m_{r,j-1})+h_{r,n}\max\left(-m_{r,j-1},0\right)\\&+U_{r,n}A_{m,n}(T_{r,n}-T_{m,n})=0\end{aligned}$$

This equation can be simplified as follows:

$$\begin{aligned}&h_{r,n}\left[\frac{V_{r,n}\bar{\rho}_{r,n}}{\Delta t}+\max\left(m_{r,j},0\right)+\max\left(-m_{r,j-1},0\right)+m_{r,j-1}-m_{r,j}\right]\\&=h_{r,n+1}\max\left(-m_{r,j},0\right)\\&+h_{r,n-1}\max\left(m_{r,j-1},0\right)+\frac{V_{r,n}\bar{\rho}_{r,n}\bar{h}_{r,n}}{\Delta t}-U_{r,n}A_{m,n}(T_{r,n}-T_{m,n})=0\end{aligned}$$

Both of the above equations together represent Equation 3.56.

By assuming that $\max\left(m_{r,j},0\right)-m_{r,j}=\max\left(-m_{r,j},0\right)$

And $\max\left(-m_{r,j-1},0\right)+m_{r,j-1}=\max\left(m_{r,j-1},0\right)$,

The final discretised equation for the refrigerant zone for the evaporator and condenser can be written as:

$$Continuity\text{: }m_{r,j}=m_{r,j-1}-\frac{V_{r,n}}{\Delta T}\left(\rho_{r,n}-\bar{\rho}_{r,n}\right) \tag{3.57}$$

$$Energy\text{: }h_{r,n}=\frac{Ah_{r,n-1}+Bh_{r,n+1}-U_{r,n}A_{m,n}\left(T_{r,n}-T_{m,n}\right)+\frac{V_{r,n}\bar{\rho}_{r,n}\bar{h}_{r,n}}{\Delta t}}{C} \tag{3.58}$$

Where:

$$A = \max(m_{r,j-1}, 0),\ B = \max(-m_{r,j}, 0),\ C = A + B + \frac{V_{r,n}\bar{\rho}_{r,n}}{\Delta t}$$

Xu, B., et al. [72] developed a transient dynamic model for an organic Rankine cycle bottoming diesel engine for waste heat recovery. In the heat exchangers model, some vital assumptions were adopted, such as neglecting the axial heat conduction between the working fluid and the heat source through the wall. In addition, the temperature was assumed to be distributed uniformly in the radial direction. The partial differential form of mass and energy balance equations for the working fluid across the heat exchanger is given by:

$$\frac{\partial \dot{m}}{\partial z} + \frac{\partial A\rho}{\partial t} = 0 \tag{3.59}$$

$$\frac{\partial (A\rho h - Ap)}{\partial t} + \frac{\partial \dot{m} h}{\partial z} = \pi d U \Delta T \tag{3.60}$$

Where:

ṁ	Refrigerant mass flow rate
A	Cross sectional area
ρ	Working fluid density
z	Coordinate in the axial direction
p	Working fluid pressure
U	Heat transfer coefficient
d	Working fluid effective path diameter
ΔT	Temperature difference between the working fluid and the wall

The above mass and energy equations are simplified to Ordinary Differential Equations as follows:

$$\frac{dm}{dt} = \dot{m}_{in} - \dot{m}_{out} \tag{3.61}$$

$$\frac{d(\dot{m}h-vp)}{dt} = \dot{m}_{in}h_{in} - \dot{m}_{out}h_{out} + AU\Delta T \quad (3.62)$$

3.14 Modelling the PID controller by ASPEN PLUS

Many control method are available to control the vapor compression cycle. These methods in general involve conventional, advance and intelligent controls. On/off control and refrigerant bypass are one of the earliest control methods. The on/off method include turning the system on/off to achieve the desired thermal target within a time limit. On the other hand, the bypass refrigerant method, as the name suggest, involve bypassing some refrigerant from the active refrigeration loop. The advantage of these approaches is ease of implementation however, the on/off control can result in significant energy lost in the start-up phase and higher energy consumption due to instability in the regulated temperature. While the bypass control method can result in lower system efficiency [158]. On the other hand, variable speed controls methods such as proportional integrate (PI) and proportional integrate derivative (PID) feedback loops, are already established to be more efficient and stable control mechanisms [159]. To implement feedback control, these methods involve the simultaneous use of variable speed compressor and opening valves. The PI controller performance can be satisfactory but limited to a region close to the selected working condition. While a simple PID controller is inexpensive, easy to install and can be used for a wide range of operating conditions [160, 161].

The PID controller is commonly used for regulating the flow rate in a closed loop process. Individually, the three sections in the PID control have different actions in the control process [162]. The three parts are:

$$\text{Proportional part (P): } u_P(t) = k_c(y_s(t) - y(t)) \quad (3.63)$$

$$\text{Integral part (I): } u_I(t) = \frac{k_c}{\tau_I}\int_0^t \big(y_s(\tau) - y(\tau)\big)d\tau \quad (3.64)$$

$$\text{Derivative part (D): } u_D(t) = k_c\tau_d \frac{d(y_s(t)-y(t))}{dt} \quad (3.65)$$

The transfer function of the PID controller output is the sum of these three parts:

$$u(t) = u_P(t) + u_I(t) + u_D(t) \tag{3.66}$$

While controller error $e(t) = y_s(t) - y(t)$

Where:

$y_s(t)$	Set point (the desired process output)
$y(t)$	The process output
$u(t)$	The control output of the PID controller
k_c	Proportional gain (constant)
τ_I	Integral time (constant)
τ_d	Derivative time (constant)

To calculate the output of the PID controller, the set point, proportional gain, integral and derivative time are set by the user based on the appropriate dynamic behaviour. A schematic diagram of a closed loop PID controller is shown in Figure (3.8).

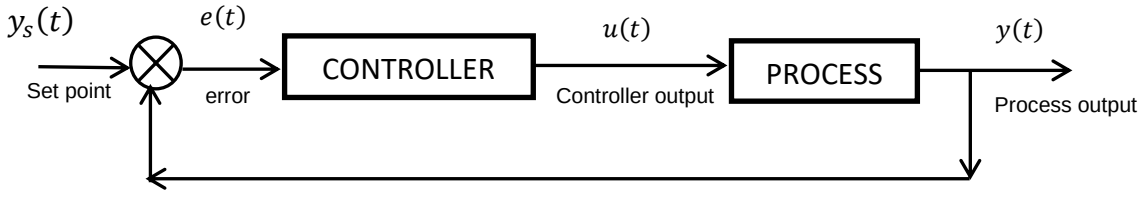

Figure 3.8: Block diagram of the PID controller of a closed loop

Chapter 4: Selection of working fluids

4.1 Introduction

One of the factors impacting upon the design and performance of any thermodynamic cycle is the selection of an appropriate working fluid. Ideally, the working fluid should satisfy modern design aspects such as system thermal efficacy and compatibility, system components' size and lifetime, safety and maintenance cost, and environmental impact [163, 164]. In addition, the thermophysical properties of the chosen working fluid play a vital role in the selection process; these include the critical temperature, the latent heat of vaporization, and the boiling point [165]. Therefore, a properly studied and selected refrigerant can significantly enhance a system's thermal efficiency [166]. In practice, however, there is no single ideal fluid that can achieve optimum levels in all these design aspects. The selection process is therefore a challenging task, and a trade-off approach is usually needed to achieve the best possible results for a given case [167, 168].

4.2 Classification of working fluids

In general, organic working fluids can be categorized into three types according to the slope value $\left(\frac{ds}{dt}\right)$ of the saturated vapor curve on the T-s diagram, as shown in Figure (4.1). For a slope of less than zero, the refrigerant is called a *wet* refrigerant, while if the slope is ∞ , it is called an *isentropic* refrigerant. The third type is named *dry* refrigerant when the slope is above zero [48, 169].

An ORC with an isentropic working fluid can achieve the highest thermal efficiency. In contrast, using a wet refrigerant could increase the possibility of refrigerant condensation during the expansion process. This can cause damage to the turbine blades and also reduce the turbine's isentropic efficiency. If a wet refrigerant is to be selected, it is recommended that the refrigerant is superheated at the turbine inlet to overcome the potential condensation problem. However, excessive superheat can move the pressure ratio away from its optimum value, consequently reducing the cycle efficiency.

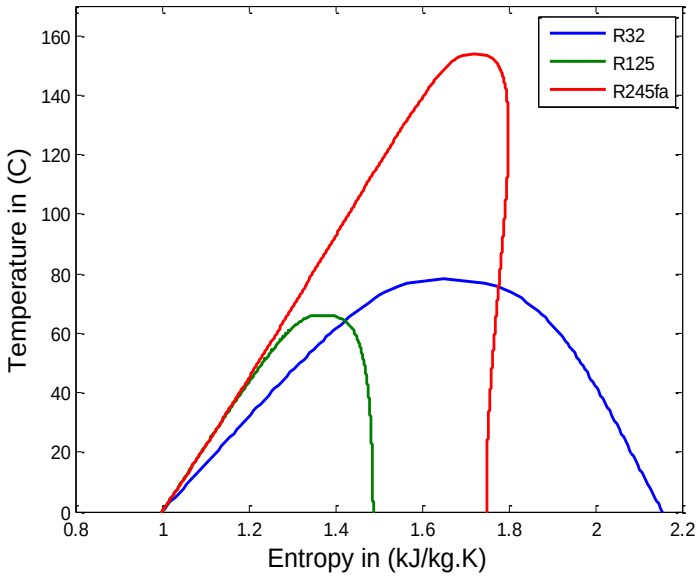

Figure 4.1: T-S diagram for wet fluids (e.g., R32), isentropic fluids (e.g., R125), and dry fluids (e.g., R245fa).

On the other hand, using a dry working fluid in the ORC will keep the refrigerant in a superheated state at the expander outlet. This will result in higher thermal energy being rejected by condensing rather than being usefully utilized in the expansion process. This could reduce thermal efficiency and increase the condenser heat exchanger area, and consequently the costs. Likewise, using isentropic fluid in a HP cycle can achieve high COP. Wallerand, A., et al. [167] revealed that among the compared fluids, propane has shown similar behaviour to an isentropic fluid in that it could reduce the compression work and hence increase the COP.

The same obstacle of a two-phase flow refrigerant entering the HP compressor can occur when a dry fluid is used, particularly at a low saturated temperature. It is therefore recommended to superheat the working fluid at the compressor inlet.

Different working fluids have been studied and compared in the literature for both HP and ORC cycles. Nasir and Kim [169] revealed that for the combined ORC-HP, the best candidate pair of working fluids are R134a and Isobutane, for ORC and HP cycles respectively. With these refrigerants, the cycle achieved a COP in the range of 0.219 to 0.281 when the outdoor air temperature is 40 ^{o}C.

Frate, G., et al. [168] conducted a comparison study on working fluids for a vapour compression heat pump cycle. Although some of the investigated working fluids such as Acetone and Benzene have shown higher performance profiles, they are highly flammable and toxic. In contrast, R1233zd (E) has been shown to be a good compromise between the COP and the volumetric heating capacity (VHC). VHC is defined as the ratio between the condenser heating capacities over the refrigerant volume flow rate at the compressor inlet. The higher the VHC value, the smaller the compressor size and, hence, the lower the cost.

For an ORC cycle driven by liquefied natural gas, Yu, H., et al. [170] revealed that R125, R143a and R1270 showed the best performance for a cycle without heat recovery. Meanwhile, for an ORC cycle that utilizes the waste heat from the flue gases of a natural gas power plant, R170, R134a and R290 are identified as being the most suitable candidates.

Scaccabarozzi, R., et al. [171] conducted a comparison study on different working fluids for an ORC cycle driven by wasted heat from the exhaust stream of a large internal combustion engine. Their results showed that the most efficient refrigerants for lower exhaust stream temperatures are HCFO-1233zde, HFE-245fa2, HFO-1336mzz, HFE-347mcc, HFE-245cb2 and Novec 649. For high engine exhaust temperature, Cyclopentane, Ammonia, HCFO-1233zde, HFE-245fa2, and HFO-1366mzz were all found to have a better performance.

In this chapter, natural, synthetic and pure refrigerants for HP and ORC cycles are selected and analysed. In addition, mixed working fluids have been studied for an ORC cycle. The comparison is based on the best possible performance for the combined cycle under the pre-set working conditions. In addition, Ozone depletion potential (ODP), Global warming potential (GWP), and Atmospheric Lifetime (ALT), for these working fluids are compared.

4.3 Working fluid selection for the heat pump cycle

To evaluate the performance of different working fluids in a conventional vapour compression heat pump cycle used for a heating or cooling application, two approaches have been proposed. In the first approach, the cycle performance for the heating application using different refrigerants is compared. In the second approach, the HP cycle is designed for cooling and/or refrigeration effects. In both approaches, the mass flow rate of the selected refrigerants is set at a constant value, and the compressor isentropic efficiency is assumed to be 70%.

4.3.1 First approach to the HP cycle

In this investigation, a list of refrigerants is selected and the T-s diagram for them is presented in Figure 4.2. In this approach, the HP-condensation temperature is varied between 30-90 ^{o}C, which is suitable for a heating application. The evaporation temperature is set constant at 2.5 ^{o}C.

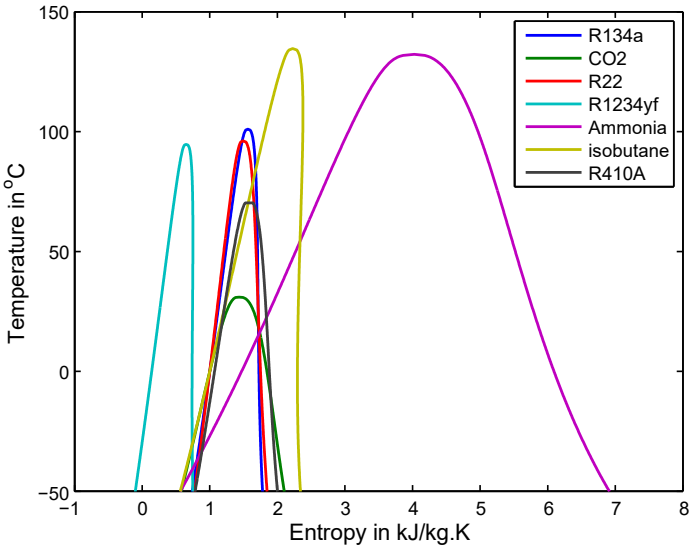

Figure 4.2: T-s diagram for the HP cycle working fluids

Figure 4.3 shows the effect of the condensation temperature on the heating coefficient of performance of the HP cycle for different working fluids. All the selected refrigerants show similar behaviour; i.e., the COP_h decreases with the rise in condensation temperature. Although these working fluids showed comparable COP_h, Ammonia and R600a achieved the best performance for all tested condensation temperatures. As the critical temperature for R410A is 63 ^oC, the evaluation for this refrigerant ended at this value, as shown in Figure 4.3.

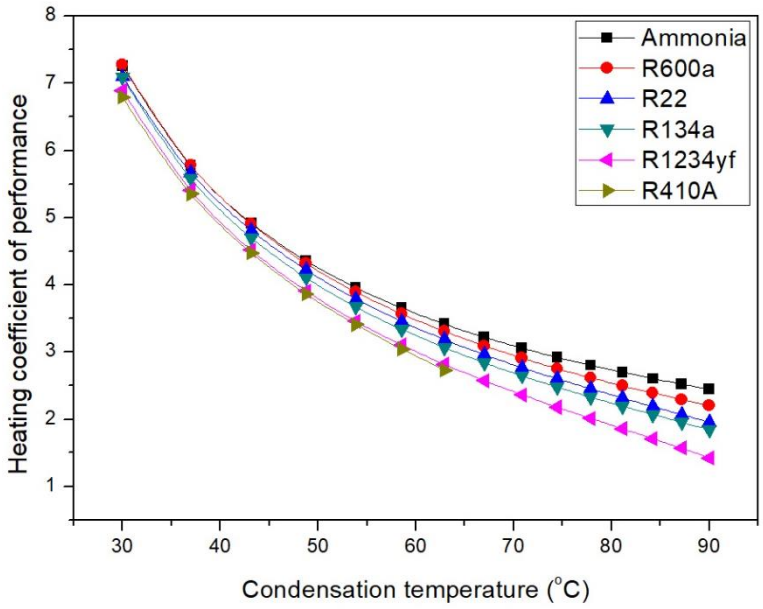

Figure 4.3: Effects of condensation temperature on HP-COP_h for different working fluids

The performance of an HP cycle using CO_2 as the working fluid was also investigated, and the results are shown in Figure 4.4. As the selected condensation temperature is above the critical temperature of CO_2 (30.9 ^oC), CO_2 will not condensate in this region, and instead becomes a supercritical fluid in a gas cooler. In addition, the condensation pressure for the CO_2 is set above its critical pressure value (73.7 bar). From the results, CO_2 has a lower coefficient of performance than the other selected working fluids. Furthermore, increasing the gas cooler exit temperature causes a decline in COP_h at various pressures. However, for each temperature value, increasing the gas cooler pressure has a positive effect on the heating coefficient of performance.

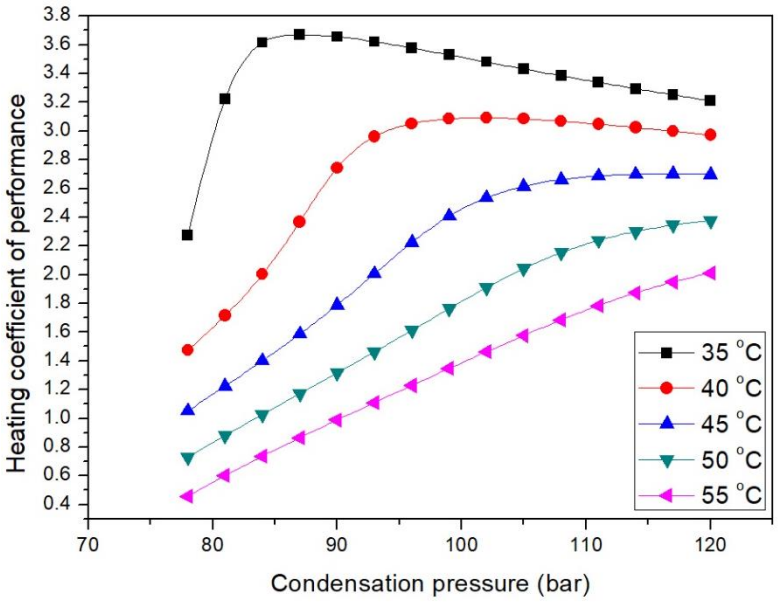

Figure 4.4: HP-COP_h for CO_2 under different gas-cooler pressures and exit temperatures

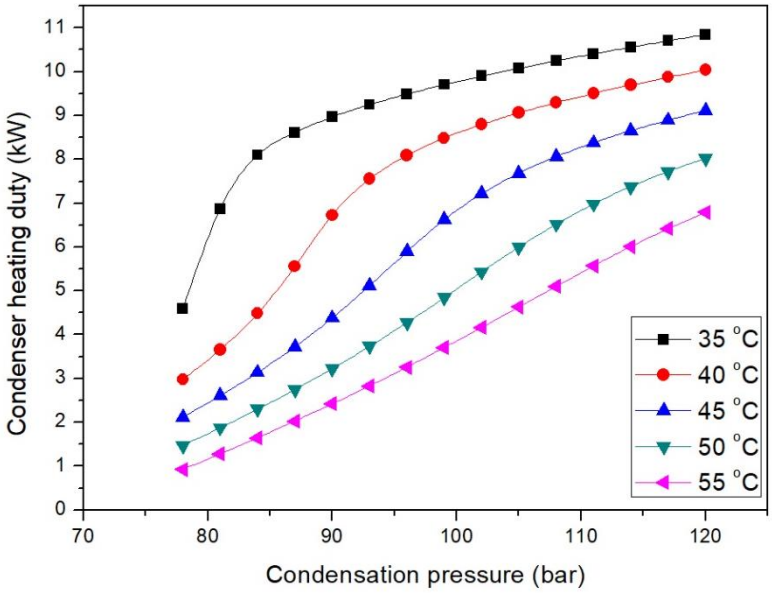

Figure 4.5: HP-Condenser heating duty for CO_2

The behaviour of the condenser heating duty for CO_2 follows the same pattern as for COP_h, with both gas-cooler pressure and exit temperature as shown in Figure 4.5. The increase in the heating duty occurs because the condensation pressure is in the supercritical region, as shown in the T-s diagram.

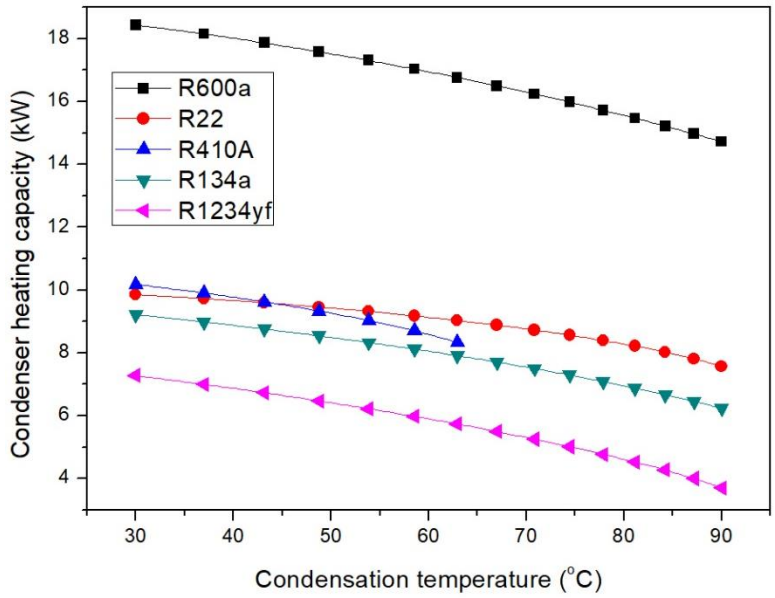

Figure 4.6: HP-Condenser heating capacity for different refrigerants with condensation temperature

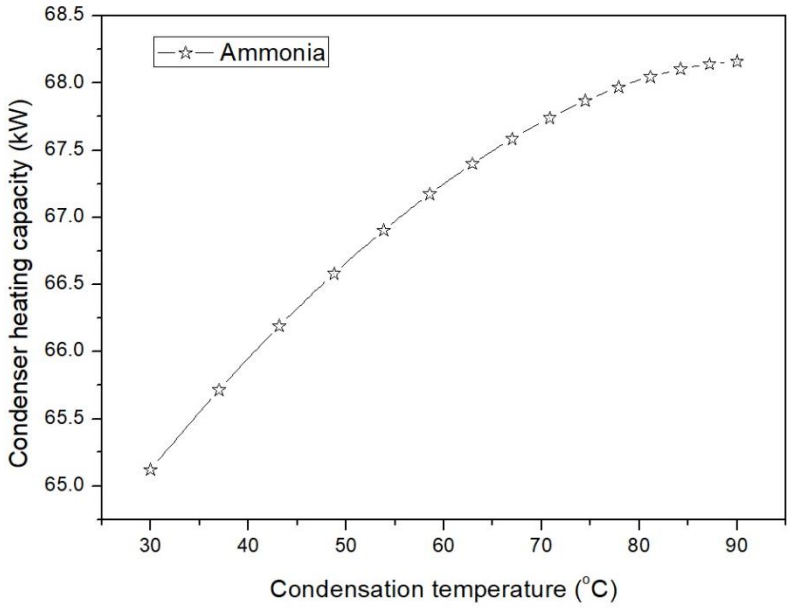

Figure 4.7: HP-Condenser heating capacity of ammonia with different condensation temperature

For all the other selected working fluids except Ammonia, increasing the condensation temperature reduces the HP-condenser heating capacity, as shown in Figure 4.6. As the condensation temperature increases from 30 to 90 ^{o}C, all refrigerants approach their critical temperature, resulting in a reduction in the heat of condensation, as shown in the T-s diagram.

In contrast to other working fluids, when Ammonia is used as HP refrigerant, an increasing condensation temperature initially increases the condenser heating duty, as illustrated in Figure 4.7. This increment gradually slows down as the condensation temperature approaches its critical temperature. This can be attributed to Ammonia's higher heat of vaporization compared to the other working fluid (see T-s diagram). Ammonia also shows a significantly higher heating capacity, which means it could have great potential in large-scale heating applications, but also indicates that the equipment size needed will be significantly larger and thus more expensive.

The evaporation pressure for each working fluid when the evaporation temperature is set at 2.5 ^{o}C is shown in Table 4.1. In addition, the corresponding condensation pressure range for each refrigerant is also presented.

Table 4.1 Working conditions for HP cycle for different working fluids (first approach).

Refrigerant	Evaporator pressure (bar)	Condenser pressure (bar)
R600a	1.448	3.538 - 4.691
R22	5.397	11.9187 - 15.335
R134a	3.202	7.701 - 10.165
R1234yf	3.434	7.835 - 10.183
R410A	8.659	18.893 - 24.256
CO_2	37.21	78-120
Ammonia	4.71	11.67-51.16

Regarding evaporator cooling capacity, Ammonia has shown a significantly higher cooling capacity, which indicates its relatively higher ability to extract heat from the heat source than

the other working fluids, as shown in Figure 4.8. This is due to its higher heat of vaporization in the selected condensation temperature range compared with the other refrigerants.

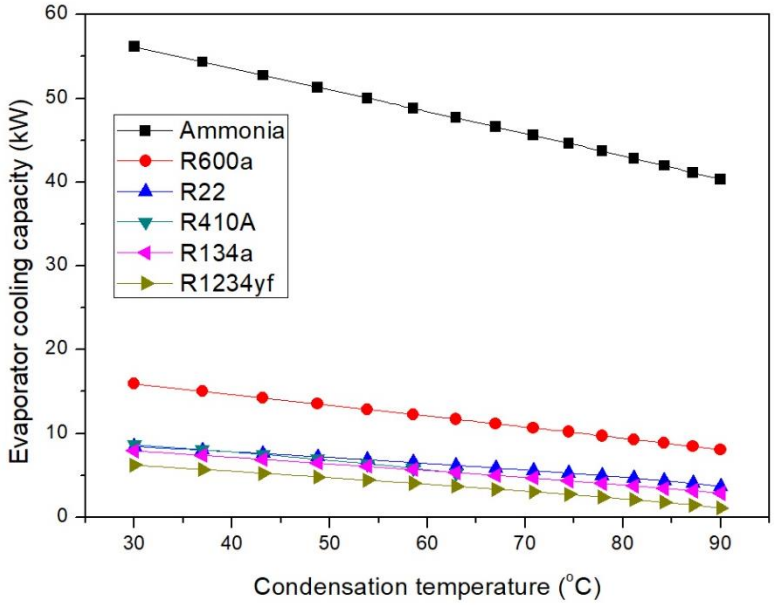

Figure 4.8: HP-evaporator cooling capacity of different working fluids

The evaporator cooling duty of CO_2 increases as the exiting temperature of the gas cooler decreases across the pressure range. At each selected temperature, the cooling duty increases

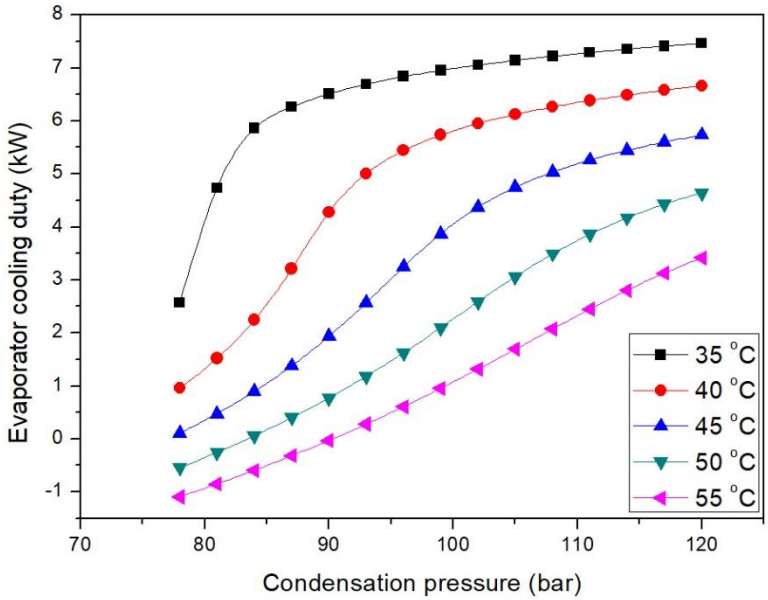

Figure: 4.9 HP-evaporator cooling capacity of CO_2

with the rise in gas cooler pressure. The highest cooling capacity is achieved at a gas cooler temperature of 35 ^{o}C, and pressure above 85 bar, as shown in Figure 4.9.

4.3.2 Second approach to the HP cycle

To investigate the performance of various working fluids in a HP cycle used for cooling purposes, the evaporation temperature was ranged between -18 and 2.5 ^{o}C when the condensation temperature was set as 30 ^{o}C.

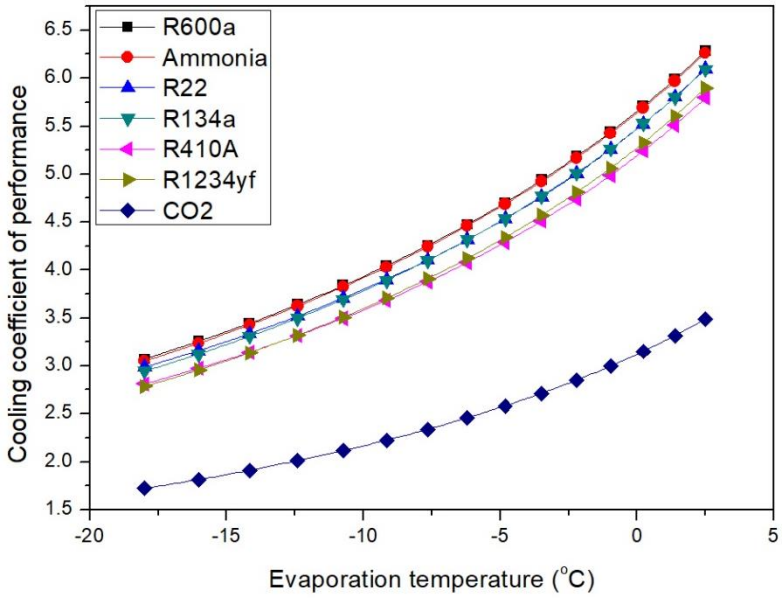

Figure 4.10 HP-COP_c for various refrigerants under various evaporation temperature

Figure 4.10 shows that the cooling coefficient of performance for all working fluids increases with the rise in evaporation temperature. The COPc of all the refrigerants except CO_2 ranged between 3-6, whereas CO_2 achieved the lowest value at between 1.72-3.48. Yu, H., et al. [80] produced comparable results, having found that the COP increases when the evaporation temperature increases for a group of working fluids used in a HP cycle.

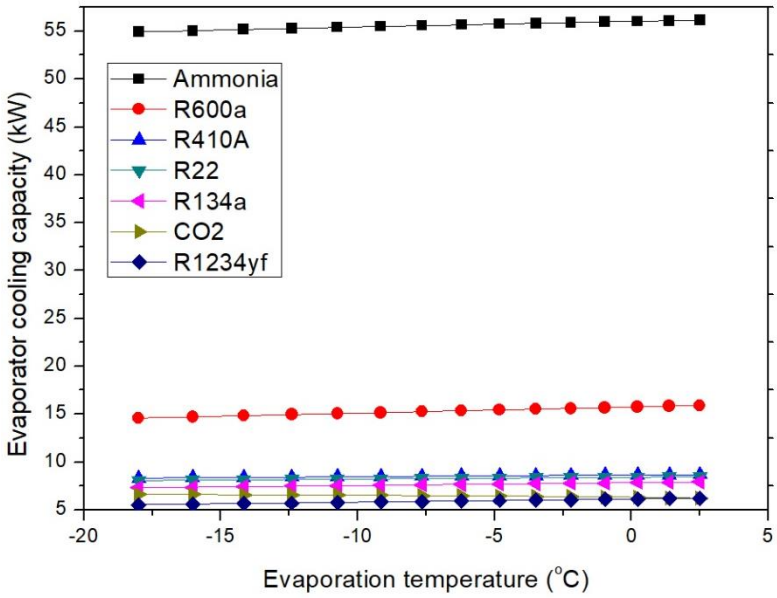

Figure 4.11: HP-evaporator cooling capacity of various working fluids

Increasing the evaporation temperature of all the selected refrigerants has insignificant effects on the evaporator cooling capacity, as shown in Figure 4.11. Similar to approach one, Ammonia displays a much higher cooling capacity, making it a good candidate for a cooling application; however, it is a toxic substance and is therefore not suitable for domestic applications.

The heating capacity of the HP-condenser declines slightly with increased evaporation temperature for all working fluids, as illustrated in Figure 4.12. For evaporator temperatures in the range of -18 to 2.5 ^{o}C, the condenser heating capacity for Ammonia varies in the range of 73-65 kW. For R600a, the heating capacity ranges from 19.3 to18.4 kW, while for other working fluids it varies between 7-11 kW.

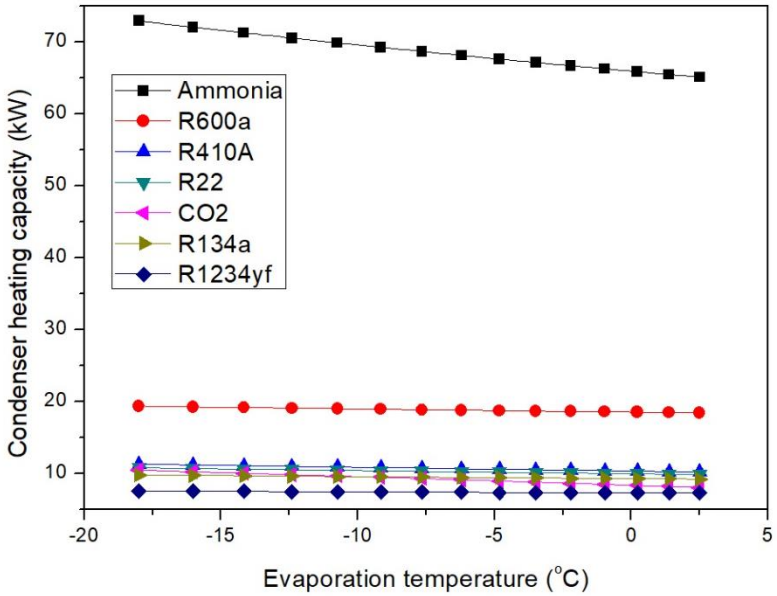

Figure 4.12: HP-evaporator heating capacity of various refrigerants

Table 4.2 shows the evaporation pressure range for evaporation temperature from -18 to 2.5 ^{o}C for each of the selected working fluids. In addition, as the condensation temperature is set to 30 ^{o}C, the table shows the condensation pressure for each working fluid.

Table 4.2 Working conditions of the HP cycle for different working fluids (second approach).

Refrigerant	Evaporator pressure in bar	Condenser pressure in bar
R600a	0.644 - 1.448	3.538
R22	2.647 - 5.397	11.918
R134a	1.446 - 3.202	7.701
R1234yf	1.634 - 3.434	7.835
R410A	4.312 - 8.659	18.893
CO_2	20.938 - 37.214	72.137
Ammonia	2.075 - 4.71	11.67

4.4 Working fluid selection for the ORC cycle

In this section, the results of the analysis of a selection of pure and mixed working fluids for an ORC power plant are presented, including pure refrigerants R123, Heptane, Hexane, Pentane and R245fa; and a mixture of Hexane (50%) and R141b (50%). Hexane is a flammable refrigerant with good thermal efficiency, so it is therefore recommended to mix it with a retardant refrigerant such as R141b or R11. This has the advantage of reducing its flammability, but with the small drawback of reduced efficiency [68]. A mixture of R245fa (80%) and R134a (20%) was also adopted Collings, P. [48].

To evaluate the ORC cycle efficiency of these working fluids, two approaches are adopted in the present study. In the first approach, the ORC-evaporation temperature is set at 95 ^{o}C, and the effect of condensation temperature on the cycle performance for each refrigerant is studied. In the second approach, the condensation temperature is kept constant and the evaporation temperature is varied for each working fluid. The T-s diagram for the selected working fluids in the ORC cycle is illustrated in Figure 4.13. It should be noted that R141b is not available in the REFPROP database, so R143a was used as a substitute solely to obtain the data for the T-s diagram.

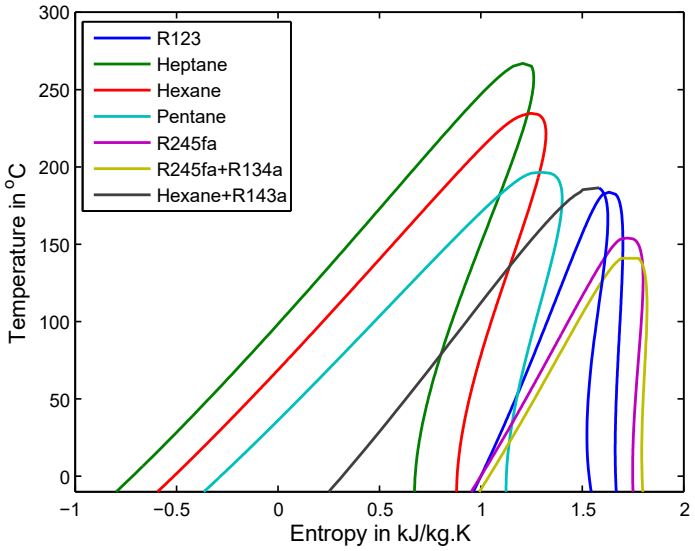

Figure 4.13: T-s diagram for the ORC cycle working fluids

4.4.1 First approach to the ORC cycle

Figure 4.14 showed that as the condensation temperature increases from 30 to 90 ^{o}C, the ORC thermal efficiency declines for all the working fluids. The highest thermal efficiency is achieved at a condensation temperature of 30 ^{o}C, when the evaporation temperature is 95 ^{o}C.

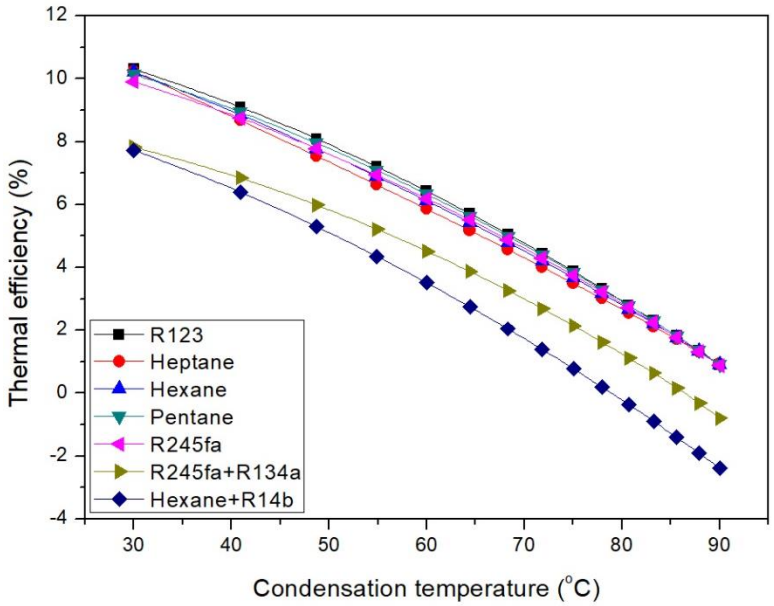

Figure 4.14: ORC-thermal efficiency for various refrigerants

Figure 4.15 shows that a higher condensation temperature has a negative impact on condenser heating capacity regardless of the working fluid. This is due to the decline in the condensation heat for the working fluid as it approaches its critical temperature, as shown in the T-s diagram above (Figure 4.13). However, Hexane, Heptane and Pentane achieved significantly higher heating capacity than the other working fluids throughout the temperature range. In addition, a mixture of Hexane and R141b achieved a good condenser heating capacity.

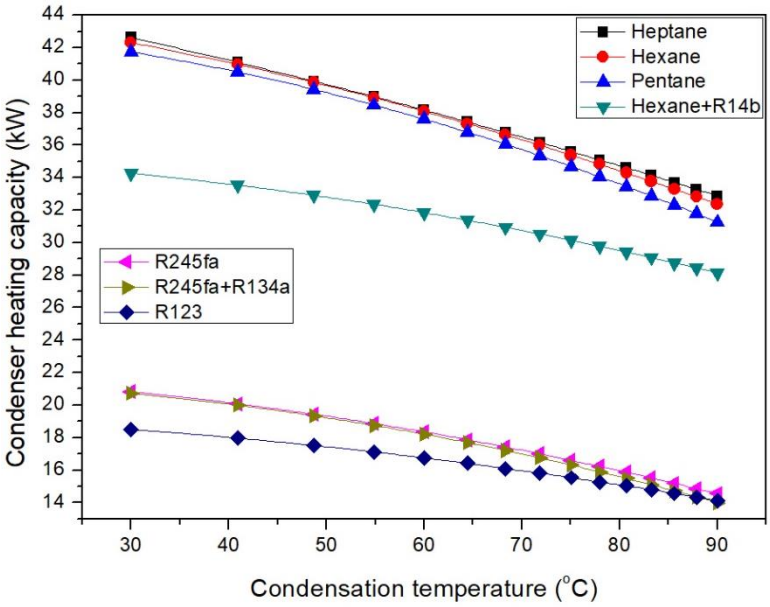

Figure 4.15: ORC-Condenser heating capacity for various refrigerants under different condensation temperatures

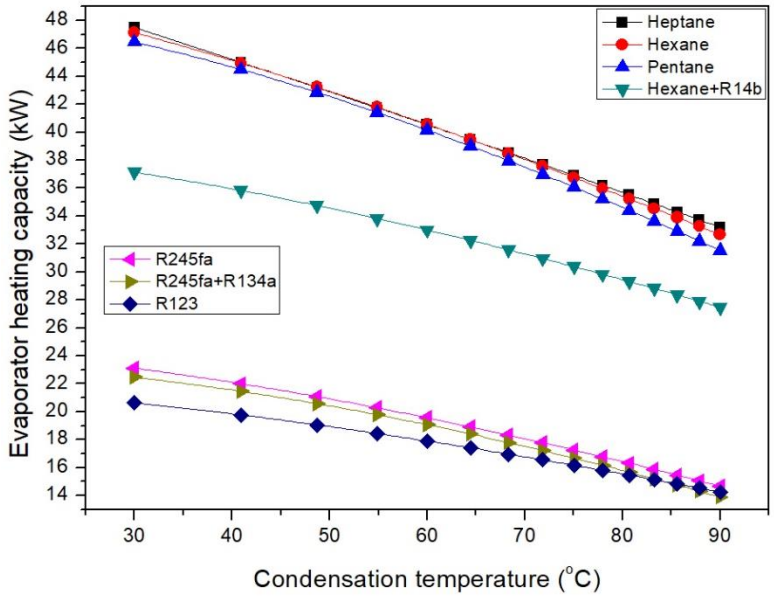

Figure 4.16: ORC-evaporator heating capacity for various refrigerants under different condensation temperatures

Figure 4.16 shows the effects of condensation temperature on ORC-evaporator heating capacity. For all the working fluids, evaporator capacity declines when the condensation temperature increases, in a pattern similar to condenser heating capacity.

Table 4.3 summarises the evaporator and condenser pressures of the ORC system using the first approach for the selected working fluids.

Table 4.3 Working conditions for the ORC cycle for different working fluids (first approach).

Refrigerant	Evaporator pressure in bar	Condenser pressure in bar
R123	7.014	1.095 - 6.242
Heptane	0.916	0.0777 - 0.786
Hexane	2.161	0.249 - 1.889
Pentane	5.288	0.819 - 4.703
R245fa	11.298	1.777 - 10.06
R245fa & R134a	14.252	3.528 - 15.685
Hexane & R141b	2.331	0.544 - 3.22

4.4.2 Second approach to the ORC cycle

In this approach, the condensation temperature of the ORC system is assumed to be constant at 30 ^{o}C, and the evaporation temperature is varied from 95 ^{o}C to the critical temperature for each working fluid.

In contrast to the condensation temperature effects on the ORC-thermal efficiency (Figure 4.14), increasing the evaporation temperature results in a significant rise in thermal efficiency for all working fluids, as shown in Figure 4.17. In addition, mixing R141b with Hexane not only increases its ability to tolerate higher evaporation temperatures and pressure, but also significantly improves its thermal efficiency. The highest thermal efficiency for Hexane alone is 17.03 % at near-critical evaporation temperature (233.6 ^{o}C) and pressure (30 bar). In contrast, Hexane with R141b recorded an efficiency of 17.4 % at a temperature of 244 ^{o}C and pressure

of 39 bar. A similar trend in ORC cycle efficiency with various working fluids has previously been noted by Yu, H., et al. [80].

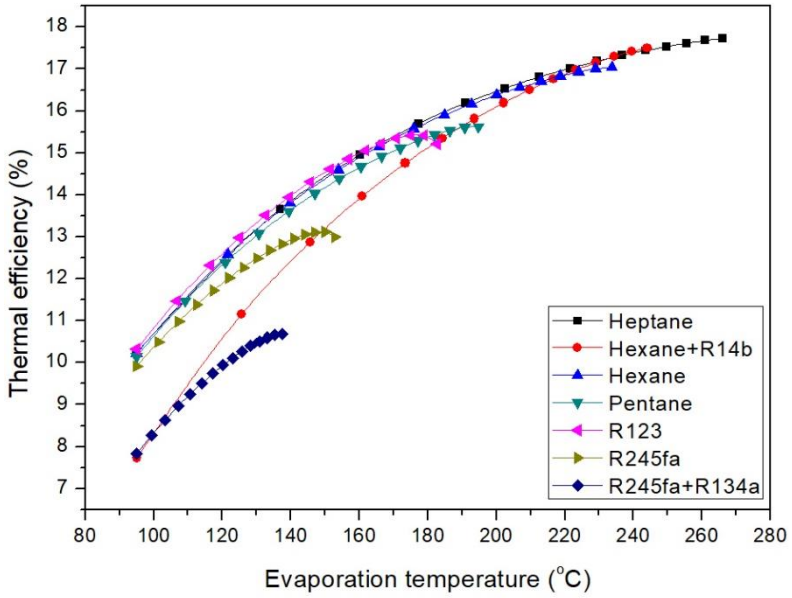

Figure 4.17: ORC-thermal efficiency for various refrigerants under different evaporation temperatures

Increasing the evaporation temperature also causes a significant rise in the thermal capacity of the ORC-evaporator for Heptane, Hexane and Pentane, whereas the effects are insignificant for the other working fluids, as shown in Figure 4.18. For instance, increasing the evaporation temperature for Heptane from 95 to 266 °C increases the evaporator heating capacity from 47.4 to 74.3 kW. In contrast, increasing the R123 evaporation temperature from 95 to 182.6 °C only slightly increases its heating capacity from 20.6 to 21.7 kW.

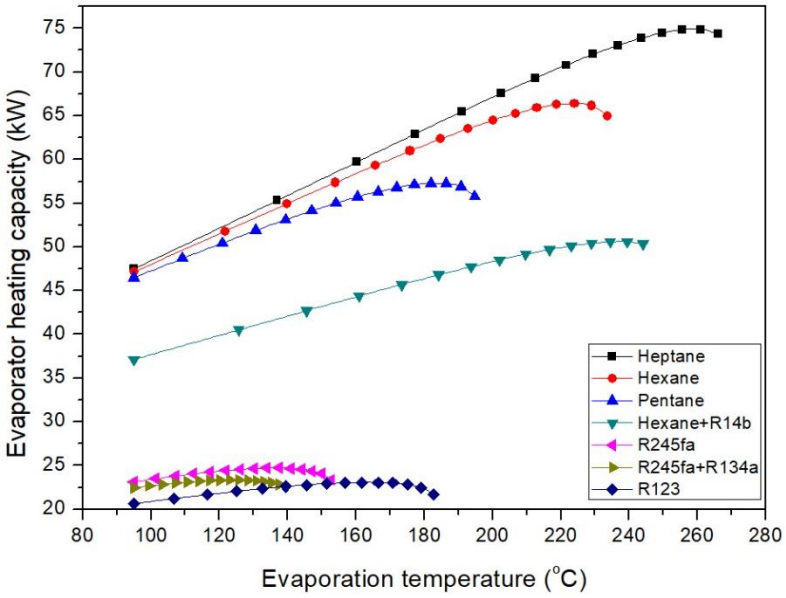

Figure 4.18: ORC-evaporator heating capacity for various refrigerants under different evaporation temperatures

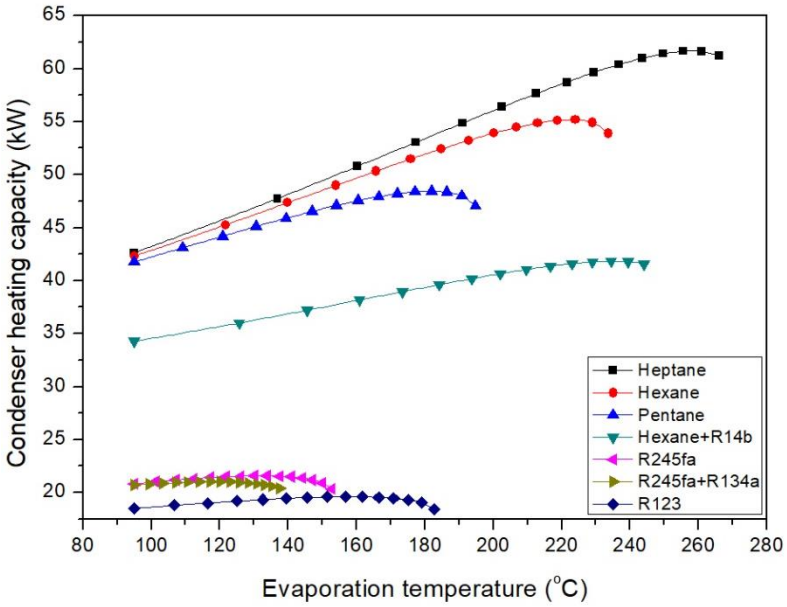

Figure 4.19: ORC-condenser heating capacity for various refrigerants under different evaporation temperatures

Figure 4.19 shows the effect of changing the evaporator temperature on the heating duty of the ORC-Condenser. Similar behaviour to that of the evaporator heating capacity is seen in the condenser heating duty, as the evaporation temperature increases for all the working fluids. For

example, for Hexane, as the evaporation temperature increases from 95 to 233.6 ^{o}C, the condenser heating capacity increases from 42.3 to 53.8 kW.

Table 4.4 shows the corresponding changes in refrigerant pressure when the evaporation temperature of the ORC-evaporator varies. In addition, the condensation pressure for each refrigerant at a condensation temperature of 30 ^{o}C is calculated using REFPROP software.

Table 4.4 Working conditions for ORC cycle for different working fluids (second approach).

Refrigerant	Evaporator pressure (bar)	Condenser pressure (bar)
R123	7.014 - 36	1.095
Heptane	0.916 - 27	0.0777
Hexane	2.161 - 30	0.249
Pentane	5.288 - 32.8	0.819
R245fa	11.298 - 35.7	1.777
R245fa & R134a	14.252 - 34.9	3.528
Hexane & R141b	2.331 - 39	0.544

4.5 Environmental and safety profiles of the working fluids

In order to evaluate the environmental impact of a refrigerant, three indexes are commonly used: Ozone depletion potential, Global warming potential, and Atmospheric Lifetime. The ODP is the relative amount of degradation a chemical compound can cause to the Ozone layer. The GWP is the global warming effect of a given mass of gas; it is a relative scale which compares the amount of heat trapped by a greenhouse gas to that produced by the same mass of CO_2. Lastly, the ALT is the amount of time gases can remain in the atmosphere before being neutralized by chemical reaction or deposition. Moreover, flammability, toxicity and corrosion are additional safety factors considered in the working fluid selection process. Some of the working fluids have been phased out due to their high ODP value, such as R11, R12, R113, R114, and R115. With the increased awareness of global warming, further refrigerants are expected also to be phased out due to their high GWP, such as R22, R123, R124, R141b, and

R142b. Table 4.5 shows the ODP, GWP and ALT of most of the working fluids used in this study.

Table 4.5 Environmental indices for the working fluids [67, 172].

Refrigerant	**ODP relative to R11**	**GWP relative to CO_2 (100-year time horizon)**	**ALT (year)**
R-134a Tetrafluoro-ethane	0.000015	1430	14
R-141b Dichloro-1-fluo-roethane	0.12	713	9.3
R-22 Chlorodifluoro-methane	0.05	1780	12
R-245fa Pentafluoropro-pane	0	950	7.2
R-717 Ammonia - NH_3	0	0	0.25
R-744 Carbon Dioxide - CO_2	0	1	120
R-600a Isobutane	0	20	0.019
R-410A, Puron, AZ-20 (R-32/R-125 (50/50)	0.037	2088	none
R-601 Pentane	0	11	0.01
R-123	0.022	76	1.3
R-1234yf	0	4	none
R143a	0	4400	52
Hexane	0	Very low	None
Heptane	0	Very low	None

From the table, it is clear that natural refrigerants such as Ammonia and CO_2 have excellent environmental profiles; however, Ammonia is a toxic substance and therefore might not be suitable for domestic applications. Likewise, refrigerants such as Hexane, Heptane, Propane and Isobutane have good environmental indices, but they are all flammable. The other refrigerants selected in this chapter have comparable ODP results, while for GWP, R410A and R22 have the highest impacts.

4.6 Conclusion

In this chapter, various working fluids have been selected and analysed for heat pump and ORC cycles. A comparison between the working fluids was conducted based on the efficiency of their performance, thermal cooling and heating capacities, and environmental and safety aspects. For the heat pump cycle, in terms of COP_h, all the selected refrigerants have shown comparable results with a condensation temperature of 30 ^oC. However, as the condensation temperature increases, Ammonia, R600a, R22 and R134a have shown the highest performance. Both Ammonia and R600a showed significantly higher condenser thermal capacity. For the cooling application, increasing evaporation temperature causes a rise in COPc, with comparable results for all the selected refrigerants. Regarding condenser and evaporator thermal capacity, Ammonia has shown a significantly higher capacity, followed by R600a. For the ORC cycle, the selected pure refrigerant showed a comparable result in terms of thermal efficiency and heat exchanger capacities for the first approach. For the mixture of Hexane and R141b, the thermal efficiency was shown to be comparable to that of pure Hexane at a higher evaporation temperature. However, pure Hexane has a higher thermal capacity than the mixture. Apart from pure R245fa and mixed R245fa with R134a, other working fluids obtained similar ORC thermal efficiency. From a safety perspective, Ammonia, Hexane, Heptane, Pentane and R600a might not be suitable for domestic applications due to their flammability and toxicity. For the HP cycle, CO_2 and R1234yf have lower environmental impacts, as they showed lower COP than R134a. Meanwhile, for the ORC cycle, R123 and R245fa have comparable environmental safety profiles and comparable thermal efficiency. Based on these results, R123 and R245fa have been selected as the working fluids for the ORC cycle in this research. For the HP cycle, R134a has been nominated as the working fluid based on its comparable performance to the other working fluids for heating and cooling modes with a safe environmental profile.

Chapter 5 Combining ORC-HP cycles to provide hot water for domestic use

5.1 Introduction

In this chapter, a gas fuelled heating system based on combined heat engine and heat pump cycles is proposed and investigated. This system consists of a gas burner, an organic Rankine cycle power generator, and an air source heat pump cycle. The intended application of the system proposed in this chapter is domestic hot water supply. Comprehensive simulation assessments were carried out to investigate the combined system performance in terms of final water temperature, total system thermal capacity, individual cycle efficiency, and overall fuel-to-heat efficiency. In-house MATLAB code as well as ASPEN PLUS software were used, and the REFPROP database was adopted for the working fluid thermophysical properties. The combined cycle performance for domestic hot water supply was investigated under different working conditions, including varying evaporation and condensation pressures in both cycles. In addition, the pinch point temperature approach was adopted in all the heat exchangers and applicable ORC evaporation pressure was used. The aim was to maximize the wasted heat recovery and improve overall system efficiency. The best design configuration for water heating is identified in the chapter, and steady state results are plotted. An exergy analysis and the second law of thermodynamic efficiency were also included. In addition, control strategies were adopted to tackle the effects of ambient temperature variation on system performance with the aim of maintaining steady system performance while keeping the HP-evaporator frost free. A dynamic model using ASPEN PLUS software was used to verify and validate these control strategies.

5.2 The thermodynamic concept

The thermal energy generated from natural gas combustion in the burner is used to drive an ORC cycle (assuming no heat is lost), and the resultant mechanical power is used to directly drive a vapour compression heat pump cycle (assuming no power is lost). The ambient air stream and the rejected thermal energy contained in the flue gases are mixed then used as a heat source for the heat pump cycle. The rejected latent thermal energy from both cycles' condenser

as well as the sensible heat from the post heater is used to raise the water temperature to the desired value.

5.3 Preliminary design of the combined cycle

In this proposed configuration, the total heating capacity of the system is assumed at 20 kW and the cold tap water heating occurs in three stages, as shown in Figure 5.1. Initially, the water which enters at a temperature of 10 ^{o}C is heated in the HP condenser. A further increase in its temperature is achieved by the ORC condenser. Finally, the water reaches the desired level temperature of (65 ^{o}C) at the outlet of the post heater by obtaining some of the heat contained in the flue gases exiting the burner. After leaving the post heater, the flue gases (assumed to be at 70 ^{o}C) are mixed with ambient fresh air to enter the HP evaporator for further energy recovery. The water mass flow rate can be directly calculated from the inlet and outlet temperature difference and from the total system heating capacity.

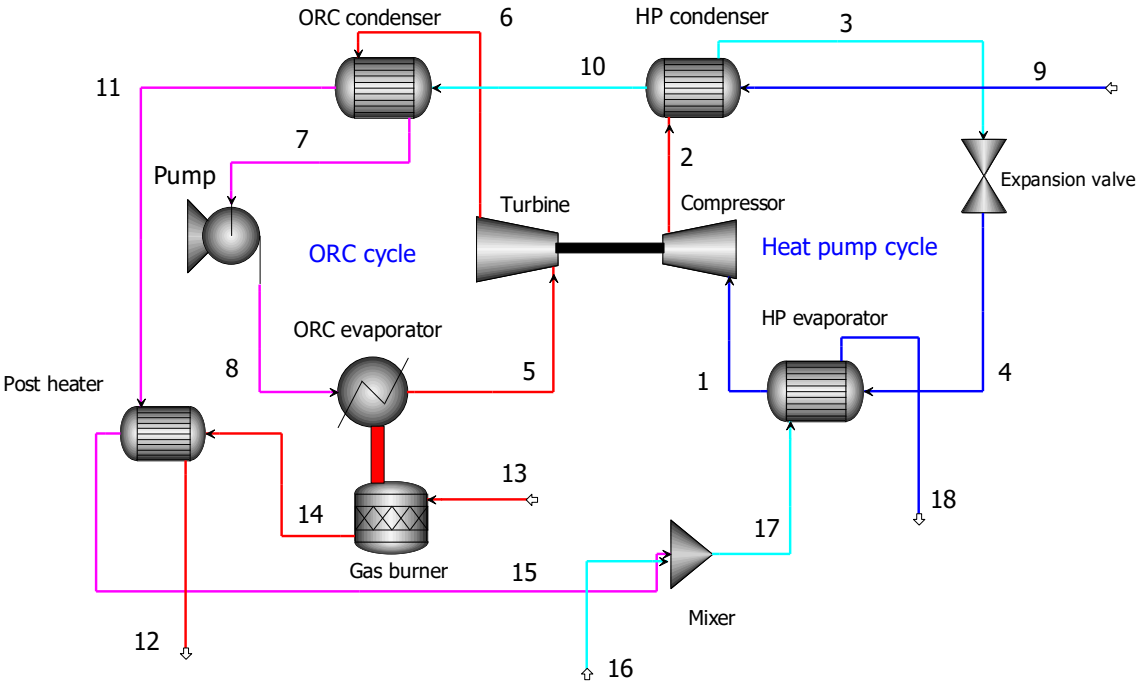

Figure 5.1: Schematic diagram of the proposed natural gas fuelled water heater system.

The working fluid in the ORC and HP cycles are Hexane and R134a respectively, in order to investigate the maximum theoretical limit of best system performance. Temperature - entropy (T-s) diagrams of the HP and ORC cycles are shown in Figure (5.2 a and b). The green line represents water, pink refers to R134a, blue stands for Hexane, red for flue gases, and a brighter blue for the mixture of fresh air and flue gases. As Hexane is a dry working fluid, only minimal superheat is required.

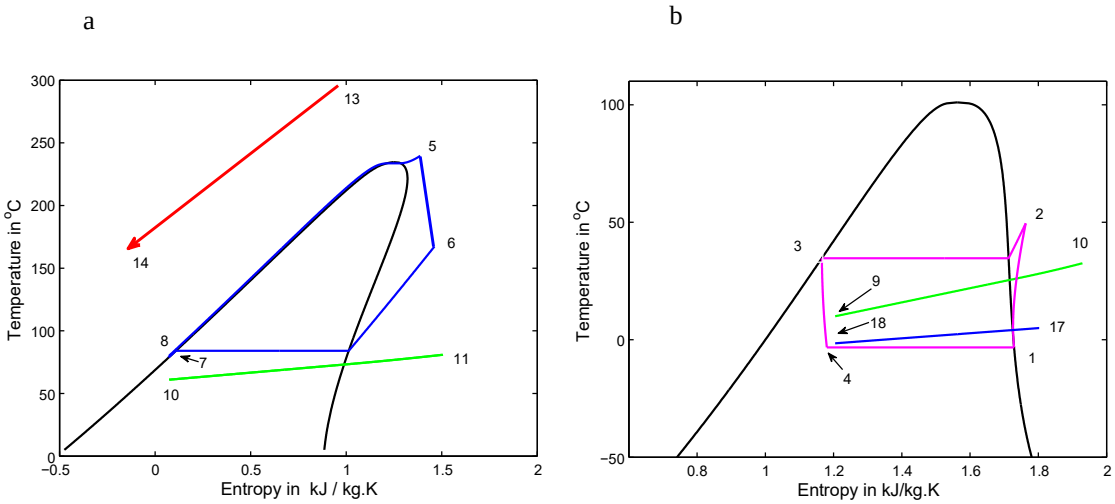

Figure 5.2: Temperature-Entropy diagrams of both the ORC (Hexane) and heat pump cycle (R134a)

5.3.1 Modelling HP cycle for steady state

As was mentioned in chapter three, modelling the HP cycle involves identifying the evaporation and condensation temperatures and their corresponding pressures. These temperatures can be identified by maintaining the minimum pinch point temperature difference between the hot and cold streams across the evaporator inlet and the condenser exit [97].

In this modelling stage, the temperature of the mixture of air and exhaust gases leaving the evaporator is set randomly to 3.5 ^{o}C (without considering the evaporator frost condition) and by maintaining the minimum pinch point, the temperature difference at the evaporator exit, the evaporating temperature (T_1), and its related pressure can be directly estimated, and are equal

to 0.5 ^{o}C and 2.981 bar, respectively. Furthermore, other thermophysical properties such as enthalpy and entropy can be calculated at state 1.

The same assumption is used with the water temperature upon leaving the condenser to recognise the condensation temperature (T_3). The water temperature upon leaving the condenser is set to 35 ^{o}C, and because the refrigerant temperature should be higher than the sink temperature, a condensation temperature of around 38 ^{o}C is adopted. The corresponding condensation pressure is obtained from REFPROP, and is equal to 9.63 bar. Enthalpy and entropy at state 3 can be estimated. Furthermore, the isentropic efficiency of the compressor is set to 70%.

5.3.2 Modelling ORC cycle for steady state

In the ORC cycle, the evaporator pressure and temperature (state 5) are set near the critical values for Hexane, as the ORC can achieve higher thermal efficiency when it operates near to critical pressure. Although Hexane is dry refrigerant, only 5 ^{o}C of superheat degree is required to ensure no wet refrigerant enters the turbine as shown in T-s diagram (Figure 5.2 a). Therefore, the evaporation pressure and temperature are 30 bars and 234 ^{o}C respectively. The condensation temperature (state 7) is assumed to be around 60 ^{o}C, which is a trade-off value between the water temperature upon exiting the HP condenser and the final desired water temperature. Isentropic efficiencies of 70% and 90% for turbine and liquid pump are respectively assumed. The Hexane mass flow can be directly calculated by assuming that the power produced by the ORC turbine is fully transferred to the HP compressor. Under these working conditions, other ORC cycle design and performance parameters are calculated using Equations 3.8-3.12.

5.3.3 Steady state results of combined ORC-HP system for the preliminary design

The steady state results of the ORC-HP cycles obtained from MATLAB code and ASPEN PLUS software are summarized in Tables (5.1 to 5.5). These results represent the working fluids states at specific points in the combined cycle as demonstrated in Figure 5.1.

Table 5.1 HP and ORC refrigerants thermophysical properties from MATLAB and ASPEN PLUS.

State point	Temperature ^{o}C		Pressure bar		Enthalpy kJ/kg		Entropy kJ/kg. K		Vapour quality	
	MATLAB code	ASPEN	MATLAB code	ASPEN	MATLAB code	ASPEN	MATLAB code	ASPEN	MATLAB code	ASPEN
1	0.5	0.5	2.9814	2.981	398.8950	-8807.01	1.7268	-2.4428	1	1
2	58.7	58.71	9.6315	9.632	440.8311	-8765.066	1.7811	-2.3885	1	1
3	38	38	9.6315	9.632	253.4333	-8952.468	1.1811	-2.9885	0	0
4	0.5	0.5	2.9814	2.981	253.4333	-8952.468	1.1952	-2.9744	0.2662	0.2661
5	234	234	30	30	571.6124	-1630	1.3028	-5.9454	1	1
6	140.97	142.68	0.7901	0.79	483.3801	-1714.5	1.3961	-5.8432	1	1
7	61	61	0.7901	0.79	-18.7902	-2220.39	-0.0555	-7.3037	0	0
8	64.95	62.232	30	30	-13.5754	-2215.16	-0.0539	-7.3021	0	0

Table 5.2 HP and ORC cycles design parameters from MATLAB and ASPEN PLUS.

Parameters	HP cycle		ORC cycle	
	MATLAB code	ASPEN	MATLAB code	ASPEN
Condenser heat duty, kW	9.125	8.937	11.655	11.973
Evaporator heat duty, kW	7.083	6.937	13.5842	13.85
Power produced by the ORC expander, and consumed by HP compressor, kW	2	2	-2	-2
Refrigerant mass flow, kg/s	0.0487	0.04768	0.0216	0.02366
ORC liquid pump power, kW	--	--	0.1207	0.124

Table 5.3 HP and ORC cycles efficiencies.

Parameters	Values	
	MATLAB code	ASPEN
HP heating coefficient of performance COPh, %	4.4687	4.46
ORC thermal efficiency, %	14.2	13.54

5.3.4 Modelling the gas burner and post heater for steady state mode

Methane mass flow can be directly calculated from the conservation energy equation for the stoichiometric combustion of Methane (Eq. 3.21), by assuming that the required heat production from the burner is the same as the heating capacity of the ORC evaporator and a constant exhaust temperature value (120 ^{o}C) (state 14). To identify the optimum air to fuel ratio that ensures maximal thermal energy production in the burner, the air mass flow is increased gradually under a constant Methane mass flow (2.8253e-04 kg/s) until lean combustion is secured; i.e. the full combustion of Methane with excess air at the burner exhaust. In these working conditions, the mass fraction of Oxygen and Methane at the burner exhaust are estimated, and the results are shown in Figure 5.3. As air mass flow increases gradually, the Methane mass fraction starts to decrease with no Oxygen fraction showing in the exhaust. When the air mass flow reaches 0.00544 kg/s, Oxygen starts to appear in the flue gases but with some residual Methane mass, indicating incomplete combustion. A further increase in air mass flow results in a continuous decline in the Methane mass fraction, reaching zero at an air mass of 0.00555 kg/s which reflects the complete burning of the fuel.

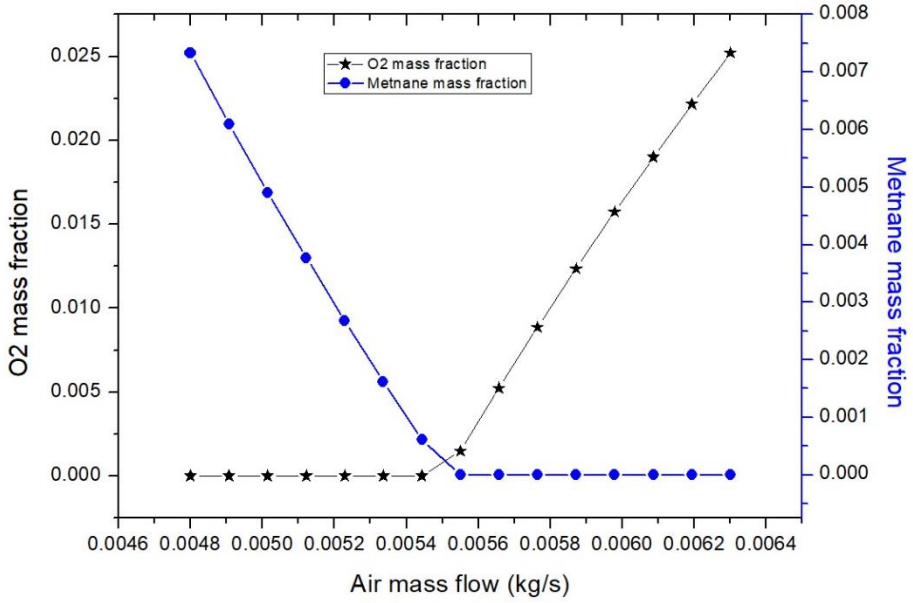

Figure 5.3 CH_4 and O_2 mass fraction in the burner exhaust under variable air mass flow entering the burner.

At this point, the thermal energy produced by the burner reaches its maximum value of around 13.8 kW, and the air to fuel ratio is approximately 19, as shown in Figure 5.4. As the obtained air to fuel ratio is higher than the stoichiometric ratio for Methane (17.5), this indicates that the combustion is lean, and the percentage of excess air is 7.89%.

For the post heater modelling, the flue gases temperature at the outlet (state 15) is higher than the acid dew-point in order to keep the exhaust stream in a vapour state and avoid corrosion from condensation. Other relevant design parameters for the combined system are summarized in Tables 5.4 and 5.5. In Table 5.4, temperature and pressure of water running across the combined cycle are presented by state 9-12. State 13 correspond to the fuel state entering the gas burner. While state 14-18 are the temperature and pressure values for ambient air and combustion product passing through the post heat, mixer and HP evaporator as shown in Figure 5.1. Table 5.5 shows the combined cycle efficiency parameters and performance. It is clear that the results obtained from MATLAB and ASPEN PLUS are in high agreement. The small different noted in the fuel to heat efficiency obtained by MATLAB and ASPEN PLUS is due to the different in Methane mass flow rate.

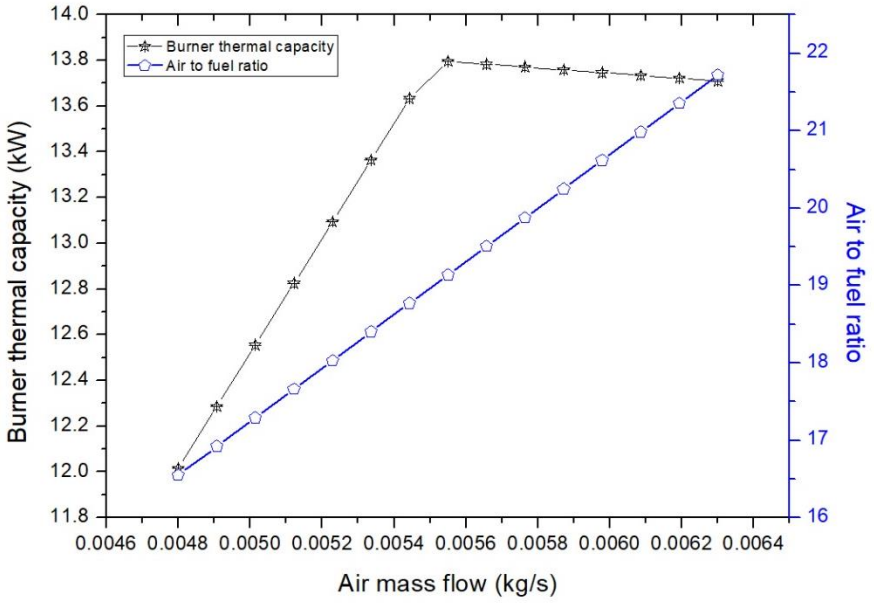

Figure 5.4: Increasing air mass flow against burner thermal capacity and air to fuel ratio.

Table 5.4 Thermophysical properties of other working fluids in the combined cycle by MATLAB and ASPEN.

State point	Temperature °C		Pressure bar	
	MATLAB code	ASPEN PLUS	MATLAB code	ASPEN PLUS
9	10	10	1	1
10	35	34.55	1	1
11	66.93	67.45	1	1
12	67.8	68.35	1	1
13	25	25	1	1
14	120	120	1	1
15	70	70	1	1
16	8	8	1	1
17	8.1	8.276	1	1
18	3.5	3.5	1	1

Table 5.5 Combined cycle efficiency parameters and performance.

Parameters	Values	
	MATLAB code	ASPEN
Total heating capacity, kW	21.099	21.236
Fuel to heat efficiency, %	134.55	131.46
Post heater thermal capacity, kW	0.319	0.326
Methane mass flow rate, kg/s	2.8253e-04	2.9105e-04

5.4 Effects of evaporation temperature of HP and ORC cycles on combined system performance

In the heat pump cycle, the evaporator plays an important role as it is responsible for both free heat extraction from ambient air and heat recovery from flue gases. In the ORC cycle, the cycle efficiency is highly dependent on the evaporation temperature and its corresponding pressure. Therefore, these two evaporators will be comprehensively investigated, including their thermo-physical properties under different working conditions. The heat recovery by the post heater as a final heating stage is also evaluated.

The evaporation temperature (T_1) is varied from -10 to 20 ^{o}C at a constant condensation temperature (T_3). In the ORC cycle, the evaporation pressure (P_5) is iterated between 10-30 bar at a constant condensation temperature.

The combined effects of these variables on the system performance and thermal capacity are shown below.

Figure 5.5 shows that increasing the evaporation temperature will reduce the temperature lift across the HP cycle, which will favourably reduce the work of the compressor, hence increasing the HP heating coefficient of performance (COP_h).

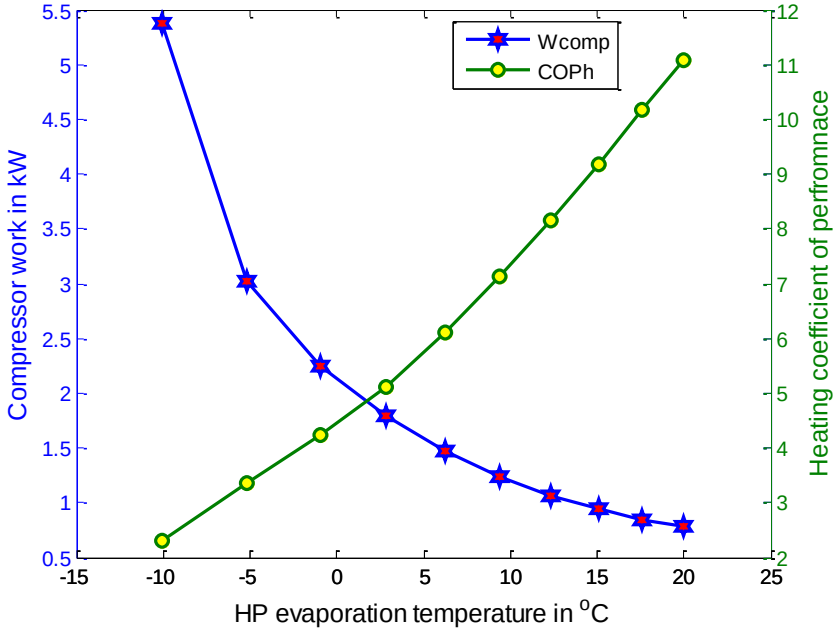

Figure 5.5: Effect of changing HP evaporation temperature on compressor work and COP_h.

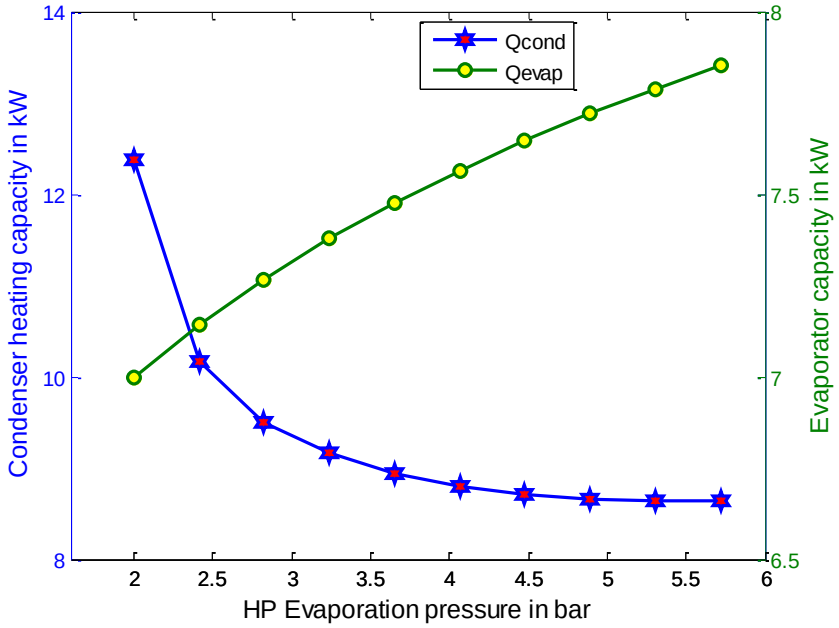

Figure 5.6: Effect of changing HP evaporation pressure on HP heating capacities.

However, for the same working conditions, increasing the evaporation temperature and its corresponding pressure results in a steep drop in condenser thermal capacity between 2-3 bar, then a steady decline. Regarding evaporator capacity, a nearly steady increase is evident along all pressure increments, as shown in Figure 5.6. This happens because increasing the evaporation temperature will increase the enthalpy of the refrigerant at the evaporator inlet (h_4), which will in turn increase the evaporator capacity and reduce the compressor work. According to the first law of thermodynamics, the summation of these two quantities represents the condenser heating capacity, which closely follows the compressor behaviour.

Figure 5.7 shows the changes in the mass flow of the ORC working fluid against the variation in the evaporation pressure and temperature for both combined cycles under the assumption of equality in power between the HP compressor and the ORC turbine. Increasing HP evaporation temperature causes a gradual decline in ORC mass flow for all ORC evaporation pressure. The changes in the Hexane mass flow are relatively small with the increase in the ORC evaporator pressure for each HP evaporator temperature. This reduction in ORC mass flow is a response to the equivalent reduction in the power produced and consumed by the ORC turbine and the HP compressor respectively, as shown in Figure (5.5).

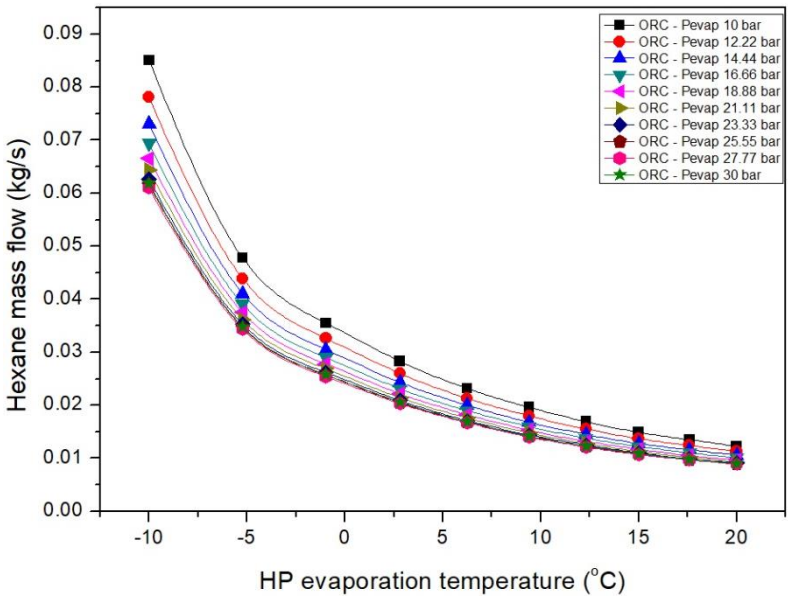

Figure 5.7: Varying the Hexane mass flow as a function of varying the HP evaporation temperature and the ORC evaporation pressure.

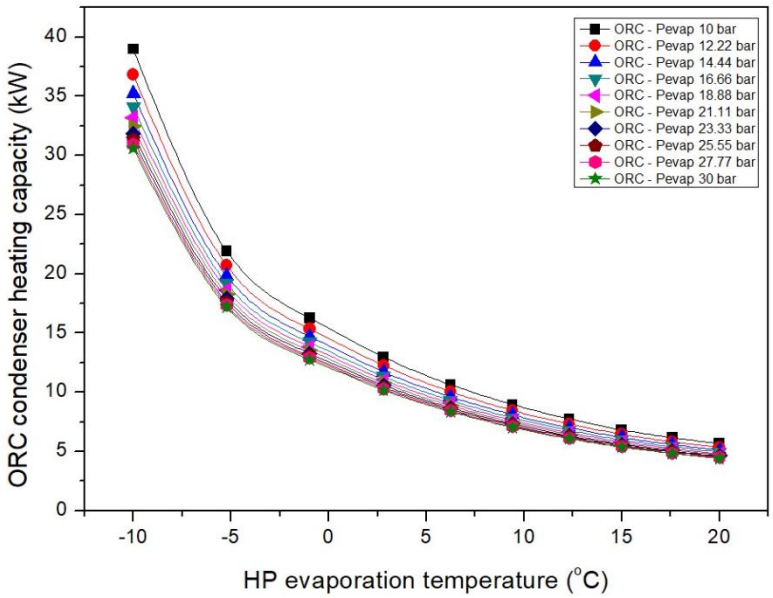

Figure 5.8: Effect of changing the HP evaporation temperature and the ORC pressure on the ORC condenser's thermal capacity.

Figure 5.8 shows the variations in the ORC condenser's capacity due to changes in the HP evaporation temperature and the ORC evaporation pressure. It shows that the condenser capacity trend is similar to the ORC mass flow, as shown in Figure 5.7. It also shows that the HP evaporation temperature has a greater effect compared with that of the ORC cycle. For instance, for the HP evaporation temperature selected, the ORC-condenser capacity declines from approximately 30-5 kW, whereas for the adopted ORC evaporation pressure range, the changes in the ORC condenser capacity are limited to between around 40-30 kW at a lower HP evaporation temperature and between 8-5 kW at a higher HP evaporation temperature. The decline in the ORC condenser capacity due to an increase in the evaporation pressure is similar to the results obtained from an experimental study by Zhou, N., et al. [47]. More results from this study show that increasing the ORC evaporator pressure will result in higher thermal efficiency. This study outcome verified the results obtained in this model.

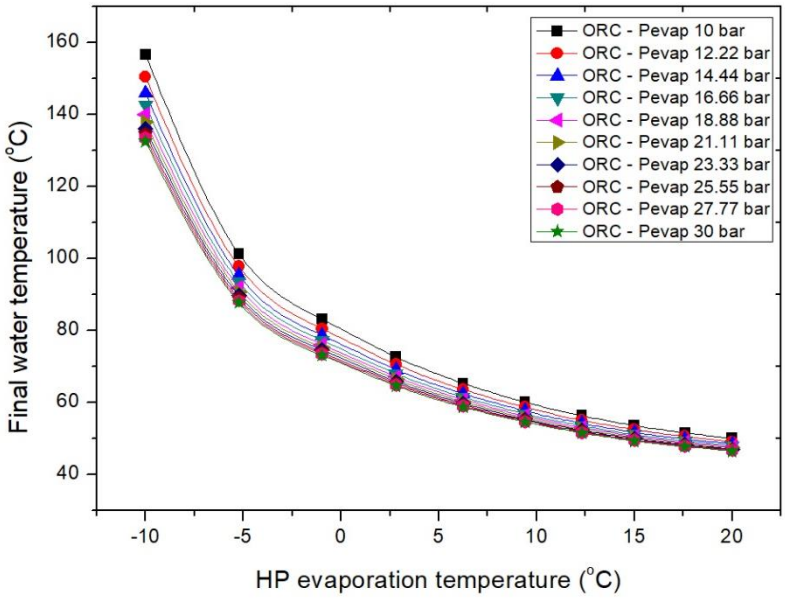

Figure 5.9: Effect of changing the HP evaporation temperature and the ORC pressure on final water temperature.

Figure 5.9 demonstrates the changes in the temperature of water at final heating stage with changing the HP evaporation temperature and the ORC evaporation pressure. It is clear that water temperature declined significantly with the increase in the HP evaporation temperature but slightly with the reduction in the ORC evaporation pressure. This can be explained by the behaviour of ORC condenser heating capacity (see Figure 5.8) which is influenced by the variations in the ORC mass flow (Figure 5.7).

Figure 5.10 shows that increasing the ORC evaporation pressure from 10 to 30 bar results in enhanced ORC thermal efficiency from 12 to 14.4%.

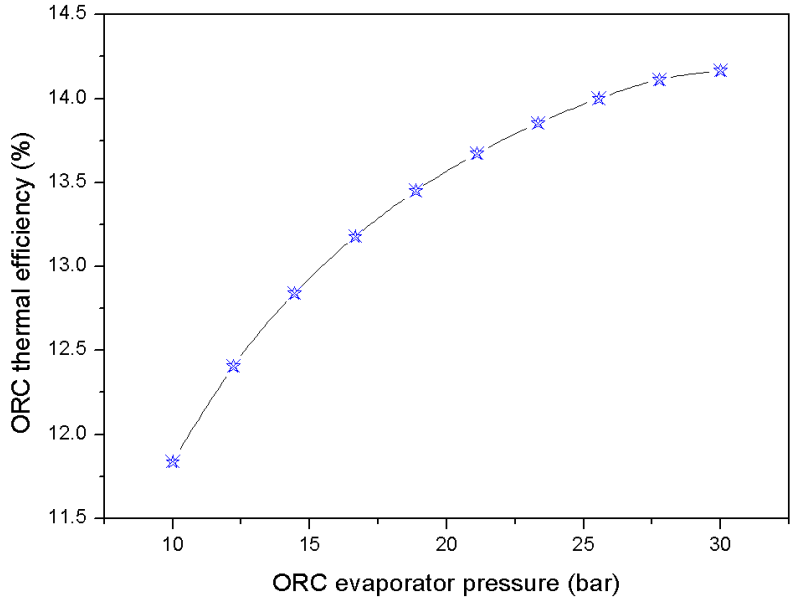

Figure 5.10: ORC thermal efficiency as a function of ORC evaporation pressure.

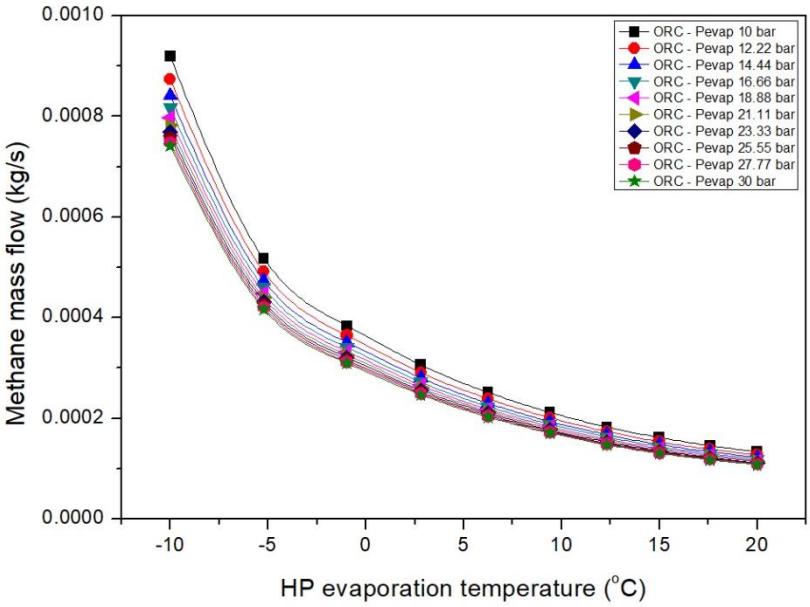

Figure 5.11: Variation in natural gas needed due to changes in evaporation temperatures and pressure of HP and ORC cycles.

As shown in Figure 5.11, the mass flow of natural gas drops as the HP evaporation temperature increases towards 20 ºC for various ORC evaporation pressures. It is clear that when the HP evaporation temperature decreases as a result of a reduction in the heat source temperature, less thermal energy will be available for extraction. Thus, more natural gas is needed to compensate for this reduction. For a given evaporation temperature, the mass flow of the natural gas initially decreases in increments in line with ORC evaporation pressure, reaching a minimal value when pressure is 30 bar.

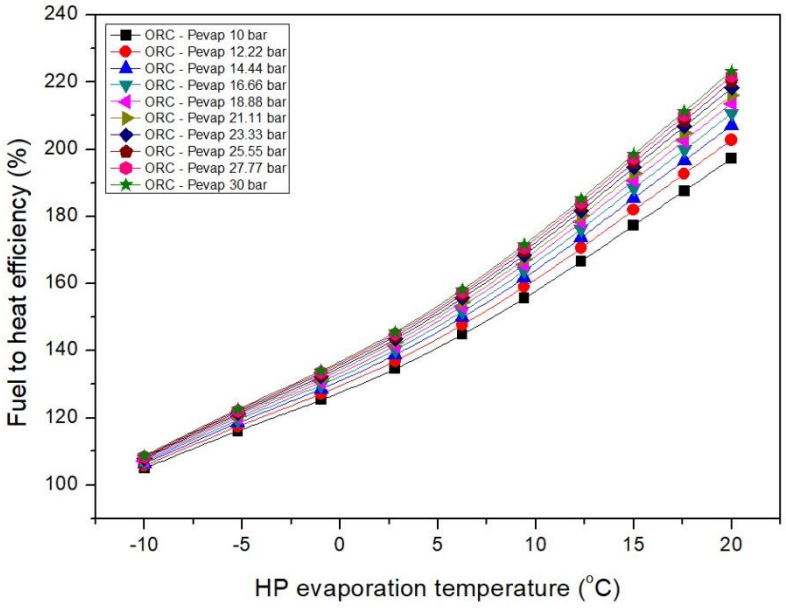

Figure 5.12: Fuel to heat efficiency as a function of varying HP and ORC evaporation temperature and pressure.

Figure 5.12 illustrates that an increasing HP evaporation temperature will significantly increase the fuel to heat efficiency of the combined cycle compared with slight increments in efficiency when the ORC evaporation pressure increases. Also, it shows that the increments in efficiency due to an increase in the ORC evaporation pressure are higher at high HP evaporation temperatures compared with those at low temperatures.

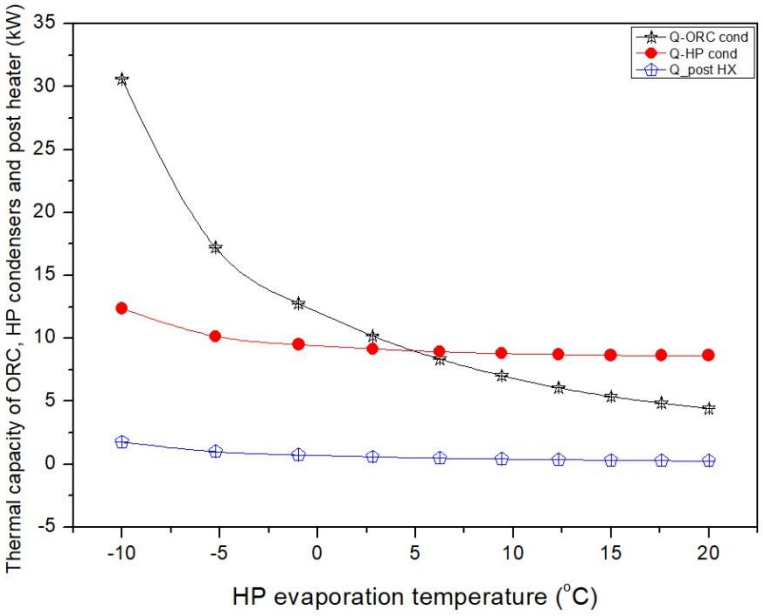

Figure 5.13: Heat capacities of the three heat exchangers.

Figure 5.13 shows a comparison between the thermal capacity of the ORC condenser, the HP condenser, and the post heater under variable HP evaporation temperatures. The capacities of the ORC condenser and the post heater are adopted at an optimum ORC evaporation pressure (30 bar). As the HP evaporation temperature (T_1) increases, the heat capacity of those heat exchangers declines. For the HP condenser, increasing HP evaporation pressure results in reductions in both compressor work and condenser capacity, as explained in Figures 5.7 and 5.8. Due to the decline in the compressor work, the mass flow of the Hexane reduces, which will also significantly reduce the thermal capacity of the ORC condenser. The slight reduction in the post heater capacity is due to the reduction in the CH_4 mass flow shown in Figure 5.11.

Figure 5.14 shows the heat share of the three heat exchangers responsible for water heating under various operating conditions. It is clear that the main contributors in water heating are both ORC and HP condensers, whereas the post heater has a marginal impact on the system's total heating capacity. The variation in HP evaporation temperature for a given ORC evaporation pressure has a significant impact on the heat shared by these heat exchangers. For instance, when T_{HP_evp} increases to the maximum, under minimum ORC evaporation pressure, the heating capacities of ORC condenser and post heater decline with an opposite trend in the HP condenser capacity, as shown in Figures 5.14 a and b.

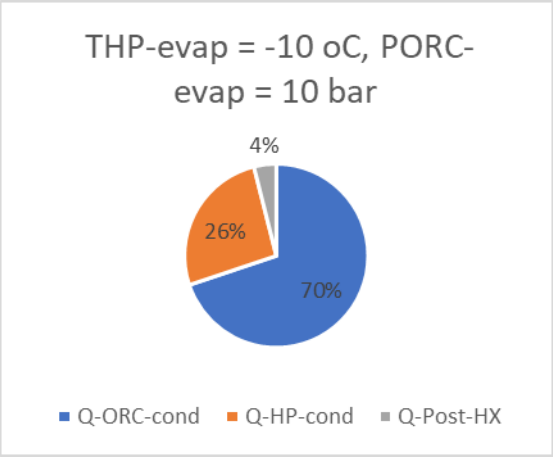

Figure 5.14, a

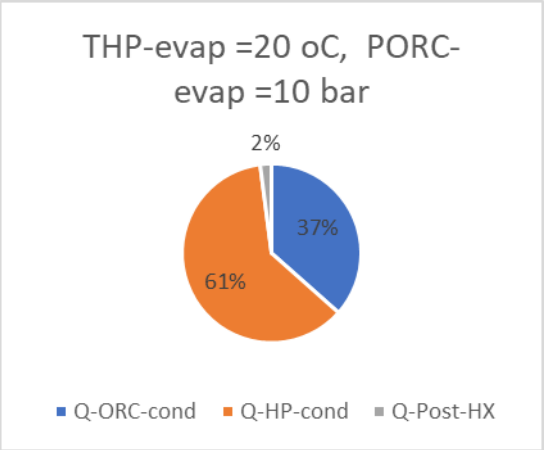

Figure 5.14, b

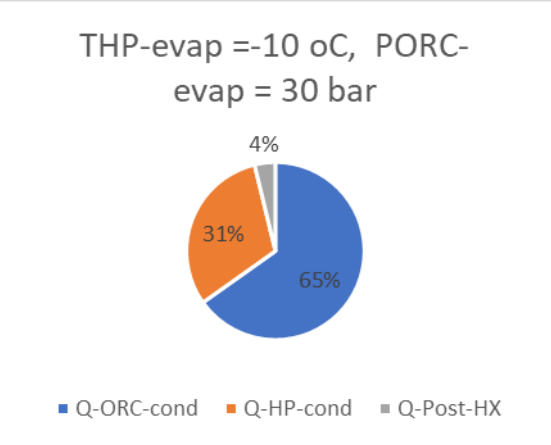

Figure 5.14, c

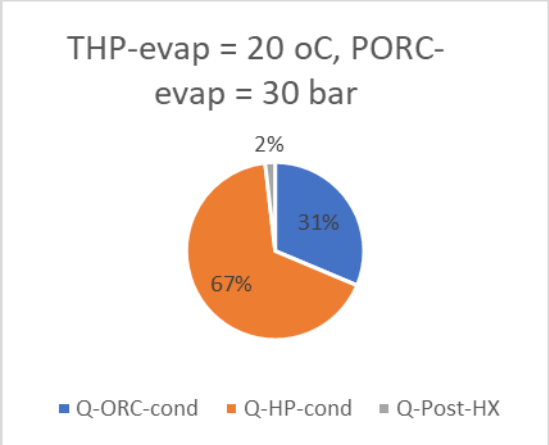

Figure 5.14, d

Figure 5.14 Share of heat supply by the three heat exchangers under different operational conditions.

The reduction in the ORC condenser heating duty is significant. Therefore, the heating capacity of the HP condenser becomes the main contributor to the system's total heating capacity. Similarly, at an ORC evaporation pressure of 30 bar as shown in Figures 5.14 c and d, increasing HP evaporation temperature results in a greater reduction in the ORC and post heater heat share with a corresponding increase in the HP condenser capacity from 11.7 to 9 kW.

At a constant HP evaporation temperature, Figures 5.14 a and c, or b and d, increasing ORC evaporation pressure causes a small decline in the ORC heating capacity, with minimal rise on the HP condenser duty. Thus, the heat share of the ORC cycle declines, with a corresponding increase in the HP condenser contribution while the post heater heat share remains constant.

Figures 5.13 and 5.14 clearly show that the impact of the HP evaporator temperature and hence the pressure on the heat contribution of the three HXs is greater than the effect of changing the ORC evaporation pressure and temperature. In addition, the overall contribution to the total heating capacity by the post heater is small in all working conditions. Thus, it can be removed from the proposed system in order to simplify the design while also having the potential of cost saving.

5.5 Comparison between two layout designs

To identify the best design for hot water supply, two proposed layouts were simulated. In the first approach, water is assumed to enter the heat pump cycle first, and further heating occurs in the ORC cycle to uplift the water temperature to the desired target. In the second approach, the reverse approach is adopted. Therefore, the term $Q_{post\ heater}$ will be removed from Equation 3.23. For both approaches, water is assumed to be heated from 10-65 ^{o}C by absorbing approximately 20 kW of thermal energy from the combined cycle. The required water mass flow is calculated to be 0.087kg/s. The selected refrigerants are R134a and R245fa for the HP and ORC cycles respectively. The selection of R245fa is based on its safety profile, wide use, and environmentally friendly behaviour. A prior study suggested that air temperature exiting the HP evaporator preferred to be maintained above 5.5 ^{o}C, especially in a cold humid atmosphere, to avoid frost formation on the evaporator surface [173]. Thus, the current simulation is conducted under a constant HP evaporation temperature of 2.5 ^{o}C, which can secure a minimum pinch point temperature difference of 3 ^{o}C and maintain an evaporator outlet temperature of around 5.5 ^{o}C. The corresponding evaporation pressure obtained from REFPROP is 3.2 bar. The ORC-evaporator pressure is set at 36.5 bar, which is near the critical pressure of R245fa, to maximise the thermal efficiency of the cycle. However, a superheat degree of 5 ^{o}C over the refrigerant critical temperature is added to the ORC-evaporation temperature to ensure that no wet flow enters the turbine.

5.5.1 First layout: Water heated by HP cycle first

In this design, cold tap water enters through the heat pump cycle where the first heating stage occurs, then passes through the ORC cycle to exit with the final temperature shown in Figure 5.15. To identify the design parameters for both the HP and ORC cycles, both cycle condensation temperatures and pressure are iterated under constant HP working fluid mass flow, and HP and ORC evaporation pressures and temperatures.

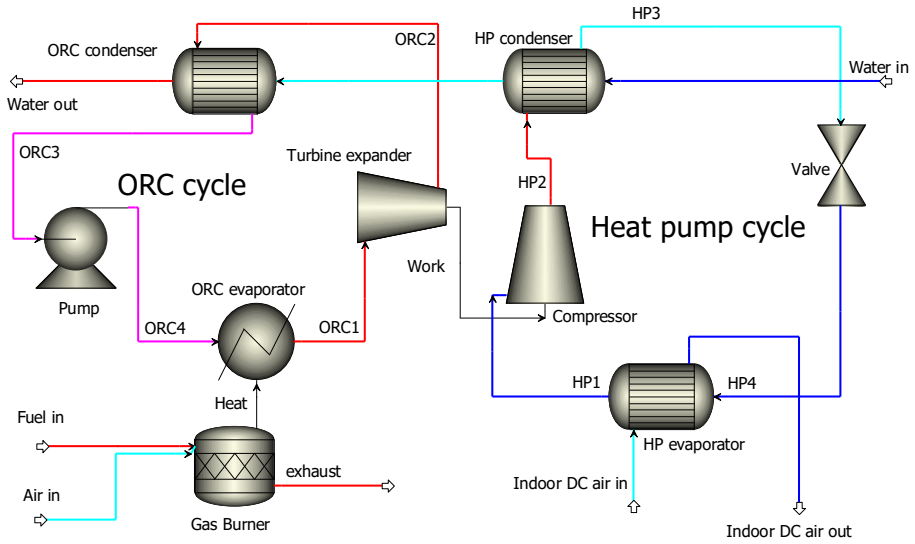

Figure 5.15: Combined cycle configuration for hot water supply.

Figure 5.16 shows the effects of increasing the condensation pressure on condenser heating duty and compressor work in the HP cycle. Increasing the condensation pressure causes an exponential decline and rise in condenser heating duty and compressor work respectively. Higher condensation pressure causes an increase in refrigerant enthalpy at compressor outlet (h_2) which consequently increases the (h_2-h_1) across the compressor. However, higher discharge pressure causes a slight decline in enthalpy difference across the condenser (h_2-h_3) as enthalpy at the exit increases more than the inlet enthalpy, as explained in Figure 5.17. This is because enthalpy at the condenser inlet (h_2) is situated in the supercritical region while the exit enthalpy (h_3) lies on a saturated liquid curve which is skewed to the right (dry working fluid).

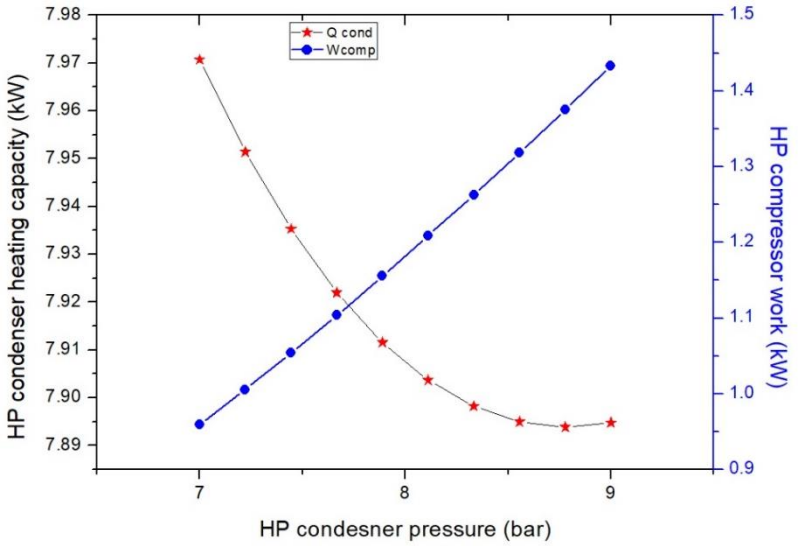

Figure 5.16 HP-condenser heating duty and condensation pressure.

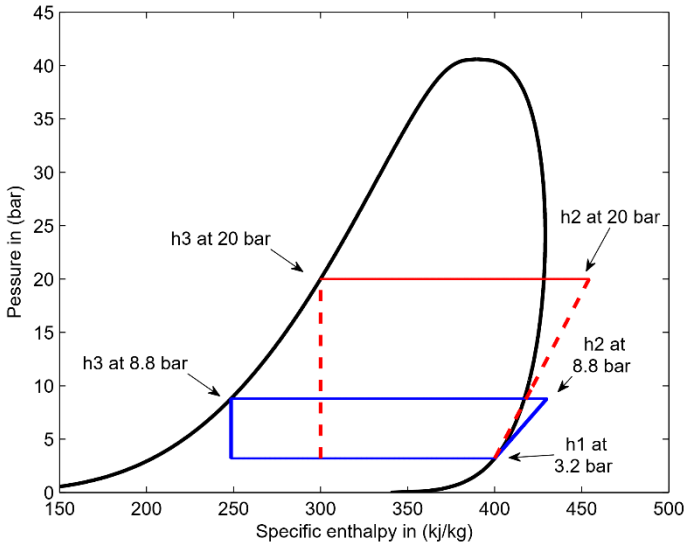

Figure 5.17: PH diagram for R134a HP cycle under variable condensation pressure.

Figure 5.18 shows that increased condensation pressure causes a significant decline in the COP_h, which reaches a low value of 5.5 at a pressure of 9 bar. This behaviour is expected, as the HP condenser heating duty declines with an opposite increase in compressor work as condensation pressure increases (Figure 5.16).

As HP-condenser heating duty declines with the rise in pressure, the amount of heat delivered to the water and thus its exit temperature is expected to decline, as shown in Figure 5.18. This figure shows that the water temperature is maintained at around 31.5 ^{o}C as the condensation pressure increases from 7 to 9 bar. Similar behaviour was shown in results obtained from Kang, S., et al. [50].

In order to identify the condensation pressure for the ORC cycle that secures the desired final outlet water temperature of 65 ^{o}C, this parameter was iterated under constant water mass flow and ORC-evaporation pressure. Also, from the results above, the water temperature entering the ORC condenser was assumed to be of that existing of the HP condenser.

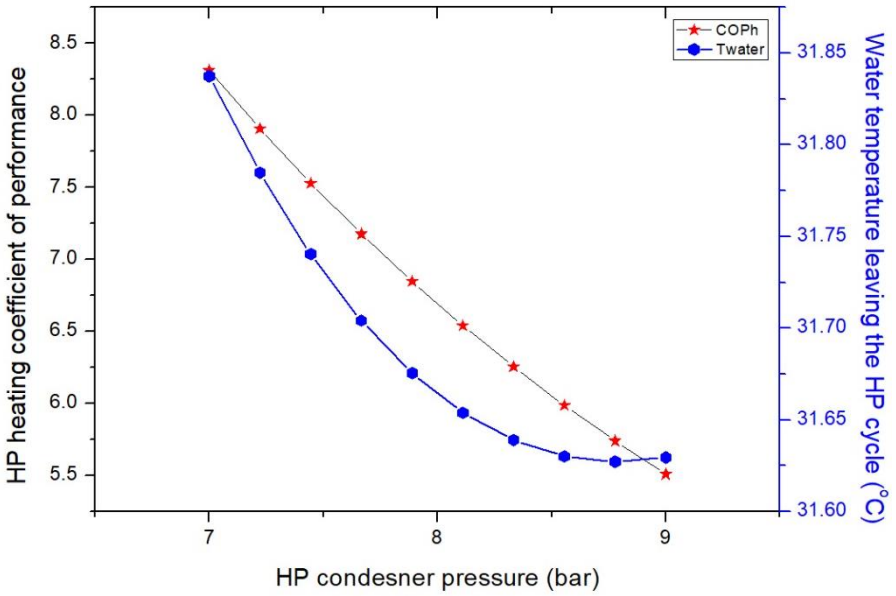

Figure 5.18 Effects of increasing HP condensation pressure on COP_h and water temperature leaving the cycle.

In addition, as mentioned in the assumptions section, the power produced by the ORC expander is directly used to drive the HP compressor. As a result, the effects of varying the HP condensation pressure will be transferred to the ORC cycle via the calculated ORC mass flow.

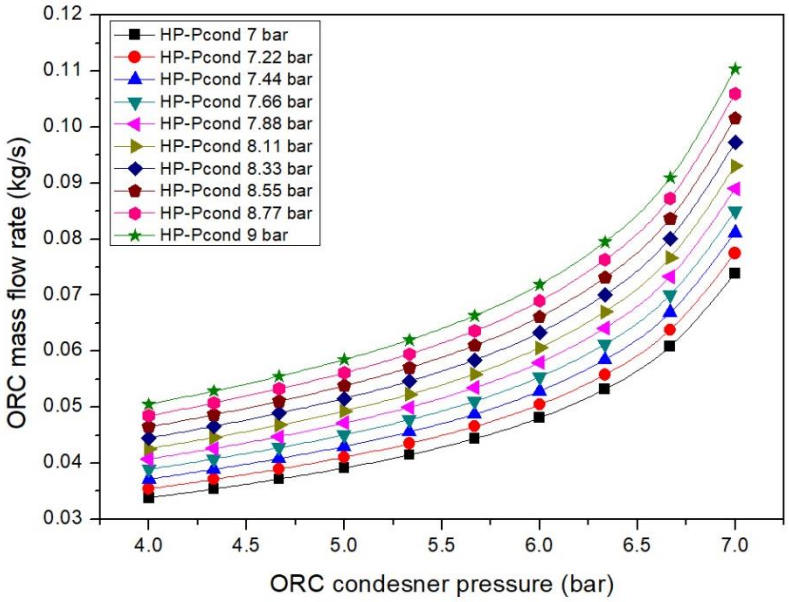

Figure 5.19: R245fa mass flow under variable ORC and HP condensation pressure.

Figure 5.19 shows the effects of increasing the HP and ORC condensation pressure on the R245fa mass flow. Increasing both pressure values causes a gradual rise in the ORC mass flow. As illustrated in Figure 5.16 above, with increasing HP condensation pressure, the compressor work increases, and the turbine power also increases which will lead to an increased ORC mass flow.

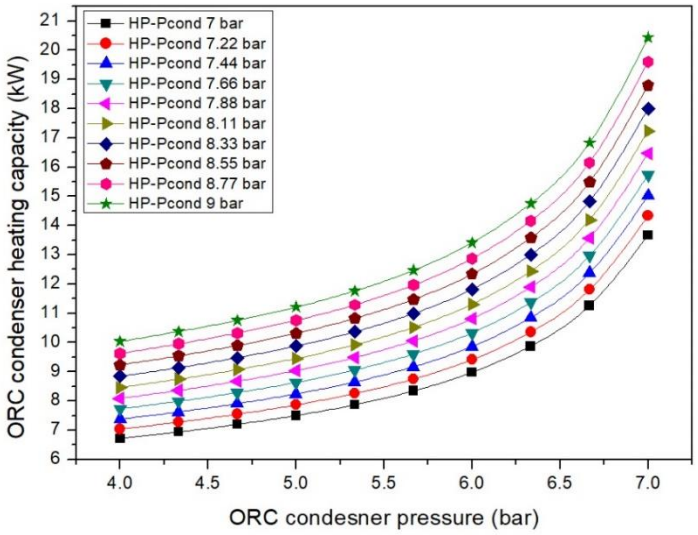

Figure 5.20: ORC-Condenser heating duty under variable ORC and HP condensation pressure.

The effects of condensation pressure of ORC and HP cycles on ORC heating capacity are shown in Figure 5.20, which illustrates that the ORC condenser capacity exponentially increases with increasing ORC condenser pressure between 4-7 bar. For each ORC condenser pressure level, increasing the HP condensation pressure increases the condenser capacity by approximately 3.5 kW at lower ORC condenser pressure levels. However, in the higher ORC condenser pressure range, the increase in the condenser capacity due to the rise in the HP discharged pressure doubles to around 7 kW.

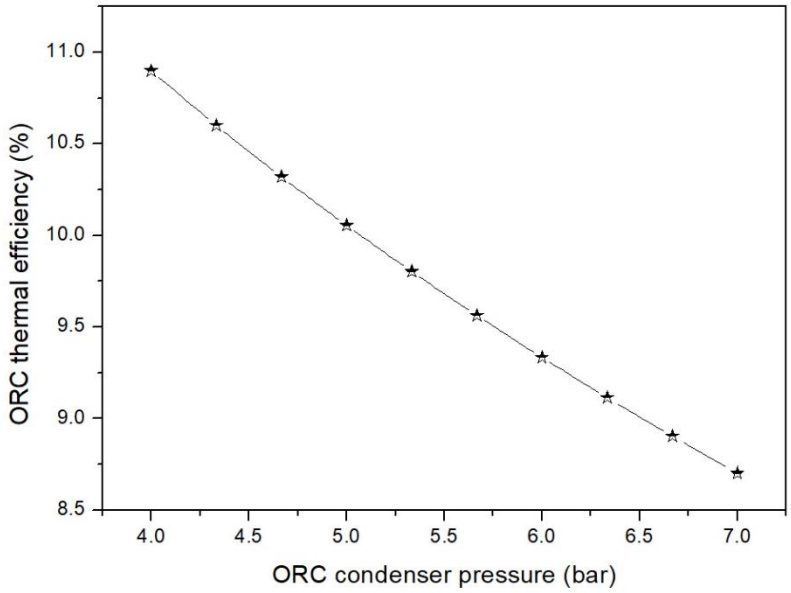

Figure 5.21: ORC-thermal efficiency under variable ORC-condensation pressure.

Figure 5.21 shows the variation in the overall ORC thermal efficiency under different ORC condensation pressures. It shows that the ORC thermal efficiency declines as the ORC condensation pressure increases at constant ORC evaporation pressure.

Figure 5.22 shows the final water temperature upon leaving the combined system under different ORC and HP condensation pressure levels. The optimization results show that increasing both condenser pressures will boost the final water temperature, particularly at higher pressure values in both condensers. The final water temperature is highly influenced by

the ORC condenser capacity (Figure 5.20) which is dependent on the R245fa mass flow rate (Figure 5.19).

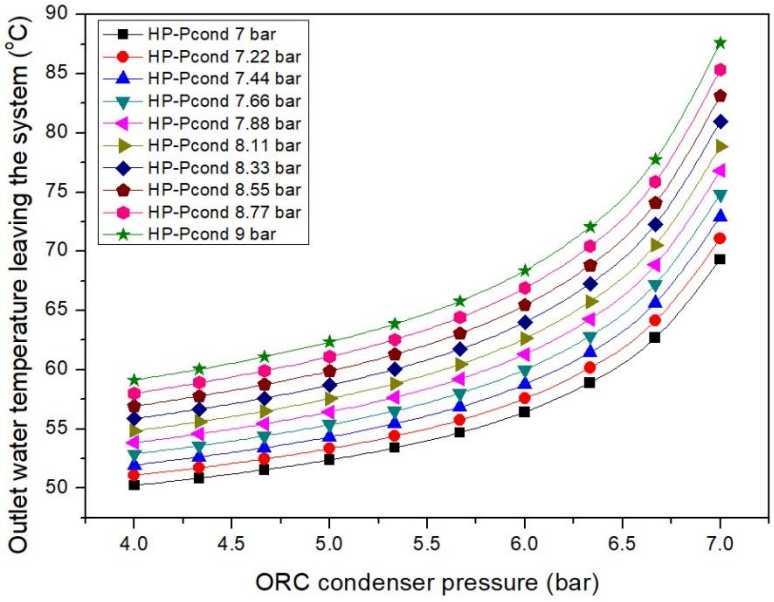

Figure 5.22: Water temperature at ORC exit under variable ORC and HP condensation pressures.

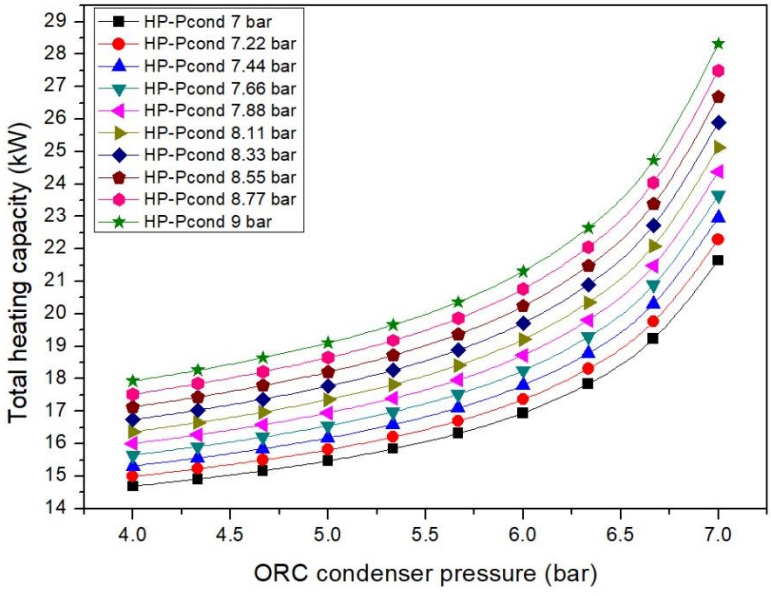

Figure 5.23: Combined cycle total heating capacity under variable ORC and HP condensation pressure.

The total heating capacity of the combined cycle is defined by the amount of thermal energy added to the water by both the ORC and HP condensers. As shown in Figure 5.23, the total heating capacity increases in a similar pattern to the ORC condenser capacity (Figure 5.20). The target total combined heat capacity of 20 kW is satisfied at HP condenser pressure of 9 bar and ORC condenser pressure of 5.5 bar.

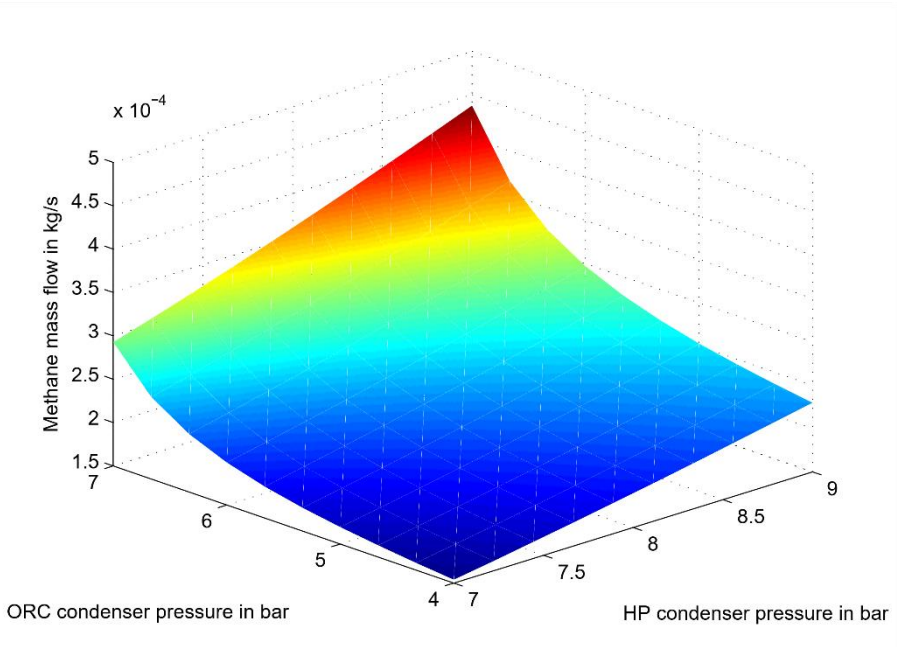

Figure 5.24: CH_4 mass flow under variable ORC and HP condensation pressure.

Figure 5.24 shows the effects of increased both condensers pressure on the Methane mass flow of the burner. From the previous results, it is clear that increasing both pressures causes an increase in R245fa mass flow and in the ORC condenser thermal duty. These lead to an increase in the fuel mass flow in the gas burner to generate the heat the ORC evaporator requires to evaporate the increment in the working fluid mass flow.

From Methane mass flow, the total heat released from the gas burner is calculated by assuming a constant Methane heating value of 55.5 kJ/kg. The overall fuel to heat efficiency is the percentage ratio of total heating capacity of the combined cycle to the total heat released by the burner. From Figure 5.25, the fuel to heat efficiency declines as ORC and HP condensation pressure increases. At the optimum condensation pressures of 9 and 5.5 bars for HP and ORC respectively, the combined cycle can achieve a total efficiency of around 136%.

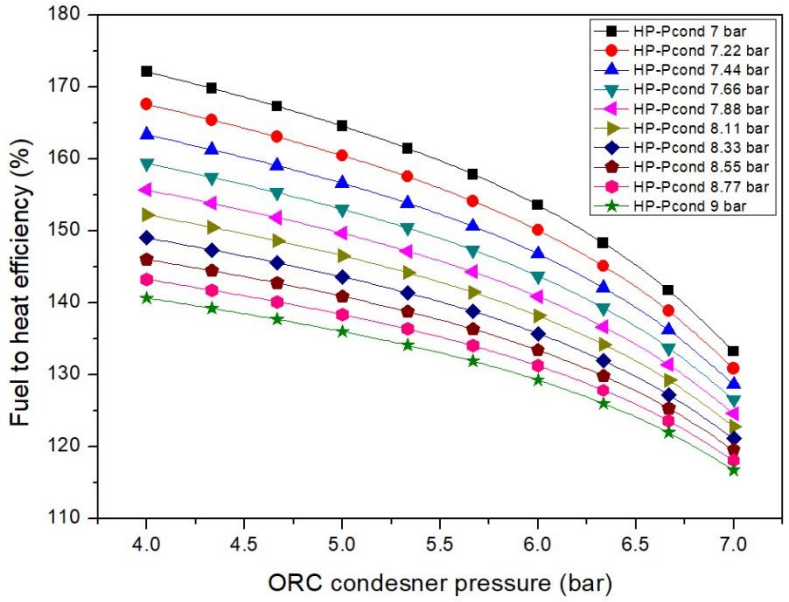

Figure 5.25: Fuel to heat efficiency under variable ORC and HP condensation pressures.

5.5.1.1 Pinch point temperature difference in the HP and ORC condensers

As mentioned previously in section 5.3.1, the water temperature upon exiting the HP condenser (at the first heating stage) was assumed to be 35 ^{o}C in order to identify the condensation temperature by maintaining the minimum pinch point $\Delta T_{min.p.p}$ between the two streams at the condenser exit. However, this temperature might not reflect the optimal value; in addition, this evaluation does not consider the pinch point assessment in depth. Therefore, another optimization process was carried out based on varying the water temperature at the HP condenser exit ($T_{w\text{-}exit\text{-}HP}$) but with the condition of maintaining the $\Delta T_{min.p.p}$ of 3 ^{o}C across the HP and ORC condensers. For each conditional loop, all the unknown parameters that satisfy that condition will be identified; namely, condenser pressure and temperature, refrigerant mass flow, and cycle efficiency. Knowing that, the same assumptions in section 5.5 were adopted in this evaluation.

Figure 5.26 shows the variations in the HP condensation temperature and pressure due to increasing the water temperature at the condenser exit. It can be noted that both parameters have been increased linearly with the rise in the $T_{w\text{-}exit\text{-}HP}$. These increments are essential to keep the refrigerant hot stream over the water cold flow throughout the condenser. It can also be seen that when the water temperature is 30 ^{o}C, only a condensation temperature of 30.7 ^{o}C satisfies the formula $\Delta T_{min.p.p}$ across the HP condenser. When the water temperature is 35 ^{o}C, a condensation temperature of 35.2 ^{o}C satisfies the minimum pinch point, which is lower than the value adopted in the first evaluation (38 ^{o}C).

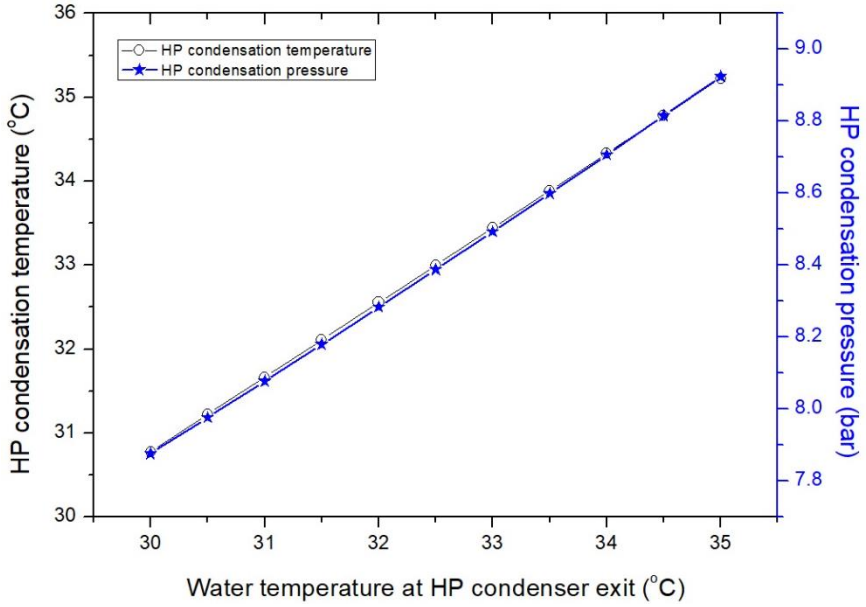

Figure 5.26: HP condensation temperature and pressure under variable $T_{w\text{-}exit\text{-}HP}$.

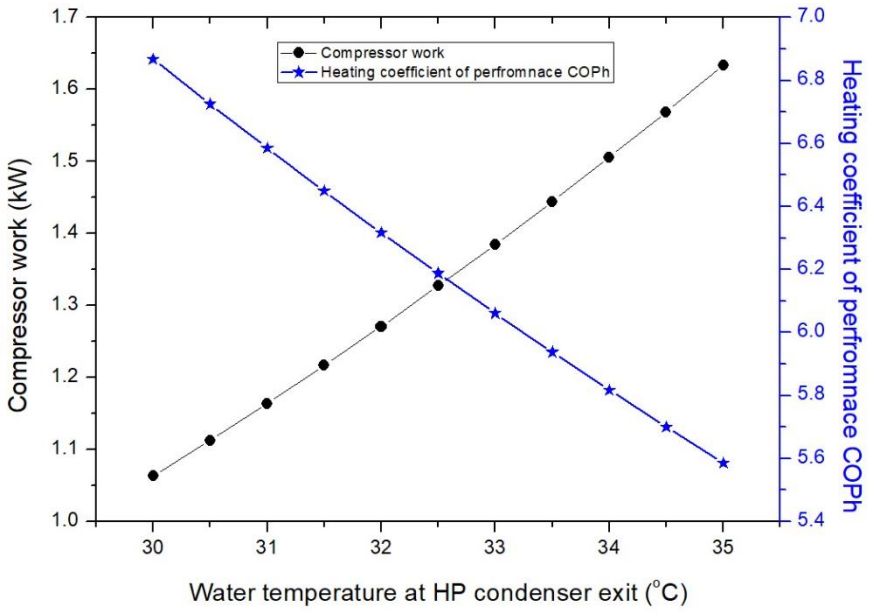

Figure 5.27: HP compressor work and COPh under variable $T_{w\text{-}exit\text{-}HP}$.

Figure 5.27 shows the variation in the HP compressor work and COP_h due to changes in the water temperature upon leaving the first heating stage. Increasing the water temperature causes a rise in the condensation pressure from 7.8 bar to 8.9 bar, as shown in Figure 5.26. This pressure increment range causes a steady increase in the compressor work, which consequently

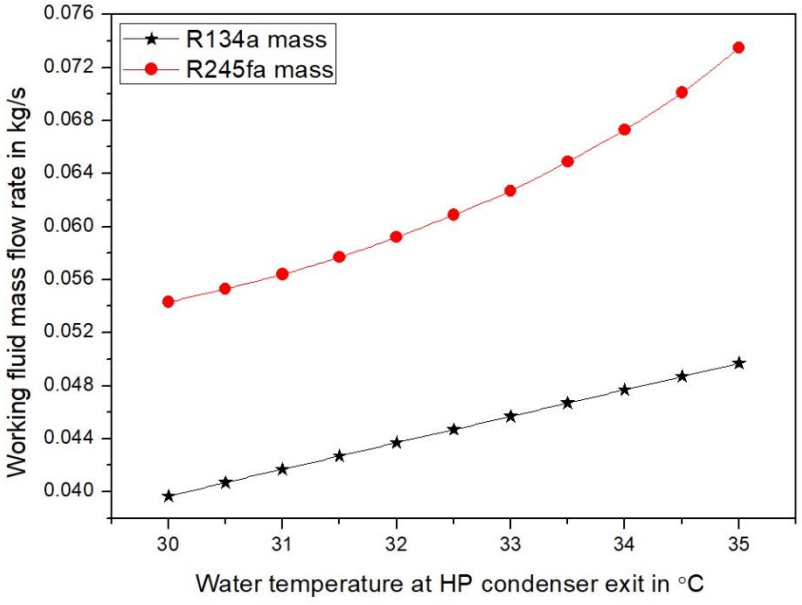

Figure 5.28: R134a and R245fa mass flow under variable $T_{w\text{-}exit\text{-}HP}$.

reduces the heating coefficient of performance of the HP cycle (COP_h). Similar results and explanations are provided above in Figures 5.16 and 5.18.

Figure 5.28 shows the variation in both cycles' working fluids mass flow due to changes in the water temperature. These results show that R134a mass flow increases linearly as result of increasing the $T_{w\text{-}exit\text{-}HP}$ and the increase in both enthalpy at the condenser inlet (h_2) and outlet (h_3), as shown in Equation 3.15. Meanwhile the R245fa mass increases exponentially as a result of optimizing the ORC condensation pressure to maintain the minimum pinch point across the ORC condenser. Also, due to the direct coupling between the HP compressor and the ORC expander, the optimized ORC mass flow will drive the expander to produce the same amount of mechanical work needed for the HP cycle.

The effects of varying the water temperature on the ORC condenser pressure and thermal efficiency are shown in Figure 5.29. It can be seen that with the increase in the water temperature upon entering the ORC condenser, a higher level of ORC condenser pressure is required to maintain the minimum pinch point temperature. The increase in the ORC condensation pressure under constant evaporation pressure will enhance the ORC thermal efficiency, as has been shown in previous results.

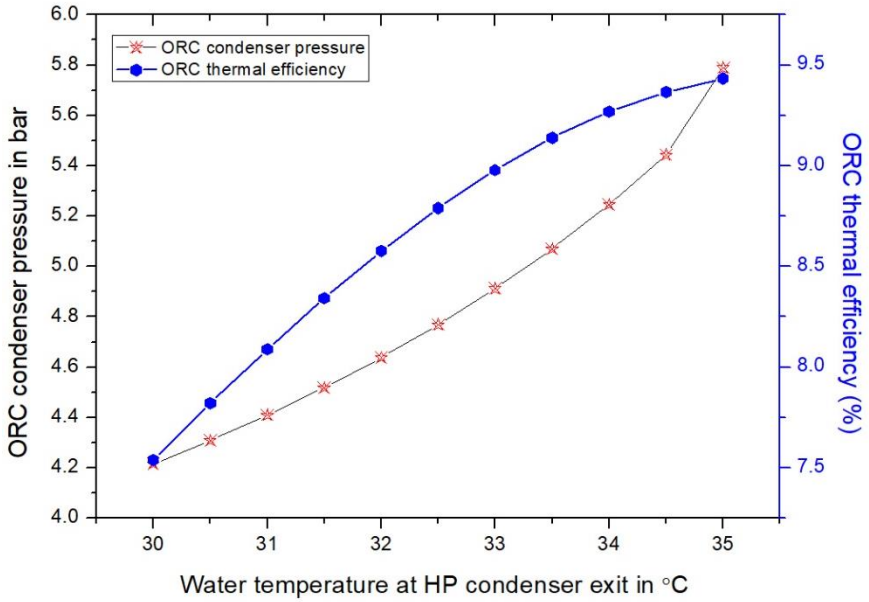

Figure 5.29: Effects of varying $T_{w\text{-}exit\text{-}HP}$ on the ORC condenser pressure and thermal efficiency.

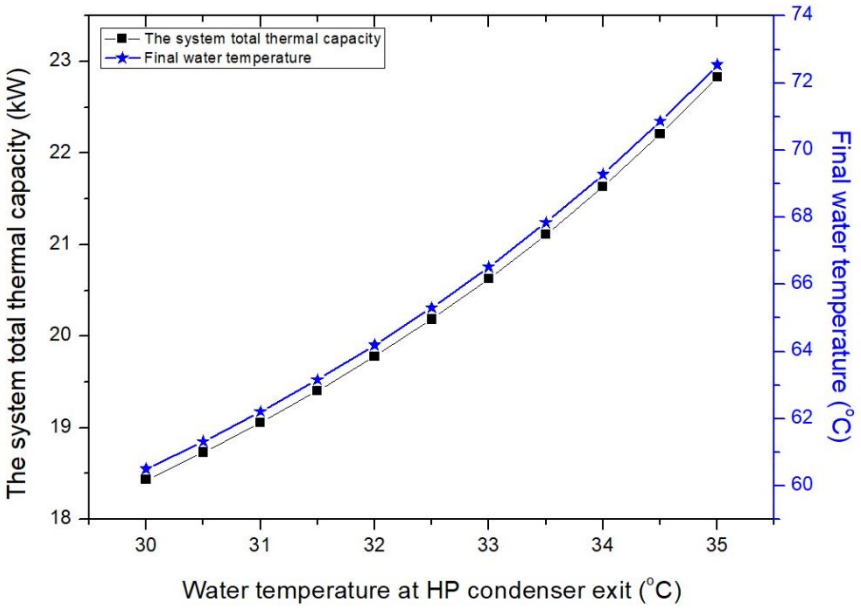

Figure 5.30: Total system thermal capacity and final water temperature under variable $T_{w\text{-}exit\text{-}HP}$.

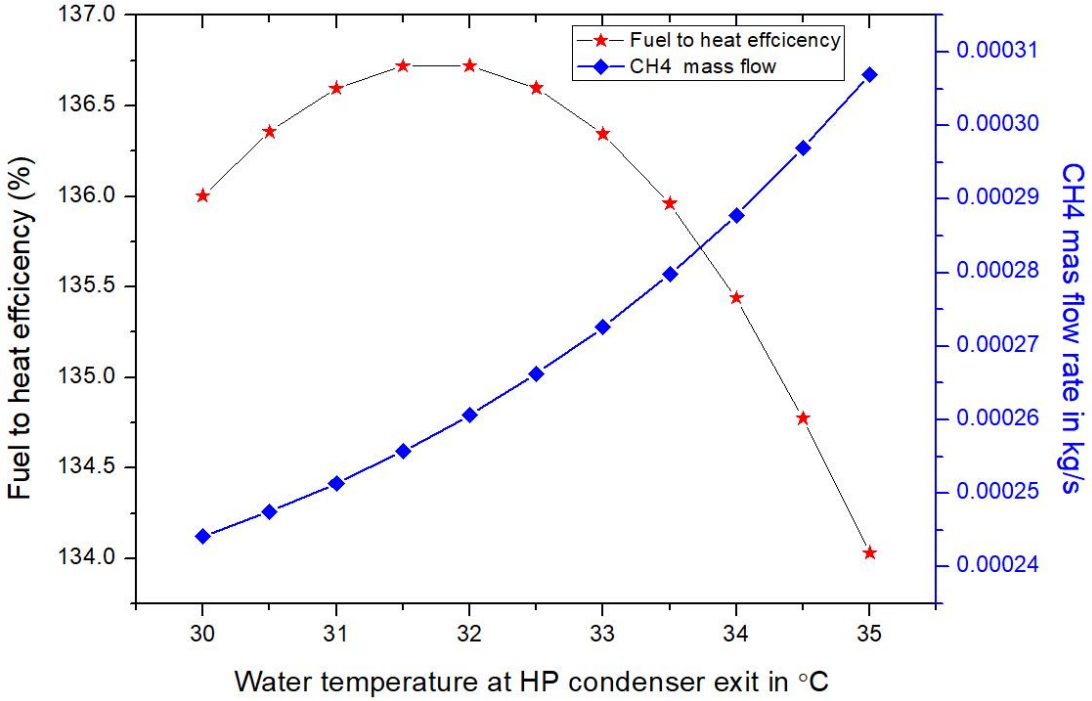

Figure 5.31: Fuel to heat efficiency and CH_4 mass flow under variable $T_{w\text{-}exit\text{-}HP}$.

The total heat added to water (i.e., the thermal system capacity) and hence the final water temperature at the ORC condenser exit are expected to increase as both condenser pressure and mass flow for both cycles increase with the rise in the $T_{w\text{-}exit\text{-}HP,}$ as shown in Figure 5.30.

Figure 5.31 shows the variations in the fuel to heat efficiency and Methane mass flow due to changes in the water temperature. The fuel to heat efficiency increases exponentially, reaching a maximum value when the water temperature is around 32 ^{o}C, then it declines afterwards. The fuel to heat efficiency is the ratio of the total thermal energy added to the water by the HP and ORC condensers to the total heat released from burning Methane. Thus, this ratio increases initially as the total energy added (Figure 5.30) is greater than the energy spent. In contrast, at water temperatures of more than 32 ^{o}C, the increment in Methane mass flow and hence energy production exceed the amount of added total thermal energy to water.

From the above results, it is clear that at a $T_{w\text{-}exit\text{-}HP}$ of around 32 ^{o}C, the combined system achieves optimal performance in terms of total heating capacity and final water temperature (20 kW and 65 ^{o}C respectively, as shown in Figure 5.30). In addition, at this temperature value, the fuel to heat efficiency reaches a remarkable value of around 136.5% (Figure 5.31).

5.5.1.2 Comparison between MATLAB and ASPEN PLUS models

The steady state results acquired from MATLAB code for the first approach after maintaining the minimum PPTD across the HP and ORC condensers were verified using ASPEN PLUS software (Appendix A). The results from these models are shown in Tables 5.6 to 5.8, below. These tables summarise the calculated temperatures, heat duties, and work transfer within the key components and the evaluation indicators of the proposed system. As can be seen, there is only a very small difference (<8.3%) between the predictions made by the two models regarding the calculated heat transfer at each of the heat changers. The maximum deviation between these two models is in relation to the ORC condensation pressure, at 8.3%. Such a difference can be attributed to the different control strategies and the different PPTD approaches used in calculating the heat transfer and controlling the energy balance in the system. These results therefore demonstrate good overall agreement in the simulation results between the MATLAB and ASPEN PLUS models, offering the confidence to use the present model to further analyse the performance and characteristics of the proposed system.

Table 5.6 Combined cycle parameters as per ASPEN PLUS and MATLAB code

	HP cycle			ORC cycle		
	MATLAB code	ASPEN	Difference	MATLAB code	ASPEN	Difference
Condenser heat duty, kW	8.2125	8.044	2.1%	11.9751	12.098	1.0%
Water temperature leaving the cycle, ^{o}C	32.5	32	1.6%	65.3084	65.35	0.1%
Evaporator heat duty, kW	6.8853	6.744	2.1%	13.1291	13.221	0.7%
Condensation temperature, ^{o}C	33	33	0	61	64.157	4.9%
Condensation pressure, bar	8.3878	8.388	0	4.7683	5.2	8.3%
Evaporation temperature, ^{o}C	2.5	2.5	0	159	159	0
Evaporation pressure, bar	3.2	3.203	0	36.5	36.5	0
Power produced by ORC expander, kW	-	-		-1.3272	-1.3	2.1%
Power input to the HP compressor, kW	1.3272	1.3	2.1%	-	-	
Work of the liquid pump, kW	-	-		0.1732	0.178	2.7%
Cycle mass flow rate, kg/s	0.0447	0.0438	2.1%	0.0609	0.0625	2.6%

Table 5.7 Cycle efficiency (first layout)

	MATLAB code	ASPEN	Difference
Heating coefficient of performance COP_h	6.1877	6.1879	0
ORC thermal efficiency, %	8.7899	8.488	3.6%
Total heating capacity, kW	20.1876	20.1428	0.2%
Fuel to heat efficiency, %	136.5976	134.2662	1.7%

Table 5.8 Gas burner design parameters

	MATLAB code	ASPEN	Difference
Mass flow rate of methane, kg/s	2.6629e-04	2.7031e-04	1.5%
Exhaust outlet temperature, ^{o}C	60	60	0

Figure 5.32 shows the T-Q curve (acquired from ASPEN) for the HP condenser (at the first heating stage) after the optimization process in the HP cycle. It shows that cold tap water enters the condenser at 10 ^{o}C, and after absorbing 8 kW of latent heat due to the condensation of R134a, the water temperature increases to 32 ^{o}C at the condenser exit. The figure also shows that the optimization has secured the required pinch point temperature difference between the cold stream (water) and the heat stream (working fluid, R134a).

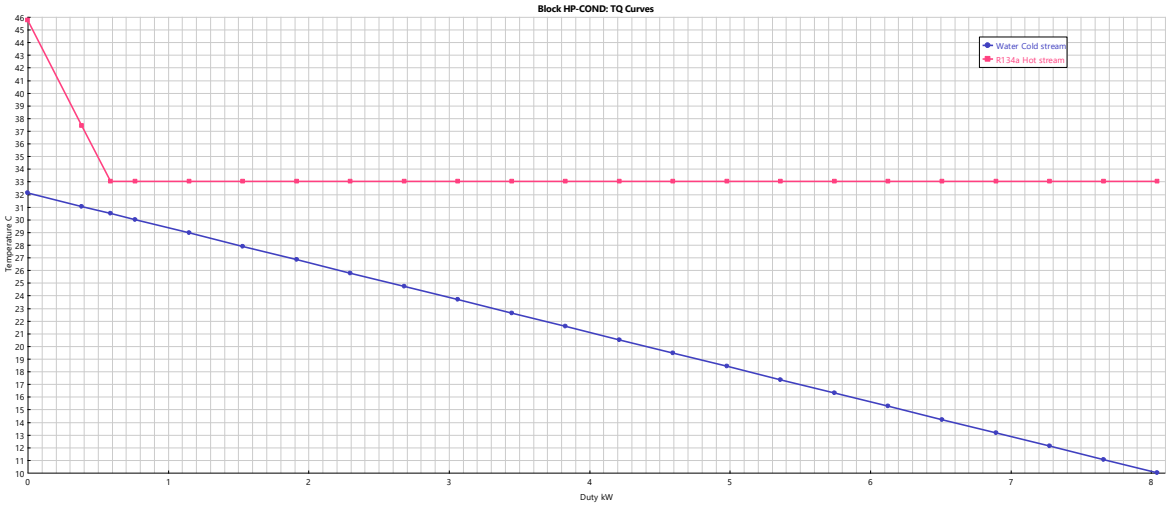

Figure 5.32: T-Q curve across the HP condenser.

Figure 5.33 shows the T-Q curves for the ORC condenser (obtained from MATLAB code). It shows that the R245fa condensation released 12 kW of latent heat to be absorbed by the water to raise its temperature from 32 to 65 ^{o}C. Furthermore, the optimal ORC condenser pressure maintained a 3 ^{o}C pinch point temperature difference between the two streams.

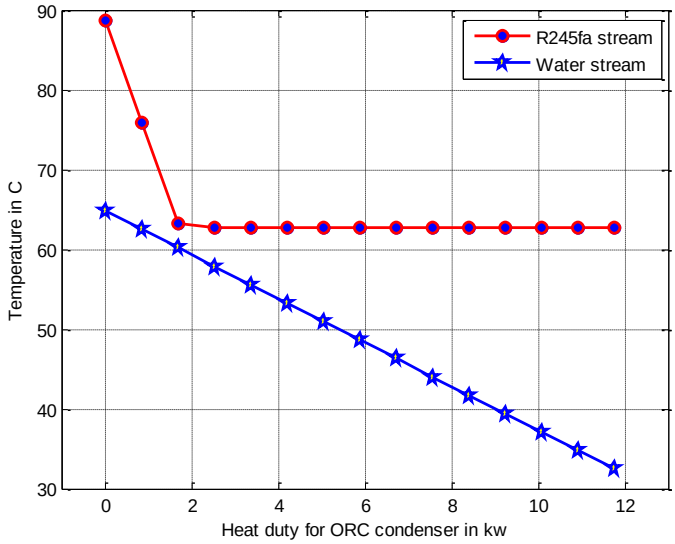

Figure 5.33: T-Q curve across the ORC condenser.

5.5.1.3 Modelling the combined cycle with practical ORC evaporation pressure

The above approach assumes that the ORC evaporation pressure is set to a high value close to the critical pressure in order to achieve the maximum ORC cycle efficiency. However, such high-pressure can be considered not feasible, and can add additional stress to the ORC cycle [48]. In addition, some countries have set an upper limit of 20 bar for vapour pressure to comply with safety regulations [132, 157]. Therefore, a pressure of 20 bar was implemented in this analysis, and the results are shown in Table 5.9. This optimization was carried out by maintaining 3 ºC PPT at the HP and ORC condensers.

Table 5.9 Combined cycle results at ORC evaporation pressure of 20 bar.

Main combined system parameters	Results with ORC evaporation pressure of 36.5 bar	Results with ORC evaporation pressure of 20 bar
ORC condenser pressure, bar	4.7683	4.5174
Expander power, kW	1.3272	1.3272
ORC thermal efficiency, %	8.7899	8.8145
ORC cycle pressure ratio	7.6547	4.4
ORC expander isentropic efficiency %	61.23	72.78
Total system heating capacity, kW	20.1876	21.152
Final water temperature, ^{o}C	65.3084	67.95
ORC evaporator thermal capacity kW	13.1291	14.1903
Mass flow rate of methane, kg/s	2.6629e-04	2.8781e-04
ORC mass flow, kg/s	0.0609	0.0552
Fuel to heat efficiency, %	136.5976	132.4202

Table 5.9 shows that reducing the evaporation pressure from 36.5 to 20 bar has a minimal effect on most designed parameters, such as expander power, condenser pressure, ORC thermal efficiency, final water temperature, and total thermal capacity. However, due to the increase in the ORC evaporator thermal capacity (1 kW), Methane mass flow increases and therefore, the fuel to heat efficiency declines by 3%.

5.5.1.4 Modelling the combined cycle under PPTD of 10 ^{o}C

In practise, the PPTD selected in designing a heat exchanger could be higher than 3 ^{o}C that is adopted in simulation studies. Therefore, a practical PPTD of 10 ^{o}C is selected to study the effect of this PPTD on the combined system performance and compare the results with that obtained with 3 ^{o}C PPTD. The results are shown in Tables 5.10 and 5.11. Tables 5.10 shows that increasing the PPTD to 10 ^{o}C results in a reduction in the condenser and evaporator heating duties of the HP cycle with a corresponding increase in these parameters in the ORC cycle in order to satisfy a total heating duty of 20 kW. To achieve the target water temperature of 65 ^{o}C, the condensation temperature of HP and ORC cycles increased by around 5.2 and 7 ^{o}C respectively.

Table 5.10 Comparison results of the combined cycle parameters at different PPTD.

Combined system design parameters	HP cycle		ORC cycle	
	Results at PPTD of 3 ^{o}C	Results at PPTD of 10 ^{o}C	Results at PPTD of 3 ^{o}C	Results at PPTD of 10 ^{o}C
Condenser heat duty, kW	8.2125	7.4825	11.9751	12.8388
Water temperature leaving the cycle, ^{o}C	32.5	30.5	65.3084	65.6747
Evaporator heat duty, kW	6.8853	5.9515	13.1291	14.1759
Condensation temperature, ^{o}C	33	38.22	61	68.79
Condensation pressure, bar	8.3878	9.6898	4.7683	5.9
Evaporation temperature, ^{o}C	2.5	2.5	159	159
Evaporation pressure, bar	3.2	3.2	36.5	36.5
Power produced by ORC expander, kW	-	-	-1.3272	-1.531
Power input to the HP compressor, kW	1.3272	1.531	-	-
Work of the liquid pump, kW	-	-	0.1732	0.194
Cycle mass flow rate, kg/s	0.0447	0.0407	0.0609	0.0693

Table 5.11 Combined cycle efficiency at different PPTD.

Combined system performance	Results at PPTD of 3 ^{o}C	Results at PPTD of 10 ^{o}C
Heating coefficient of performance COP_h	6.1877	4.8872
ORC thermal efficiency, %	8.7899	9.4321
Total heating capacity, kW	20.1876	20.3213
Fuel to heat efficiency, %	136.5976	127.3491

Increasing HP and ORC condensation temperature and pressure under constant evaporation temperature have resulted in reduction in HP heating coefficient of performance by 1.3 as shown in Table 5.11. In additions, the fuel to heat efficiency have declined by around 9% despite the small increment in the ORC thermal efficiency by 0.7%.

5.5.1.5 Validation of theoretical results with experimental data

To validate the steady state results obtained from ASPEN PLUS model used in this thesis, an experimental data from the open literature on a similar HP and ORC cycles are used. For the HP cycle, results from Liang, Y. et al [114] study were used for the validation as shown in Table 5.12.

Table 5.12 Validation of theoretical model for the HP cycle.

HP cycle design parameters	Liang, Y. et al [114] results	ASPEN results
Condenser heat duty, kW	3.31	8.044
Water temperature entering the cycle, ^{o}C	15	10
Water temperature leaving the cycle, ^{o}C	25.2	32
Water mass flow, kg/s	0.0576	0.087
Evaporator heat duty, kW	3.26	6.744
Condensation temperature, ^{o}C	23.4	33
Condensation pressure, bar	7.696	8.388
Evaporation temperature, ^{o}C	2.4	2.5
Superheat degree, ^{o}C	3.3	0
Power input to the HP compressor, kW	1.01	1.3
Compressor isentropic efficiency	0.5	0.7
R134a mass flow rate, kg/s	0.0776	0.0438
COP_h, %	3.28	6.1

From Table 5.12, the obtained COP_h from the experimental results is different from that obtained from the theoretical model. This can be explained by a number of factors including: (1) The assumption of no pressure and heat loss across the HP cycle parts. (2) The lower isentropic efficiency of the compressor by 20% achieved in the experimental test. (3) The difference in condensation pressure and hence temperature by around 0.7 bar and 9.6 ^{o}C respectively, despite similar evaporation temperature.

For the ORC cycle, experimental results from Collings, P et al. [126] study were used to validate the simulation results as shown in Table 5.13.

Table 5.13 Validation of theoretical model for the ORC cycle.

ORC cycle design parameters	Collings, P et al. [126] results	ASPEN results
Condenser heat duty, kW	--	12.098
Evaporator heat duty, kW	3.617	13.221
Condensation temperature, ºC	--	64.157
Condensation pressure, bar	1.4	5.2
Evaporation temperature, ºC	--	159
Evaporation pressure, bar	5.82	36.5
Net power, kW	0.262	1.122
Turbine isentropic efficiency	0.74	0.7
ORC thermal efficiency, %	6.8	8.488

The ORC cycle adopted in Collings, P. et al [126] is a regenerative cycle designed for power production where the condenser thermal energy is rejected to the environment. This can explain the difference in the condensation pressure by 3.8 bar from the ASPEN model. In the simulation model, the evaporation pressure is set near the critical pressure of the working fluid. However, this might not be achievable in the experimental test due to the expander design limitation. The ORC cycle efficiency obtained from the experimental and theoretical simulation were close, with a difference of approximately 1.6%. This could be due to the close value of turbine isentropic efficiency.

5.5.2 Second approach: water heated by ORC cycle first

In this approach, the first heating stage for water is assumed to occur via the ORC-condenser then the HP condenser. Generally, the modelling procedure is the same as for the previous model in which the evaporation pressures for both cycles are kept constant, the same as in the first approach. The isentropic efficiency for the expander and compressor is set to 70% for comparison purposes. In addition, the condenser pressures for both cycles are iterated until the water temperature at the HP cycle exit reaches the final design value. Furthermore, the ORC mass flow is increased gradually until the total heating capacity of the combined cycle is equal to 20 kW. A summary of the simulation results for approach two is presented in Tables 5.14 and 5.15.

Table 5.14 Steady state results for the second approach.

Parameters	ORC first	
	HP cycle	ORC cycle
Condenser heat duty, kW	6.109	14.173
Water temperature leaving the cycle, ^{o}C	65.73	48.95
Evaporator heat duty, kW	4	16.1
Condensation temperature, ^{o}C	66.36	46.45
Condensation pressure, bar	19.5	3
Evaporation temperature, ^{o}C	2.5	159
Evaporation pressure, bar	3.203	36.5
Power produced by the expander of ORC, kW	--	2.1
Power input to the compressor of HP, kW	2.1	--
Work of the liquid pump, kW	--	0.198

Table 5.15 Combined cycle performance second approach.

Parameters	ORC first
Heating coefficient of performance COPh	2.91
ORC thermal efficiency	11.832
Total heating capacity, kW	20.282
Fuel to heat efficiency, %	111.540669
CH_4 mass flow kg/s	0.00032763
Total heat released from CH_4 combustion, kW	18.183

From these two tables, it is clear that both approaches can secure the thermal energy of 20 kW which is required to heat water from 10 to 65 ^{o}C. Although both approaches have achieved nearly equal overall heating duties, the first approach with the heat pump as the first heating stage shows a higher overall fuel to heat efficiency of 136%, as compared with 111% for the second approach. This is because the HP heating coefficient of performance declined by 47% despite the 21% increase in ORC efficiency achieved by the second approach. Furthermore, 10% more Methane mass is required in the second approach to achieve the thermal energy required by the ORC evaporator.

5.6 Exergy destruction analysis and the second law efficiency

Exergy is the maximum theoretical work obtainable from a system, i.e. the maximal useful energy. It is thus an overall system property that depends on the system's other thermophysical properties (temperature, pressure and enthalpy) as well as on atmospheric temperature and pressure. To investigate the quality of energy produced by the combined cycle, exergy destruction at each component of the system is calculated. In addition, the second law of efficiency is estimated for the heat pump and ORC cycles.

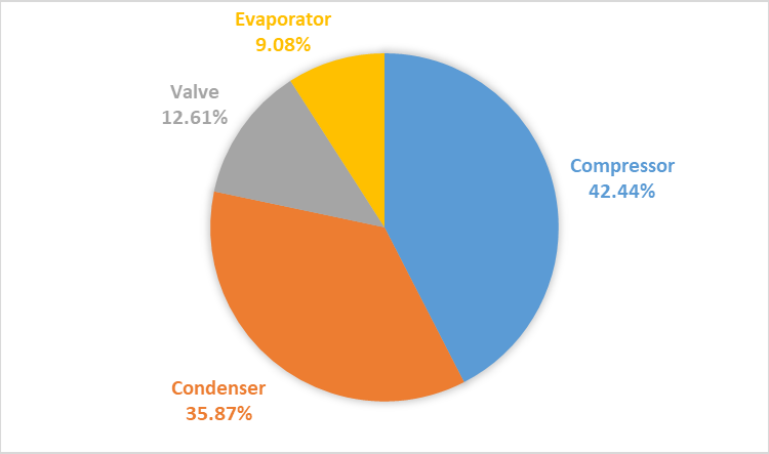

Figure 5.34: Exergy destruction in each component of the HP cycle.

In the heat pump cycle, exergy loss occurs at higher rate in the compressor and condenser, as shown in Figure 5.34, with both components responsible for 78.3% of exergy destruction from a total value of 1.1279 kW. This is because the amount of entropy generation inside these components is high.

The exergy destruction ratio in each part of the ORC cycle is shown in Figure 5.35. It is clear that the evaporator has higher exergy losses than other cycle components. This is because there are high temperature and enthalpy differences between the cold and hot streams across the evaporator. The same results were found by Nasir and Kim [169].

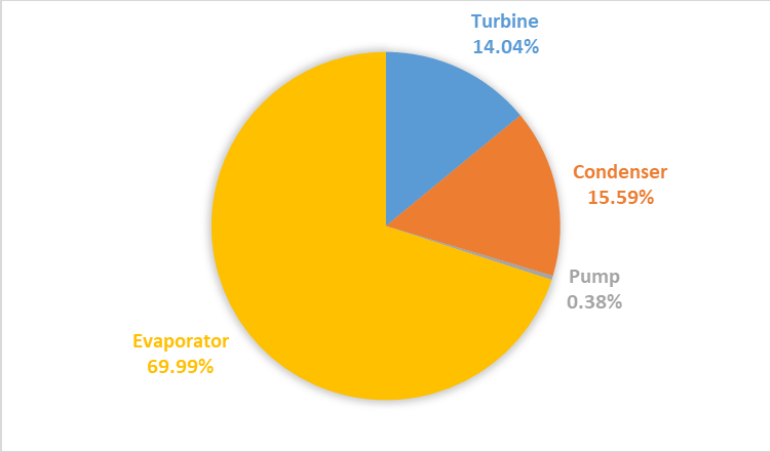

Figure 5.35: Exergy destruction in each component of the ORC cycle.

A summary of the energy and heat production and exergy loss across each part of the combined system is shown in Table 5.16.

Table 5.16 Heat, power and exergy loss in the combined system

Cycle	Parameters	Compressor / turbine	Evaporator	Condenser	Valve / pump
HP	Heat / power, kW	1.3272	6.8853	8.2125	--
	Exergy loss, kW	0.4787	0.1024	0.4046	0.1422
ORC	Heat / power, kW	1.3272	13.1291	11.9751	0.1732
	Exergy loss, kW	0.5771	2.878	0.6409	0.0158

The second law of efficiency measures the usefulness of a process or a cycle by comparing actual output with the ideal results. Thus, in the HP cycle, the second law of efficiency is taken as the ratio of actual COP_h to the ideal (reversible) COP_h. Similarly, in the ORC cycle, it is the ratio between actual and ideal thermal efficiency.

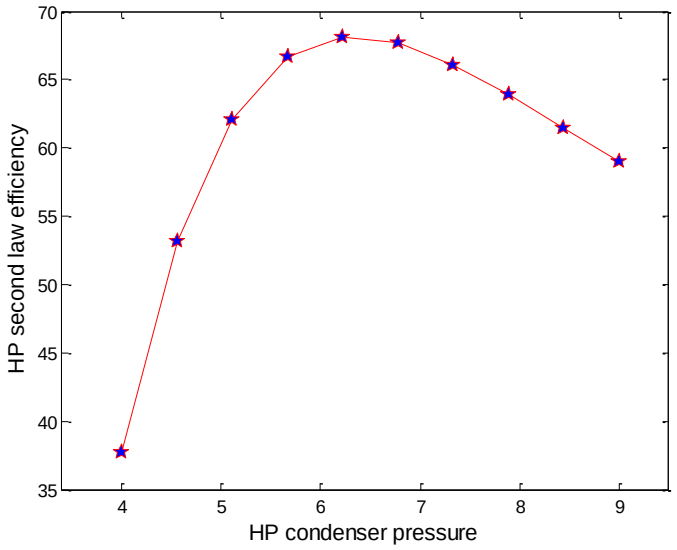

Figure 5.36: Second law of efficiency for the HP cycle under variable HP condensation pressures.

The effects of HP condensation pressure on the HP second law of efficiency is shown in Figure 5.36. As the condensation pressure increases, the second law of efficiency increases exponentially to reach a maximum value of around 68% when the condenser pressure reaches 6 bar. Thereafter, a gradual decline is noted in the efficiency to a value of 58% at the optimum HP condensation pressure. This is explained by the fact that the actual COP_h declines with the rise in condensation pressure, as demonstrated in the previous results. Also, higher pressure causes higher temperatures in the condenser and hence lower ideal COP_h when the evaporation temperature is constant.

In the ORC cycle, the second law of efficiency's correlation with the ORC condenser pressure is shown in Figure 5.37. With the initial rise in condenser pressure, the second law of efficiency maintains a nearly constant value at the maximum achievable efficiency of around 47 %.

However, further increments in the pressure beyond 7 bar result in a sharp decline in the second law of efficiency, which reaches its lowest level of 12.2% at a condensation pressure of 9 bar.

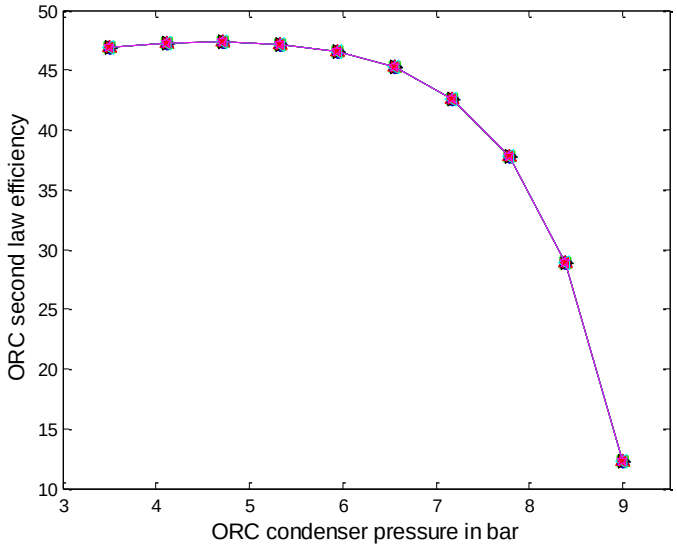

Figure 5.37: Second law of efficiency for the ORC cycle under variable ORC condensation pressure.

5.7 Control strategies in the combined system when the ambient temperature varies

Over the course of the year, the ambient air temperature varies considerably. For instance, the average air temperature in the UK might range between 5 to 15 ^{o}C, but it can also drop to below zero on some winter days. The variation in ambient temperature is one of the main factors that affects the performance of any air-sourced heat pump system, as shown in the results above. It is therefore essential to propose and investigate some control strategies that can tackle such variation. These are discussed in the following sub-sections.

5.7.1 First control strategy

Generally, for air sourced heat pump systems, as the ambient temperature drops, the thermal energy available for extraction declines. Thus, to improve heat extraction when the air

temperature falls, the air mass flow rate is adjusted accordingly. However, this strategy alone is only sufficient in certain temperature ranges.

In this approach, the air mass flow is initially iterated under variable HP evaporator areas and ambient air temperatures to secure the designed heating capacity. The temperature of the gas burner exhaust gas is assumed to be 60 ^{o}C. Other design parameters were obtained from the results of the combined cycle with HP as the first heating stage simulation.

As the ambient air temperature drops, the required air mass flow and evaporator heat transfer area increase gradually, as shown in Figure 5.38. However, when the temperature drops below 7 ^{o}C, a rapid increase in air mass to 11 kg/s is needed. Similarly, the evaporator area increases as the air temperature drops, reaching a maximum value of around 2.5 m^2 when the ambient temperature reaches 6 ^{o}C.

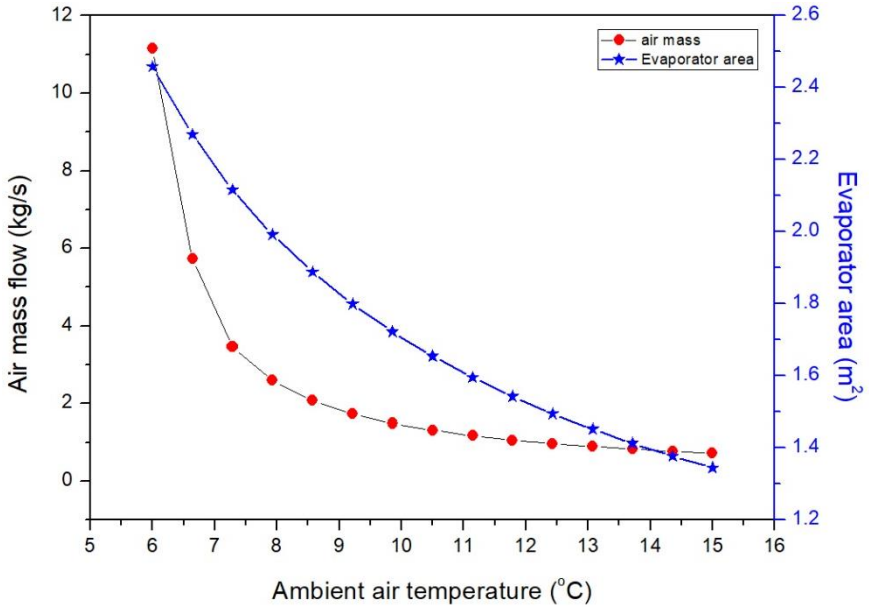

Figure 5.38: Effects of ambient temperature on evaporator design parameters.

As ambient air is also used to feed the gas burner, the heat from the combustion is expected to decline when the ambient temperature decreases. Thus, to compensate for the reduction in the

burner-produced thermal energy, the Methane mass flow needs to be increased slightly, as shown in Figure 5.39.

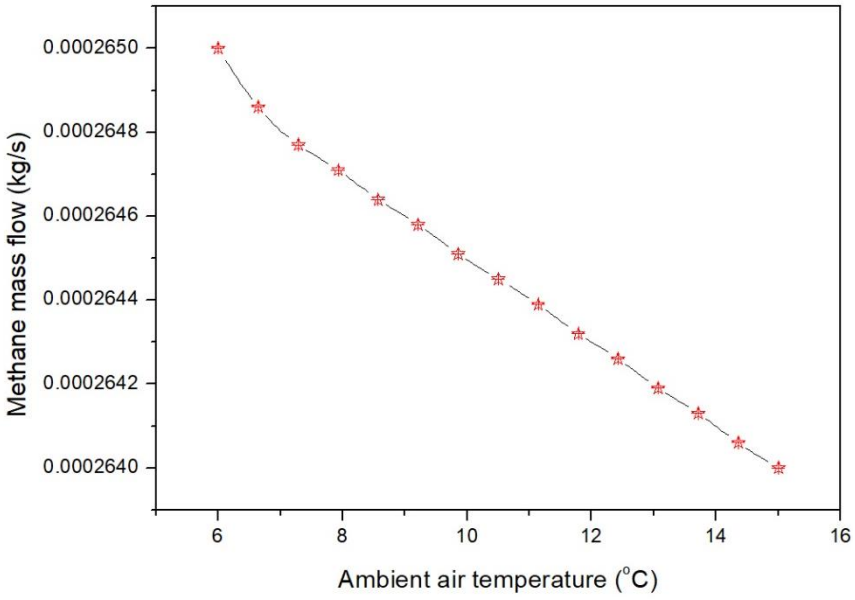

Figure 5.39: Effects of air temperature on Methane mass flow.

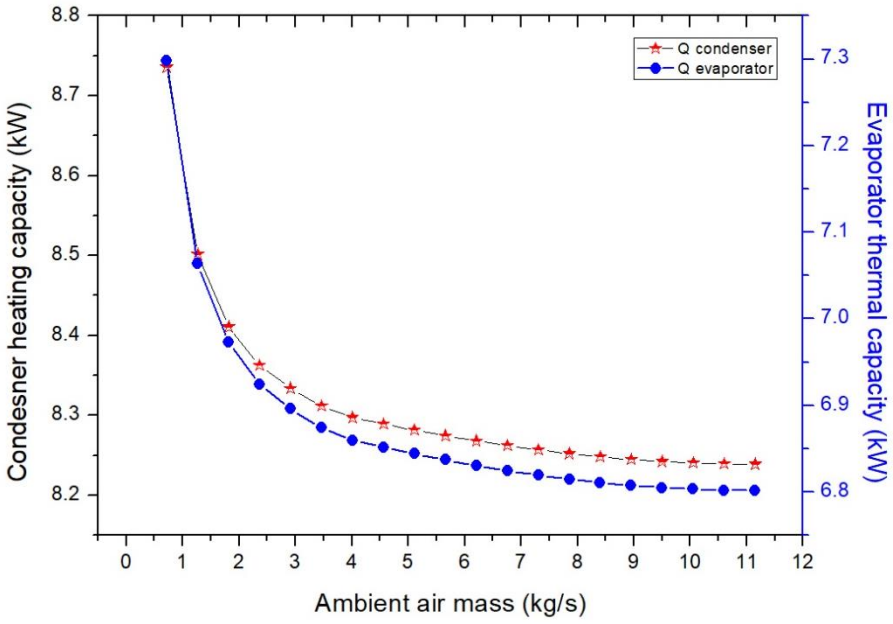

Figure 5.40: Effects of increasing ambient air mass on the HP evaporator and condenser thermal duties.

Figure 5.40 shows the effects of varying the air mass flow on the HP evaporator and condenser thermal duties. With the initial increase in air mass from 0.7 to 3 kg/s, evaporator thermal duty declines sharply from 7.29 to around 6.9 kW. A further increase in air mass has a minimal effect on this parameter, which maintains a nearly constant value of around 6.8 kW. Similar results have been presented in the literature by Chen and Yu [174] for an air source heat pump water heater. The dynamic results of that study, which were compared with experimental results, revealed that increasing the air velocity of the evaporator unit always enhances the overall cycle performance. However, it should be noted that this advantage is reduced when the air velocity exceeds 3 kg/s. In their study, the increase in the air mass flow was carried out under constant ambient air temperature. Therefore, the compressor work and the evaporator capacity were increased by 9.79% and 39.62% respectively.

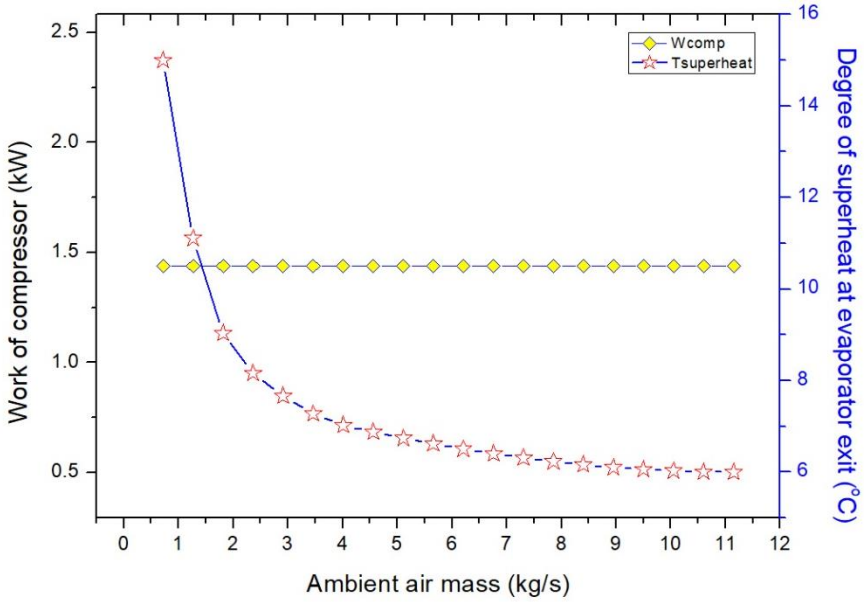

Figure 5.41: Effects of increasing ambient air mass flow on compressor work and superheat degree.

In our present model, such a reduction in the evaporator capacity can be considered acceptable, as this process aims at maintaining the minimum pinch point temperature difference between the hot and cold streams across the evaporator. The heat pump condenser heating duty declines in a similar manner to the evaporator thermal duty, as shown in Figure 5.40. This is because the HP condenser heating duty is the sum of the HP evaporator thermal duty and the compressor

power consumption, which is assumed to be constant (Figure 5.41). Likewise, the superheat degree of the refrigerant at the evaporator exit declines gradually as air mass flow increases.

The pinch point temperature difference across the HP evaporator between the hot stream (a mixture of ambient air and burner flue gases) and the cold stream (R134a) is maintained as constant when the air mass varies, as shown in Figure 5.42. This temperature difference is maintained at 3 ^{o}C, with the temperature of the mixture at the evaporator exit set at 5.5 ^{o}C to avoid frost formation on the evaporator.

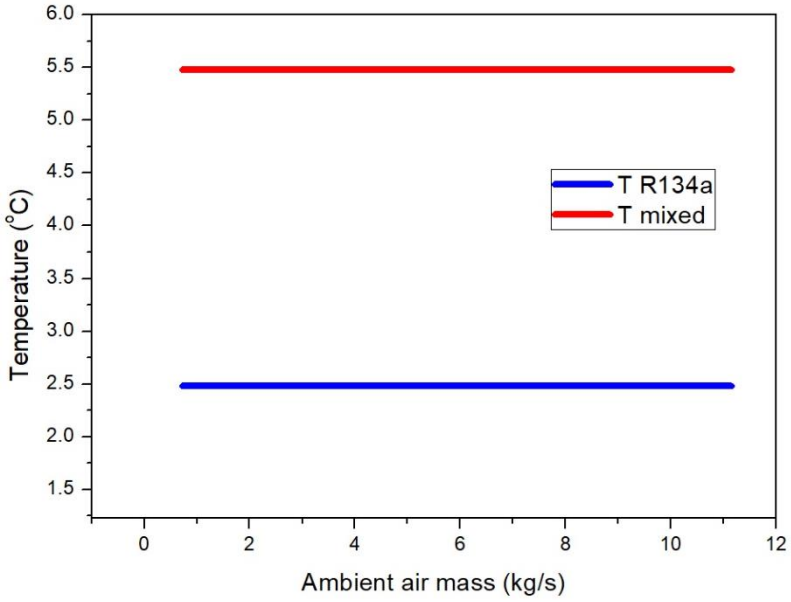

Figure 5.42: Temperature difference between hot and cold streams across the HP evaporator.

As the heating capacity of the HP condenser decreases with a constant compressor power, the heat pump COP will decrease. In addition, with the decline in both HP exchanger heating capacities, the actual power required from the compressor will be lower than the supply. Thus, the excess power will lead to a slight increase in the discharge pressure, as demonstrated in Figure 5.43. When ambient temperature drops from 15 to 6 ^{o}C, the condenser pressure steadily increases from 9 to 9.4 bar, with an opposite reduction in the COP_h from 5.5 to 5.2. The fuel-to-heat efficiency will similarly decrease from 132 to 129 % due to the increased Methane mass flow (Figure 5.39). In addition, the outlet water temperature slightly decreases when air

temperature drops, reaching a value of 64.7 ºC when the air temperature is 6 ºC, as shown in Figure 5.44.

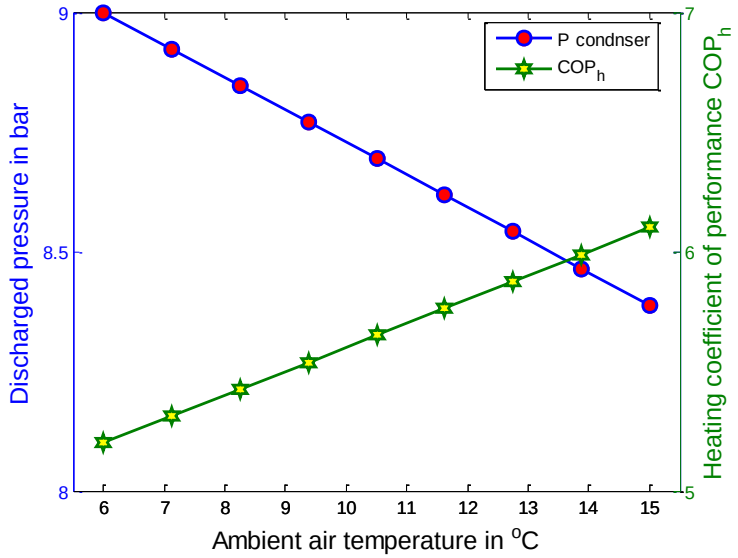

Figure 5.43: Effects of decreasing ambient air temperature on system design parameters.

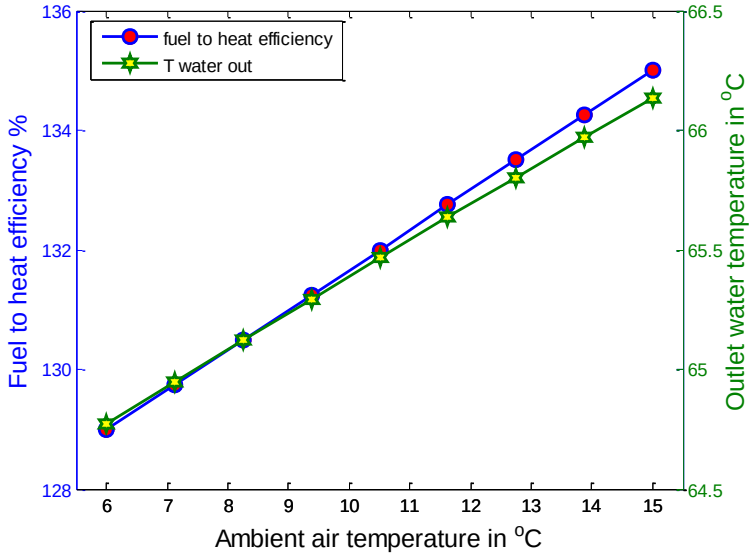

Figure 5.44 Effects of ambient air temperature on outlet water temperature and fuel to heat efficiency.

5.7.2 Second control strategy

As shown in the above results, when the air temperature drops to 6 ^{o}C, the thermal energy available in the ambient air is not enough even when its mass flow is increased. Thus, another control strategy is proposed for when the air temperature drops to 6 ^{o}C and below. In this strategy, the ambient air stream entering the mixture that feeds the HP evaporator is suspended, and the gas burner flue gases stream is used as the only heat source for the evaporator. It is clear that ambient air will still be needed for the combustion process in the burner. Therefore, further Methane mass flow will be needed as a substitute for the reduction in the thermal energy being produced. As a result of these changes, lower fuel-to-heat efficiency is predicted when the ambient temperature drops below 6 ^{o}C.

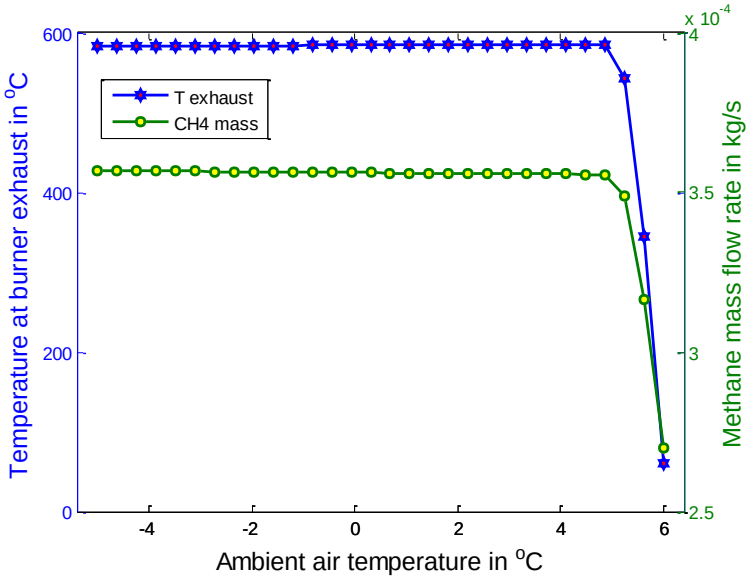

Figure 5.45: Effects of ambient temperature below 6 ^{o}C on Methane mass flow.

Figure 5.45 shows the effects of the ambient temperature drop from 6 to -5 ^{o}C on both Methane mass flow and flue gas temperature. With the initial drop in air temperature to 5 ^{o}C, the Methane mass flow needs to be increased significantly to produce the thermal energy required. After that, the Methane mass flow is maintained at a nearly constant level of around 0.000355 kg/s, despite further falls in air temperature. A similar trend is noted in the temperature of the flue gases, with a rapid initial increment from 60 to 585 ^{o}C when the air temperature drops to 5 ^{o}C.

Thereafter, a further fall in air temperature has a minimal impact on the flue gas temperature as the heat production in the burner is fixed at 13.3 kW.

5.8 Dynamic modelling to verify the control strategies

In order to verify and validate the control strategy mechanism and the obtained results, a dynamic model was developed using ASPEN PLUS dynamic software. Since the HP evaporator is the only section that extracts free energy from the ambient air, and hence is significantly affected by ambient temperature variations, the dynamic evaluation focuses on this part. The same working conditions as used in the steady state simulation were adopted. The evaporator area was set to 2.5 m^2, which is the maximum value obtained from the results above in control strategy one.

In order to provide a continuously controlled feedback mechanism to adjust for the variations in ambient air temperature, a proportional integral derivative (PID) controller is used. The function of this tool is to calculate the error value as the difference between a measured process variable (PV) and a desired set point (ST), and it applies a correction to the controller output (OP) based on proportional, integral, and derivative coefficients to gain an optimal response.

5.8.1 Modelling and results of control strategy one

Figure 5.46 shows a schematic diagram of the dynamic model for control strategy one. A PID controller (B1) is used between the ambient air stream entering the mixer and the evaporator outlet mixed stream. The PID controller output (OP) is the ambient air mass flow in kg/s, while the process variable (PV) is the temperature of the mixture leaving the evaporator. The set point (ST) is constant at 5.5 ^oC to avoid frost formation on the evaporator. The tuning parameters for the PID controller are set at a controller gain of 1% and an integral time of 5 minutes under reverse control action. This setting can ensure the gradual distribution of the ambient temperature over a half day course, with the highest temperature assumed to occur at midday, as shown in Figure 5.47.

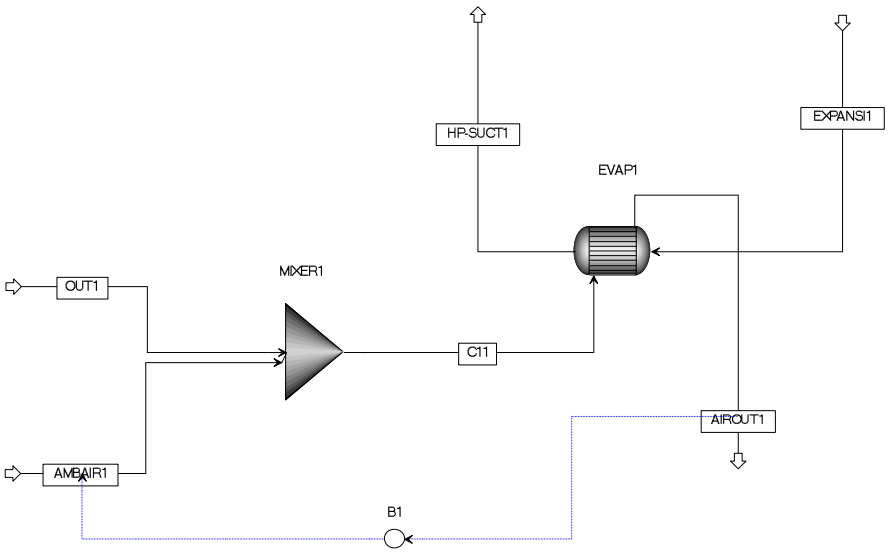

Figure 5.46: Schematic diagram of the dynamic model for control strategy one.

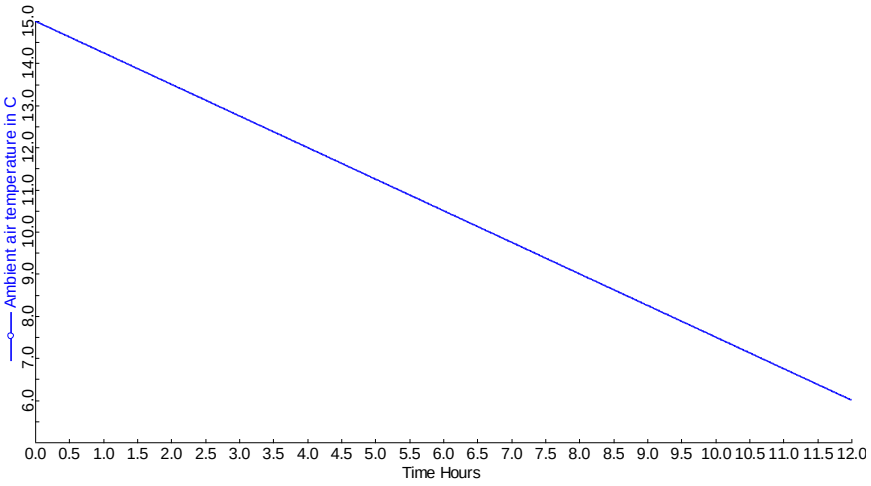

Figure 5.47: Variation of the ambient air temperature over the time lapse.

Figure 5.48 shows the PID performance when the ambient air temperature varies between 6-15 ^{o}C. It shows that the controller maintained the evaporator outlet temperature at 5.5 ^{o}C by adjusting the air mass flow. As the air temperature drops over the course of the day, the controller increases the air mass flow to secure more heat for extraction by the heat pump

evaporator. However, when the ambient temperature approaches 6 ^{o}C, the air mass flow increases significantly to approximately 11 kg/s and the evaporator outlet temperature drops slightly below 5.5 ^{o}C. This result is consistent with that obtained in the steady state results in control strategy one.

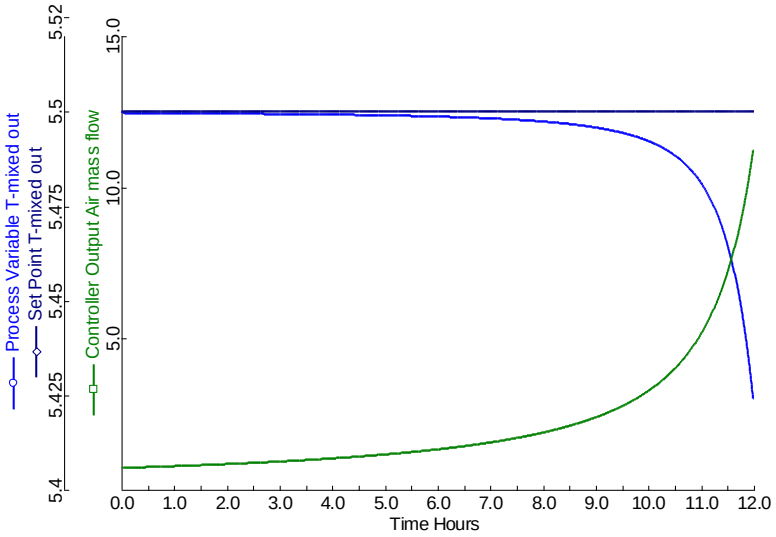

Figure 5.48: PID controller performance for ambient temperature range 6-15 ^{o}C.

Figure 5.49 shows the changes in R134a temperature in the suction line when the ambient air temperature varies. As the air temperature drops towards 6 ^{o}C, the refrigerant temperature declines from 15 to 6 ^{o}C. At the same time, the evaporator cooling capacity decreases from around 7.3 to 6.9 kW, as shown in Figure 5.50. These results are in agreement with those shown in Figures 5.40 and 5.41.

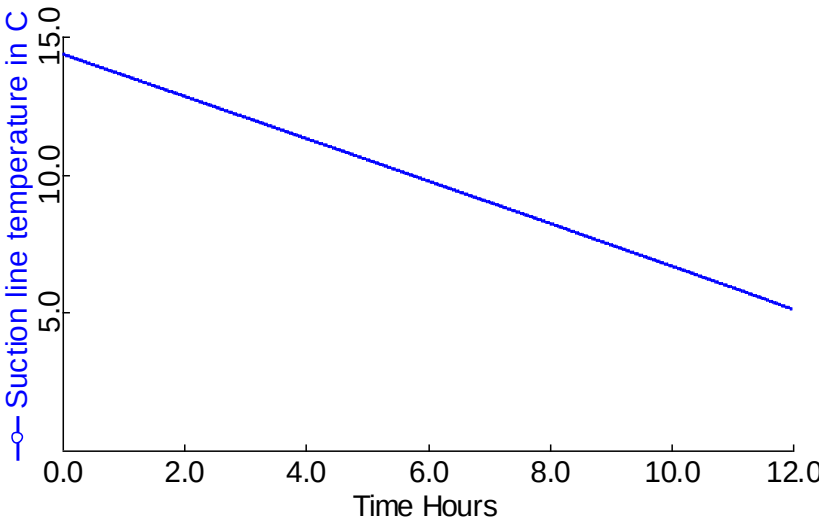

Figure 5.49: Variations in suction line temperature over the time lapse.

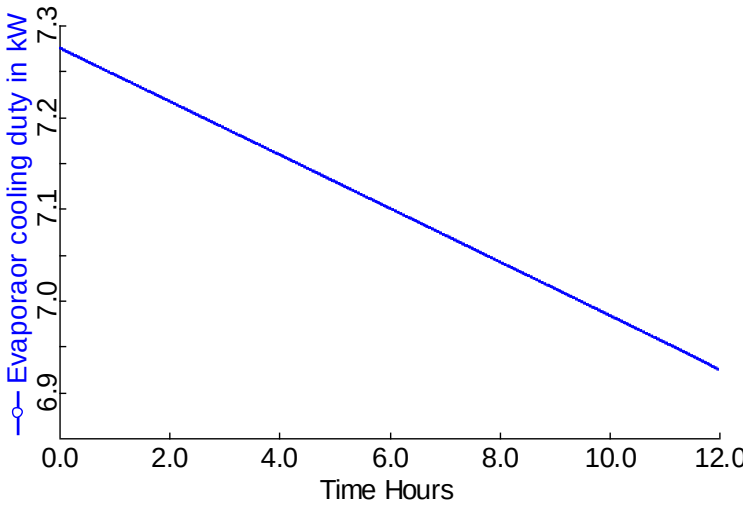

Figure 5.50: Variations in evaporator cooling capacity over the time lapse.

5.8.2 Modelling and results of control strategy two

As illustrated in strategy two, when the ambient air temperature drops below 6 ^{o}C, the ambient air stream is terminated as not enough thermal energy is available for extraction from air. Thus, the exhaust stream will be the evaporator's only heat source. In this model, the PID controller is set between the Methane stream and the evaporator outlet stream to maintain a constant outlet temperature of 5.5 ^{o}C by manipulating Methane mass flow. A schematic diagram of this model is shown in Figure 5.51.

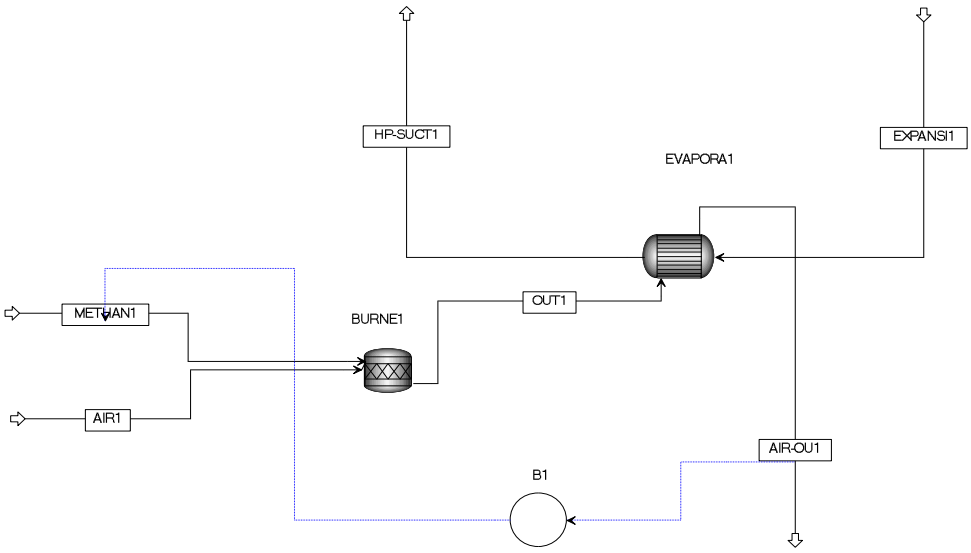

Figure 5.51: Schematic diagram of the dynamic model for control strategy two.

Figure 5.52 shows the PID controller performance for control strategy two. With the decline in ambient air temperature (Figure 5.53), the PID controller responds to these changes by increasing the CH_4 mass flow in kg/s (OP) to maintain the evaporator outlet temperature (PV) at a level close to 5.5 ^{o}C (ST).

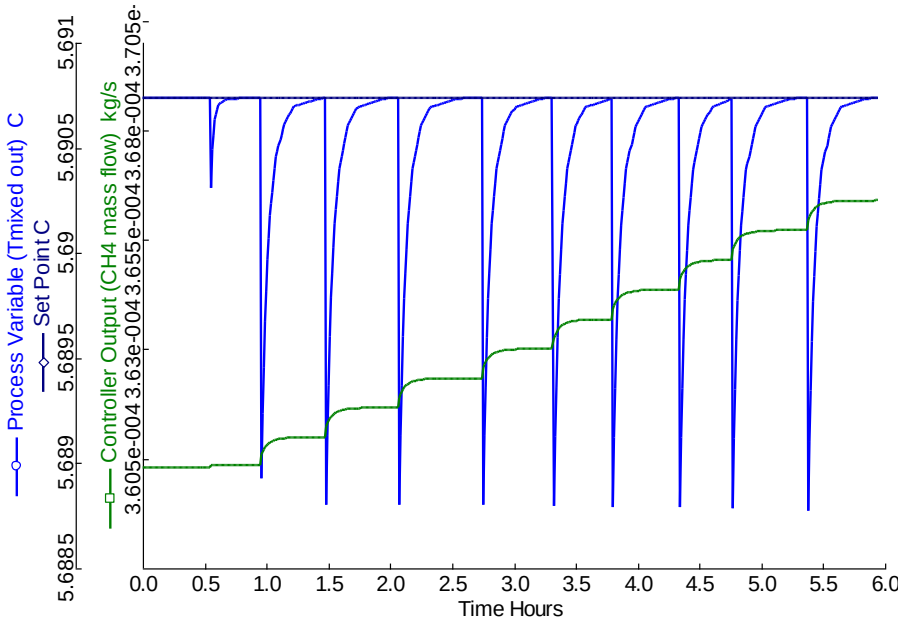

Figure 5.52: PID controller performance for ambient temperature range -5 to 5 ^{o}C.

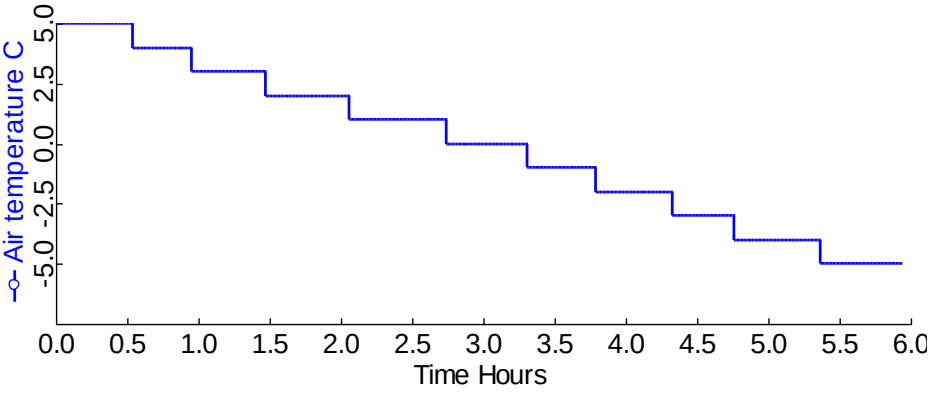

Figure 5.53: Variations of the ambient air temperature over the time lapse.

The corresponding changes in exhaust temperature when the ambient temperature and methane mass flow change over time are shown in Figure 5.54. These results are consistent with those obtained in the steady state evaluation for control strategy two (Figure 5.45).

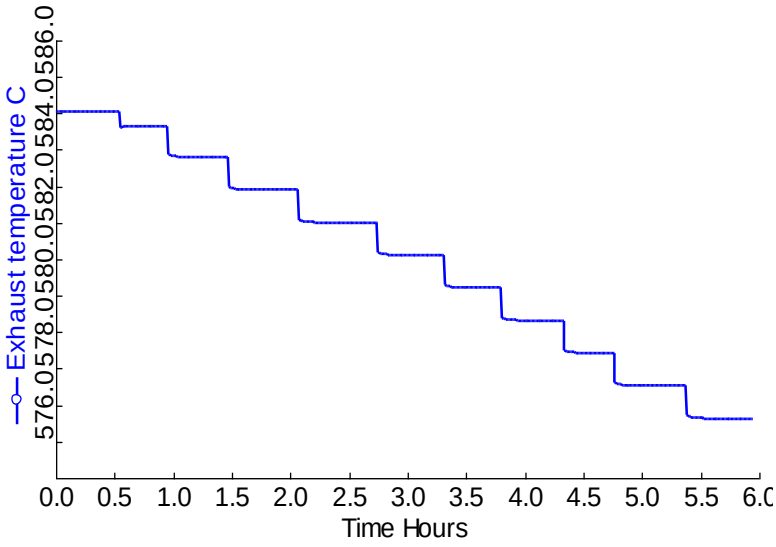

Figure 5.54: Variation in burner exhaust temperature over the time lapse.

5.9 Conclusion

In this chapter, a combined ORC and HP system was proposed to produce hot water for domestic application. A preliminary design was proposed and investigated to explore the maximum theoretical limit of the cycle performance. In this design, water heating happens in three stages: at the HP-condenser, the ORC-Condenser, and post heater. The results reported for this approach support that the system can achieve a maximum fuel-to heat efficiency of 136%. In addition, the post heater could only supply a limited amount of heat to the water, thus it can be removed from the proposed system with a potential cost saving. The optimum design configuration was investigated, and the results showed that water heating by HP cycle then ORC cycle achieved a more efficient performance than the reverse design. Furthermore, the final design configuration was optimized in terms of pinch point approach in both the HP and ORC condensers. The combined system was then evaluated in terms of exergy destruction and the second law efficiency. Control strategies were also proposed to tackle the effects of ambient temperature variation on system performance while maintaining the HP evaporator as frost free. These control strategies were verified and validated by dynamic model, which showed good agreement with the steady state results. The overall results showed that the combined cycle can

achieve a fuel to heat efficiency of around 129% for domestic hot water applications. Such efficiency is competitive with the currently available heating technologies, such as Combi boilers, which have an efficiency of around 90%.

Chapter 6 Utilizing the wasted heat from a data centre to cool and heat applications via the combined ORC-HP system

6.1 Introduction

Data centres are a pivotal facility of modern life that are expected to expand in numbers over the coming years. However, the electricity consumption by these facilities is also expected to rise at a rate of 20% per annum. Currently, it is estimated that 1.2-1.5% of all electricity being produced is utilized by DCs worldwide [22]. Electricity is mainly used in the operation of IT servers and to cool equipment due to the high heat flux generated as a by-product. The cooling process can consume around 40% of the total electricity supplied [175]. The wasted thermal energy from DC rooms has the potential to be recovered using various technologies such as organic Rankine cycle (ORC), heat pump (HP), combined heat and power cycle (CHP), absorption refrigeration, thermosyphon, and combinations between them. The combined ORC-HP cycle investigated in previous chapter showed the potential for efficient waste heat recovery from gas burner flue gases and the ORC condenser. However, the results also showed that the system performance fluctuates with ambient temperature changes. The prior literature supports that the rejected heat from DCs is higher than the air or ground temperatures currently used as heat sources for modern heat pump systems [22]. In this chapter, a combined system is designed to provide a cooling effect and the recovered wasted heat is utilised in hot water supply or central heating.

6.2 Thermodynamic concept

A schematic diagram of the proposed system is shown in Figure 6.1. The gas driven ORC cycle provides the required mechanical work to run the vapour compression heat pump cycle. The HP evaporator absorbs the heat from DC room to provide a cooling effect. The waste heat rejected by both cycle condensers is used to heat water for central heating. The working conditions and design parameters of a small DC were taken from an experimental study by Zhou, F. et al. [175]. The maximum cooling load is 12 kW, to keep the DC indoor temperature between 18-25 ^{o}C in compliance with the regulations applied in most countries. In this chapter, to

demonstrate the steady state system performance, R134a and R245fa are selected as refrigerants for the HP and ORC cycles, respectively. In addition, Methane is used as a fuel for the gas burner. Furthermore, system performance and system heating capacity under a variable DC cooling load are comprehensively studied, and the control strategies needed to tackle this issue are proposed.

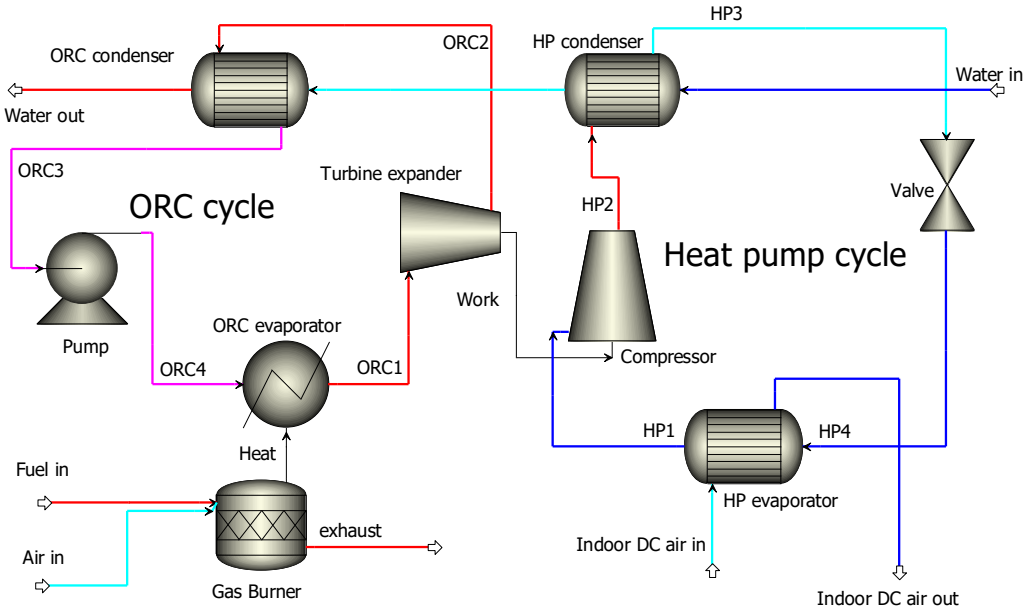

Figure 6.1: Combined cycle configuration for DC application.

6.3 Modelling of the combined system

The modelling presented in this chapter is based on utilizing the heat recovered from the DC for water heating to be used in a central heating application. The thermal network return water temperature is commonly taken as between 50-60 ^{o}C (Wang, Z., et al.) [8], while the final hot water temperature is set to 80 ^{o}C [176]. Therefore, the proposed heating system will heat up water from 50-80 ^{o}C. In-house MATLAB code linked with REFPROP software has been developed to evaluate the energy balance across the combined cycle components. In addition, the steady state results are verified using ASPEN PLUS software. In the heat pump cycle, the inlet and outlet DC air temperature are assumed to be 18 and 25 ^{o}C respectively. The evaporation temperature is set at a constant 15 ^{o}C to secure a 3 ^{o}C pinch point temperature difference with

the indoor DC air out temperature and by assuming that the refrigerant is fully vaporized at the evaporator exit. The corresponding evaporation pressure is calculated using REFPROP software as equal to 4.8837 bar. Similar working conditions for the gas burner are adopted from the previous model in chapter five. In addition, the same assumptions regarding the expansion process and isentropic efficiencies are made.

6.3.1 Heat pump cycle optimization

To identify the optimum refrigerant mass flow and condensation temperature for an HP cycle that achieves a 12 kW cooling load, iterations of R134a mass flow under a range of condensation temperatures between 55-65 ^{o}C were conducted under constant evaporation temperature and pressure. The effects of these variables on the cycle's performance are studied.

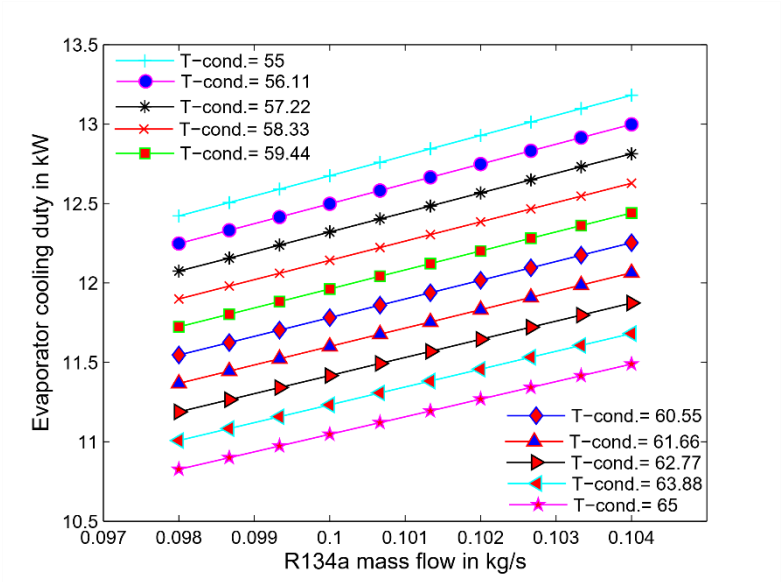

Figure 6.2 : Effects of variations in R134a mass and condensation temperature on HP evaporator capacity.

Figure 6.2 shows the effects of variations in evaporator thermal capacity with refrigerant mass flow rates under different condensation temperatures for the HP cycle. For the selected range of condensation temperatures, the evaporator cooling duty increases with the rise in R134a mass flow. For each mass flow, an increased condensation temperature will reduce the thermal

capacity. In general, the thermal capacity of a heat exchanger is a function of the refrigerant mass flow and enthalpy difference (Delta *h*) across the exchanger. For the evaporator, the enthalpy at the inlet will increase with a rising condensation temperature, whereas the enthalpy at the evaporator exit is assumed to be constant. Hence, the evaporator capacity will decrease as Delta *h* increases.

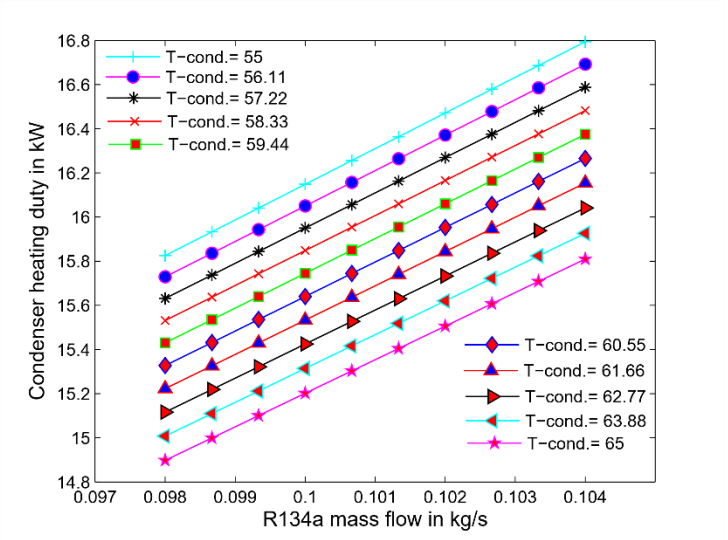

Figure 6.3: Effects of variations in R134a mass and condensation temperature on HP condenser capacity.

Likewise, regarding the evaporator cooling capacity, the condenser heating duty increases with refrigerant mass flow and decreases with rising condensation temperatures, as shown in Figure 6.3. With the rise in the condenser temperature, enthalpies at both the inlet and the exit of the heat pump condenser increase. However, the increment in the enthalpy at the condenser outlet is higher than that at the inlet, resulting in a reduction in Delta *h* and hence a decline in the condenser heating duty, as was explained in the previous chapter.

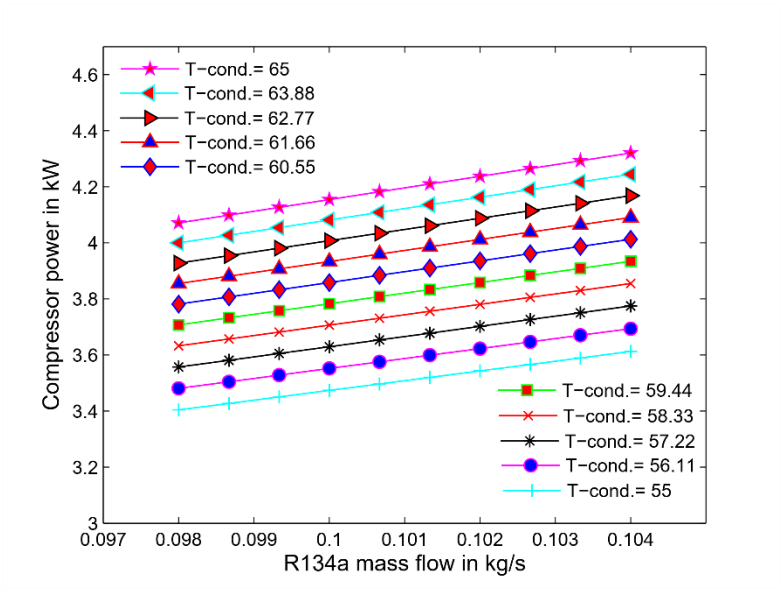

Figure 6.4: Effects of variations in R134a mass and condensation pressure on compressor network.

The work of the HP-compressor has been shown to increase with the rise in R134a mass at various condensation temperatures (see Figure 6.4). Similarly, the compressor will achieve higher net power when the HP condensation temperature increases due to higher enthalpy at the compressor outlet.

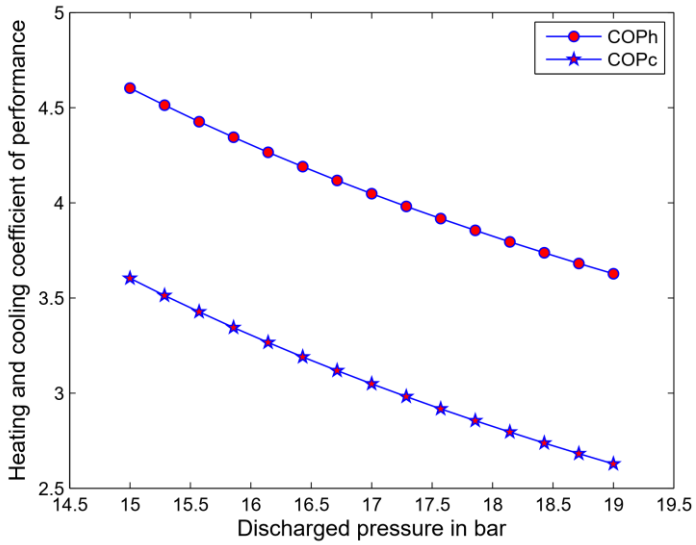

Figure 6.5: Effects of HP discharged pressure on COP_c and COP_h.

Figure 6.5 shows that the heating and cooling coefficients of performance decrease with the increase in condensation temperature. This happens because an increasing condenser temperature results in more compressor work and a lower heating capacity for the evaporator and condenser, as was explained in the results above.

6.3.2 ORC cycle optimization

In the ORC cycle, the same working conditions and assumptions as those used in the modelling approach in the previous chapter are deployed, including the ORC turbine and pump efficiencies. To identify the optimum ORC evaporator pressure for this case study, the pressure was optimized as shown in Figure 6.6.

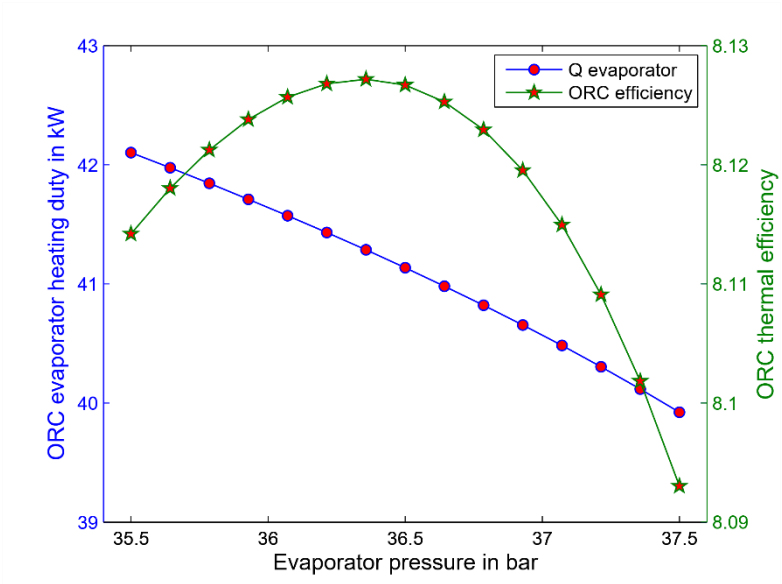

Figure 6.6: Effects of HP discharged pressure on COP_c and COP_h.

Figure 6.6 shows the effects of variations in ORC evaporator pressure at a constant mass flow on the evaporator heating duty and thermal efficiency. The results verify that at an evaporator pressure of 36.5 bar, thermal efficiency reaches the maximum value of 41 kW. However, variable ORC refrigerant mass flow is calculated assuming full mechanical power transformation between the ORC expander and the HP compressor. Figure 6.7 shows the

variations in the ORC condenser heating duty due to the increase in the R245fa mass flow under variable HP-condensation temperatures.

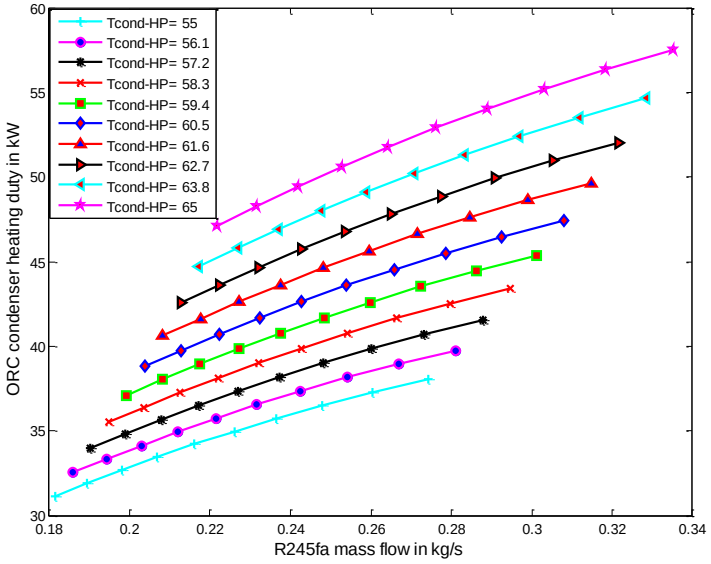

Figure 6.7: Effects of increasing R245fa mass flow and HP condensation temperature on ORC condenser heating duty.

As mass flow increases, the heating duty rises for all condensation temperature ranges. Similarly, an increasing condensation temperature in the HP cycle causes a rise in ORC-condenser heating duty in a pattern opposite to that which was noted in the HP-condenser (Figure 6.3). This is because an increasing HP-condensation temperature will require more compressor work, which means more turbine power and mass flow, and therefore, a higher ORC condenser heating capacity.

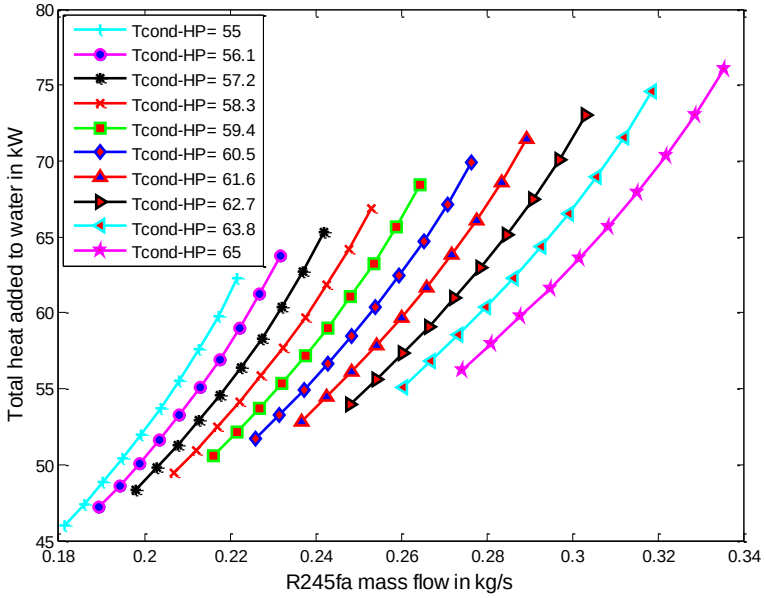

Figure 6.8: Effects of increasing R245fa mass flow and HP condensation temperature on total heat capacity added to water.

The total heat added to water is the sum of the heat added by both cycle condensers. As the HP condensation temperature increases, the total heating capacity rises for all R245fa mass flow, as shown in Figure 6.8. This is because the increment in ORC condenser heating duty (Figure 6.7) is higher than the reduction in HP condenser heating duty (Figure 6.3).

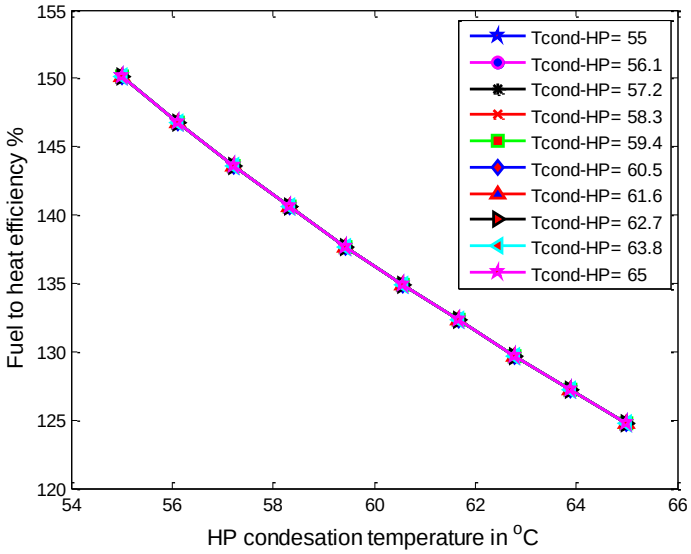

Figure 6.9: Fuel to heat efficiency of the combined cycle under variable HP condensation temperature.

The overall fuel to heat efficiency achieves a significant level, ranging from 125% to 150% for all condensation ranges, as illustrated in Figure 6.9. The fuel to heat efficiency includes the total heat added to water and the heat removed from the data centre, i.e. 12 kW divided by the total heat released from Methane combustion, as shown in Equation 6.1.

$$\eta_{fuel-to-heat} = \frac{\sum \dot{Q}_w}{\dot{Q}_g} = \frac{\dot{Q}_{HP,cond} + \dot{Q}_{ORC,cond} + \dot{Q}_{HP,evap}}{\dot{Q}_g} \qquad 6.1$$

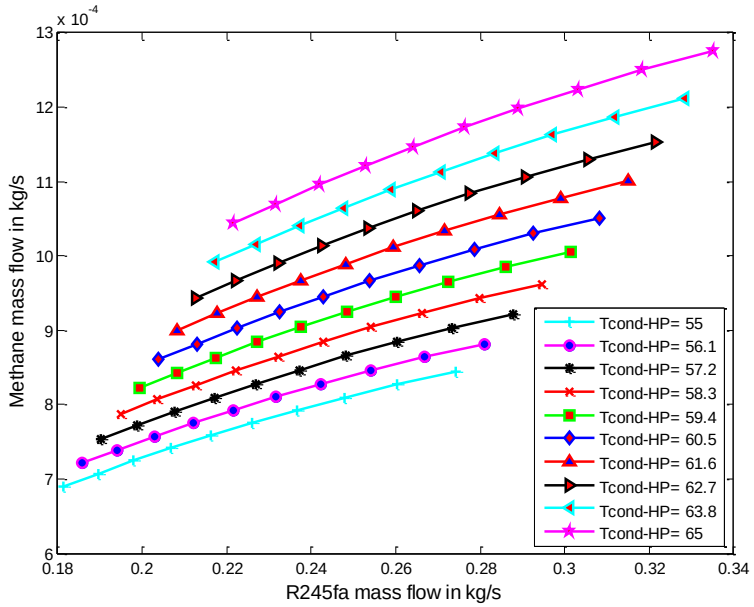

Figure 6.10: Methane mass flow of the combined cycle under variable ORC mass flow and HP condensation temperatures.

In the burner, the methane mass flow increases with rises in R245fa mass flow and HP condensation temperature, as shown in Figure 6.10. As the R245fa mass flow increases, the ORC condenser and consequently the evaporator thermal capacities increase, thus more methane mass is required to make up for these changes.

6.3.3 Optimization of combined cycle under minimum PPT approach

In order to accomplish optimum performance for the combined system, the design parameters were optimized by maintaining a minimum PPT across all the integrated system heat exchangers. The optimization process involved the following conditions: R134a is iterated until the HP evaporator cooling load reaches its desired value (12 kW); Water mass flow and ORC condenser pressure are iterated until the minimum PPT value is satisfied across the HP and ORC condensers, respectively; the HP condenser temperature is optimized in order to satisfy the final water temperature. The results are summarised in the figures shown below:

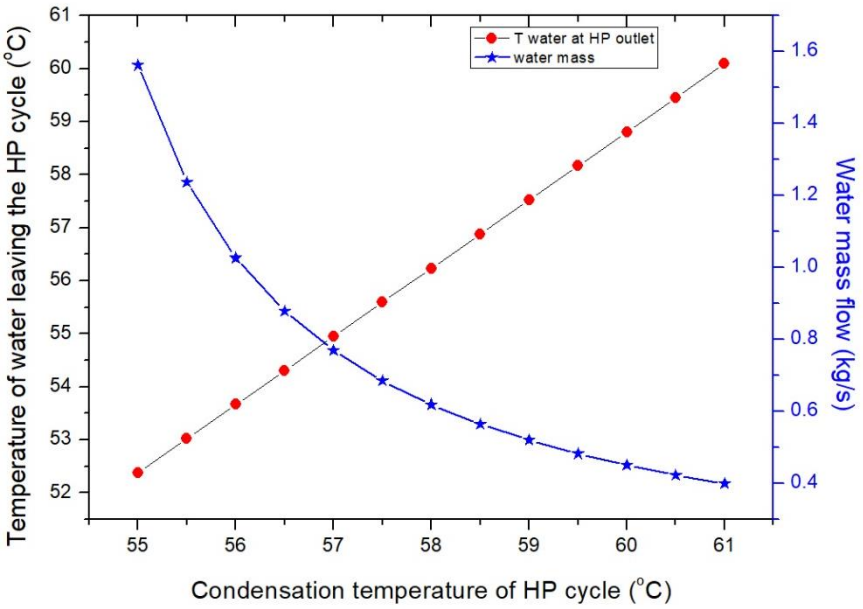

Figure 6.11: Effect of HP condensation temperature on water temperature and mass flow rate.

Figure 6.11 shows the optimization results across the HP condenser. With an increased condensation temperature in the HP cycle, the water mass flow is gradually reduced in order to maintain the minimum PPT across the HP condenser. The figure also shows that the increasing HP condensation temperature results in a linear rise in water temperature at the condenser outlet.

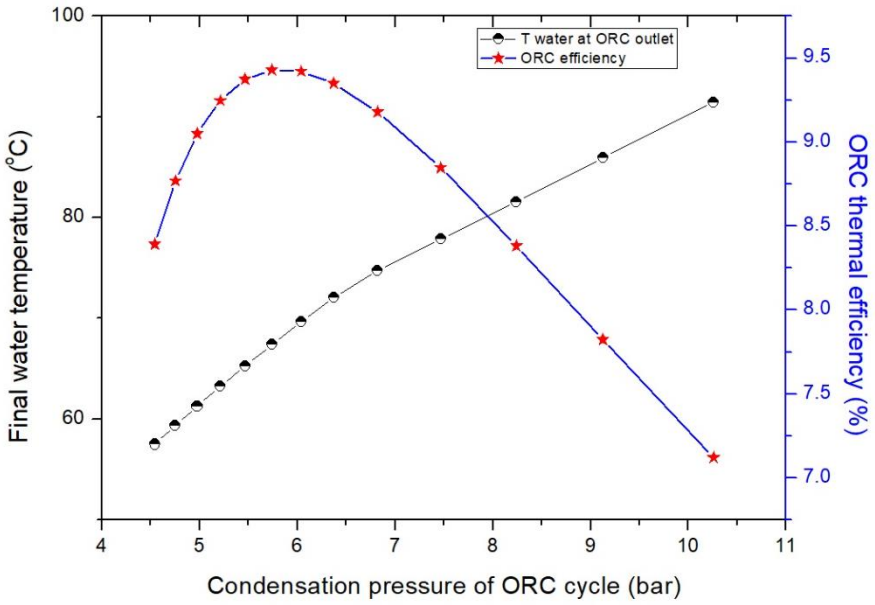

Figure 6.12: Optimization results across the ORC condenser.

Figure 6.12 shows the optimization of the ORC condenser pressure to secure the PPT approach across the ORC condenser. The ORC thermal efficiency increases exponentially to reach a maximum value before declining. As the condenser pressure increases, the ORC cycle pressure ratio is changed accordingly. Therefore, the ORC efficiency will follow the expander's isentropic efficiency performance curve (see Figure 5.22). In this optimization, the final water temperature (80 ^{o}C) is secured at an ORC condenser pressure of 8 bar and an ORC efficiency of 8.5%. Although the efficiency is not at its optimal level (9.5%), the difference can be considered reasonable.

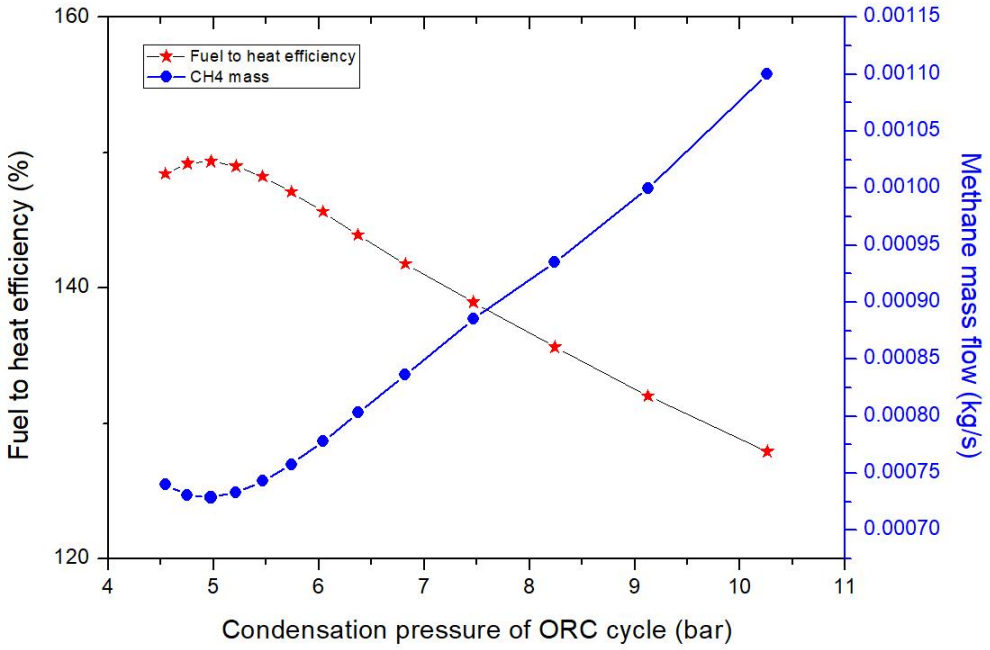

Figure 6.13: Effect of ORC condenser pressure on CH4 mass flow and fuel to heat efficiency.

Figure 6.13 shows the results of the optimization procedure on the overall combined system performance. The figure reveals that with the increase in the ORC condensation pressure, the fuel to heat efficiency declines from its maximum value (149.3%). This behaviour is strongly related to the exponential increase in the Methane mass flow (Figure 6.13) and the ORC thermal efficiency (Figure 6.12). At the condensation pressure of 8 bar which secures the desired outlet water temperature, the fuel to heat efficiency is around 137%.

The steady state results for the combined cycle used for DC cooling with waste heat utilization to provide hot water for central heating are shown in Tables 6.1 and 6.2.

Table 6.1 Combined cycle operating parameters

Parameters	MATLAB CODE		ASPEN PLUSE	
	HP cycle	ORC cycle	HP cycle	ORC cycle
Condenser heat duty, kW	16.553	41.539	16.553	41.541
Evaporator heat duty, kW	12	45.441	12	45.439
Condensation temperature, ^{o}C	59.79	80	59.64	80
Condensation pressure, bar	16.678	7.9	16.679	7.9
Evaporation temperature, ^{o}C	15	159	15	159
Evaporation pressure, bar	4.883	36.5	4.884	36.5
Power produced by the ORC expander, kW	--	-4.553	--	-4.553
Power input to the HP compressor, kW	4.553	--	4.553	--
Work of the liquid pump, kW	--	0.651	--	0.655
Cycle mass flow rate, kg/s	0.0999	0.2413	0.09988	0.24134

Table 6.2 Cycle efficiency (Data center application).

Parameters	MATLAB CODE	ASPEN PLUSE
Heating coefficient of performance COP_h	3.635	3.635
Cooling coefficient of performance COP_c	2.635	2.635
ORC thermal efficiency, %	8.58	8.578
Total heating capacity, kW	58	58.09
Fuel to heat efficiency, %	137	136.9
Mass flow rate of methane, kg/s	9.2164e-04	0.00092247
Air inlet temperature, ^{o}C	25	25
Air outlet temperature, ^{o}C	18	18
Water temperature entering the cycle, ^{o}C	50	50
Water temperature leaving the cycle, ^{o}C	80	80

6.4 Superheating the R134a at the compressor inlet

In practice, it is recommended that the HP refrigerant is superheated before entering the compressor in order to prevent any damage being caused by the wet refrigerant. However, excessive superheat is not a favourable solution because it will increase the compressor's work and consequently reduce the COP. In this case study, the refrigerant is superheated to only 4 ^{o}C, and the temperature of the working fluid at evaporator is set to 17 ^{o}C.

6.5 Control strategies for the combined cycle under variable DC workload

When the DC server heat production decreases as a result of reduced data processing demand, the DC indoor temperature will inevitably decrease. Thus, the heat extracted by the indoor HP evaporator will consequently decline, as shown in Figure 6.14.

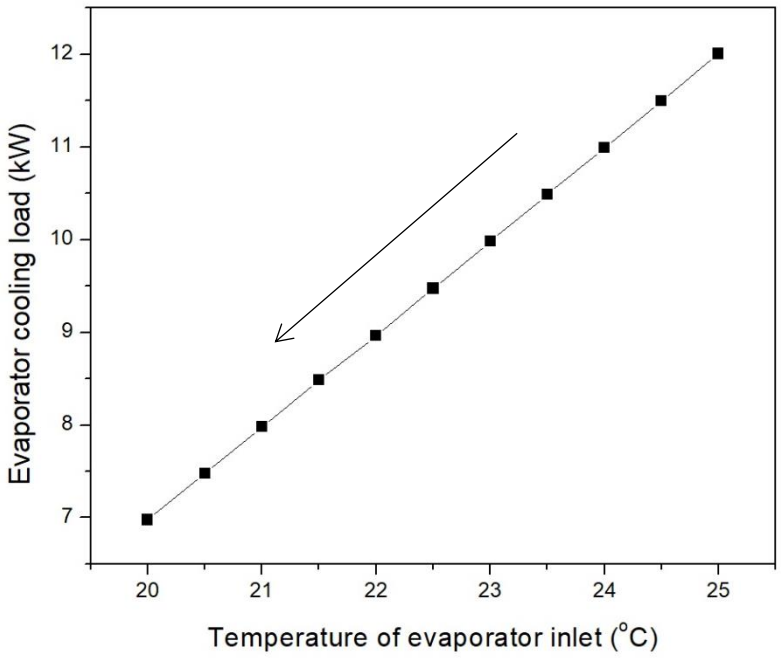

Figure 6.14: Evaporator cooling duty under variable evaporator inlet temperature.

Figure 6.14 shows the variation in the HP evaporator cooling duty when evaporator inlet temperature decline as DC's indoor temperature changes. For instance, when the temperature falls from 25-20 ^{o}C, the DC cooling load production is reduced linearly from 12-6.9 kW under a constant air mass flow of 1.6879 kg/s. From this result, it is clear that the cooling load is highly dependent on the indoor temperature. Thus, a series of control procedures for the combined cycle are proposed to cope with these changes. A control strategy for a HP and ORC cycles can be achieved by optimizing the heat sink, heat source, and refrigerant mass flow [177].

6.5.1 Strategy one: Using the ambient air as a supplementary heat source

As chapter 4 demonstrated, ambient air can provide a free and reliable heat source for the combined system when the air temperature is above 7 ^{o}C. To extract thermal energy from ambient air, an additional external evaporator is proposed for the HP cycle, as shown in Figure 6.15. This unit is installed outside the DC room in order to keep the DC equipment free from dust and pollution, and to prevent any mould formation. In addition, this external evaporator works under different temperatures from the indoor evaporator, at 2.5 ^{o}C or above to avoid frost formation on the unit (as was explained in chapter Four). The R134a mass for the HP cycle flows into the two evaporators through a splitter valve which controls the fraction of the mass for each evaporator. The splitter fraction is determined by the amount of thermal energy extracted by each evaporator. The heat transfer area has been calculated at the maximum thermal capacity for each evaporator, i.e. at the evaporator inlet temperature of 25 ^{o}C for DC, and at 7 ^{o}C for ambient air. In addition, the constant superheat degree is set at the evaporator exit to meet the PPT limitation. Other working conditions and parameters are adopted based on Tables 6.1 and 6.2.

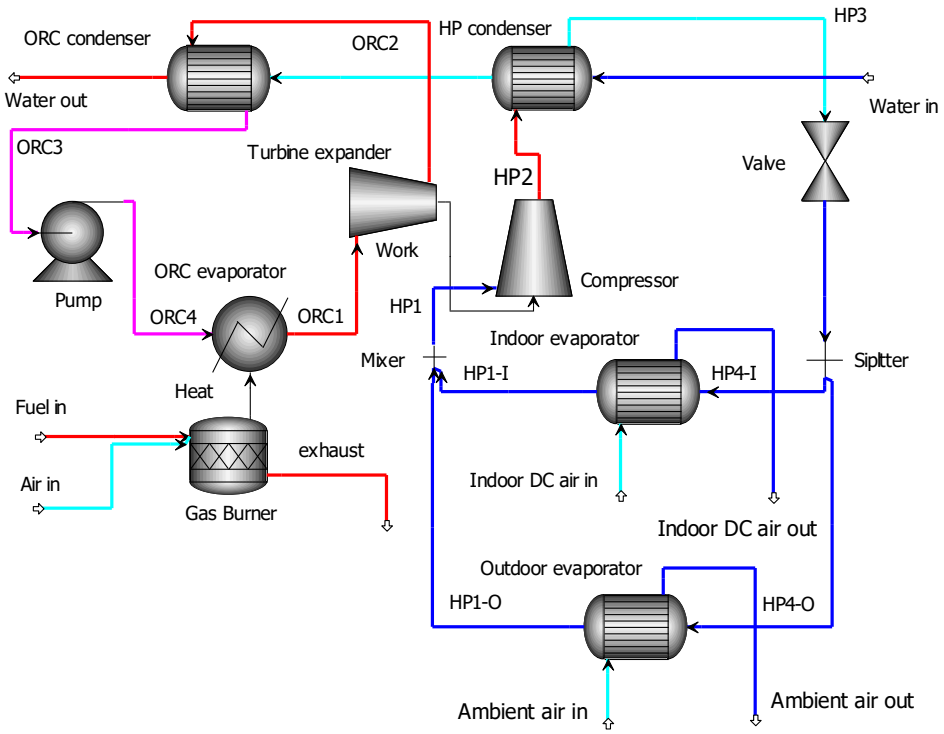

Figure 6.15: Combined cycle configuration with double HP evaporator.

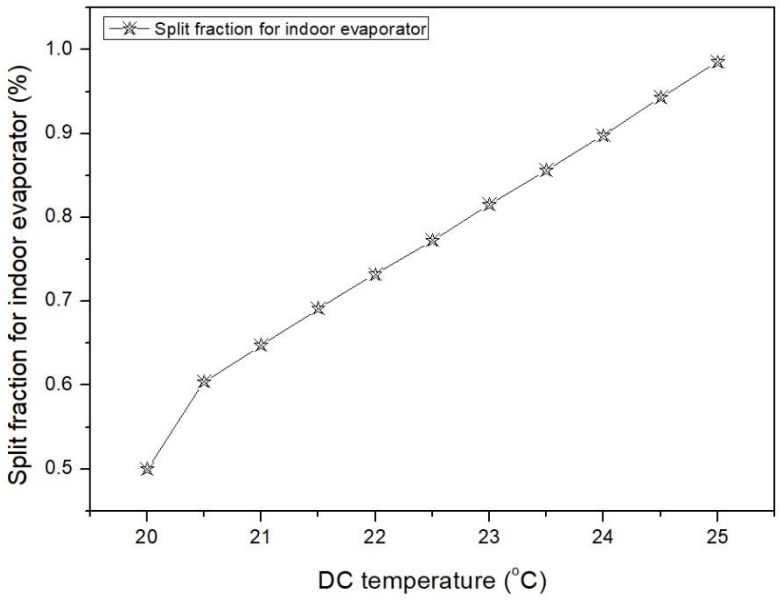

Figure 6.16: Split mass fraction for R134a through the indoor evaporator.

Figure 6.16 shows the percentage of R134a mass flow passing through the indoor evaporator at different DC room temperatures. At the target room temperature of 25 ^{o}C, 100% of the refrigerant mass will be directed to the indoor evaporator. However, as the room temperature falls, more working fluid mass will be directed by the valve splitter to the outdoor evaporator to compensate for the reduction in the thermal energy extracted from the DC with the heat absorbed from the ambient air stream.

The thermal capacities extracted by both evaporators are shown in Figure 6.17. With the fall in DC temperature to below 25 ^{o}C, the thermal capacity of the outdoor evaporator increases gradually in an opposite trend to that extracted by the indoor evaporator. This behaviour is dependent on the mass fraction of the working fluid passing through the evaporator, which is controlled by the valve splitter based on the variations in the DC's indoor temperature.

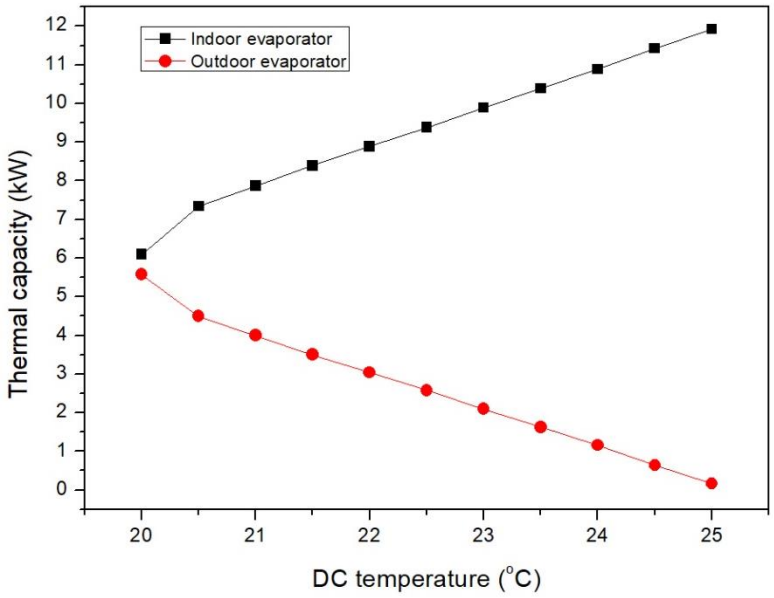

Figure 6.17: Thermal capacities for both HP cycle evaporators.

The total thermal capacity for both evaporators slightly decreases with the reduction in DC temperature, as shown in Figure 6.18. This reduction is associated with a slight reduction in the total heat being added to the water. This occurred because this particular optimization was carried out under constant evaporator areas and a fixed superheat degree at the evaporator exit.

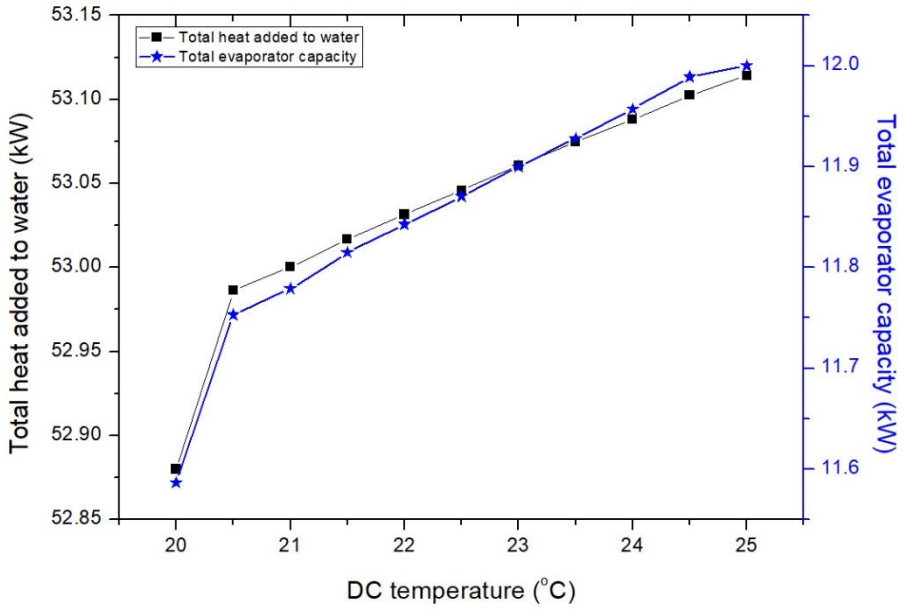

Figure 6.18: Total HP evaporators capacity and total heat added to the water in control strategy one.

The fuel to heat efficiency of the combined cycle in this control strategy is shown in Figure 6.19. With a fall in the DC temperature to below 25 ^{o}C, the fuel to heat efficiency declines from 137% to 134.8% while maintaining a final water temperature of around 80 ^{o}C. This behaviour is expected as the total heat added to the water by the HP cycle has reduced, as illustrated in Figure 6.18.

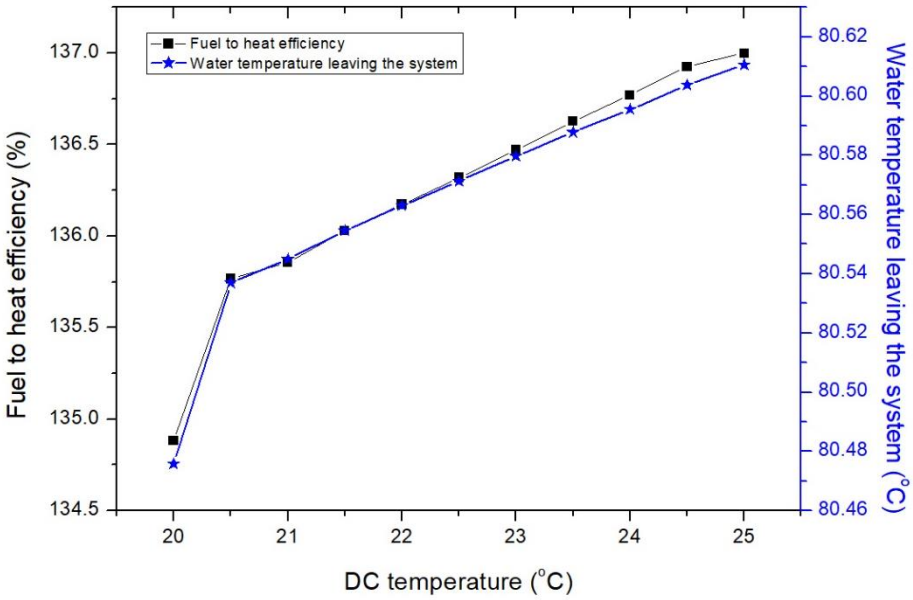

Figure 6.19: Fuel to heat efficiency and final water temperature in control strategy one.

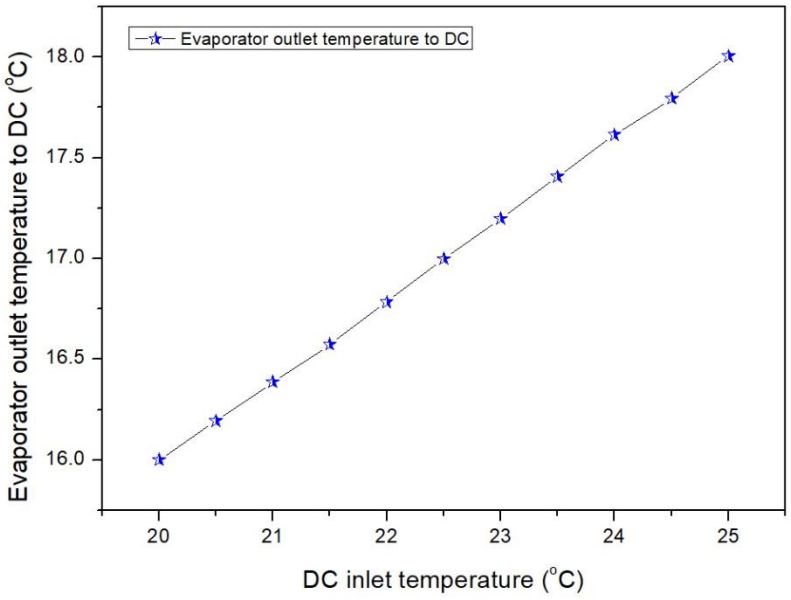

Figure 6.20: Evaporator outlet temperature to DC inlet temperature in control strategy one

Although this control strategy maintains the final outlet water temperature at the designated target with a higher overall fuel to heat efficiency, the evaporator outlet temperature at the DC has declined below the target value of 18 ^{o}C, as shown in Figure 6.20. Other design parameters obtained for the combined cycle are shown in Table 6.3.

Table 6.3 Combined cycle design parameters for control strategy one

Parameters	Values
Evaporation temperature (internal evaporator), ^{o}C	15
Evaporation temperature (external evaporator), ^{o}C	2.5
COPc	2.55
COPh	3.55
ORC thermal efficiency, %	7.9
Evaporator one area, m^2	1.77
Evaporator two area, m^2	1.77
R134a temperature at internal evaporator exit, ^{o}C	17
R134a temperature at external evaporator exit, ^{o}C	6

6.5.2 Strategy two: Using an exhaust stream as a supplementary heat source

In this strategy, the reduction in the DC load is proposed to be substituted by the heat available in the exhaust stream in order to keep the combined cycle working under conditions of constant heat capacity. This can be achieved by installing a small heat exchanger between the suction line and the compressor, as shown in Figure 6.21.

When the indoor DC temperature falls, the heat extracted by the HP evaporator will consequently reduce. Therefore, the fuel mass flow is proposed to be increased to produce excess thermal energy in the burner exhaust stream. This extra heat will be used to superheat the refrigerant in the superheat heat exchanger (HX). A PID controller is used to maintain the refrigerant superheat degree at the compressor inlet at a constant value. In this strategy, the temperature of the refrigerant at the compressor inlet is set to around 17 ^{o}C, as shown in Figure 6.22.

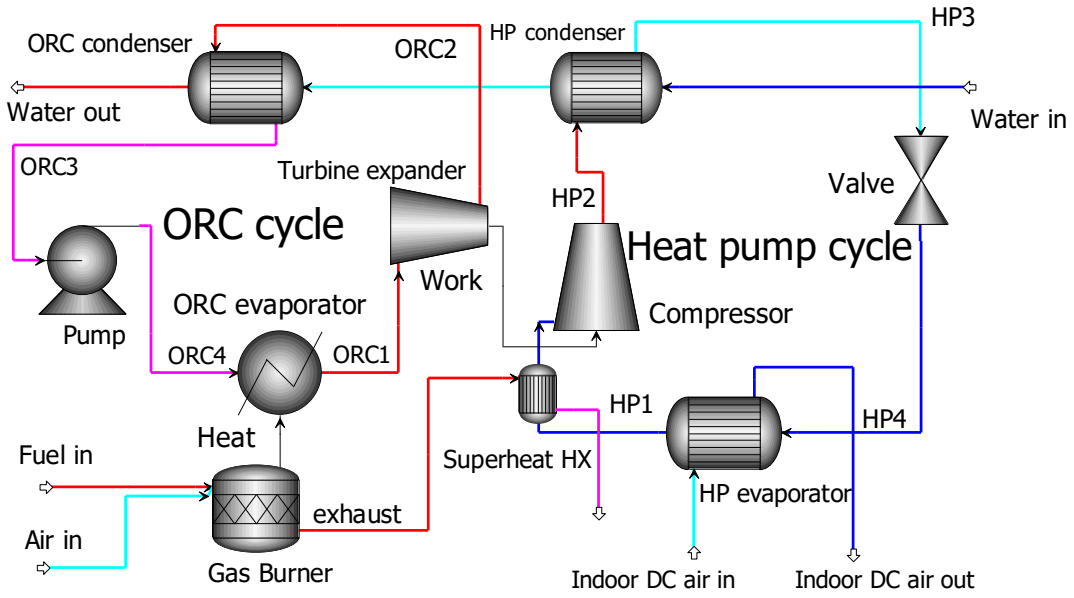

Figure 6.21: Combined cycle configuration with superheat heat exchanger.

The control process is carried out when the DC inlet temperature varies from 20-25 ^{o}C. Therefore, the area of the small HX is calculated and fixed when the DC inlet temperature is 20 ^{o}C, which is equal to 0.32 m^2.

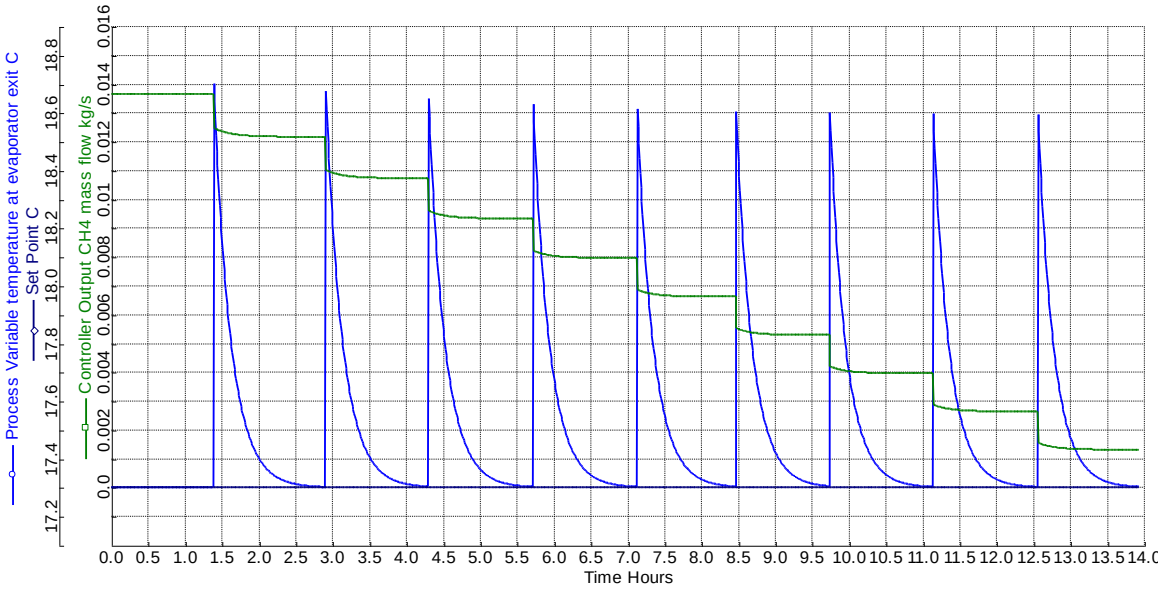

Figure 6.22: PID controller performance in control strategy two.

Figure 6.22 shows the PID controller performance when the DC temperature increases from 20-25 ^{o}C. The blue line represents the (PV) R134a temperature before entering the compressor, and the green line shows the Methane mass flow in the gas burner. When the DC inlet temperature ranges from 20-20.5 ^{o}C, this leads to an increase in the refrigerant temperature from the set point of 17.3 to 18.6 ^{o}C, which could increase the evaporator pressure and hence reduce the HP efficiency. Therefore, the PID controller adjusts the Methane mass flow to reduce the refrigerant temperature to the set point. By adapting this procedure, the evaporator pressure is maintained at a constant level, and hence the HP cycle performance is stabilized.

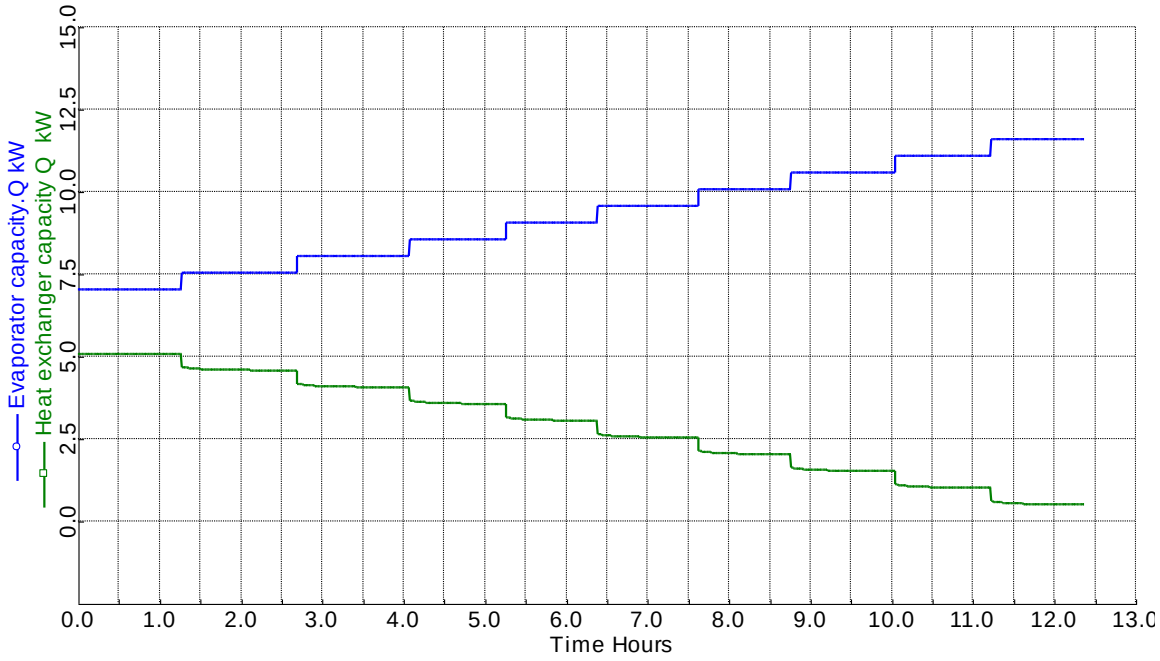

Figure 6.23: HP cycle heat exchangers capacities in control strategy two

With the change in the DC inlet temperature there is a corresponding decline in the HP evaporator capacity, which is assumed to be substituted by the superheat HX, as shown in Figure 6.23. For instance, at a DC temperature of 20 ^{o}C, the evaporator capacity is around 7 kW and the superheat HX capacity is approximately 5 kW. Thus, the total heat capacity for both exchangers is 12 kW, which is the design target. In contrast, when the DC temperature is 25 ^{o}C, the target total heat capacity is almost completely provided by the HP evaporator, and the superheat HX contribution is consequently limited.

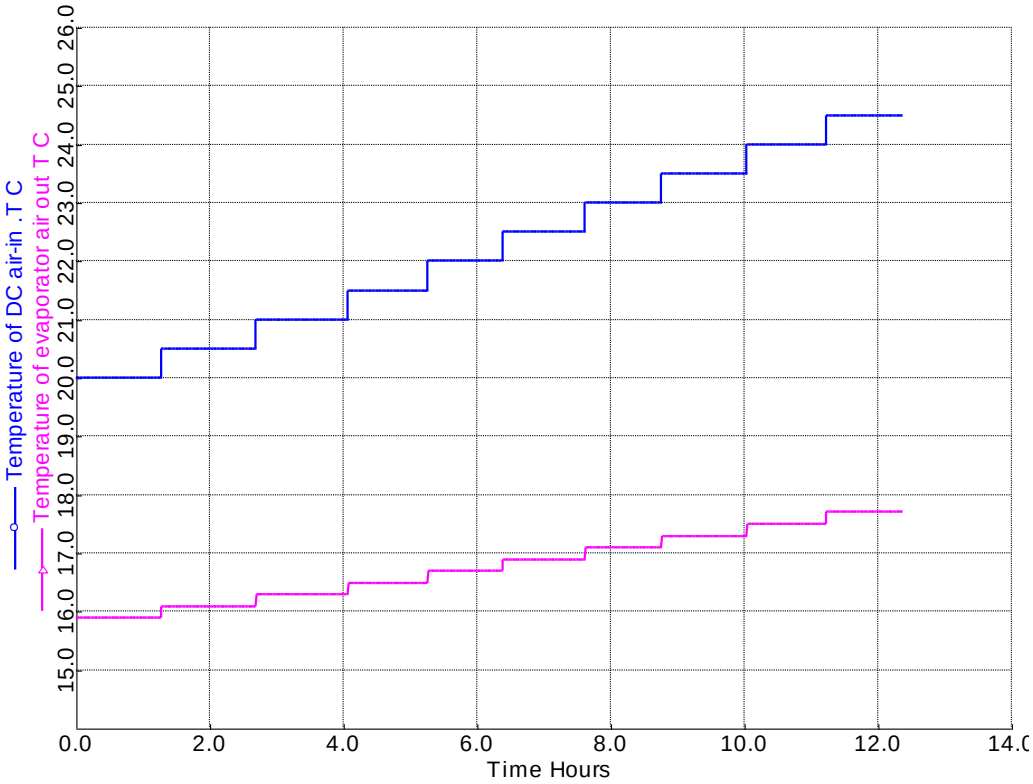

Figure 6.24: DC inlet and outlet temperature in control strategy two

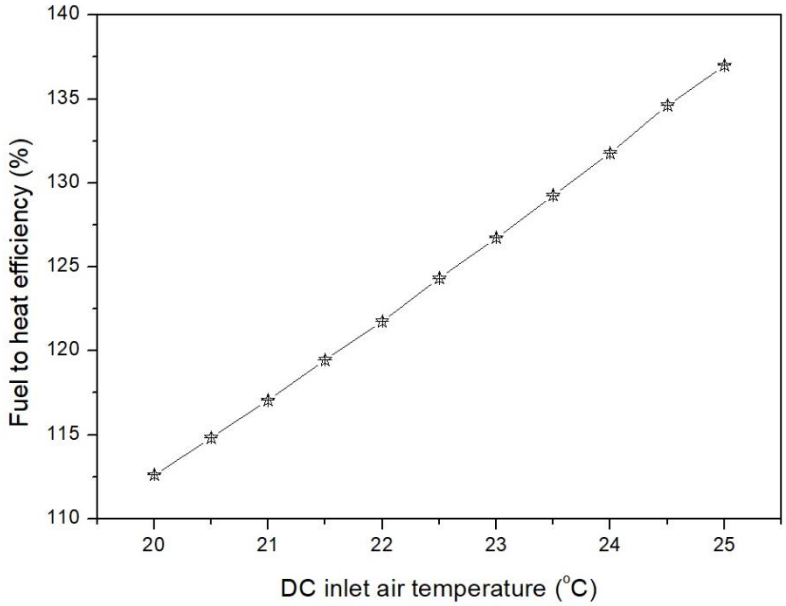

Figure 6.25: Fuel to heat efficiency in control strategy two.

Although the total heat capacity provided by the heat pump cycle by both heat exchangers is maintained at a constant of around 12 kW, the DC outlet temperature drops below the target value of 18 ^{o}C, as shown in Figure 6.24.

The fuel-to-heat efficiency in this control strategy is expected to decline with the rise in Methane mass flow as a consequence of the fall in the DC inlet temperature, as shown in Figure 6.25. For example, the achieved fuel to heat efficiency when the DC temperature is 20 ^{o}C is around 112 %. In contrast, control strategy one has been shown to have achieved significantly high efficiency (134.8%) at this temperature value.

6.5.3 Strategy three: Adjusting the combined cycle heating capacity

In this approach, the refrigerants mass flow rate for all cycle components (except air) is optimized to compensate for the reduction in DC workload. This optimization aims to maintain nearly constant overall system performance in terms of fuel to heat efficiency and of an outlet water temperature of 80 ^{o}C.

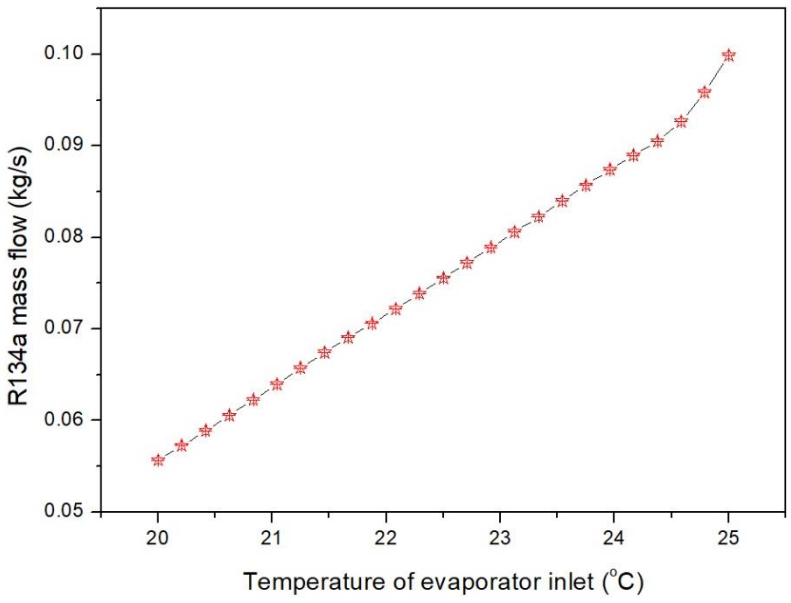

Figure 6.26: R134a mass flow optimization in control strategy three.

Figure 6.26 shows the iteration of the R134a mass flow of the HP cycle when the DC's indoor temperature falls from 25-20 ^{o}C. The optimization is carried out under a constant superheat degree of 17 ^{o}C at the evaporator exit. The results show that the mass flow rate declines linearly between 0.099 to 0.055 kg/s as the temperature drops from 25 to 20 ^{o}C.

Based on Figure 6.14, the HP evaporator cooling load declines linearly with the reduction in the DC's indoor temperature. Thus, the work of the compressor and the condenser capacity are both expected to decline.

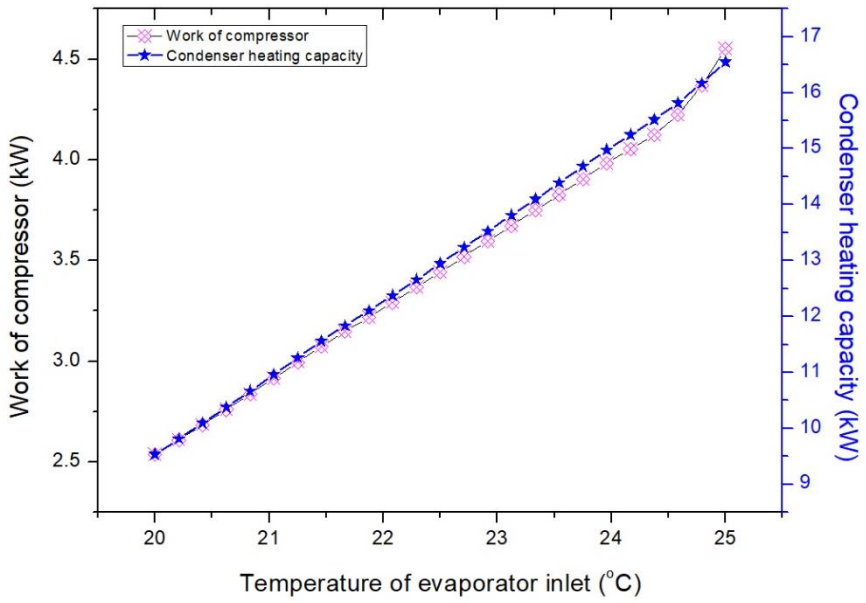

Figure 6.27: HP compressor work and condenser heat capacity in control strategy three.

With the reduction in the HP refrigerant mass flow rate (Figure 6.26), the work of the compressor declines from 4.5 to 2.5 kW. Similarly, as the DC cooling load drops from 12 kW (100%) to 6.97 kW (58%), as illustrated in Figure 6.14, the HP condenser heating capacity decreases from 16.5 to 9.5 kW, as shown in Figure 6.27.

As the HP compressor work decreases, and due to the direct coupling of the ORC turbine to the HP compressor, the amount of mechanical work needed from the ORC cycle will correspondingly fall. Thus, the ORC cycle refrigerant mass flow will need to be optimized.

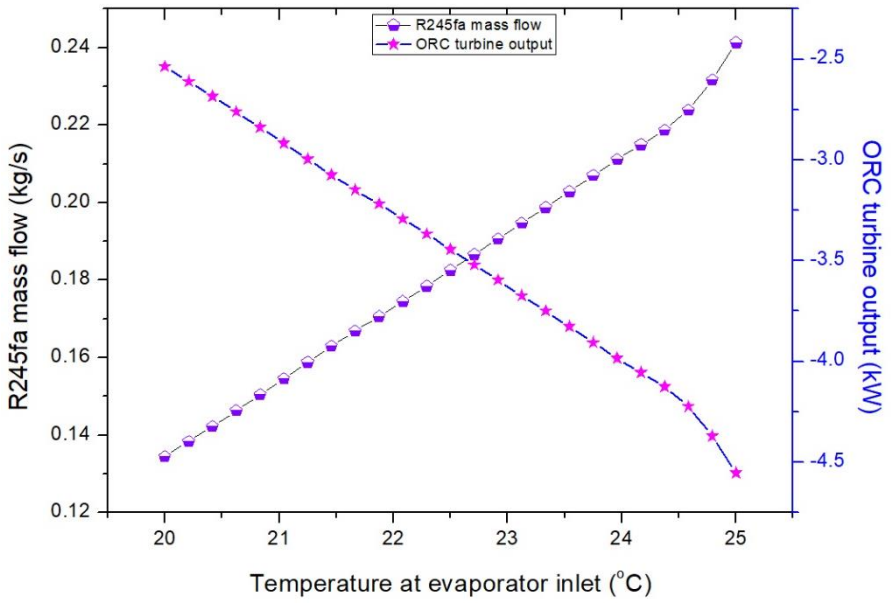

Figure 6.28: Optimization of R245fa mass flow and ORC expansion power in control strategy three.

Figure 6.28 shows the optimisation of the R245fa mass flow and the turbine power for the ORC cycle. When the DC workload varies, the R245fa mass flow falls from 0.24 to 0.13 kg/s with a corresponding reduction in turbine power production from 4.5-2.5 kW, which is equal to the HP compressor work consumption shown in Figure 6.27.

To maintain a constant outlet water temperature of 80 ^{o}C, the water mass flow rate is adjusted to compensate for the reduction in thermal energy rejected by the HP and ORC condensers, as shown in Figure 6.29.

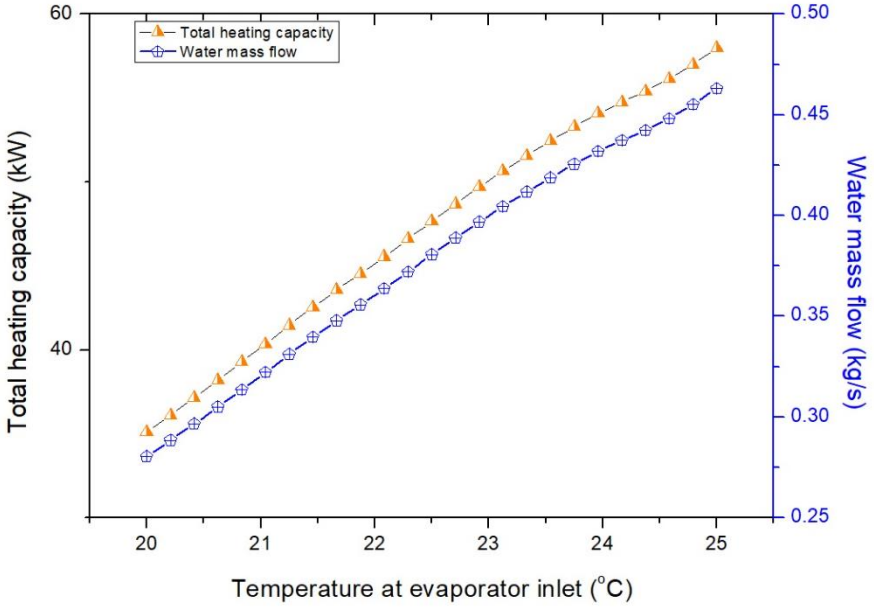

Figure 6.29: Total system heating capacity and water mass in control strategy three.

Figure 6.29 shows that the water mass is reduced from 0.46 to 0.28 kg/s with a corresponding reduction in total system heat capacity from 58 to 35.1 kW. Although the heating capacity is lower, the fuel to heat efficiency is maintained at a nearly constant 137 %. In addition, this approach has maintained a hot water supply of 80 ^{o}C and an evaporator outlet temperature of around 15-18 ^{o}C, as shown in Figure 6.30.

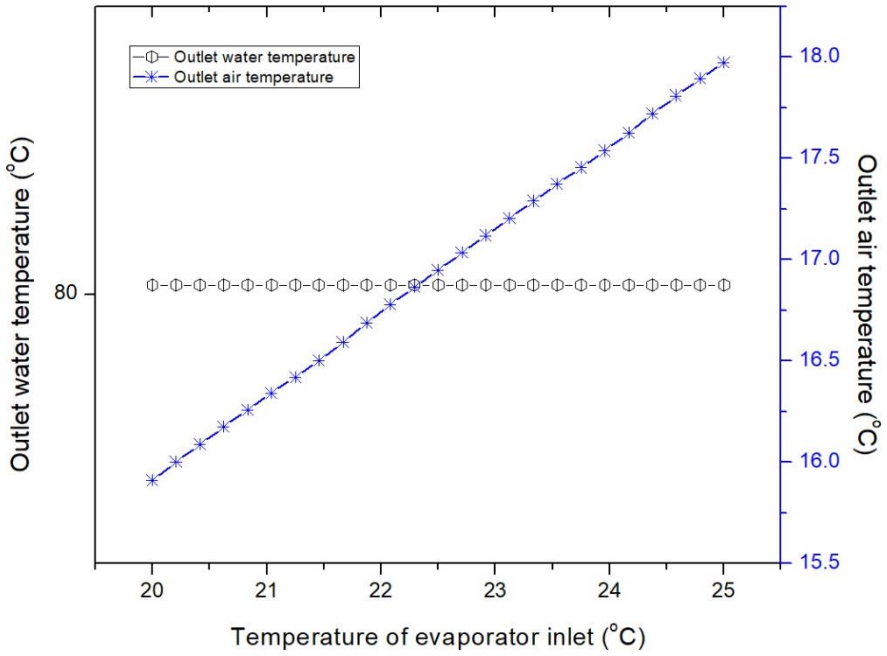

Figure 6.30: Outlet water temperature and air temperature as per variations in the inlet evaporator temperature.

When the DC temperature falls below 20 ^{o}C, the minimum pinch point temperature difference (3 ^{o}C) between the air inlet temperature and the refrigerant at the evaporator exit is violated. Therefore, the heat available in the exhaust gas burner can be deployed to superheat the working fluid to 17 ^{o}C using a small heat exchanger, as demonstrated in control strategy two.

In this design, the mass flow rate of the working fluids in each cycle is set to remain constant at the values obtained when the inlet temperature is 20 ^{o}C. The results of this approach are shown in Table 6.4.

Table 6.4 Combined system results in control strategy 3 for DC temperature below 20 ^{o}C.

Temperature at evaporator inlet, ^{o}C	Superheat HX capacity, kW	Evaporator capacity, kW	CH_4 mass flow, kg/s	Fuel to heat efficiency, %	Temperature of air outlet, ^{o}C
19.5	0.4575579	6.5043218	0.000506	131.287	15.68356
19	0.9616085	6.0002712	0.000516	126.988	15.47928
18.5	1.4587681	5.5031116	0.000527	122.9	15.27096
18	1.9573035	5.0045763	0.000537	118.978	15.06346

From Table 6.4, it can be noted that with the decline in the inlet evaporator temperature towards 18 ^{o}C, the evaporator capacity falls by approximately 1.5 kW. This reduction in thermal capacity is compensated by the heat recovered from the burner exhaust flue gas. Thus, the system heating capacity is maintained at a constant level. However, the fuel to heat efficiency has declined from approximately 131-118.9 %, due to an increase in the CH_4 mass flow from 0.0005-0.000537 kg/s to produce more heat for extraction in the flu gases. This approach has achieved a constant hot water supply of 80 ^{o}C with a DC outlet temperature of 15 ^{o}C.

6.5.4 Strategy four: Optimizing indoor air mass flow.

In this approach, the DC air mass flow is iterated to compensate for variations in the DC work-load. The system thermal capacity is proposed to be kept constant by maintaining a steady re-frigerant mass flow for all cycle components.

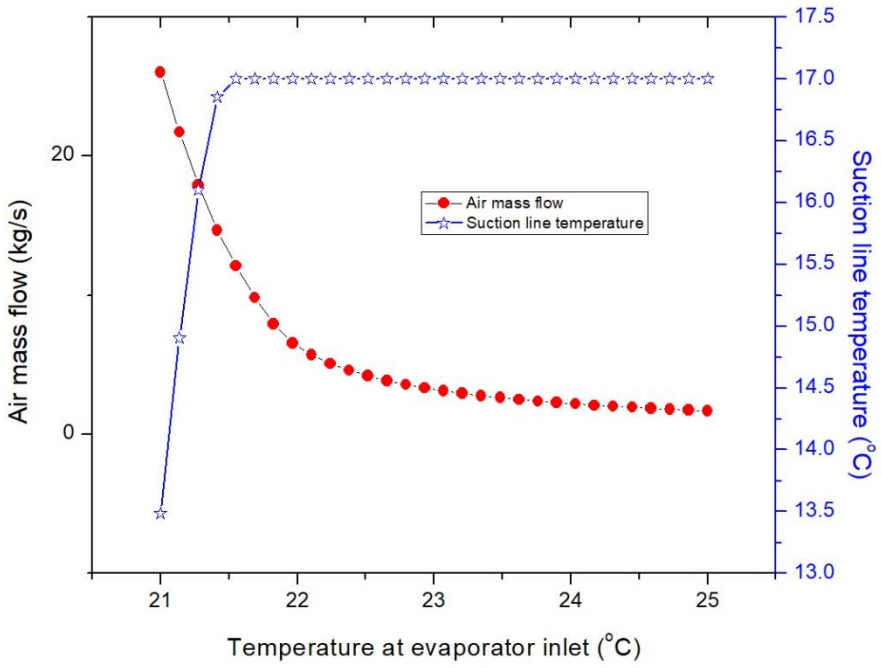

Figure 6.31: Effects of optimizing air mass flow on suction line temperature in strategy four.

Figure 6.31 shows that with a falling DC temperature, the air mass flow had to be increased to supply the evaporator with the thermal energy required to keep the system running with the same heating capacity. It can be noted that despite the decrease in the DC temperature from 25-21.5 ^{o}C, the temperature of the R134a at the evaporator exit is maintained at 17 ^{o}C by increasing the DC air mass flow from 1.6879 to 13 kg/s. However, when the falling DC temperature reaches 21 ^{o}C and below, increasing the mass flow to 26 kg/s is insufficient to superheat the R134a at the evaporator exit to the desired value.

The DC outlet temperature in this strategy is in the range of 18-20.5 ^{o}C when the DC inlet temperature is in the range of 25-21.5 ^{o}C, as shown in Figure 6.32. This outlet temperature is still within the desired target.

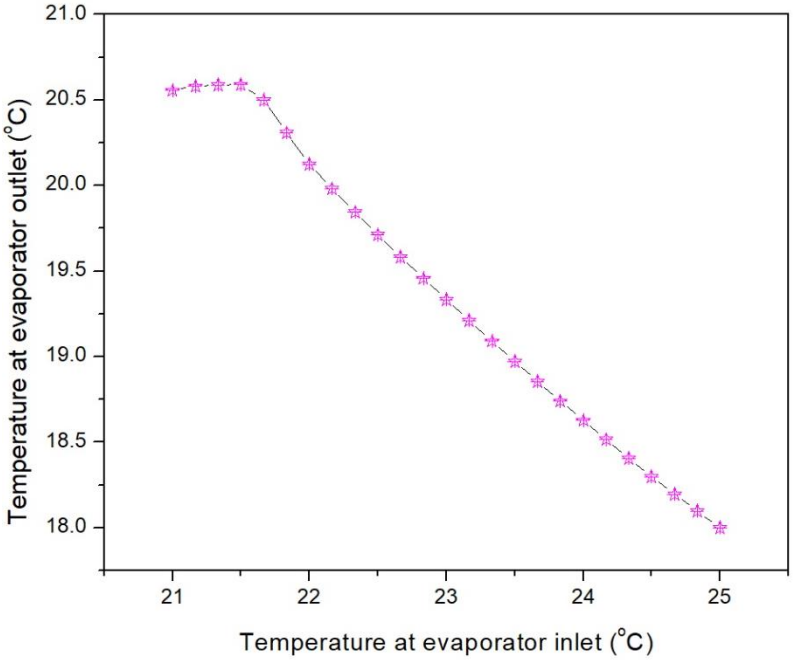

Figure 6.32: DC room temperatures obtained from the fourth approach.

Based on these two Figures, it is evident that when the DC inlet temperature drops below 21.5 ^{o}C, the air mass flow needs to be increased significantly. In addition, the temperature difference of the air stream across the evaporator is reduced. Therefore, not enough heat is available for extraction and at this temperature value, superheating the refrigerant is necessary by extracting heat from the burner exhaust stream using the superheat heat exchanger as per strategy two.

By using the flue gases as a heat source to superheat the refrigerant to 17 ^{o}C, the air mass flow is set as constant at the value obtained when the DC inlet temperature is 21.5 ^{o}C, which is 13 kg/s.

Similar to strategy two, the reduction in the HP evaporator capacity is proposed to be substituted by the capacity provided by the superheat heat exchanger.

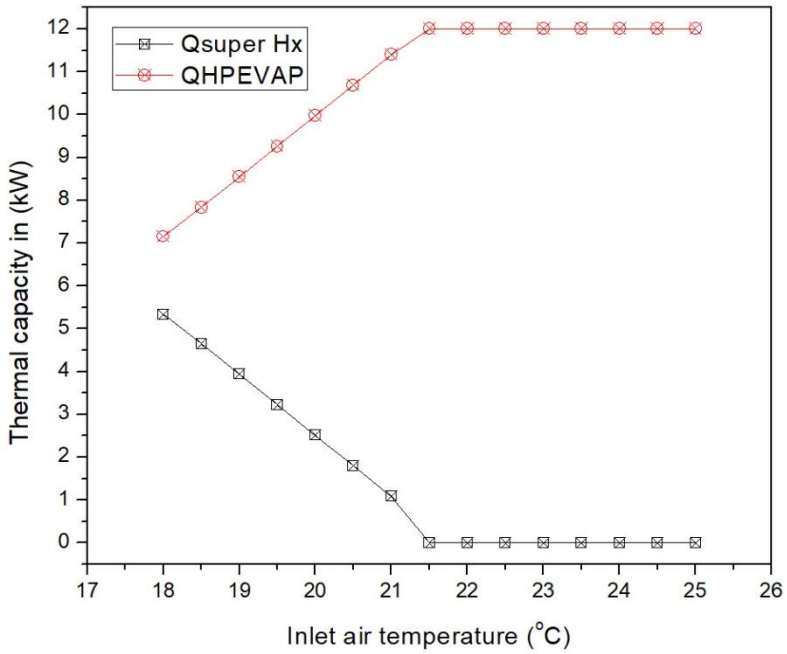

Figure 6.33: Evaporator and superheat heat exchanger thermal capacities for fourth approach.

Figure 6.33 shows the changes in the thermal capacities of the HP evaporator and the superheat heat exchanger when the DC inlet temperature drops below 25 ^{o}C. When the evaporator inlet temperature falls from 25-21.5 ^{o}C, the evaporator's thermal capacity is maintained at a constant 12 kW as a result of optimizing the air mass flow. However, when the temperature drops below 21.5 ^{o}C, the decline in the thermal capacity is compensated by an equivalent capacity obtained from the superheat HX. Thus, the overall HP capacity is maintained at a constant level, set at the desired target.

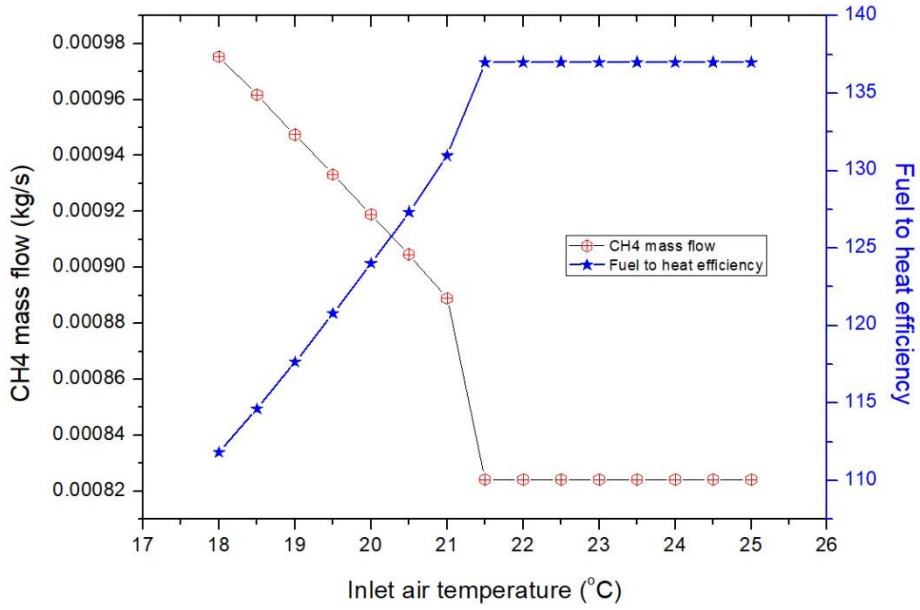

Figure 6.34: Methane mass flow and fuel to heat efficiency for the fourth approach.

Figure 6.34 shows that with the fall in DC temperature, the fuel mass flow increases from the steady state value to 0.000975401 kg/s to produce the required thermal energy to feed the ORC evaporator and superheat exchanger. As a result, the overall fuel to heat efficiency falls from 137 to 111.8%.

In this design, the total heating capacity of the system is maintained at a constant level, and the final water temperature is kept at 80 ºC.

6.6 Conclusion

In this chapter, a gas driven combined HP-ORC cycle was numerically investigated for the purpose of data centre (DC) cooling, with waste heat utilized to provide a central heating supply. A comprehensive assessment was conducted in terms of design configuration, best theoretical performance, and the control strategies needed to maintain optimal system performance despite fluctuations in DC workload.

When the DC operates at its maximum thermal workload (12 kW), the combined system has provided a cooling effect by pumping wasted heat from the DC and maintaining the indoor temperature at between 18-25 ^{o}C. This extracted heat has been recovered to provide central heating by lifting returnee water from 50-80 ^{o}C. The overall fuel to heat efficiency achieved is 137%. When the DC workload varies, four control strategies are proposed to maintain the DC indoor temperature within the target range. Additional heat extracted from ambient air was proposed as a substitute for the reduction in thermal capacity of the DC while maintaining steady fuel to heat efficiency. However, the potential of this strategy is limited by the temperature of the outdoor environment. Alternatively, the thermal energy contained in the flue gases can be used to compensate for the decline in HP evaporator duty. In this proposed strategy, Methane mass flow consequently increases, resulting in lower fuel to heat efficiency (112 %). In both these strategies, the total heating capacity of the combined system is maintained at a constant level (58 kW). However, in the third control strategy, the total capacity was reduced by adjusting working fluids (water, R134a and R245fa) mass flow to maintain an optimum level of fuel to heat efficiency. The DC indoor air mass flow can be adjusted to increase heat extraction when the DC indoor temperature drops below 25 ^{o}C. This mechanism is valid in a limited DC indoor temperature range (25- 21.5 ^{o}C). In both strategies three and four, when the proposed mechanism is limited, heat from flue gases can be used to overcome the reduction in thermal energy at the expense of the fuel to heat efficiency.

Chapter 7 Bottoming ORC-HP cycles with DE for refrigeration effects

7.1 Introduction

In the previous chapters, the combined ORC-HP system was used to provide hot water by utilizing the ambient air or wasted heat from the data centre as a heat source for the heat pump cycle. In addition, the wasted heat from the ORC condenser and the gas burner exhaust stream were recovered to further enhance the system's overall thermal efficiency. The results showed that this system can achieve a high fuel to heat efficiency compared with conventional heating technologies. In this chapter, the proposed cycle is used to provide a refrigeration load by recovering the wasted heat from a diesel engine exhaust stream. A steady state thermodynamic evaluation under rated diesel engine working conditions is conducted for the combined system. In addition, the effects of variable expander power due to variable diesel engine working conditions are investigated. Furthermore, a control strategy for the HP to cope with variations in diesel engine working conditions is also considered.

7.2 The concept

The rejected thermal energy from the diesel engine via the exhaust stream (DE exhaust in) is used to power the ORC power generator cycle to produce mechanical work. This work is utilized to drive a vapour compression heat pump cycle. The heat pump cycle is used to provide cold air at around -18 ^{o}C for refrigeration purposes. The low-grade heat from both the ORC and HP cycle is rejected to the environment. A configuration of the combined cycle is shown in Figure 7.1.

7.3 Modelling the combined system for diesel engine rated condition

In practice, to adapt to a variable power demand, a diesel engine can produce variable power by changing the fuel mass flow and hence the crankshaft rotation speed. The consequences of that include variable exhaust stream thermal power (mass flow and temperature). However, when the DE power production meets the demand, the DE is said to work in rated condition. In

this section, the combined system is modelled for the DE rated condition taken from experimental results in the literature [45].

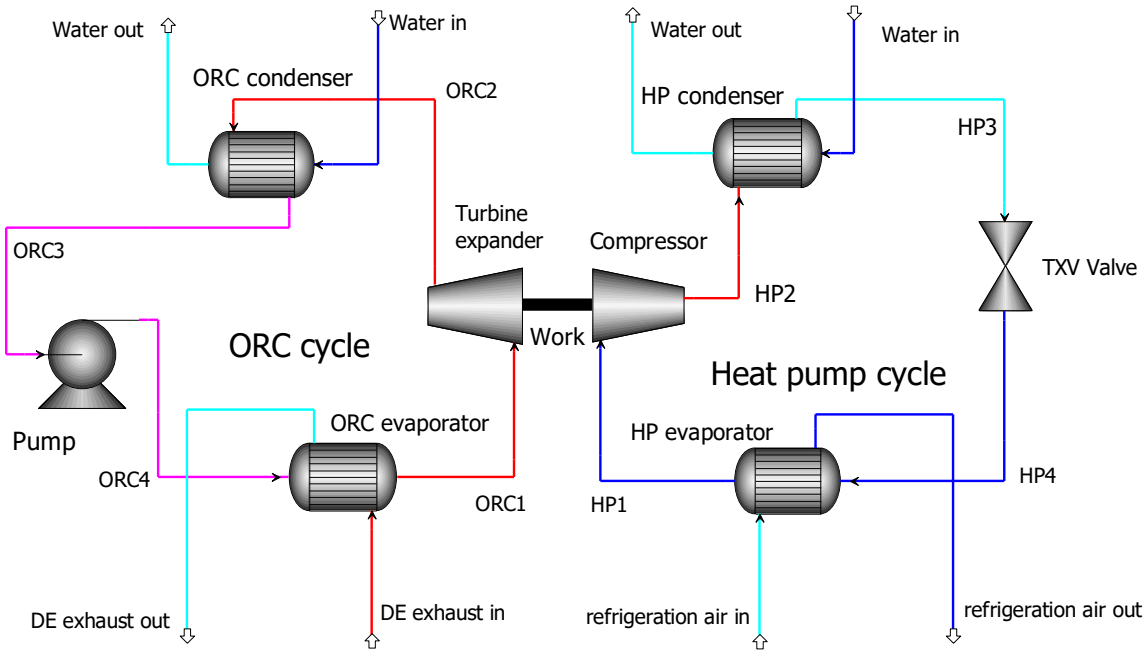

Figure 7.1: Combined system configuration for recovering heat from the diesel engine exhaust stream.

7.3.1 Modelling the heat source

The mass fraction of the chemical composition of the exhaust stream adapted from Yu, G. et al. [45] are as follows: CO_2= 0.151, H_2O= 0.055, N_2= 0.716, O_2= 0.078. Under the DE rated condition, the exhaust stream temperature is 519 ^oC and the mass flow is 0.2752 kg/s. By identifying the optimum temperature at the DE exhaust stream out as shown in Figure 7.1, the total thermal capacity of the heat source can be estimated. The optimal temperature value occurs when the exhaust stream is kept in the vapour state to avoid corrosion in the ORC evaporator caused by vapour condensation. Therefore, initial calculations have been made for this purpose.

Figure 7.2 shows the changes in the vapour fraction of DE exhaust out and the ORC evaporator thermal capacity due to a reduced exhaust stream temperature. The figure shows that when the stream temperature falls from 200 ^oC, the exhaust stream is kept in a vapour state. In addition,

the ORC evaporator capacity is significantly increased. However, at a stream temperature below 50 °C, the exhaust stream starts to change into a two phase flow due to the condensation effect. Therefore, the DE exhaust out temperature is set to 50 °C for further evaluation.

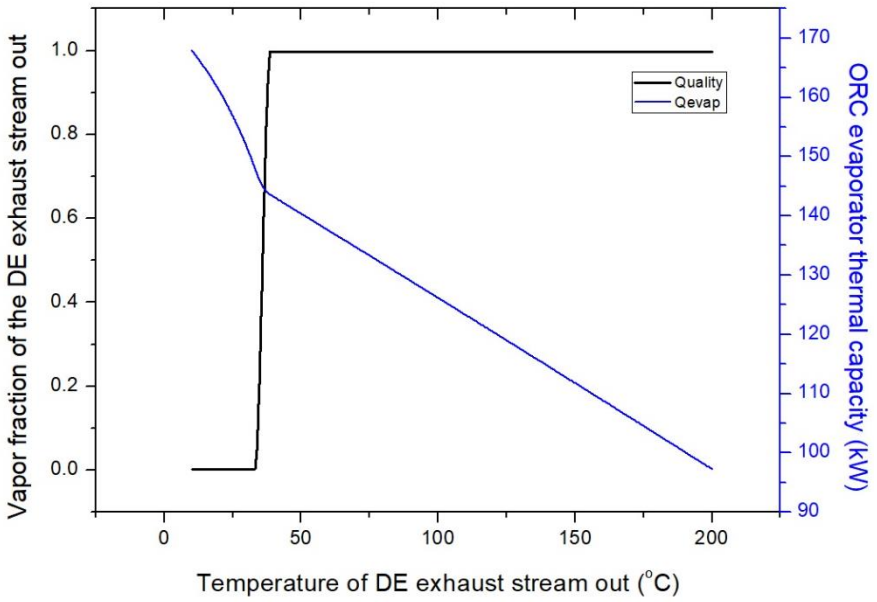

Figure 7.2: Relation between vapour fraction and ORC evaporator capacity under variable temperatures of the DE exhaust stream out.

7.3.2 Optimizing the combined system under variable ORC mass flow

In this evaluation, the ORC mass flow is optimized under the assumption of constant heat source thermal capacity in order to study its effects on the combined system performance. The adapted refrigerant for the ORC cycle is R245fa, and the evaporation pressure is set at 36.5 bar. For the HP cycle, an evaporation temperature of -21 °C is adopted to produce air at a temperature of -18 °C, as recommended for the refrigeration application. For both cycles, the condensation temperature is assumed to be as low as possible to improve both cycle efficiencies. By assuming the sink stream is a sea or cold tap water, the adapted condensation temperature is 25 °C. Constant isentropic efficiencies of 70% for the compressor and expander and 90% for the liquid pump are adopted.

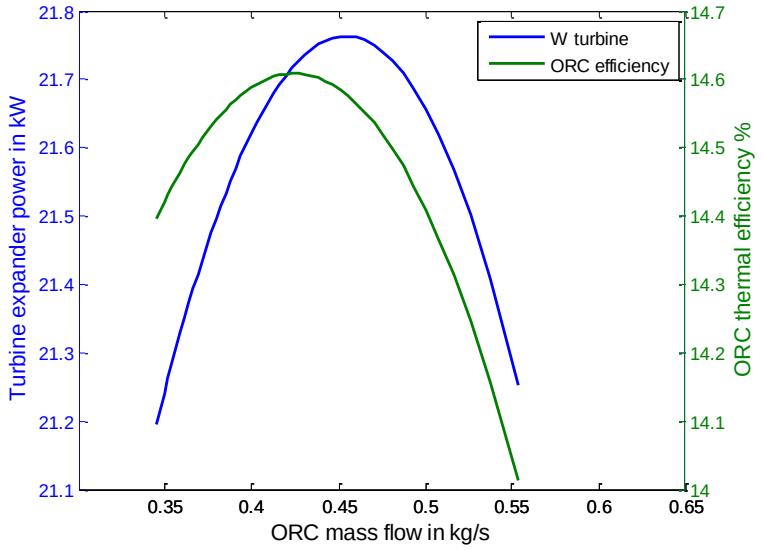

Figure 7.3: Relation between ORC expander power and thermal efficiency under variable ORC mass flow.

Figure 7.3 shows the changes in ORC turbine power and thermal efficiency when the ORC mass flow increases. It shows that an increasing mass flow under constant heat source thermal capacity causes an exponential increase then a decrease in both designed parameters. This indicates that at each parameter's maximum values, no more heat is available in the heat source

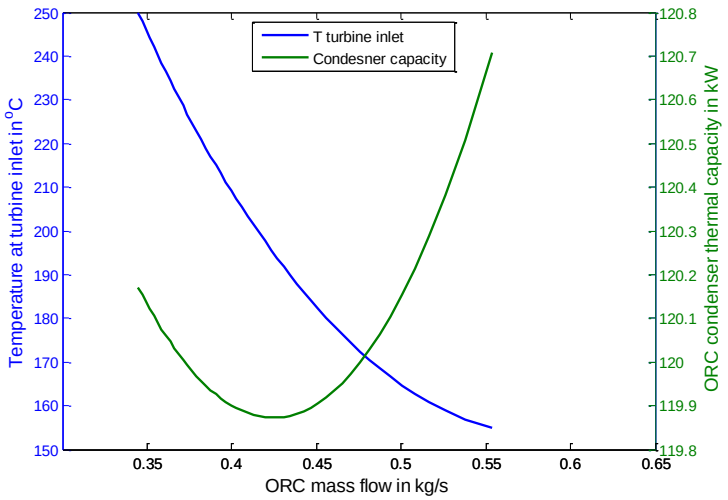

Figure 7.4: Relation between ORC turbine temperature and condenser thermal capacity under variable ORC mass flow.

to evaporate the extra mass flow. Turbine power reaches its maximum value at a different ORC mass flow than that needed for thermal efficiency.

Figure 7.4 demonstrates the behaviour of refrigerant temperature at the expander inlet and the ORC condenser capacity when the R245fa mass flow is increased. The figure shows that the refrigerant temperature declines with a rise in mass flow due to the constant heat source capacity. Similarly, the condenser capacity initially falls to its lowest value at a specific mass value then increases again after that. Minimizing the condenser capacity supports the cycle efficiency, as shown in Figure 7.3.

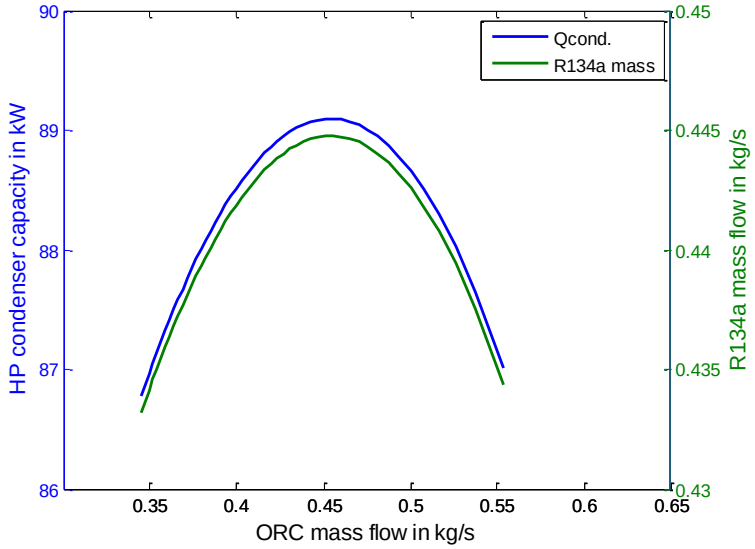

Figure 7.5: Relation between HP condenser thermal capacity and R134a mass flow under variable ORC mass flow.

Figure 7.5 shows the changes in the HP condenser capacity and the HP working fluid mass flow as a function of varying the ORC mass flow. Both increase exponentially, with a linear increase in the ORC mass flow up to maximum values of around 0.45 kg/s. The rise in the condenser capacity is in response to the increase in the HP refrigerant mass flow. Both parameters reach optimum performance when the turbine achieves its maximum value, as shown in Figure 7.3.

Figure 7.6 shows the variations in HP evaporator capacity and the conversion ratio when the ORC mass flow increases. The conversion ratio is the ratio between the thermal capacities of the ORC and HP evaporators. The results show that both parameters increase in a similar

manner to the R134a mass flow in Figure 7.5. The R245fa mass flow of 0.45 kg/s secures the maximum HP condenser capacity, R134a mass flow, and HP evaporator capacity, as well as the maximum energy conversion ratio.

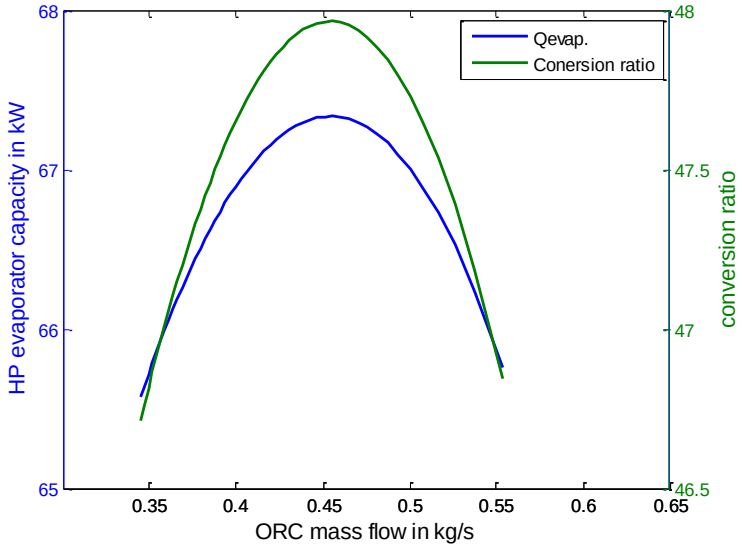

Figure 7.6: Relation between HP evaporator thermal capacity and conversion ratio under variable ORC mass flow.

7.3.3 The effects of superheating the refrigerant at the ORC evaporator exit

It has been widely cited in the literature that adding more heat to the ORC cycle by superheating the refrigerant at the turbine inlet has many advantages. These can include keeping the refrigerant in a vapour state at the turbine inlet and outlet (especially with wet refrigerants) and recovering more heat from the heat source, which consequently produces more mechanical power. In this section, a degree of superheat temperature will be added to the refrigerant to study the effects of this action on the combined system performance. The optimization process is conducted under a constant pinch point temperature (30 ^{o}C) at the evaporator inlet and by assuming constant condensation pressure. In this approach, the range of superheat degree is initiated from the refrigerant critical temperature value to the maximum applicable temperature adopted from REFPROP.

Figure 7.7 shows the effects of increasing the degree of refrigerant superheat at the turbine inlet on the expander power and cycle mass flow. The figure shows that increasing the working fluid

temperature causes a slight and gradual rise in expander power from 22.1-22.65 kW due to the rise in the enthalpy difference across the turbine. In the pinch point temperature optimization process of the ORC evaporator, the mass flow of the heat source stream is commonly optimized. However, in this model, the mass flow of the ORC is optimized instead, as heat source quantity and quality are assumed to be constant in the rated condition of the DE. The optimized working fluid values fall from 0.59 kg/s to 0.52 kg/s as shown in Figure 7.7.

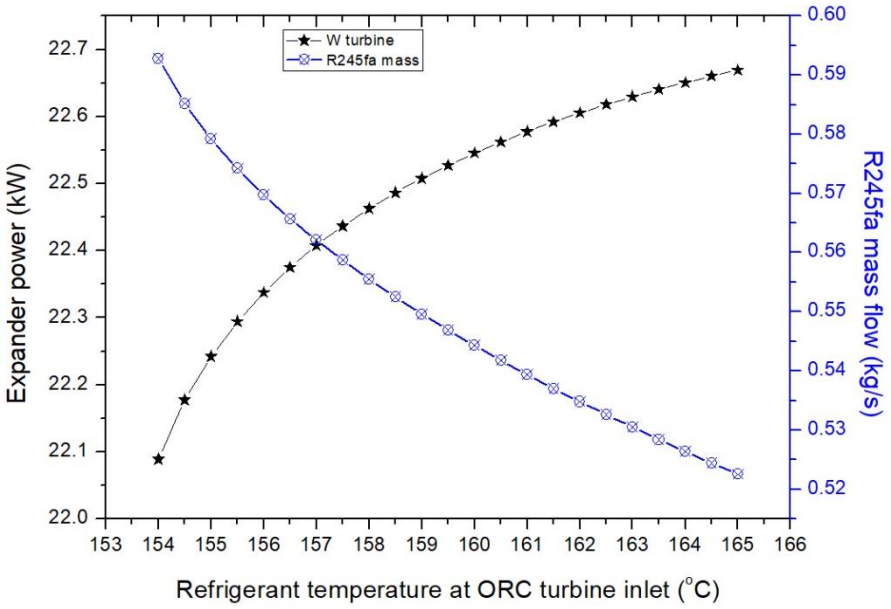

Figure 7.7: Effects of superheating ORC refrigerant at expander inlet on turbine power and ORC mass flow.

Figure 7.8 illustrates the changes in the ORC condenser thermal duty and the cycle efficiency due to changes in the refrigerant superheat degree at the turbine inlet. Superheating the refrigerant leads to a slight increase in cycle thermal efficiency, from 13.9 to 14.4%. This result is explained by the behaviour of the turbine power noted in Figure 7.7. A minimal reduction was observed in the condenser thermal capacity. The trend of the condenser capacity strongly follows that of the mass flow shown in Figure 7.7.

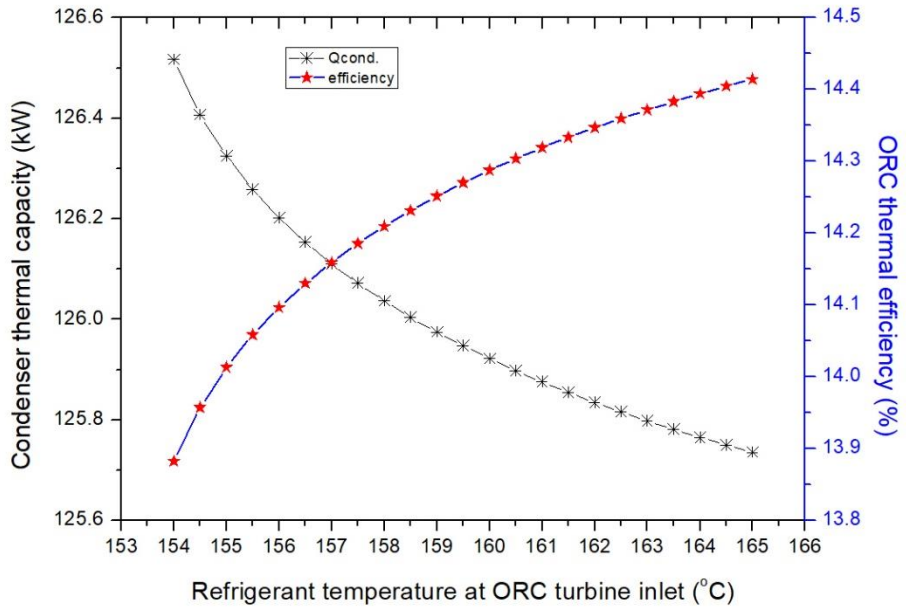

Figure 7.8: Effects of superheating the ORC refrigerant at the expander inlet on turbine power and ORC mass flow.

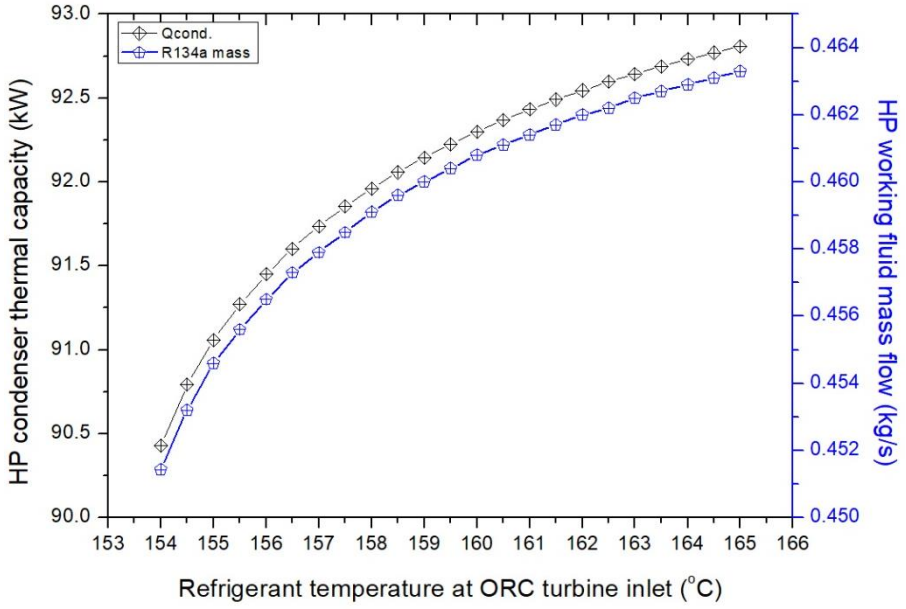

Figure 7.9: Effects of superheating the ORC refrigerant at the expander inlet on HP condenser thermal capacity and working fluid mass flow.

The effects of superheating the ORC refrigerant on the HP cycle parameters are shown in Figure 7.9. Doing so causes an exponential rise in both HP condenser capacity and R134a mass flow due to the rise in the expander power that consequently leads to a similar increment in HP compressor work due to the direct coupling between them. These increments in compressor power increase the condenser capacity. Meanwhile, the R134a mass flow increases because the temperature of the R245fa has increased, which will raise the inlet enthalpy for the turbine (h_{in}), as explained in the following equation:

$$\dot{m}_{HP} = \frac{\dot{m}_{ORC} \times (h_{in} - h_{out})_{turbine}}{(h_{out} - h_{in})_{compressor}} \tag{5.1}$$

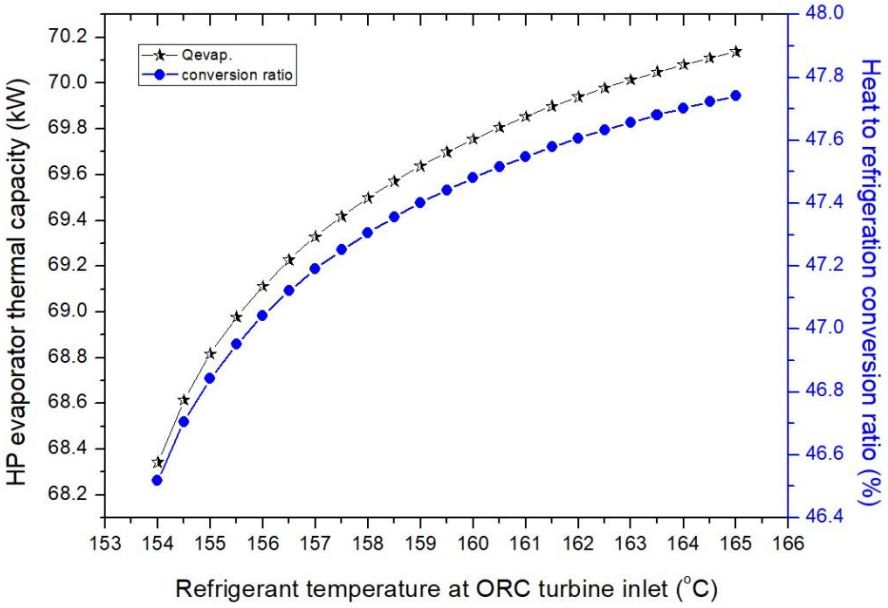

Figure 7.10: Effects of superheating the ORC refrigerant at the expander inlet on HP evaporator thermal capacity and the heat to refrigeration conversion ratio.

The effects of superheating the ORC working fluid on the HP evaporator thermal capacity and the heat to refrigeration conversion ratio are shown in Figure 7.10. The HP thermal capacity has increased from approximately 68.4 kW to 70.1 kW when using the superheat approach. In addition, the heat to refrigeration conversion ratio improves from 46.5 to 47.7% when the ORC refrigerant is superheated by 11 ºC.

7.4 Combining DE, ORC and HP cycles in the steady state working condition

The steady state results for the combined ORC-HP system using R245fa as an ORC working fluid under the DE rated working condition are summarised in Tables 7.1 and 7.2.

Table 7.1 Steady state results for the combined system bottoming DE.

Parameters	MATLAB code		ASPEN PLUSE	
	Heat pump cycle	ORC cycle	Heat pump cycle	ORC cycle
Condenser heat duty, kW	92.8	125.735	87.528	118.56
Evaporator heat duty, kW	70.1379	146.912	66.133	138.554
Condensation temperature, ^{o}C	25	25	25	25
Condensation pressure, bar	6.6538	1.4825	6.654	1.483
Evaporation temperature, ^{o}C	-21	154	-21.03	154
Evaporation pressure, bar	1.2710	36.5	1.269	36
Degree of superheat, ^{o}C	None	11	-	11
Mass flow rate, kg/s	0.4633	0.5225	-	-
Power produced by the ORC expander, kW	-	-22.6693	-	-21.395
Power input to the HP compressor, kW	22.6693	-	21.395	-
Cooling coefficient of performance COPc	3	-	3	-
Work of liquid pump, kW	-	1.4928	-	1.4
ORC thermal efficiency, %	-	14.4144	-	14.43
Compressor and turbine isentropic efficiency, %	0.7			
Minimum PPT at ORC evaporator, ^{o}C	30		30	
Percentage of thermal heat recovered to refrigeration effect, %	47.7415		47.73	

Table 7.2 Diesel engine working conditions

Exhaust temperature, ^{o}C	519
Exhaust mass flow, kg/s	0.2752
Temperature of the exhaust leaving ORC evaporator, ^{o}C	56.394

7.5 Modelling the ORC cycle with different working fluids

As can be concluded from the above results, the higher the refrigerant temperature at the turbine inlet, the greater the heat recovery obtained from the DE exhaust stream. Therefore, a comparison assessment has been made using the same modelling procedure as has previously been outlined and the same assumptions on other ORC working fluids. The aim of doing so was to investigate the performance of the combined cycle with different ORC refrigerants at higher temperatures for the turbine inlet. In this assessment, the temperature of each refrigerant has been increased from the critical temperature to the highest applicable temperature. For all the compared working fluids, the evaporation pressure was set near the critical pressure value, and the condensation pressure was iterated until the condensation temperature reached 25 ^{o}C, as shown in Table 7.3.

Table 7.3 Different ORC working fluids at different evaporation and condensation pressures.

ORC Refrigerant	Evaporation pressure, bar	Condensation pressure, bar
R123	36.6	0.9136
R22	49.9	10.439
R134a	40.59	6.6538
R245fa	36	1.4825
Butane	37.96	2.4329

Figure 7.11 shows the changes in the ORC turbine power when the refrigerant temperature at the turbine inlet increased for the selected working fluids.

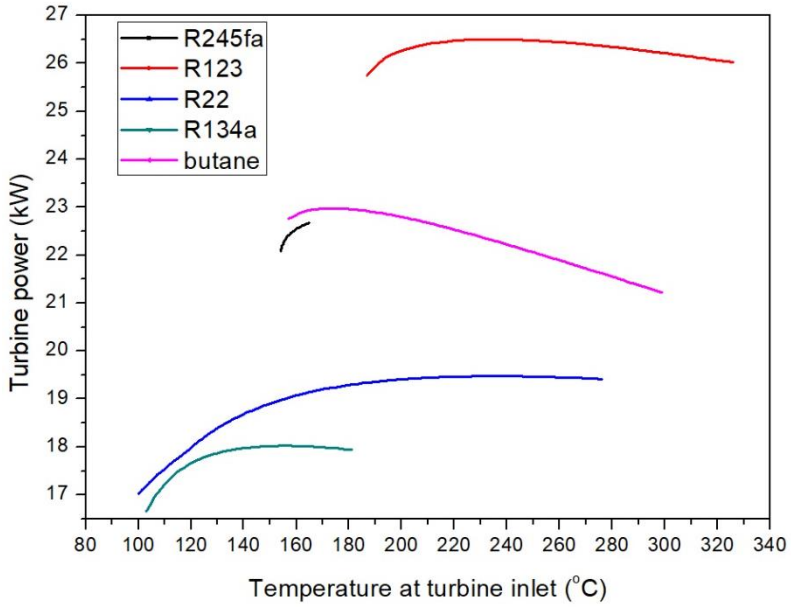

Figure 7.11: Comparison results of expander power for different ORC working fluids when the temperature at the turbine inlet is increased.

The previous figure shows that for most working fluids, the expander power increases with a rise in the refrigerant temperature, then declines again. For each refrigerant, there is an optimum temperature value that achieves the highest expander power. For example, for R22 and R123, a refrigerant temperature of around 240 ^{o}C could be the optimum value. For other working fluids, a temperature of 165 ^{o}C achieves the highest expander power. The figure also reveals that R123 achieves the highest expander power, of around 26.5 kW, among all the working fluid options.

The results regarding ORC thermal efficiency in relation to different working fluids are shown in Figure 7.12, which shows a similar trend to that of turbine power. Furthermore, at the optimum temperature value of each working fluid, each cycle achieves the highest thermal efficiency for that working fluid. The best thermal efficiency is achieved by R123, at around 17%.

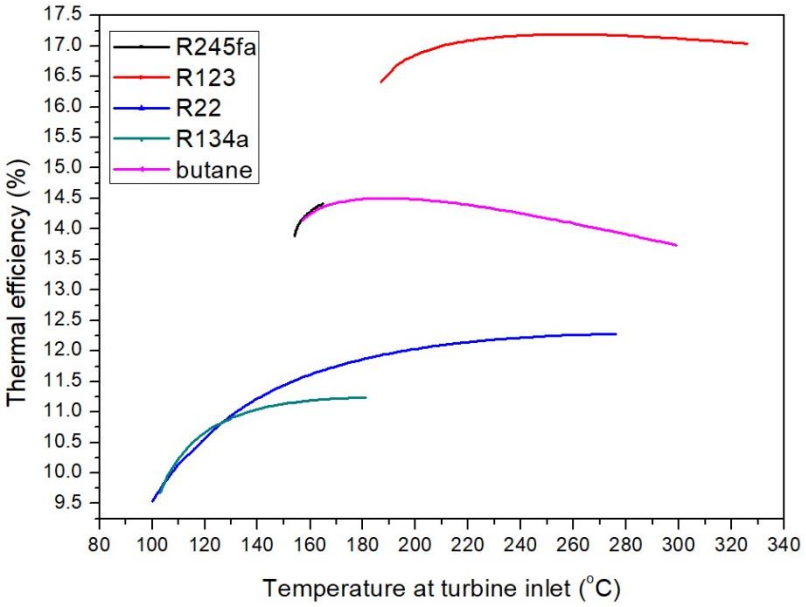

Figure 7.12: Comparison results of thermal efficiency for different ORC working fluids when temperature at turbine inlet is increased.

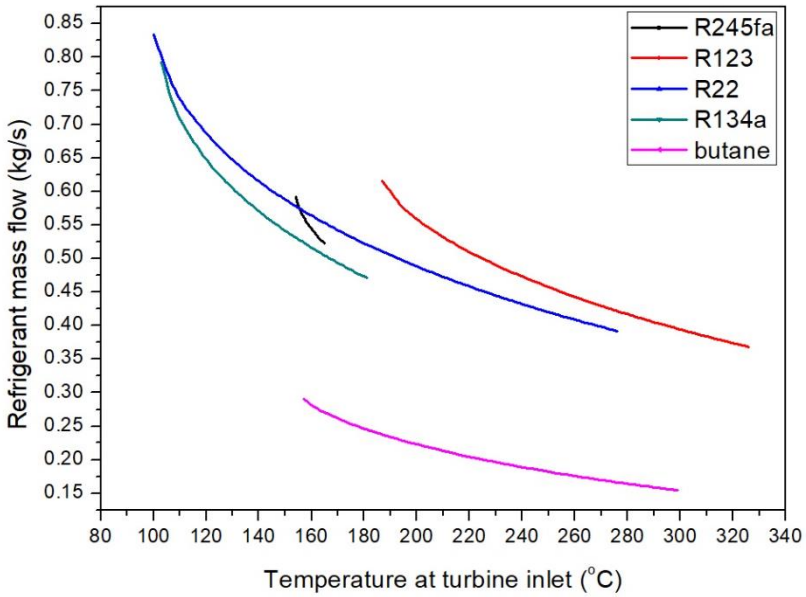

Figure 7.13: Comparison results of mass flow for different ORC working fluids when temperature at turbine inlet is increased.

Figure 7.13 shows the variations in mass flow for the selected working fluids due to an increased refrigerant temperature at the turbine inlet. The working fluid mass flow could indicate the sizing of the evaporator and hence have a cost impact. The results reveal that R123 shows a

slightly higher mass flow than R22 at their optimum temperature (240 ^{o}C), which is better than the other refrigerants.

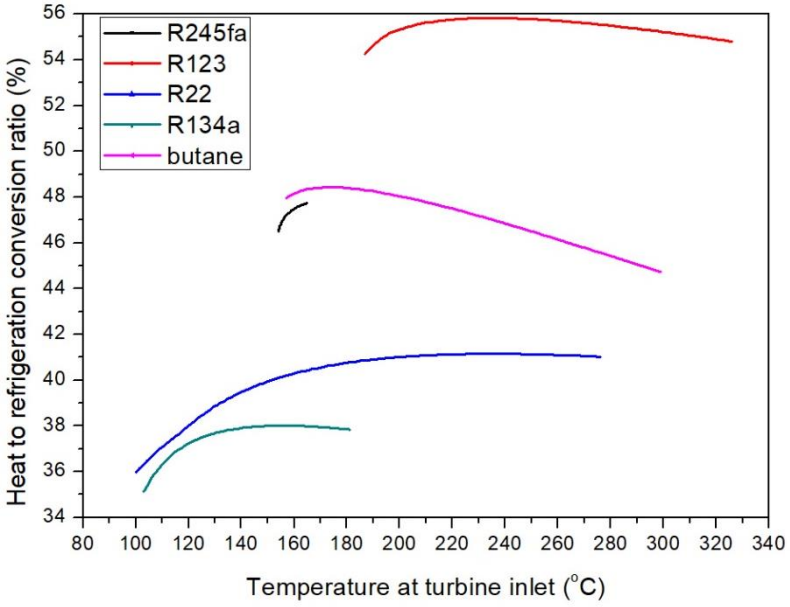

Figure 7.14: Comparison results of percentage of thermal heat recovered to refrigeration effect for different ORC working fluids when temperature at the turbine inlet is increased.

From Figure 7.14, it is clear that working fluid R123 achieves the highest heat to refrigeration conversion ratio, at approximately 56% at the optimum refrigerant temperature. Butane and R245fa recover around 48% from the rejected heat in the exhaust stream into useful refrigeration load.

For the next evaluation process, the refrigerant R123 will be adopted with its optimum temperature value at the turbine inlet.

7.6 Modelling the combined cycle for variable diesel engine speed and loads

7.6.1 Modelling a diesel engine exhaust stream with an ORC cycle

To provide variable mechanical power and load, DE can work under variable engine rotation speeds. This will affect the quantity and quality of the thermal energy contained in the exhaust stream. This situation will consequently mean that the ORC cycle will produce variable output expansion power. To investigate the combined cycle under variable diesel engine working conditions, experimental results for a heavy duty diesel engine working as a stationary electrical power plant generator have been taken from a prior study by Guopeng, Y. [178] see appendix B. These results include eight different engine crank shaft rotation speeds and engine output powers, as well as engine exhaust stream mass flow rates and temperatures, as shown in Figures 7.15 and 7.16.

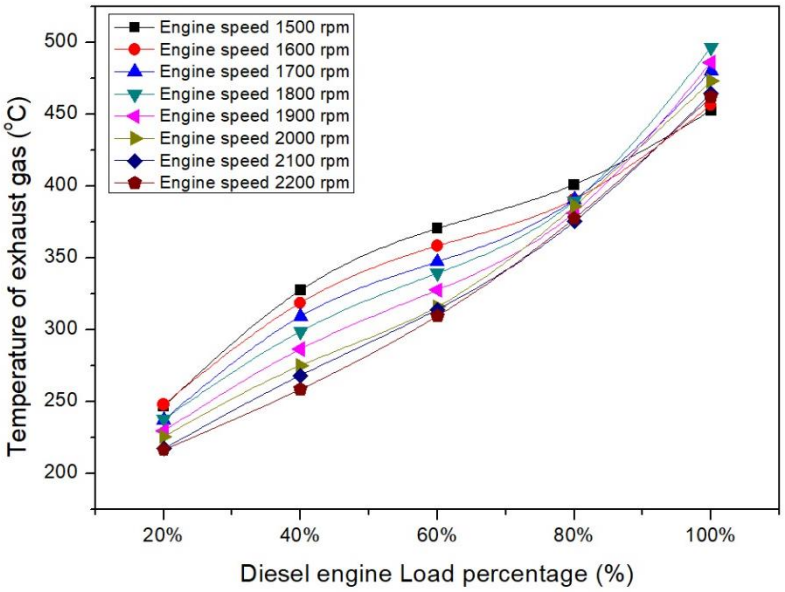

Figure 7.15: Variable DE exhaust stream temperature under variable engine load percentages.

From both figures, it is evident that with a rising diesel engine load, both the exhaust stream temperature and the mass flow increase. These increments will affect the combined cycle performance in terms of the amount of heat recovered from the exhaust stream, the ORC turbine output power, and the percentage of heat converted to the refrigeration load.

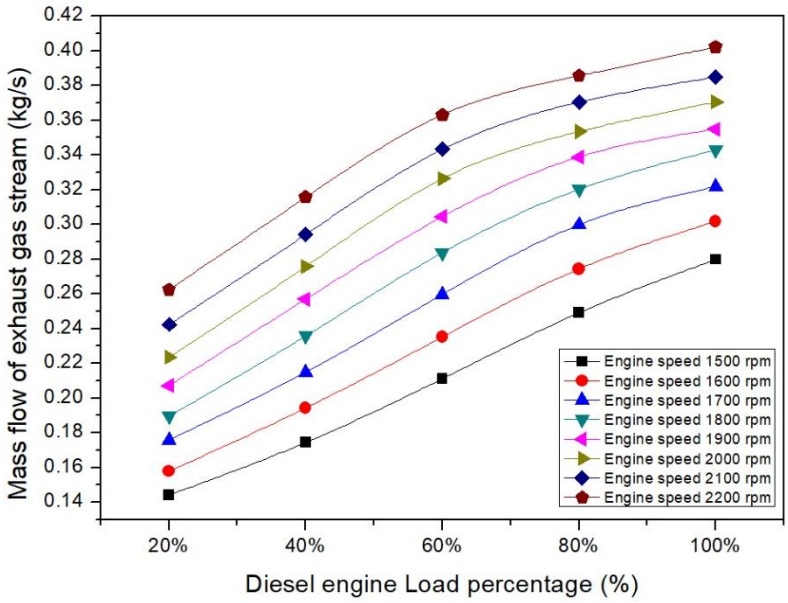

Figure 7.16: Variable DE exhaust stream mass flow under variable engine load percentages.

The optimization process for the combined system working under variable DE working conditions has been carried out with the following assumptions. The selected working fluid for the ORC is R123 and the optimum evaporator pressure and condensation temperature are taken from the calculations conducted in the previous section. Furthermore, instead of assuming a 30 ^{o}C temperature difference at the evaporator exit between the exhaust and refrigerant streams, multi temperature difference values have been iterated in order to investigate the PPT temperature difference across the evaporator.

Figure 7.17 shows the temperature profile of R123 and the exhaust stream across the evaporator under various temperature differences at the evaporator exit. The selected temperature difference values were 60 ^{o}C, 80 ^{o}C, and 100 ^{o}C. It is clear that all these temperature values produce the same temperature difference at the evaporator inlet. However, in depth investigation revealed that the pinch point inside the heat exchanger is reduced in line with the decrease in the selected temperature difference at the evaporator exit. Therefore, a constant temperature difference value of 100 ^{o}C between the hot and cold streams is adopted. This approach secured a minimum temperature difference of around 20 ^{o}C across the evaporator.

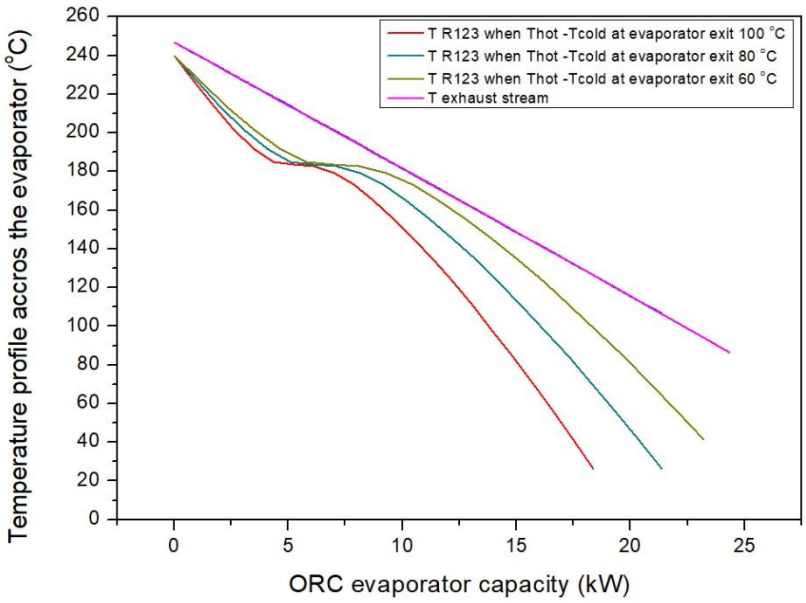

Figure 7.17: TQ curve for the ORC evaporator for variable exhaust stream outlet temperatures.

Moreover, as can be seen in Figure 7.15, the lowest heat source temperature is around 215 ^{o}C at the DE percentage load of 20%. For the sake of the optimization process which aims to investigate all DE working conditions, the refrigerant temperature at the turbine inlet is set to 185 ^{o}C to maintain 30 ^{o}C as the minimum heat source temperature.

Figures 7.18 and 7.19 show how the ORC turbine output power and the R123 mass flow respond to changes in the diesel engine load and rotation speed. In Figure 7.18, when the percentage of engine load increases from 20-70 %, a steady increase in net power can be observed. As the engine approaches full load, the expansion power produced by the ORC cycle markedly increases. Likewise, the mass flow of the ORC cycle increases in a similar pattern to the turbine power, as shown in Figure 7.19.

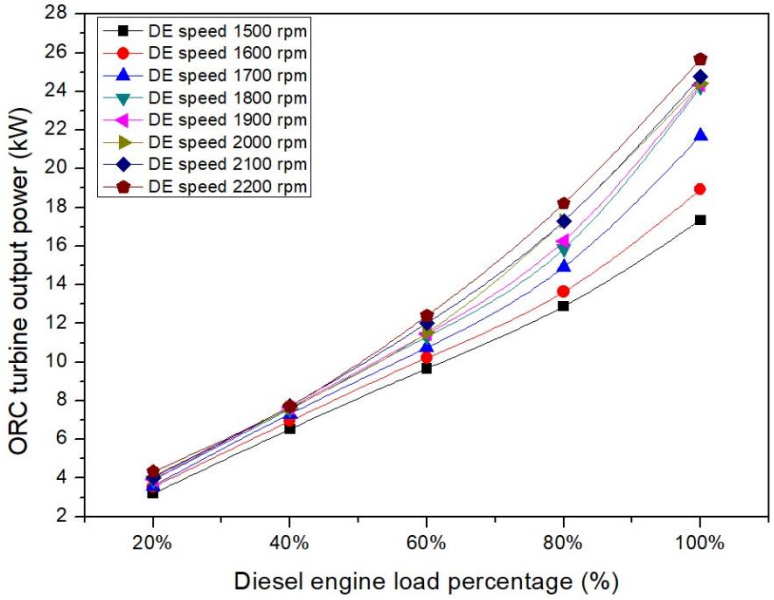

Figure 7.18: Variations in ORC turbine net-power under variable diesel engine load and rotation speed.

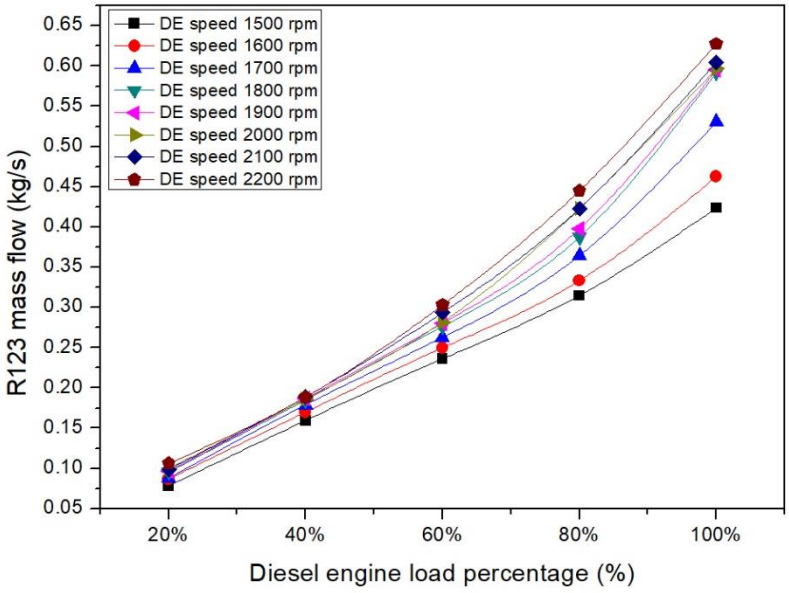

Figure 7.19: Variations in ORC R123 mass flow under variable diesel engine load and rotation speed.

This behaviour can be explained by the fact that greater mass flow is needed to recover the extra heat produced when the diesel engine load increases. The obtained mechanical power from the ORC cycle varies from approximately 3.1 kW at the lowest diesel engine speed and load, to 25.6 kW at the highest diesel engine working condition.

7.6.2 Utilizing the output expansion net-power in a vapour compression refrigeration cycle

Most conventional vapor compression refrigeration systems work on steady cooling duty and compressor consumption power which uses a switch on/off mode when the cooling load is satisfied [127]. However, for this particular design, in order to transform the variable thermal energy contained in the DE exhaust stream into a useful refrigeration load, a variable HP refrigerant mass flow approach is adopted. In the following results, the R134a mass flow rate is optimized in response to the changes in the HP compressor work which is directly coupled with the ORC turbine.

Figure 7.20 shows the variations in the R134a mass flow which occur in response to fluctuations in the diesel engine speed and power output. It can be noted that HP mass flow rate gradually increases with the rise in the diesel engine output power. Also, the Figure shows only a minimal impact of the engine shaft rotation speed on the HP mass flow.

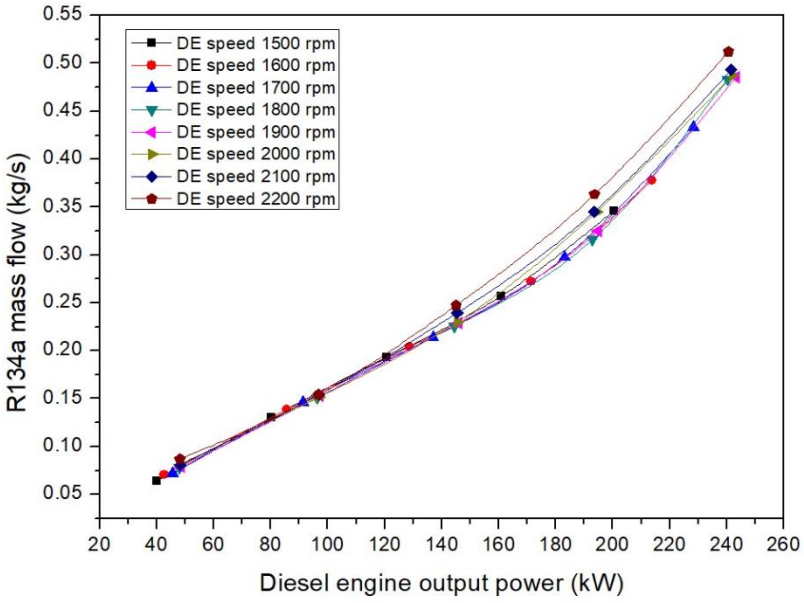

Figure 7.20: Variations in the R134a mass flow rate due to variable diesel engine power and rotation speeds.

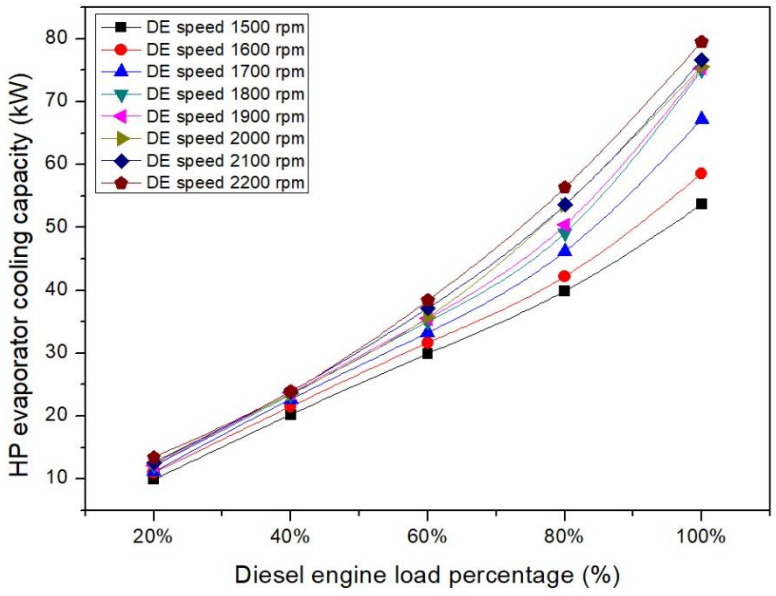

Figure 7.21: HP evaporator cooling capacity via variable diesel engine load and speeds.

Figure 7.21 shows the variations in the HP evaporator cooling duty due to variable diesel engine performance. Increasing the DE load from 20-100% causes a rise in the evaporator cooling duty of between approximately 9.9 – 79.4 kW, while increasing the engine speed from 1800- 2200 rpm results in a further increase in evaporator capacity when approaching the full engine load. This happens because a higher evaporator cooling load occurs as a response to the increase in the refrigerant mass flow, as demonstrated in figure 7.20.

7.6.3 Varying the mass flow rate in the heat pump system

The mechanism of changing the refrigerant mass flow in the heat pump cycle can be practically achieved by varying the compressor frequency (rotation speed), or by using an expansion valve that can optimize the required mass for a certain cooling load [127].

An expansion valve such as thermostatic expansion valve (TXV) can optimize the refrigerant mass flow passing through the evaporator by maintaining a constant degree of superheat at the evaporator exit. The sensor bulb of the TXV valve is charged and sealed with the same HP working fluid in a vapour state at a set temperature and pressure. This sensor is set up on the evaporator exit pipe to measure the temperature of the passing vapour refrigerant. When the cooling load increases (i.e. the temperature in the cooling chamber increases), the temperature of the refrigerant leaving the evaporator also increases, leading to a rise in the temperature and pressure of the refrigerant inside the TXV sensor bubble. Then, the pressure of the working fluid in the connecting pipe of the TXV valve increases, leading to an adjustment in the valve gate to allow more refrigerant to enter the evaporator in order to absorb the extra heat load.

7.6.4 Superheating the refrigerant at the evaporator exit

Superheating the working fluid at the evaporator exit ensures that no wet refrigerant enters the compressor, and secures constant evaporation pressure and temperatures, which can contribute to maintaining constant cycle performance. Usually, a constant superheat degree of 10 ^{o}C is recommended at the evaporator exit. However, for this case study, a constant superheat degree of 5 ^{o}C of R134a is assumed to allow a higher temperature and cooling load to be involved in the evaporation process.

7.7 Optimizing the evaporator cooling load

As was stated earlier in this chapter, the HP evaporator is designed to produce a constant refrigeration temperature of around -18 ^{o}C. According to the sensitive heat equation, the evaporator cooling capacity can be optimized by adapting one or both of the approaches outlined in the following sub-sections.

7.7.1 Optimizing the HP evaporator cooling load by varying the air temperature at the evaporator inlet

Under the assumptions of constant air mass and outlet air temperature, the evaporator cooling capacity can be optimized by varying the inlet air temperature. The lowest value of this air temperature is restricted by the value of the refrigerant temperature at the evaporator exit (-16 ^{o}C). Figure 7.22 shows the variations in the evaporator inlet air temperature when the diesel engine load and rotation speed vary. It can be noted that an increased DE load is associated with a gradual increment in the air temperature at the evaporator inlet. When the DE load is between 20-30%, the air temperature is below approximately -16 ^{o}C, a temperature which could violate the PPT limitation at the evaporator exit. This produces the conclusion that the lower the superheat degree, the higher cooling load absorbed by the evaporator. Therefore, diesel

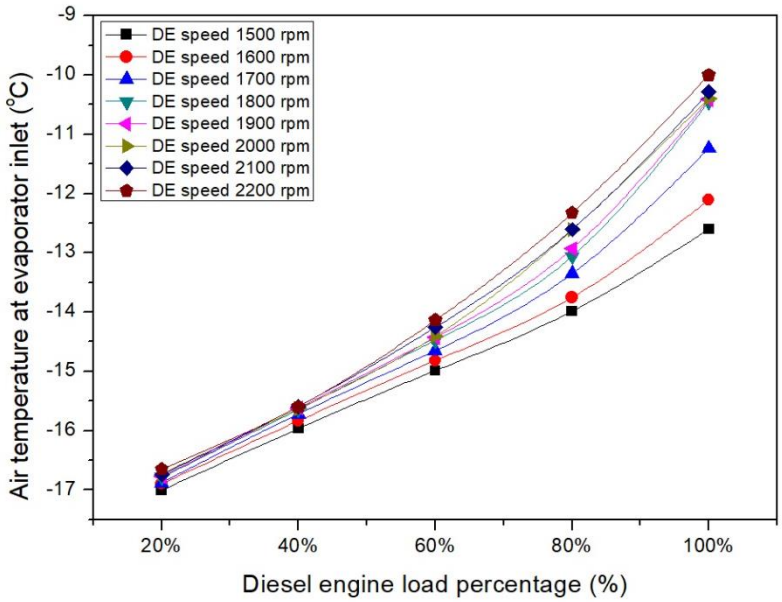

Figure 7.22: HP evaporator inlet air temperature via variable diesel engine loads and speeds.

engine percentage loads of below 40 % lack the potential to produce a useful refrigeration load. The figure also shows that at a constant DE load, increasing the engine speed results in a slight increase in the evaporator air inlet temperature. This effect is greater at higher DE load percentages.

7.7.2 Optimizing the evaporator cooling load by varying the air mass under a constant evaporator inlet air temperature

By assuming a constant inlet air temperature (-10 ^{o}C), and an outlet designed evaporator air temperature (-18 ^{o}C), the evaporator cooling capacities produced from fluctuations in the DE loads and rotation speeds can be optimized based on varying the air mass flow.

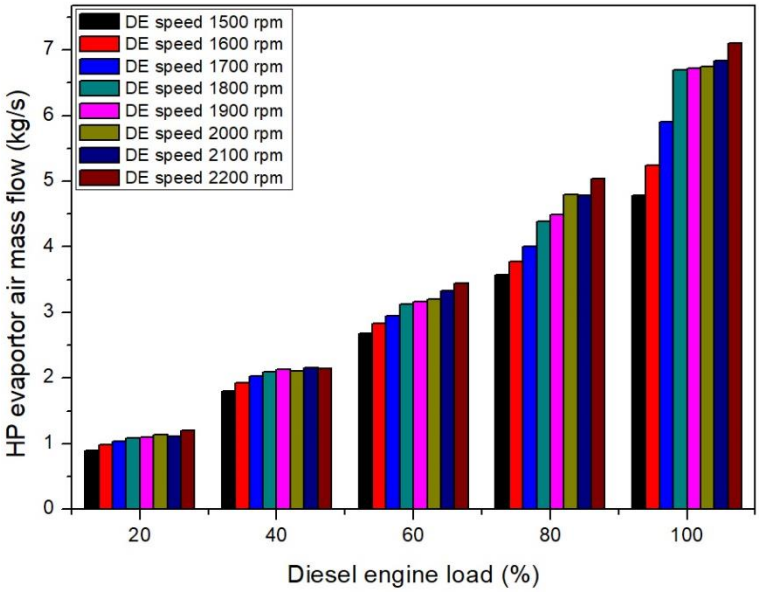

Figure 7.23 HP evaporator air mass flow via variable DE loads.

Figure 7.23 shows the effects of increasing the diesel engine load and crankshaft rotation speed on the air mass flow entering the HP evaporator. The figure reveals that the air mass flow increases significantly with the rise in the engine load from 20% to 100%, recording the lowest value of 0.89 kg/s at an engine speed of 1500 rpm and the highest value of 7 kg/s at an engine speed of 2200 rpm. However, the engine speed showed less of an effect on the air mass at low engine loads. At higher engine loads (80-100%), the engine speed increments result in higher

air mass flow. The behaviour of the air mass flow is influenced by the behaviour of the HP evaporator cooling capacity, as shown in Figure 7.21.

7.8 The percentage of cooling load obtained from the DE rejected thermal energy

As can be concluded from the results presented above, diesel engine loads below 40% have no ability to convert the thermal energy available in the exhaust stream of the diesel engine into a refrigeration effect. Therefore, the results of the diesel engine below the 40% load are excluded from the following analysis.

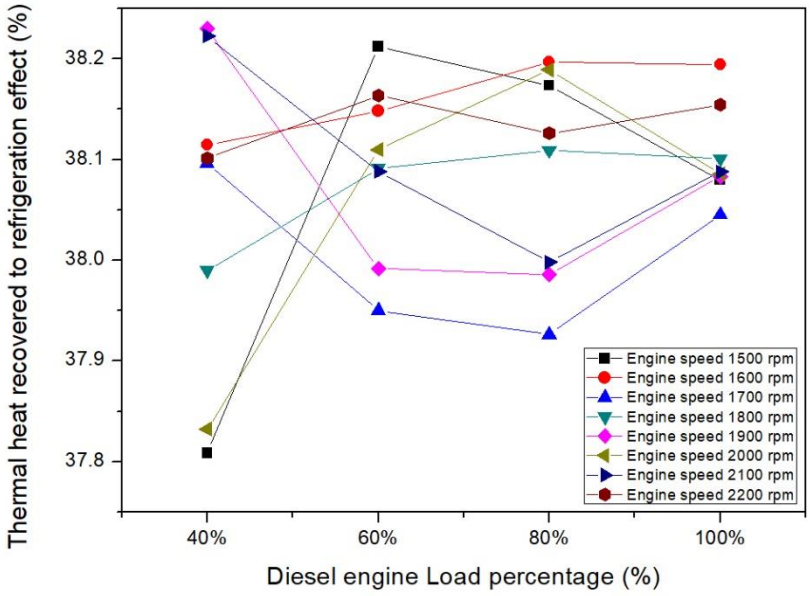

Figure 7.24: The effect of DE load on the percentage of thermal energy converted into cooling load.

Figure 7.24 shows the variations in the heat to refrigeration conversion ratio against fluctuations in diesel engine load and rotation speed. The variation in conversion ratio shows three different behaviours. For DE speeds of 1500 and 2000 rpm, the conversion ratio rises in increments in DE load to reach a maximum value at 60-80% engine load, then declines. At engine speeds of 1600 rpm, 1800 rpm and 2200 rpm, the conversion energy ratio increases with the rise in the

DE load to reach an optimum value, then stabilizes. With the last group of engine speeds (1700, 1900, and 2100 rpm), the conversion ratio declines with the rise in engine load then increases. These results can be attributed to the performance of the DE exhaust stream temperature, as shown in Figure 7.15. In general, the results show that increasing the engine load has no significant impact on the heat conversion ratio for most engine speeds.

7.9 Dynamic behaviour and control strategy for the HP employing a TXV valve

A dynamic evaluation is used to validate the concept of using the TXV as a mass flow optimizer for a variable heat pump cooling load, as shown in Figure 7.25. The thermophysical properties of the R134a acquired from the steady state evaluation are used as boundary conditions for the dynamic model, including pressure, temperature, mass flow rate, and vapour fraction. In addition, the dynamic evaluation requires fixed equipment sizes in aspects such as area or volume flow rate. Therefore, the HP evaporator area is calculated at the maximum engine speed and load using Equation 3.32, which works out at equal to approximately 15 m^2.

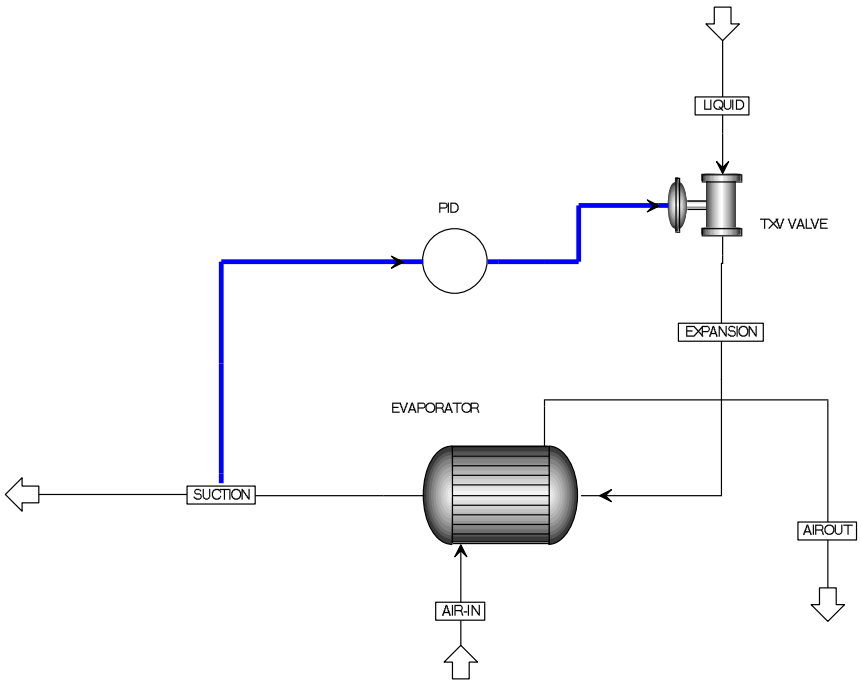

Figure 7.25: Configuration of the control strategy for a variable HP load.

The PID controller in the ASPEN dynamic model is set as follows: the set point is -16 ºC which represents the temperature of the vapour refrigerant at the evaporator exit. The time integral is set to 5 minutes and the gain is set to 1%. The PID controller will optimize R134a mass flow in response to changes in the evaporator cooling load when the inlet air temperature decreases from -10 ºC to -15.5 ºC.

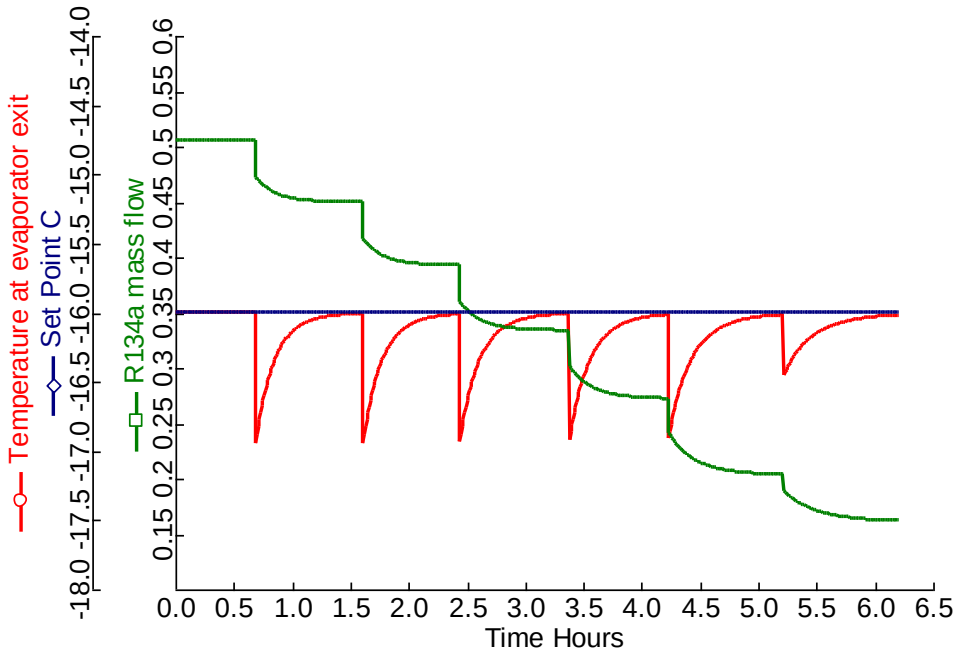

Figure 7.26: PID controller performance.

Figure 7.26 shows the PID controller performance across the entire optimization process. The blue straight line represents the set point of the PID controller. For each time step, the PID controller optimises the R134a mass flow (the green curve) in order to maintain the refrigerant temperature at the evaporator exit at the set point (the red curve).

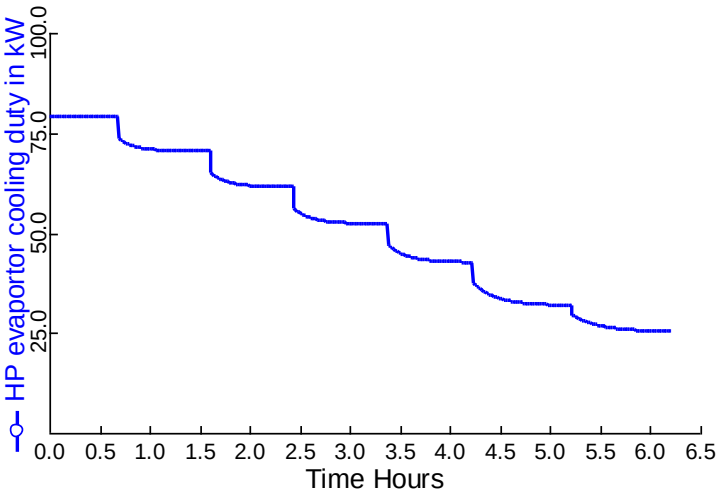

Figure 7.27: Variable evaporator cooling loads in dynamic mode.

As the inlet air temperature decreases, the evaporator cooling duty also decreases. Figure 7.27 shows a gradual decline in evaporator cooling duty from approximately 79.2 to 24.4 kW. These results verify those obtained in the steady state evaluation shown in Figure 7.21.

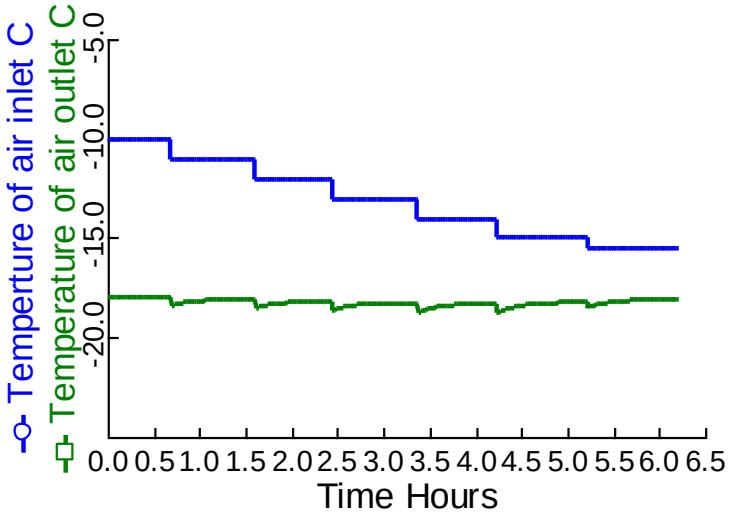

Figure 7.28: Air temperature at evaporator inlet and exit in dynamic evaluation.

Figure 7.28 shows the temperature of the air entering and leaving the evaporator. It shows the time steps of decreasing inlet air temperature (blue curve) from -10 to -15.5 when the PID

controller stops its execution due to the pinch point temperature difference conflicting with the temperature of the refrigerant at the evaporator exit. In addition, it proves that the temperature obtained from the evaporator is kept constant at around the designed value (-18 ^{o}C) in the green curve.

7.10 Utilizing the oil thermal circuit

One common problem which occurs in the ORC cycle is the decomposition of the working fluid due to the high temperature of the combustion flame or heat source. This can cause a rise in working fluid temperature to a value higher than its applicable temperature. One of the proposed solutions is to prevent any direct contact between the heat source and the ORC working fluids by using an intermediate fluid able to tolerate high temperatures which also has good thermal conductivity. Thermal oil can be used in a close loop circuit to address this issue [179], as shown in Figure 7.29.

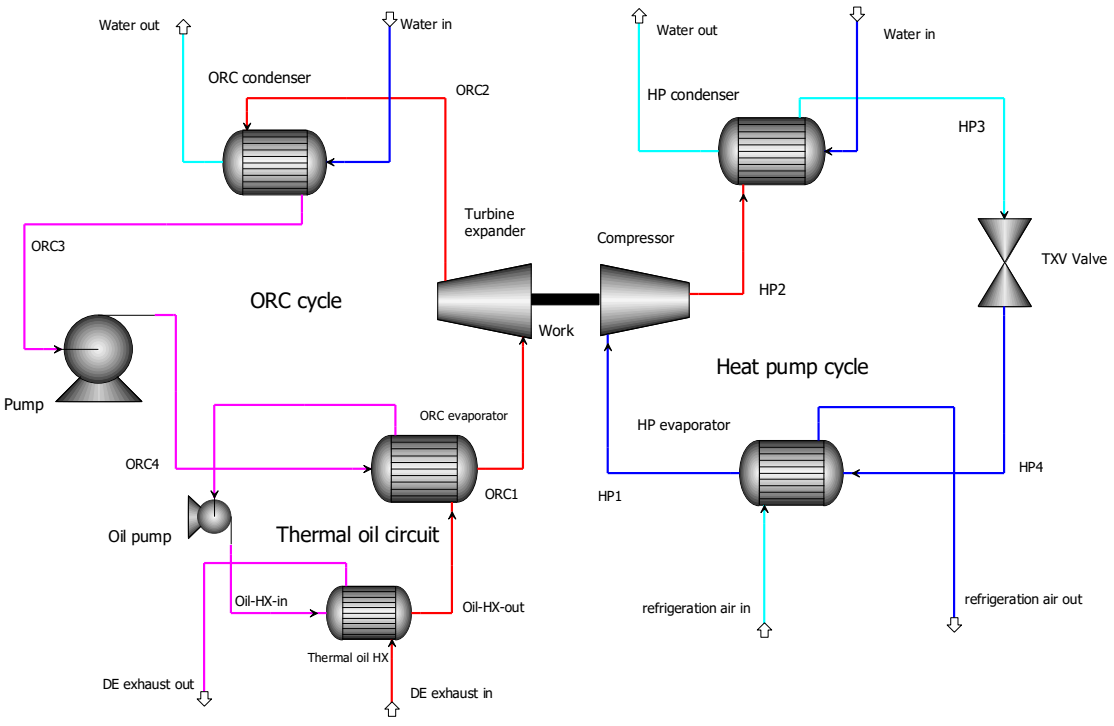

Figure 7.29: Combined system configuration for recovering heat from the diesel engine exhaust stream with a thermal oil circuit.

7.10.1 Modelling the combined cycle with a thermal oil circuit

The combined cycle is modelled in design mode in order to reach the optimum cycle performance. The mass flow of the thermal oil is increased gradually under the assumptions of maintaining a 30 ºC difference between the hot stream (thermal oil) and the cold flow (R123) at the ORC evaporator exit (ORC1). In addition, the pinch point across the evaporator is also monitored.

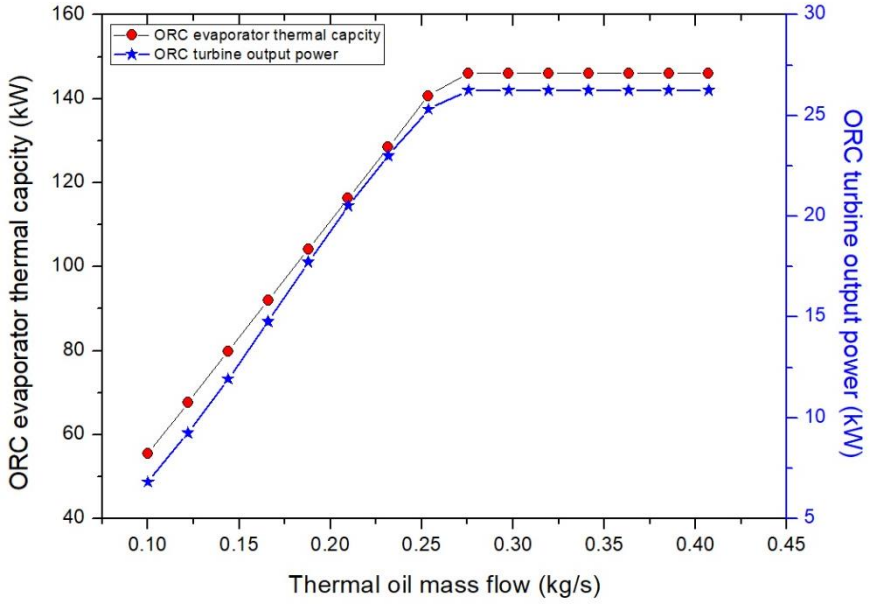

Figure 7.30: ORC evaporator thermal capacity and turbine power under variable thermal oil mass flow.

Figure 7.30 shows the variations in the ORC evaporator capacity and the turbine output power when the thermal oil mass flow is increased. Increasing the oil mass flow to 0.2755 kg/s satisfies the optimization process in terms of the ORC turbine power output, which reaches the steady state values mentioned in Figure 7.18. However, at this mass flow value, the PPT between the refrigerant and the thermal oil has fallen to an unacceptable value, as shown in Figure 7.31. Therefore, a refrigerant mass of around 0.4 kg/s is selected to satisfy the optimization process. At this stage, the area of the thermal oil HX can be calculated. The optimization results of the combined cycle employing a thermal oil circuit are shown in Table 7.4.

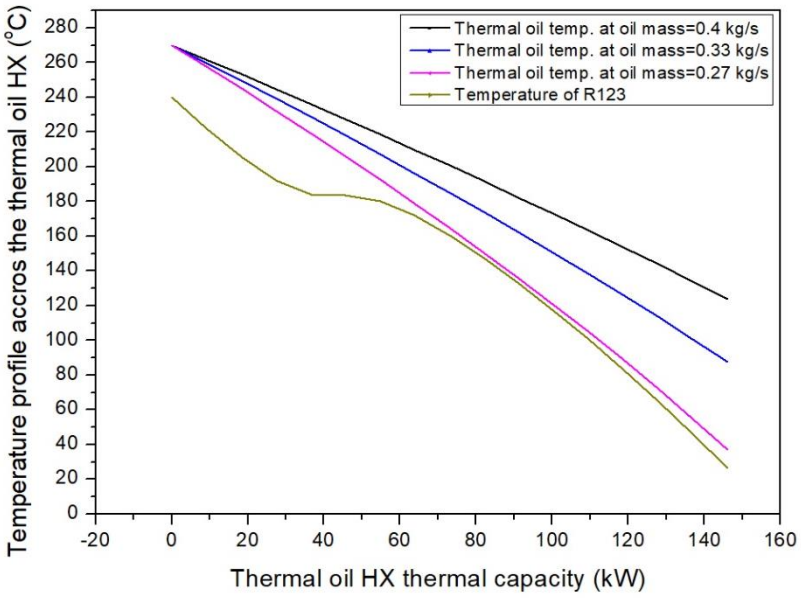

Figure 7.31: TQ curve for the thermal oil HX under variable thermal oil mass flows.

Table 7.4 Steady state for the combined cycle utilizing the thermal oil HX circuit.

Parameters	Heat pump cycle	ORC cycle
Condenser heat duty, kW	107.545	121
Evaporator heat duty, kW	81.286	146.021
Condensation temperature, ^{o}C	25	25
Condensation pressure, bar	6.654	0.915
Evaporation temperature, ^{o}C	-21	240
Evaporation pressure, bar	1.269	36.5
Degree of superheat, ^{o}C	5	-
Evaporator heat transfer area, m^2	15.519	3
Mass flow rate, kg/s	0.523	0.473
Power produced by the ORC expander, kW	-	26.259
Power input to the HP compressor, kW	26.259	-
Cooling coefficient of performance COPc	3	-
Work of the liquid pump, kW	-	1.243
ORC thermal efficiency, %	-	17.131
Oil temperature at thermal oil HX inlet	126.4	
Oil temperature at thermal oil HX outlet	270	
Thermal oil mass flow, kg/s	0.407	
Thermal oil heat exchanger area, m^2	3.722	
Minimum PPT at ORC evaporator, ^{o}C	30	
Percentage of thermal heat recovered to refrigeration effect, %	55.66	

7.11 Conclusion

The potential offered through using a combined ORC-HP system as a heat recovery machine has been investigated in this chapter. The heat source for the ORC cycle is the rejected thermal energy contained in the diesel engine's exhaust stream. An integrated system has been proposed here to convert this wasted heat into a useful refrigeration load with cold air of around -18 ^{o}C. A steady state evaluation of the combined cycle powered by a constant DE working condition was performed. The results showed that for the combined system using R245fa and R134a as working fluids for ORC and HP respectively, about 47% of the wasted heat can be converted into a useful refrigeration load. Furthermore, a comparison evaluation of ORC cycle working fluids was carried out and the R123 refrigerant showed the greatest potential in terms of higher ORC turbine power and cycle thermal efficiency.

Further, a control strategy for the combined system working with variable DE loads and speeds has been proposed. This strategy is based on varying the ORC and HP working fluids mass flow to cope with the variations in the quantity and quality of the heat source. The results show that not all the power recovered from the ORC cycle can be converted into a useful refrigeration effect. More specifically, the thermal energy contained in the exhaust stream when the DE load is below 40% might not have the potential to be transferred into a refrigeration load due to the decline in temperature difference (pinch point) between the inlet evaporator air temperatures and the superheated vapour refrigerant at the HP evaporator exit. However, when the DE works at over the 40% percentage load, around 55% of the wasted heat available in the exhaust stream is recovered by the ORC and transformed into useful refrigeration effects by the HP cycle. Moreover, the mechanism of optimizing the refrigerant mass flow in the HP cycle was investigated by adopting the TVX valve concept. In addition, a dynamic model using ASPEN PLUS was employed to validate the concept of the TXV, and to verify the results obtained from the steady state simulation.

Chapter 8 Conclusion and future work

In this chapter, the findings presented in the thesis are summarised, and a plan for future work is presented.

8.1 Summary

This thesis has theoretically examined a new integrated heating and cooling system consisting of an Organic Rankine cycle directly driving a vapour compression heat pump cycle. The primary heat sources are burning fossil fuel via a gas burner or using diesel engine exhaust gas. Supplemental heat sources have also been utilised, including ambient air, waste heat from gas burner flue gases, and wasted heat from data centre IT equipment.

In chapter four, a comparative study of the performance of various working fluids for HP and ORC cycles was presented. The selected refrigerants for the HP cycle were: Ammonia, R600a, R22, R134a, R1234yf, R410a and CO_2. The ORC cycle working fluids were: R123, Heptane, Hexane, Pentane, and R245fa as pure refrigerants, R245fa+R134a, and Hexane+R141b as zeotropic mixtures. The analysis was based on the performance of these working fluids in terms of cycle efficiency, heating and cooling capacities, as well as environmental and safety concerns.

For the HP cycle in heating mode, at low condensation temperature (30 ^{o}C), all refrigerants apart from CO_2 showed comparable heating COP. In contrast, at a high condensation temperature, ammonia, R600a, R22 and R134a achieved higher COP_h. For the HP cycle in cooling mode, all the refrigerants showed similar COP_c behaviour as evaporation temperature increased at constant condensation pressure.

In the ORC cycle, all the selected refrigerants showed reductions in thermal efficiency with a rising condensation temperature. Also, pure refrigerants showed better thermal efficiency than zeotropic mixtures.

Natural refrigerants such as ammonia and CO_2 have minimal environmental impacts, with no global warming potential or risk of damage to the ozone layer. Similarly, Pentane, Hexane, Heptane, and Isobutane (R600a) have low GWP and ODP profiles. However, from a safety point of view, these refrigerants as well as ammonia, might be not suitable for domestic application due to their flammability or toxicity. R134a as a HP cycle working fluid has shown good thermal performance and is widely used with a good safety profile and environmentally friendly

behaviours. Similarly, R123 and R245fa as ORC working fluids have achieved comparable thermal efficiency with good safety and environmental profiles. These working fluids were therefore selected for the combined cycle studied in this thesis.

Chapter five investigated the use of the combined cycle powered by a gas burner for domestic hot water application. A preliminary design was proposed and analysed in order to explore the highest achievable cycle performance. The results suggested that the system can achieve an overall fuel to heat efficiency of around 136%. In addition, the contribution of the post heater to water heating is minimal.

Based on these results, a combined system without a post heater was proposed and investigated further in terms of the sequence of water heating in the HP and ORC condensers. In the first approach, the fuel to heat efficiency decreases with the rise in both condensers' pressure. The second approach examined a system with a reversed water heating process in which the ORC condenser is the first heating stage. The overall results showed that the first approach achieved higher system efficiency than the reverse design.

To tackle the effects of ambient temperature variation on the HP cycle while maintaining the HP evaporator in a frost free state, various control strategies were proposed and investigated. The results were verified and validated via a dynamic model, which showed good agreement with the steady state results.

Chapter six examined the potential use of the combined system for data centre cooling, with the wasted heat recovered from the DC room used to heat returnee water for central heating application. The HP cycle achieves heating and cooling COP of around 3.6 and 2.6, respectively. The ORC thermal efficiency is approximately 8.5% and the overall system fuel to heat efficiency is 137%.

To tackle the effects of various DC workloads on the system performance, four control strategies were proposed and analysed with the aim of maintain the DC room temperature within the target range. In the first strategy, DC room temperature is maintained below 25 ^{o}C, with returnee water of 80 ^{o}C and a fuel to heat efficiency of over 134%.

In the second strategy the resulting fuel to heat efficiency is around 112%, which is lower than for strategy one. In both these strategies, the total heating capacity of the combined system is maintained at a constant 58 kW.

In the third strategy, the total heating capacity of the system is reduced while maintaining constant fuel to heat efficiency (137%). The final water temperature is maintained at 80 ^{o}C, but the mass flow of water is reduced from 0.46 to 0.28 kg/s with a corresponding reduction in total system heat capacity from 58 to 35.1 kW.

Strategy four is only valid for a limited range of indoor temperatures (25- 21.5 ^{o}C), after which the increasing indoor air mass flow to 26 kg/s becomes insufficient to superheat the refrigerant at the evaporator exit to the desired value. In both strategies three and four, the fuel to heat efficiency declines to around 111%.

In chapter seven, a combined ORC-HP system was used to produce a refrigeration load by utilising diesel engine exhaust wasted heat as a primary energy source. The target cold air temperature was -18 ^{o}C and R245fa and R134a were the initial selected working fluids for ORC and HP respectively. The achieved HP cooling COP is 3, the ORC thermal efficiency is 14.4%, and the heat to refrigeration conversion ratio is 47.7%.

Modelling of the combined system under various diesel engine loads and speeds was also conducted. In addition, a control strategy was proposed to adapt to these variations. A reduction in diesel engine load from 100% to 20% causes a decline in the HP evaporator cooling capacity from 79.4 to 9.9 kW. In addition, the air temperature at the evaporator inlet falls to -16 ^{o}C at diesel engine loads below 40%.

8.2 Suggested future work

Overall, the work conducted in this thesis supports the proposed system as an efficient heating and cooling technology. Some other potentially beneficial areas of research that could be carried out in the future on this system can be summarised as follows:

8.2.1 Theoretical work

- It is well documented in the literature that an air source HP cycle performance varies with fluctuations in ambient temperature. In this thesis, ambient air has been used as the heat source for the HP evaporator, and the system performance was shown to be significantly affected by falling ambient temperatures. The potential of using more steady heat sources

such as geothermal, solar, surface water, or other waste heat sources instead of air could therefore be theoretically explored.

- Various experimental and theoretical researches have examined the potential of enhancing the performance of the standalone ORC and HP cycles using various methods including the use of cascade configuration, an ejector as an expansion device instead of an expansion valve, and others. The potential of employing these technologies in the combined system proposed in this thesis could be explored and compared to the performance results reported in the present work.

- A wider range of working fluids for the combined system could be selected and compared.

- The definition of fuel to heat efficiency conducted in this research can be used as a comparison tool by applying it to other combined ORC-VCC cycles published in the literature.

- The potential for using the combined system for large scale industrial heating and cooling application purposes could be investigated. In addition, other sources of waste heat, such as sewage water and industrial waste heat, could be used to further investigate the potential of the combined system as a waste heat recovery technology.

- Investigating other power and heat recovery systems used for similar applications and comparing the results with the combined system studied in this thesis.

8.2.2 Experimental work

- Building a lab rig of the combined system with the intended application of domestic hot water supply would provide new insights. The results obtained in this thesis can be used as a guide in selecting the thermodynamic specifications of each of the cycle components. The design parameters could include the refrigerant type, evaporation and condensation pressure, and compressor and turbine power capacity. Ambient air source could initially be used as a heat source for the HP evaporator, either on its own or mixed with the gas burner flue gases.

- Alternative heat sources could be used to simulate the waste heat from a data centre or a diesel engine exhaust. For instance, a hot air blower with variable mass flow and temperature could be used for this purpose. The rig could be modified to simulate the combined cycle proposed in chapters six and seven.

Appendix A: Combined Gas burner-ORC-HP cycles by ASPEN PLUS

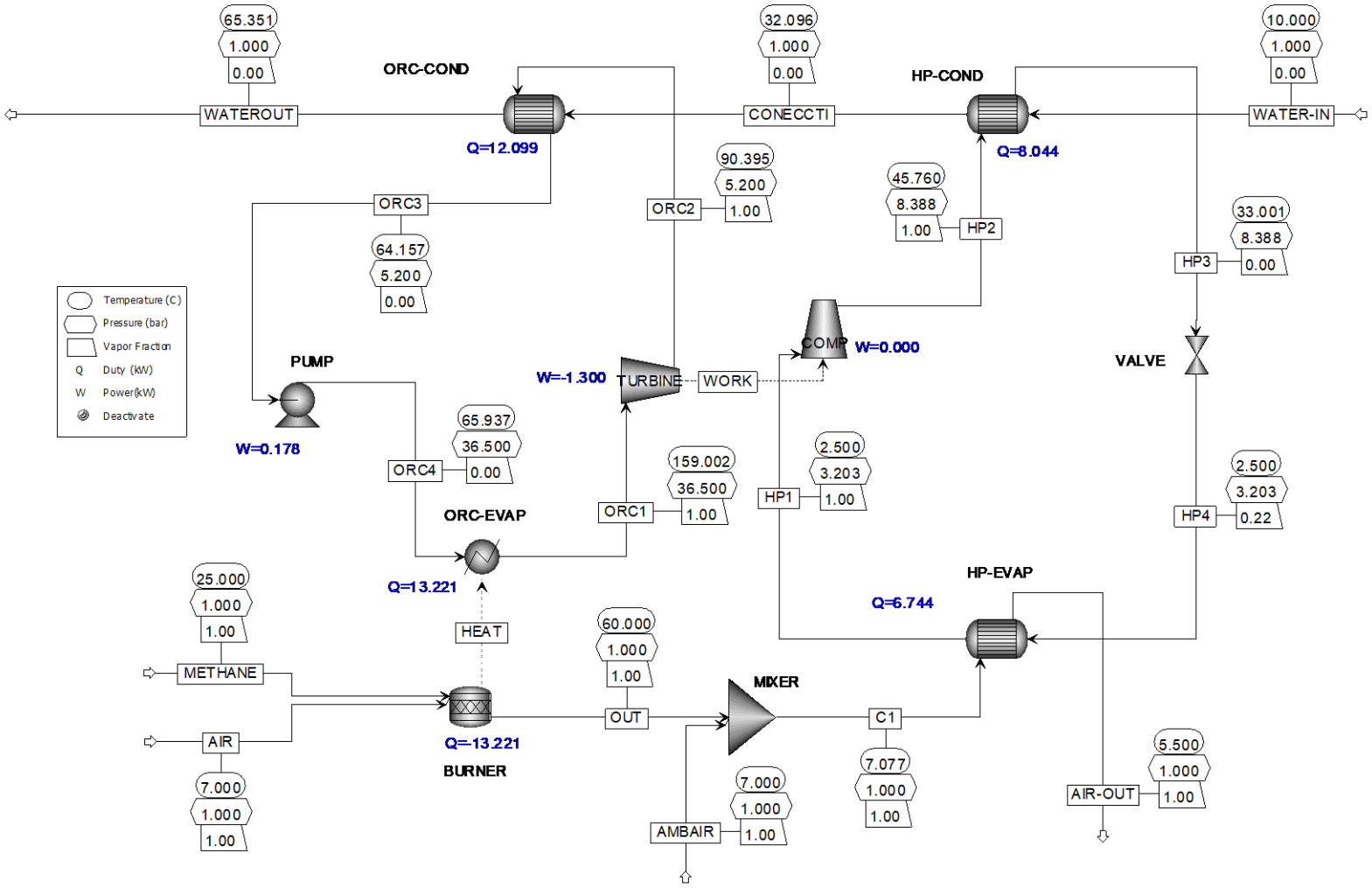

Appendix B: Diesel engine experimental results [178].

Engine Load	Engine speed(r/min)	Engine Power(kW)	Temperature of exhaust gas (℃)	Mass flow rate of exhaust gas (kg/s)	Pressure of exhaust gas (bar)
20%	1500	39.980	246.640	0.144	1.422439995
40%		80.180	327.560	0.174	1.625960007
60%		120.540	370.660	0.211	1.896199997
80%		160.767	401.050	0.249	2.239800003
100%		200.325	452.775	0.280	2.490800026
20%	1600	42.660	247.940	0.158	1.476199997
40%		85.660	318.700	0.194	1.730600006
60%		128.660	358.460	0.235	2.048360001
80%		171.420	390.800	0.274	2.390360046
100%		213.833	456.550	0.302	2.673199992
20%	1700	45.600	237.280	0.176	1.556360008
40%		91.420	309.280	0.215	1.851080002
60%		137.040	347.380	0.260	2.236280014
80%		183.100	390.620	0.300	2.604440002
100%		228.400	480.440	0.267	2.831720001
20%	1800	48.040	237.620	0.190	1.646839996
40%		96.240	298.840	0.236	1.987159988
60%		144.500	339.380	0.284	2.390839966
80%		192.960	389.700	0.320	2.725160004
100%		240.200	496.560	0.343	2.935640015
20%	1900	48.580	229.500	0.207	1.747399994
40%		97.200	286.540	0.257	2.106440002
60%		145.980	327.700	0.305	2.55523999
80%		194.800	381.700	0.339	2.874799978
100%		243.200	486.240	0.355	3.002600006
20%	2000	48.400	225.520	0.224	1.832599991
40%		97.020	275.060	0.276	2.245160004
60%		145.500	316.000	0.326	2.699
80%		194.420	386.100	0.354	2.959159973
100%		242.000	473.320	0.370	3.10123999
20%	2100	48.163	217.063	0.242	1.951249979
40%		96.880	268.160	0.294	2.393960022
60%		145.440	314.240	0.343	2.847320038
80%		193.540	375.340	0.370	3.104600006
100%		241.600	464.620	0.385	3.273800018
20%	2200	48.1600	216.3600	0.2624	2.0913
40%		96.7400	258.5400	0.3156	2.5488
60%		145.0200	309.6600	0.3631	3.0175
80%		193.6211	377.4892	0.3857	3.2798
100%		240.6000	462.2400	0.4023	3.4334

List of References

1. Statista. *Daily demand for crude oil worldwide from 2006 to 2019*. 2019; Available from: https://www.statista.com/statistics/271823/daily-global-crude-oil-demand-since-2006/.
2. Huijbregts, M.A.J., et al., *Is Cumulative Fossil Energy Demand a Useful Indicator for the Environmental Performance of Products?* Environmental Science and Technology, 2006. **40**(3): p. 641-648.
3. Covert, T., M. Greenstone, and C.R. Knittel, *Will We Ever Stop Using Fossil Fuels?* The Journal of Economic Perspectives, 2016. **30**(1): p. 117-137.
4. Mahmoudi, A., M. Fazli, and M.R. Morad, *A recent review of waste heat recovery by Organic Rankine Cycle.* applied thermal engineering, 2018. **143**: p. 660-675.
5. Léger, J., et al., *Comparing electric heating systems at equal thermal comfort: An experimental investigation.* Building and Environment, 2018. **128**: p. 161-169.
6. Balke, E.C., W.M. Healy, and T. Ullah, *An assessment of efficient water heating options for an all-electric single family residence in a mixed-humid climate.* Energy & Buildings, 2016. **133**: p. 371-380.
7. Hinrichs, J., et al., *Numerical and experimental investigation of pollutant formation and emissions in a full-scale cylindrical heating unit of a condensing gas boiler.* Applied Energy, 2018. **229**: p. 977-989.
8. Wang, Z., et al., *A theoretical fundamental investigation on boilers equipped with vapor-pump system for Flue-Gas Heat and Moisture Recovery.* Energy, 2019. **171**: p. 956-970.
9. Shang, S., et al., *A total heat recovery system between the flue gas and oxidizing air of a gas-fired boiler using a non-contact total heat exchanger.* Applied Energy, 2017. **207**: p. 613-623.
10. Wei, M., et al., *Experimental investigation on vapor-pump equipped gas boiler for flue gas heat recovery.* Applied Thermal Engineering, 2019. **147**: p. 371-379.
11. Qu, M., O. Abdelaziz, and H. Yin, *New configurations of a heat recovery absorption heat pump integrated with a natural gas boiler for boiler efficiency improvement.* Energy Conversion and Management, 2014. **87**: p. 175-184.
12. Hebenstreit, B., et al., *Techno-economic study of a heat pump enhanced flue gas heat recovery for biomass boilers.* Biomass and Bioenergy, 2014. **71**: p. 12-22.
13. Rees, S.J., *Advances in ground-source heat pump systems*. Vol. no.100.;number 100;. 2016, Duxford, UK: Woodhead Publishing is an imprint of Elsevier.
14. Dinçer, I.b. and M. Rosen, *Exergy analysis of heating, refrigerating and air conditioning: methods and applications*. 2015, Amsterdam: Elsevier.
15. Latorre-Biel, J.-I., et al., *Replacement of electric resistive space heating by an air-source heat pump in a residential application. Environmental amortization.* Building and Environment, 2018. **141**: p. 193-205.
16. european council for an energy efficient economy. *Getting warmer: a field trial of heat pumps*. 2011, June 9; Available from: https://www.eceee.org/library/conference_proceedings/eceee_Summer_Studies/2011/7-monitoring-and-evaluation160/getting-warmer-a-field-trial-of-heat-pumps/.
17. Wu, D.W. and R.Z. Wang, *Combined cooling, heating and power: A review.* Progress in Energy and Combustion Science, 2006. **32**(5): p. 459-495.
18. Cho, H., A.D. Smith, and P. Mago, *Combined cooling, heating and power: A review of performance improvement and optimization.* Applied Energy, 2014. **136**: p. 168-185.

19. Breeze, P., *Chapter 3 - Combined Heat and Power Principles and Technologies*, in *Combined Heat and Power*, P. Breeze, Editor. 2018, Academic Press. p. 21-32.
20. Macháčková, A., et al., *Numerical and experimental investigation of flue gases heat recovery via condensing heat exchanger.* International Journal of Heat and Mass Transfer, 2018. **124**: p. 1321-1333.
21. Oró, E., et al., *Design and economic analysis of liquid cooled data centres for waste heat recovery: A case study for an indoor swimming pool.* Sustainable Cities and Society, 2018. **36**: p. 185-203.
22. Davies, G.F., G.G. Maidment, and R.M. Tozer, *Using data centres for combined heating and cooling: An investigation for London.* Applied Thermal Engineering, 2016. **94**: p. 296-304.
23. Ebrahimi, K., G.F. Jones, and A.S. Fleischer, *The viability of ultra low temperature waste heat recovery using organic Rankine cycle in dual loop data center applications.* Applied Thermal Engineering, 2017. **126**: p. 393-406.
24. Snijders, A.L. and B.C. Drijver, *9 - Open-loop heat pump and thermal energy storage systems*, in *Advances in Ground-Source Heat Pump Systems*, S.J. Rees, Editor. 2016, Woodhead Publishing. p. 247-268.
25. Jensen, J.K., et al., *Design of serially connected district heating heat pumps utilising a geothermal heat source.* Energy, 2017. **137**: p. 865-877.
26. Singh, R.M., A.K. Sani, and T. Amis, *15 - An overview of ground-source heat pump technology*, in *Managing Global Warming*, T.M. Letcher, Editor. 2019, Academic Press. p. 455-485.
27. Zhen, J., et al., *Groundwater source heat pump application in the heating system of Tibet Plateau airport.* Energy & Buildings, 2017. **136**: p. 33-42.
28. Naicker, S.S. and S.J. Rees, *Performance analysis of a large geothermal heating and cooling system.* Renewable Energy, 2018. **122**: p. 429-442.
29. Liu, X.H., Y.F. Zhang, and J. Shen, *System performance optimization of ORC-based geoplant with R245fa under different geothermal water inlet temperatures.* Geothermics, 2017. **66**: p. 134-142.
30. Li, T.L., et al., *Entransy dissipation/loss-based optimization of two-stage organic Rankine cycle (TSORC) with R245fa for geothermal power generation.* Science China-Technological Sciences, 2016. **59**(10): p. 1524-1536.
31. Gaudard, A., A. Wüest, and M. Schmid, *Using lakes and rivers for extraction and disposal of heat: Estimate of regional potentials.* Renewable Energy, 2019. **134**: p. 330-342.
32. Shen, C., et al., *Experimental performance evaluation of a novel anti-fouling wastewater source heat pump system with a wastewater tower.* Applied Energy, 2019. **236**: p. 690-699.
33. Guo, X., et al., *Experimental study on the performance of a novel in–house heat pump water heater with freezing latent heat evaporator and assisted by domestic drain water.* Applied Energy, 2019. **235**: p. 442-450.
34. Liu, Z., H. Tan, and Z. Li, *Heating and Cooling Performances of River-Water Source Heat Pump System for Energy Station in Shanghai.* Procedia Engineering, 2017. **205**: p. 4074-4081.
35. Zou, S. and X. Xie, *Simplified model for coefficient of performance calculation of surface water source heat pump.* Applied Thermal Engineering, 2017. **112**: p. 201-207.
36. Zhang, H., H. Zhao, and Z. Li, *Thermodynamic performance study on solar-assisted absorption heat pump cogeneration system in the coal-fired power plant.* Energy, 2016. **116**: p. 942-955.

37. Zhao, M., et al., *Experimental investigation and feasibility analysis on a capillary radiant heating system based on solar and air source heat pump dual heat source.* Applied Energy, 2017. **185**: p. 2094-2105.
38. Eisavi, B., et al., *Thermodynamic analysis of a novel combined cooling, heating and power system driven by solar energy.* Applied Thermal Engineering, 2018. **129**: p. 1219-1229.
39. Freeman, J., et al., *A small-scale solar organic Rankine cycle combined heat and power system with integrated thermal energy storage.* Applied Thermal Engineering, 2017. **127**: p. 1543-1554.
40. Wang, J. and Y. Yang, *Energy, exergy and environmental analysis of a hybrid combined cooling heating and power system utilizing biomass and solar energy.* Energy Conversion and Management, 2016. **124**: p. 566-577.
41. *Aspen plus v8.8 , Aspen Technology Inc.:USA*. 2014.
42. Lemmon, E.W., Huber, M. L., McLinden, M. O., *NIST Standard Reference Database 23: Reference Fluid Thermodynamic and Transport Properties-REFPROP, Version 9.1., National Institute of Standards and Technology, Standard Reference Data Program, Gaithersburg*. 2013.
43. Breeze, P., *Chapter 6 - Gas Turbine Combined Heat and Power Systems*, in *Combined Heat and Power*, P. Breeze, Editor. 2018, Academic Press. p. 51-59.
44. Al Moussawi, H., F. Fardoun, and H. Louahlia, *Selection based on differences between cogeneration and trigeneration in various prime mover technologies.* Renewable and Sustainable Energy Reviews, 2017. **74**: p. 491-511.
45. Yu, G., et al., *Simulation and thermodynamic analysis of a bottoming Organic Rankine Cycle (ORC) of diesel engine (DE).* Energy, 2013. **51**: p. 281-290.
46. Qiu, S., et al., *Development of an advanced free-piston Stirling engine for micro combined heating and power application.* Applied Energy, 2019. **235**: p. 987-1000.
47. Zhou, N., et al., *Experimental study on Organic Rankine Cycle for waste heat recovery from low-temperature flue gas.* Energy, 2013. **55**: p. 216-225.
48. Collings, P., *Theoretical and experimental analysis of an organic Rankine Cycle*. 2018, University of Glasgow: University of Glasgow PhD Thesis.
49. Zhao, X., et al., *Flue gas recovery system for natural gas combined heat and power plant with distributed peak-shaving heat pumps.* Applied Thermal Engineering, 2017. **111**: p. 599-607.
50. Kang, S., et al., *A new utilization approach of the waste heat with mid-low temperature in the combined heating and power system integrating heat pump.* Applied Energy, 2015. **160**: p. 185-193.
51. Cai, B., et al., *Theoretical and experimental study of combined heat and power (CHP) system integrated with ground source heat pump (GSHP).* Applied Thermal Engineering, 2017. **127**: p. 16-27.
52. Lei, H., et al., *Study on different heat supplementation strategies for a combined cooling, heating and power system.* Applied Thermal Engineering, 2018. **144**: p. 558-570.
53. Yang, Z., W.-B. Wang, and X. Wu, *Thermal modeling and operating tests for a gas-engine driven heat pump working as a water heater in winter.* Energy & Buildings, 2013. **58**: p. 219-226.
54. Hu, B., et al., *Thermal modeling and experimental research of a gas engine-driven heat pump in variable condition.* Applied Thermal Engineering, 2017. **123**: p. 1504-1513.
55. Liu, F.-G., et al., *Experimental study on the performance of a gas engine heat pump for heating and domestic hot water*. Energy & Buildings, 2017. **152**: p. 273-278.

56. Liu, F.-G., et al., *Experimental investigation of a gas engine-driven heat pump system for cooling and heating operation.* International Journal of Refrigeration, 2018. **86**: p. 196-202.
57. Wan, X., et al., *Power management strategy for a parallel hybrid-power gas engine heat pump system.* Applied Thermal Engineering, 2017. **110**: p. 234-243.
58. Jiang, W., et al., *Simulation and validation of a hybrid-power gas engine heat pump.* International Journal of Refrigeration, 2015. **50**: p. 114-126.
59. Farrokhi, M., S.H. Noie, and A.A. Akbarzadeh, *Preliminary experimental investigation of a natural gas-fired ORC-based micro-CHP system for residential buildings.* Applied Thermal Engineering, 2014. **69**(1-2): p. 221-229.
60. Peris, B., et al., *Experimental characterization of an ORC (organic Rankine cycle) for power and CHP (combined heat and power) applications from low grade heat sources.* Energy, 2015. **82**: p. 269-276.
61. Zhao, M., et al., *Performance evaluation of a diesel engine integrated with ORC system.* Applied Thermal Engineering, 2017. **115**: p. 221-228.
62. Bombarda, P., C.M. Invernizzi, and C. Pietra, *Heat recovery from Diesel engines: A thermodynamic comparison between Kalina and ORC cycles.* Applied Thermal Engineering, 2010. **30**(2): p. 212-219.
63. Koppauer, H., W. Kemmetmüller, and A. Kugi, *Modeling and optimal steady-state operating points of an ORC waste heat recovery system for diesel engines.* Applied Energy, 2017. **206**: p. 329-345.
64. Feru, E., et al., *Two-phase plate-fin heat exchanger modeling for waste heat recovery systems in diesel engines.* Applied Energy, 2014. **133**: p. 183-196.
65. Yang, F., et al., *Thermoeconomic multi-objective optimization of a dual loop organic Rankine cycle (ORC) for CNG engine waste heat recovery.* Applied Energy, 2017. **205**: p. 1100-1118.
66. Lu, Y., et al., *Parametric study for small scale engine coolant and exhaust heat recovery system using different Organic Rankine cycle layouts.* Applied Thermal Engineering, 2017. **127**: p. 1252-1266.
67. Liu, P., et al., *Alkanes based two-stage expansion with interheating Organic Rankine cycle for multi-waste heat recovery of truck diesel engine.* Energy, 2018. **147**: p. 337-350.
68. Song, J. and C.-w. Gu, *Analysis of ORC (Organic Rankine Cycle) systems with pure hydrocarbons and mixtures of hydrocarbon and retardant for engine waste heat recovery.* Applied Thermal Engineering, 2015. **89**: p. 693-702.
69. Salek, F., A.N. Moghaddam, and M.M. Naserian, *Thermodynamic analysis of diesel engine coupled with ORC and absorption refrigeration cycle.* Energy Conversion and Management, 2017. **140**: p. 240-246.
70. Di Battista, D., M. Mauriello, and R. Cipollone, *Waste heat recovery of an ORC-based power unit in a turbocharged diesel engine propelling a light duty vehicle.* Applied Energy, 2015. **152**: p. 109-120.
71. Shu, G., et al., *Experimental investigation on thermal OS/ORC (Oil Storage/Organic Rankine Cycle) system for waste heat recovery from diesel engine.* Energy, 2016. **107**: p. 693-706.
72. Xu, B., et al., *Transient dynamic modeling and validation of an organic Rankine cycle waste heat recovery system for heavy duty diesel engine applications.* Applied Energy, 2017. **205**: p. 260-279.
73. Huster, W.R., et al., *Validated dynamic model of an organic Rankine cycle (ORC) for waste heat recovery in a diesel truck.* Energy, 2018. **151**: p. 647-661.

74. Aphornratana, S. and T. Sriveerakul, *Analysis of a combined Rankine–vapour–compression refrigeration cycle.* Energy Conversion and Management, 2010. **51**(12): p. 2557-2564.
75. Wang, H., R. Peterson, and T. Herron, *Design study of configurations on system COP for a combined ORC (organic Rankine cycle) and VCC (vapor compression cycle).* Energy, 2011. **36**(8): p. 4809-4820.
76. Kim, K.H. and H. Perez-Blanco, *Performance analysis of a combined organic Rankine cycle and vapor compression cycle for power and refrigeration cogeneration.* Applied Thermal Engineering, 2015. **91**: p. 964-974.
77. Molés, F., et al., *Thermodynamic analysis of a combined organic Rankine cycle and vapor compression cycle system activated with low temperature heat sources using low GWP fluids.* Applied Thermal Engineering, 2015. **87**: p. 444-453.
78. Asim, M., et al., *Thermodynamic and Thermo-economic Analysis of Integrated Organic Rankine Cycle for Waste Heat Recovery from Vapor Compression Refrigeration Cycle.* Energy Procedia, 2017. **143**: p. 192-198.
79. Saleh, B., *Energy and exergy analysis of an integrated organic Rankine cycle-vapor compression refrigeration system.* Applied Thermal Engineering, 2018. **141**: p. 697-710.
80. Yu, H., T. Gundersen, and X. Feng, *Process integration of organic Rankine cycle (ORC) and heat pump for low temperature waste heat recovery.* Energy, 2018. **160**: p. 330-340.
81. Patel, B., N.B. Desai, and S.S. Kachhwaha, *Optimization of waste heat based organic Rankine cycle powered cascaded vapor compression-absorption refrigeration system.* Energy Conversion and Management, 2017. **154**: p. 576-590.
82. Patel, B., et al., *Thermo-economic analysis of a novel organic Rankine cycle integrated cascaded vapor compression–absorption system.* Journal of Cleaner Production, 2017. **154**: p. 26-40.
83. Patel, B., N.B. Desai, and S.S. Kachhwaha, *Thermo-economic analysis of solar-biomass organic Rankine cycle powered cascaded vapor compression-absorption system.* Solar Energy, 2017. **157**: p. 920-933.
84. Lizarte, R., M.E. Palacios-Lorenzo, and J.D. Marcos, *Parametric study of a novel organic Rankine cycle combined with a cascade refrigeration cycle (ORC-CRS) using natural refrigerants.* Applied Thermal Engineering, 2017. **127**: p. 378-389.
85. Bounefour, O. and A. Ouadha, *Performance improvement of combined organic Rankine-vapor compression cycle using serial cascade evaporation in the organic cycle.* Energy Procedia, 2017. **139**: p. 248-253.
86. Kaşka, Ö., et al., *The performance assessment of a combined organic Rankine-vapor compression refrigeration cycle aided hydrogen liquefaction.* International Journal of Hydrogen Energy, 2018. **43**(44): p. 20192-20202.
87. Chang, H., et al., *Energy analysis of a hybrid PEMFC–solar energy residential micro-CCHP system combined with an organic Rankine cycle and vapor compression cycle.* Energy Conversion and Management, 2017. **142**: p. 374-384.
88. Collings, M.P.a.A.-T., Mr Mohammed and Yu, Dr Zhibin. *A Combined Organic Rankine Cycle-Heat Pump System for Domestic Hot Water Application*. in *12th International Conference on Heat Transfer, Fluid Mechanics and Thermodynamics* 2016. Malaga, Spain.
89. Liang, Y., M. Al-Tameemi, and Z. Yu, *Investigation of a gas-fuelled water heater based on combined power and heat pump cycles.* Applied Energy, 2018. **212**: p. 1476-1488.
90. Underwood, C.P., *14 - Heat pump modelling*, in *Advances in Ground-Source Heat Pump Systems*, S.J. Rees, Editor. 2016, Woodhead Publishing. p. 387-421.
91. Dincer, I. and M.A. Rosen, *Chapter 4 - Heat Pump Systems*, in *Exergy Analysis of Heating, Refrigerating and Air Conditioning*, I. Dincer and M.A. Rosen, Editors. 2015, Elsevier: Boston. p. 131-168.

92. Mikielewicz, D. and J. Wajs, *Performance of the very high-temperature heat pump with low GWP working fluids.* Energy, 2019. **182**: p. 460-470.
93. Wang, G.B. and X.R. Zhang, *Thermoeconomic optimization and comparison of the simple single-stage transcritical carbon dioxide vapor compression cycle with different subcooling methods for district heating and cooling.* Energy Conversion and Management, 2019. **185**: p. 740-757.
94. He, W.F., et al., *Thermodynamic, economic analysis and optimization of a heat pump driven desalination system with open-air humidification dehumidification configurations.* Energy, 2019. **174**: p. 768-778.
95. Rad, E.A. and S. Maddah, *Entropic optimization of the economizer's pressure in a heat pump cycle integrated with a flash-tank and vapor-injection system.* International Journal of Refrigeration-Revue Internationale Du Froid, 2019. **97**: p. 56-66.
96. Yang, F.B., et al., *Parametric optimization and performance analysis of ORC (organic Rankine cycle) for diesel engine waste heat recovery with a fin-and- tube evaporator.* Energy, 2015. **91**: p. 128-141.
97. Underwood, C.P., M. Royapoor, and B. Sturm, *Parametric modelling of domestic air-source heat pumps.* Energy & Buildings, 2017. **139**: p. 578-589.
98. Woodland, B.J., et al. *Experimental Testing of an Organic Rankine Cycle with Scroll-type Expander*. Publications of the Ray W. Herrick Laboratories. 2012. Paper 52.
99. Declaye, S., et al., *Experimental study on an open-drive scroll expander integrated into an ORC (Organic Rankine Cycle) system with R245fa as working fluid.* Energy, 2013. **55**: p. 173-183.
100. Cuevas, C., N. Fonseca, and V. Lemort, *Automotive electric scroll compressor: Testing and modeling.* International Journal of Refrigeration, 2012. **35**(4): p. 841-849.
101. Wang, Z.H., et al., *Dynamic character investigation and optimization of a novel air-source heat pump system.* Applied Thermal Engineering, 2017. **111**: p. 122-133.
102. Nenkaew, P. and C. Tangthien, *A study of Transient Performance of A Cascade Heat Pump System.* 2015 International Conference on Alternative Energy in Developing Countries and Emerging Economies, 2015. **79**: p. 131-136.
103. He, Z.L., et al., *Experimental study on a bifunctional heat utilization system of heat pump and power generation using low-grade heat source.* Applied Thermal Engineering, 2017. **124**: p. 71-82.
104. Kong, X.Q., et al., *Control strategy and experimental analysis of a direct-expansion solar-assisted heat pump water heater with R134a.* Energy, 2018. **145**: p. 17-24.
105. Shen, J.B., et al., *Design and experimental study of an air source heat pump for drying with dual modes of single stage and cascade cycle.* Applied Thermal Engineering, 2018. **129**: p. 280-289.
106. Kong, X.Q., et al., *Experimental performance analysis of a direct-expansion solar-assisted heat pump water heater with R134a in summer.* International Journal of Refrigeration-Revue Internationale Du Froid, 2018. **91**: p. 12-19.
107. Xu, Y.J., et al., *Experimental and theoretical study on an air-source heat pump water heater for northern China in cold winter: Effects of environment temperature and switch of operating modes.* Energy and Buildings, 2019. **191**: p. 164-173.
108. Liu, T.Q., S.F. Wang, and Y.S. Xu, *Experimental investigation of stepped short tube orifice as expansion device in domestic air conditioning/heat pump system.* Energy and Buildings, 2019. **193**: p. 240-249.
109. Fannou, J.-L.C., et al., *Cooling mode experimental analysis of a direct expansion geothermal heat pump with a control depending on the discharge pressure.* Applied Thermal Engineering, 2019. **160**: p. 113955.

110. Yang, L.-X., et al., *Experimental study on the effect of compressor frequency on the performance of transcritical CO2 heat pump system with regenerator.* Applied Thermal Engineering, 2019. **150**: p. 1216-1223.
111. Guo, X., et al., *Experimental study on the performance of a novel in–house heat pump water heater with freezing latent heat evaporator and assisted by domestic drain water.* Applied Energy, 2019. **235**: p. 442-450.
112. Mota-Babiloni, A., et al., *Experimental influence of an internal heat exchanger (IHX) using R513A and R134a in a vapor compression system.* Applied Thermal Engineering, 2019. **147**: p. 482-491.
113. Li, Z., K. Liang, and H. Jiang, *Experimental study of R1234yf as a drop-in replacement for R134a in an oil-free refrigeration system.* Applied Thermal Engineering, 2019. **153**: p. 646-654.
114. Youcai Liang, A.M., Guopeng Yu, Zhibin Yu. *Experimental research on a small air-source heat pump with an oil-free scroll compressor*. in *The 5th Sustainable Thermal Energy Management International Conference* 2019. Hangzhou(China).
115. Yun, E., et al., *Experimental investigation of an organic Rankine cycle with multiple expanders used in parallel.* Applied Energy, 2015. **145**: p. 246-254.
116. Lei, B., et al., *Development and experimental study on a single screw expander integrated into an Organic Rankine Cycle.* Energy, 2016. **116**: p. 43-52.
117. Pu, W., et al., *Experimental study on Organic Rankine cycle for low grade thermal energy recovery.* Applied Thermal Engineering, 2016. **94**: p. 221-227.
118. Pang, K.-C., et al., *Experimental study on organic Rankine cycle utilizing R245fa, R123 and their mixtures to investigate the maximum power generation from low-grade heat.* Energy, 2017. **133**: p. 636-651.
119. Li, L., Y.T. Ge, and S.A. Tassou, *Experimental Study on a Small-scale R245fa Organic Rankine Cycle System for Low-grade Thermal Energy Recovery.* Energy Procedia, 2017. **105**: p. 1827-1832.
120. Yang, S.-C., et al., *Experimental investigation on a 3kW organic Rankine cycle for low-grade waste heat under different operation parameters.* Applied Thermal Engineering, 2017. **113**: p. 756-764.
121. Nematollahi, O., et al., *Experimental study of the effect of brazed compact metal-foam evaporator in an organic Rankine cycle performance: Toward a compact ORC.* Energy Conversion and Management, 2018. **173**: p. 37-45.
122. Kim, J.-S., D.-Y. Kim, and Y.-T. Kim, *Experiment on radial inflow turbines and performance prediction using deep neural network for the organic Rankine cycle.* Applied Thermal Engineering, 2019. **149**: p. 633-643.
123. Chen, J., et al., *A flexible and multi-functional organic Rankine cycle system: Preliminary experimental study and advanced exergy analysis.* Energy Conversion and Management, 2019. **187**: p. 339-355.
124. Zhang, H.-H., et al., *Experimental study of the organic rankine cycle under different heat and cooling conditions.* Energy, 2019. **180**: p. 678-688.
125. Yamaguchi, T., S. Sasaki, and S. Momoki, *Experimental study for the small capacity organic Rankine cycle to recover the geothermal energy in Obama hot spring resort area.* Energy Procedia, 2019. **160**: p. 389-395.
126. Collings, et al., *Experimental Investigation of a Small-Scale ORC Power Plant Using a Positive Displacement Expander with and without a Regenerator.* Energies, 2019. **12**(8): p. 1452.
127. Eastop, T.D. and A. McConkey, *Applied thermodynamics for engineering technologists*. 5th ed. 1993, Harlow: Addison Wesley Longman Limited.

128. Correa, F. and C. Cuevas, *Air-water heat pump modelling for residential heating and domestic hot water in Chile.* Applied Thermal Engineering, 2018. **143**: p. 594-606.
129. Ju, F., et al., *Experimental investigation on a heat pump water heater using R744/R290 mixture for domestic hot water.* International Journal of Thermal Sciences, 2018. **132**: p. 1-13.
130. Willem, H., Y. Lin, and A. Lekov, *Review of energy efficiency and system performance of residential heat pump water heaters.* Energy & Buildings, 2017. **143**: p. 191-201.
131. Li, J., et al., *Energetic and exergetic investigation of an organic Rankine cycle at different heat source temperatures.* Energy, 2012. **38**(1): p. 85-95.
132. Saleh, B., et al., *Working fluids for low-temperature organic Rankine cycles.* Energy, 2007. **32**(7): p. 1210-1221.
133. Cao, Y., et al., *Optimum design and thermodynamic analysis of a gas turbine and ORC combined cycle with recuperators.* Energy Conversion and Management, 2016. **116**: p. 32-41.
134. Andreasen, J.G., et al., *Design and optimization of a novel organic Rankine cycle with improved boiling process.* Energy, 2015. **91**: p. 48-59.
135. Dong, B., et al., *Parametric analysis of organic Rankine cycle based on a radial turbine for low-grade waste heat recovery.* Applied Thermal Engineering, 2017. **126**: p. 470-479.
136. Ju, F., et al., *Experiment and simulation study on performances of heat pump water heater using blend of R744/R290.* Energy & Buildings, 2018. **169**: p. 148-156.
137. Högberg, M., L. Vamling, and T. Berntsson, *Calculation methods for comparing the performance of pure and mixed working fluids in heat pump applications.* International Journal of Refrigeration, 1993. **16**(6): p. 403-413.
138. Kim, M.S. and S.G. Kim, *Experiment and simulation on the performance of an autocascade refrigeration system using carbon dioxide as a refrigerant.* International Journal of Refrigeration, 2002. **25**(8): p. 1093-1101.
139. Gu, Z., et al., *A solution to the cooling and preheating of hydraulic system by organic Rankine cycle with heat pump.* Energy Conversion and Management, 2019. **180**: p. 94-105.
140. Schimpf, S. and R. Span, *Simulation of a solar assisted combined heat pump – Organic rankine cycle system.* Energy Conversion and Management, 2015. **102**: p. 151-160.
141. Deutz, K.R., et al., *Detailed and dynamic variable speed air source heat pump water heater model: Combining a zonal tank model approach with a grey box heat pump model.* International Journal of Refrigeration, 2018. **92**: p. 55-69.
142. Potter, M.C., Somerton, Craig W. , *Thermodynamics for Engineers* Third Edition ed, ed. S.s.O. Series. 2014, Untied States of America: McGraw-Hill Education.
143. Quoilin, S., V. Lemort, and J. Lebrun, *Experimental study and modeling of an Organic Rankine Cycle using scroll expander.* Applied Energy, 2010. **87**(4): p. 1260-1268.
144. Hsieh, Y.Y. and T.F. Lin, *Saturated flow boiling heat transfer and pressure drop of refrigerant R-410A in a vertical plate heat exchanger.* International Journal of Heat and Mass Transfer, 2002. **45**(5): p. 1033-1044.
145. Kuo, W.S., et al., *Condensation heat transfer and pressure drop of refrigerant R-410A flow in a vertical plate heat exchanger.* International Journal of Heat and Mass Transfer, 2005. **48**(25): p. 5205-5220.
146. Mitrovic, J., *Wärme- und Stoffübertragung: Von Prof. Dr.H. D. Baehr und Prof. Dr.K. Stephan. 2. Aufl. Berlin: Springer-Verlag 1996. 697 S., geb., Preis: 98.-DM.* Forschung im Ingenieurwesen, 1996. **62**(6): p. 167-167.
147. Gnielinski, V., *On heat transfer in tubes.* International Journal of Heat and Mass Transfer, 2013. **63**: p. 134-140.

148. Dittus, F.W. and L.M.K. Boelter, *Heat transfer in automobile radiators of the tubular type*. International Communications in Heat and Mass Transfer, 1985. **12**(1): p. 3-22.
149. Shah, M.M., *A general correlation for heat transfer during film condensation inside pipes.* International Journal of Heat and Mass Transfer, 1979. **22**(4): p. 547-556.
150. Asadi, M. and R.H. Khoshkhoo, *Effects of Chevron Angle on Thermal Performance of Corrugated Plate Heat Exchanger.* International Journal of Engineering Practical Research (IJEPR), 2014. **3**(1).
151. Shu, G., et al., *A Multi-Approach Evaluation System (MA-ES) of Organic Rankine Cycles (ORC) used in waste heat utilization.* Applied Energy, 2014. **132**: p. 325-338.
152. Keinath, C.M. and S. Garimella, *Development and demonstration of a microscale absorption heat pump water heater.* International Journal of Refrigeration, 2018. **88**: p. 151-171.
153. Guo, J.J., et al., *Experimental research and operation optimization of an air-source heat pump water heater.* Applied Energy, 2011. **88**(11): p. 4128-4138.
154. Liu, S., et al., *Energetic, economic and environmental analysis of air source transcritical CO2 heat pump system for residential heating in China.* Applied Thermal Engineering, 2019. **148**: p. 1425-1439.
155. Wang, D., Y. Lu, and L. Tao, *Optimal combination of capillary tube geometry and refrigerant charge on a small CO2 water-source heat pump water heater.* International Journal of Refrigeration, 2018. **88**: p. 626-636.
156. Lai, N.A., M. Wendland, and J. Fischer, *Working fluids for high-temperature organic Rankine cycles.* Energy, 2011. **36**(1): p. 199-211.
157. Zhang, S., H. Wang, and T. Guo, *Experimental investigation of moderately high temperature water source heat pump with non-azeotropic refrigerant mixtures.* Applied Energy, 2010. **87**(5): p. 1554-1561.
158. Yaqub, M. and S.M. Zubair, *Capacity Control for Refrigeration and Air-Conditioning Systems: A Comparative Study*. Journal of Energy Resources Technology, 2001. **123**(1): p. 92.
159. Finn, D.P. and C.J. Doyle, *Control and optimization issues associated with algorithm-controlled refrigerant throttling devices*. 2000, Univ. Coll. of Dublin (IE).
160. Marcinichen, J.B., T.N.d. Holanda, and C. Melo, *A dual SISO controller for a vapor compression refrigeration system.* 2008.
161. Goyal, A., M.A. Staedter, and S. Garimella, *A review of control methodologies for vapor compression and absorption heat pumps.* International Journal of Refrigeration, 2019. **97**: p. 1-20.
162. Sung, S.W., J. Lee, and I.-B. Lee, *Process identification and PID control*. 2009, Singapore;Hoboken, N.J;: John Wiley.
163. Saloux, E., et al., *Reconstruction procedure of the thermodynamic cycle of organic Rankine cycles (ORC) and selection of the most appropriate working fluid.* Applied Thermal Engineering, 2018. **129**: p. 628-635.
164. Qiu, G., *Selection of working fluids for micro-CHP systems with ORC.* Renewable Energy, 2012. **48**: p. 565-570.
165. Chen, G., et al., *Performance prediction and working fluids selection for organic Rankine cycle under reduced temperature.* Applied Thermal Engineering, 2019. **153**: p. 95-103.
166. Wang, X., et al., *Working fluid selection for organic Rankine cycle power generation using hot produced supercritical CO2 from a geothermal reservoir.* Applied Thermal Engineering, 2019. **149**: p. 1287-1304.
167. Wallerand, A.S., et al., *Optimal heat pump integration in industrial processes.* Applied Energy, 2018. **219**: p. 68-92.
168. Frate, G.F., L. Ferrari, and U. Desideri, *Analysis of suitability ranges of high temperature heat pump working fluids.* Applied Thermal Engineering, 2019. **150**: p. 628-640.

169. Nasir, M.T. and K.C. Kim, *Working fluids selection and parametric optimization of an Organic Rankine Cycle coupled Vapor Compression Cycle (ORC-VCC) for air conditioning using low grade heat.* Energy & Buildings, 2016. **129**: p. 378-395.
170. Yu, H., D. Kim, and T. Gundersen, *A study of working fluids for Organic Rankine Cycles (ORCs) operating across and below ambient temperature to utilize Liquefied Natural Gas (LNG) cold energy.* Energy, 2019. **167**: p. 730-739.
171. Scaccabarozzi, R., et al., *Comparison of working fluids and cycle optimization for heat recovery ORCs from large internal combustion engines.* Energy, 2018. **158**: p. 396-416.
172. Restrepo, G., et al., *Ranking of refrigerants.* Environmental Science & Technology, 2008. **42**(8): p. 2925-2930.
173. Vocale, P., G.L. Morini, and M. Spiga, *Influence of Outdoor Air Conditions on the Air Source Heat Pumps Performance.* Energy Procedia, 2014. **45**: p. 653-662.
174. Chen, J.H. and J.L. Yu, *Dynamic simulation of an air-source heat pump water heater using novel modified evaporator model.* Applied Thermal Engineering, 2018. **144**: p. 469-478.
175. Zhou, F., C.C. Wei, and G.Y. Ma, *Development and analysis of a pump-driven loop heat pipe unit for cooling a small data center.* Applied Thermal Engineering, 2017. **124**: p. 1169-1175.
176. McConkey, A., A. Poon-King, and Z. Yu, *Heating Glasgow University with River Sourced Heat Pumps.* 3rd Iir International Conference on Sustainability and the Cold Chain, 2014. **2014**(1): p. 631-638.
177. Badescu, V., et al., *Avoiding malfunction of ORC-based systems for heat recovery from internal combustion engines under multiple operation conditions.* Applied Thermal Engineering, 2019. **150**: p. 977-986.
178. Guopeng, Y., *Research on Highly Efficient Bottoming Cascaded Thermal Systems Used for Large-Temperature-Difference Waste-Heat-Recovery of Heavy-Duty Diesel Engine*. 2017, Tianjin University. p. p:11-40.
179. Li, J., et al., *Energetic and exergetic investigation of an organic Rankine cycle at different heat source temperatures.* Energy, 2012. **38**(1): p. 85-95.